







**Ordered Structures from Nanoparticles/Block Copolymer Hybrids:  
Ex-situ Approaches toward Binary and Ternary Nanocomposites**

DISSERTATION

zur Erlangung des akademischen Grades

Doktor rerum naturalium

(Dr. rer. nat.)

vorgelegt

der Fakultät Mathematik und Naturwissenschaften  
der Technischen Universität Dresden

von

**HORECHYY ANDRIY**

**geboren am 14 Oktober 1969 in Rawa-Ruska, Ukraine**

**Eingereicht am:** \_\_\_\_\_

Die Dissertation wurde in der Zeit von Mai 2007 bis April 2011 im  
Leibniz-Institut für Polymerforschung Dresden e. V. angefertigt.



# Acknowledgements

There is a long list of persons who made possible and helped me to carry out this work during last four years. The complete of this thesis gives me great pleasure in acknowledging the support and help of these people.

First of all, I would like to express my sincere thanks and appreciation to my supervisor, Prof. Dr. Manfred Stamm for providing me the opportunity to join his group and re-start my research activity, for his support, guidance, constant motivation and encouragement throughout the whole period of my work.

I express my gratitude to Prof. Dr. Nikolaos Zafeiropoulos<sup>a</sup> and Dr. Bhanu Nandan<sup>b</sup> for their continuous support and recommendations to make this work the most efficient as possible. My special thanks are addressed to Dr. Petr Formanek who thought me so much about electron microscopy and who was ready to help everyday and anytime. It was a great pleasure to work with him and it is really scarcely to overestimate the importance of his help. I would like to thank also Dr. Anton Kiriy and Dr. Leonid Ionov for helpful discussions and thesis corrections.

I am thankful to Mr. Andreas Janke for training me with AFM and everytime support, Dr. Bhoje Gowd and Markus Böhme for helping with GISAXS experiments. Dr. Ulrich Oertel and Dr. Frank Simon are acknowledged for carrying out the UVVIS and XPS measurements. I appreciate Mrs. Kerstin Arnhold and Mrs. Liane Häussler for TGA and Mrs. Gudrun Adam for FTIR experiments.

I would like acknowledge Prof. Dr. Alexander Eychmüller<sup>c</sup> and his group for providing gold and platinum nanoparticles, Dr. Daria Mikhailova<sup>d</sup> for performing magnetisation measurements and Michael Göbel for preparation of FIB lamellae.

I am very thankful to our secretaries Mrs. Janett Forkel and Mrs. Claudia Nöh for their excellent assistance in many aspects. Mrs. Ursula Umlauf, Mrs. Anja Rau, Mrs. Karin Wolf and Mrs. Sylvia Schulze are acknowledged for their support with literature from library.

---

<sup>a</sup> Department of Materials Science and Engineering, University of Ioannina, Ioannina, Greece

<sup>b</sup> Department of Textile Technology, Indian Institute of Technology, Delhi, India

<sup>c</sup> Technische Universität Dresden, Physikalische Chemie/Elektrochemie, 01062, Dresden, Germany

<sup>d</sup> Leibniz Institute for Solid State and Materials Research (IFW) Dresden, Germany

My special thanks are addressed to my colleagues and fiends, Dr. Irena Senkowska, Dr. Alla Synytska, Dr. Roman Tkachov, Dr. Vera Bocharova, Dr. Konstantin Demidenok, Ksenia Boyko and all members of our group and whole IPF for their cooperation and support during my work.

I'm greatly thankful to my wife Marta for her support and understanding whilst I spent many of 'family' hours working on this thesis. Without her countenance this work would be much more difficult. I also thank my family, friends here, in Dresden, and in Ukraine for their unfailing faith in success.

This research work was made possible by the financial support from IPF Dresden.

# Table of contents

<b>List of symbols and abbreviations</b>	v
<b>List of figures</b>	vii
<b>List of tables</b>	xiii
<b>Chapter1 Introduction and motivation</b>	1
<b>1.1 Introduction</b>	1
<b>1.2 Goals of the work</b>	3
<b>1.3 Thesis outline</b>	4
<b>Chapter2 Theoretical background and literature overview</b>	5
<b>2.1 Magnetic nanoparticles (MNPs)</b>	5
2.1.1 Magnetism of materials. Superparamagnetism	6
2.1.2 Synthetic routes for preparation of MNPs	13
<b>2.2 Silver nanoparticles (AgNPs)</b>	17
2.2.1 Origin of surface plasmon resonance (SPR)	18
2.2.2 Synthetic routes for preparation of AgNPs	23
<b>2.3 Phase behaviour of block copolymers</b>	25
2.3.1 Microphase separation of BCPs. Phase diagram	25

2.3.2 BCP morphology in thin films	33
2.3.3 Long range ordering of BCPs	37
2.3.3.1 <i>Effect of surface field. Solvent vapour annealing</i>	38
2.3.3.2 <i>Shear- and electric field induced ordering of BCPs</i>	42
<b>2.4 Block copolymers as templates for patterning of nanomaterials</b>	45
2.4.1 In-situ approach	46
2.4.2 Ex-situ approach	48
2.4.3 Step-wise approaches	50
<b>Chapter 3 Experimental techniques</b>	53
<b>3.1 Atomic force microscopy (AFM)</b>	53
<b>3.2 Transmission electron microscopy (TEM)</b>	56
<b>3.3 Grazing incidence small angle X-ray scattering (GISAXS)</b>	59
<b>3.4 Other analytical methods</b>	62
<b>3.5 Materials used and sample preparation</b>	64
<b>Chapter 4 Results and discussion</b>	67
<b>4.1 Choice of block copolymers</b>	67
<b>4.2 Preparation of magnetic nanoparticles (MNPs)</b>	68

4.2.1 Synthesis of Fe <sub>3</sub> O <sub>4</sub> MNPs by thermal decomposition route and their characterisation	69
4.2.2 Synthesis and characterisation of CoFe <sub>2</sub> O <sub>4</sub> MNPs	75
<b>4.3 Synthesis and characterisation of AgNPs</b>	78
<b>4.4 Morphology of neat PS-<i>b</i>-P2VP BCPs</b>	85
4.4.1 Morphology of as-cast PS- <i>b</i> -P2VP thin films	86
4.4.1 Morphology of as-cast PS- <i>b</i> -P4VP thin films	86
4.4.3 Evolution of polymer films morphology during solvent vapour annealing	89
4.4.4 Morphology of solvent annealed PS- <i>b</i> -P2VP thin films	91
4.4.5 Morphology of solvent annealed PS- <i>b</i> -P4VP thin films	94
<b>4.5 Preparation and investigation of MNP/BCP composites</b>	101
4.5.1 MNP/PS- <i>b</i> -P2VP composites: an effect of MNP stabilizing shell density	101
4.5.2 MNP/PS- <i>b</i> -P2VP composites: an influence of BCP composition	105
4.5.3 MNP3/PS- <i>b</i> -P4VP composites: an effect of nitrogen position	107
4.5.4 GISAXS investigation of MNP3/PS <sub>57</sub> - <i>b</i> -P4VP <sub>18</sub> composites	110
4.5.5 Investigation of magnetic properties of MNP/PS- <i>b</i> -PVP composites	116

4.5.6 Annealing of MNP/PS- <i>b</i> -PVP composites in the presence of external magnetic field	118
<b>4.6 Preparation and investigation of AgNP/BCP composites</b>	121
<b>4.7 Fabrication of ternary NP1/NP2/BCP composites</b>	131
4.7.1 Ternary MNP/AgNP/PS- <i>b</i> -PVP composites by direct mixing	131
4.7.2 Step-wise approach towards NP1/NP2/BCP ternary structures	134
<b>Chapter 5 Conclusions and outlook</b>	141
<b>Chapter 6 List of references</b>	147
<b>List of publications and contribution to the conferences</b>	163



## List of symbols and abbreviations

AFM	Atomic force microscopy
AgNP	Silver nanoparticles
AgAc	Silver acetate
Ag(acac)	Silver acetylacetonate
AuNP	Gold nanoparticles
BCC	Body centred cubic
BCP	Block copolymer
C	Cylinders
Co(acac) <sub>2</sub>	Cobalt (II) acetylacetonate
D <sub>0</sub>	Microdomain period
d <sub>NP</sub>	Nanoparticles diameter
DBE	Dibenzyl ether
DCB	1,4-Dichlorobenzene
1,2-DD	1,2-Decanediol
EFTEM	Energy-filtered transmission electron microscopy
Fe(acac) <sub>3</sub>	Iron (III) acetylacetonate
$f_i$	Volume fraction of <i>i</i> block
FFT	Fast Fourier Transform
FIB	Focused ion beam
FTIR	Fourier-transform infra-red spectroscopy
G	Gyroid
GISAXS	Grazing-incidence small-angle X-ray scattering
1,2-HDD	1,2-Hexadecane diol
NPs	Nanoparticles
NRs	Nanorods
NWs	Nanowires
L	Lamellae
LSPR	Localized surface plasmon resonance
M <sub>n</sub>	Number-average molecular weight
M <sub>w</sub>	Weight-average molecular weight
MFM	Magnetic force microscopy
MNP	Magnetic nanoparticles
N	Degree of polymerisation
OIAc	Oleic acid
OIAm	Oleylamine
ODT	Order-disorder transition
OOT	Order-order transition
PDI	Polydispersity index
PdNP	Paladium nanoparticles
PtNP	Platinum nanoparticles
PEO	Polyethylene oxide
PMMA	Polymethyl methacrylate
PL	Perforated lamellae
PS	Polystyrene
PSD	Power spectral density
PVP	Polyvinylpyridine

P2VP	Poly-2-vinylpyridine
P4VP	Poly-4-vinylpyridine
PS- <i>b</i> -PVP	Poly(styrene- <i>block</i> -vinylpyridine)
PS- <i>b</i> -P2VP	Poly(styrene- <i>block</i> -2-vinylpyridine)
PS- <i>b</i> -P4VP	Poly(styrene- <i>block</i> -4-vinylpyridine)
PSSH	Thiol terminated polystyrene
QDs	Quantum dots
q	Scattering vector
q <sub>x</sub> , q <sub>y</sub> , q <sub>z</sub>	Scattering vectors along <i>x</i> , <i>y</i> and <i>z</i> coordinates
R <sub>g</sub>	Radius of gyration
RPM	Revolutions per minute
RT	Room temperature
SAXS	Small-angle X-ray scattering
SD	Standard deviation
SMA	Supramolecular assembly
SPM	Scanning probe microscopy
SPR	Surface plasmon resonance
t	Film thickness
T	Thermodynamic (absolute) temperature
T <sub>g</sub>	Glass transition temperature
TEM	Transmission electron microscopy
TGA	Thermal gravimetric analysis
THF	Tetrahydrofuran
TOPO	Tri- <i>n</i> -octylphosphine oxide
UV-VIS	Ultra-violet visible spectroscopy
XPS	X-Ray photoelectron spectroscopy
α <sub>c</sub>	Critical angle
α <sub>i</sub>	Incident angle
δ	Solubility parameter
θ	Scattering angle
χ	Flory-Huggins interaction parameter

## List of Figures

**Figure 2.1** Typical hysteresis loop of ferromagnetic material illustrating saturation magnetization  $M_S$ , remanent magnetization  $M_R$  and coercivity  $H_C$ . Reproduced from [Kla01].

**Figure 2.2** Schematic representations of single-domain and multi-domain particles (a) and coercivity  $H_C$  as a function of particle size (b). Reproduced from [Kla01]

**Figure 2.3** Typical magnetization curve of superparamagnetic material with no coercivity and remanent magnetization. Reproduced from [Kla01].

**Figure 2.4** Schematic illustration of a localized surface plasmon of a metal sphere. Reproduced from [Wil07].

**Figure 2.5** Diagrams depicting the electric field lines for the (a) dipole, (b) quadrupole and (c) octupole resonances. Reproduced from [Eva05].

**Figure 2.6** Calculated UV-VIS spectra for silver nanocrystals of various shapes: black – extinction, red – absorption, blue – scattering. Reproduced from [Wil06].

**Figure 2.7** Selected architectures of block copolymers.

**Figure 2.8** Schematic representation of ODT induced by the change of temperature.

**Figure 2.9** Concentration profiles of A and B blocks at different conditions: disordered (a), WSR (b) and SSR (c). Reproduced from [Ham98].

**Figure 2.10** Schematics of domain size versus interface curvature.

**Figure 2.11** Calculated phase diagram and equilibrium phase morphologies for bulk *di*block copolymer:  $L$  – lamellae,  $C$  – cylinders,  $S$  – spheres,  $G$  – gyroid,  $S_{cp}$  – closely packed spheres. Modified from [Mat96].

**Figure 2.12** Resumptive phase diagram and equilibrium phase morphologies for bulk PS-*b*-PB-*b*-PMMA *tri*BCP. Reproduced from [Abe00].

**Figure 2.13** Possible configurations of lamellae ordering in BCP films confined at one surface: parallel lamellae with symmetric (a) and asymmetric wetting (b) and perpendicular lamellae (neutral surface) (c).

**Figure 2.14** Theoretical phase diagram and predicted morphologies for *di*BCP films confined between two surfaces: FL – symmetric surface-parallel full lamella, AFL – asymmetric surface-parallel full lamella, PL – surface-perpendicular lamella, HL – half lamella, HY – symmetric hybrid structure, AHY – asymmetric hybrid structure. Adopted from [Fas01].

**Figure 2.15** Schematic representation of the solvent evaporation rate effect on the ordering of BCP thin film. Reproduced from [Kim04].

**Figure 2.16** Schematics of oriented lamellar microdomains in the orthogonal coordination with velocity ( $\mathbf{v}$ ) (or shear) direction along  $x$  axis, velocity gradient ( $\nabla\mathbf{v}$ ) direction along  $y$  axis and vorticity ( $\mathbf{v}\times\nabla\mathbf{v}$ ) direction along  $z$  axis. The BCP domain orientation with the lamellar normal parallel to  $y$  is referred to as “parallel” orientation (a), parallel to  $z$  – as “perpendicular” orientation (b), and parallel to  $x$  – as “transverse” orientation (c). Adopted from [Gup96].

**Figure 2.17** Reversible thermal responsiveness of PS-*b*-P2VP(PDP) SMA loaded with alkyl-stabilized CdSe QDs. Adopted from [Zha09].

**Figure 2.18** Schematic representation of protocol implemented for fabrication of bi-nanoparticles arrays using topographical features of PS-*b*-PMMA BCP thin film. Reproduced from [Son09].

**Figure 3.1** Schematic representation of AFM principle. Adopted from [2].

**Figure 3.2** Force versus distance curve and AFM operating modes. Adopted from [2].

**Figure 3.3** Schematic view of transmission electron microscope (left) and electron beam path with the image formation diagram (bright field imaging) (right). Modified from [4] and [Rei08].

**Figure 3.4** Schematics of GISAXS geometry used for thin film investigation. Modified from [5].

**Figure 3.5** Schematics of GISAXS patterns of lamella forming BCP film with different lamellae orientation. Reproduced from [5].

**Figure 4.1** Schematics of chemical structure of PS-*b*-P2VP and PS-*b*-P4VP block copolymers.

**Figure 4.2** Schematic representation of synthetic route used for preparation of Fe<sub>3</sub>O<sub>4</sub> magnetic nanoparticles by thermal decomposition of iron (III) acetylacetonate precursor. Modified from [Sun02].

**Figure 4.3** TGA curves of MNP1 after 1<sup>st</sup>, 2<sup>nd</sup>, 3<sup>rd</sup> and 4<sup>th</sup> purification cycles.

**Figure 4.4** TEM image (a) and size distribution histogram (b) of MNP1 prepared in the presence OlAc/OlAm as surfactants. Red line – Gaussian fit.

**Figure 4.5** TEM images (a,c) and size distribution histograms (b,d) of MNP2b (a,b) and MNP3 (c,d). Inset on (c) – electron diffraction pattern of MNP3. Red lines – Gaussian fits.

**Figure 4.6** FTIR spectra of MNP1-MNP4 samples prepared by thermal decomposition of Fe(acac)<sub>3</sub> and reactants used during their syntheses.

**Figure 4.7** XPS spectra of MNP3: wide scan spectrum (a); high-resolution C1s spectrum (b); N1s spectrum (count rate x10) (c); P2p spectrum (count rate x10) (d).

**Figure 4.8** TGA traces of MNP1-MNP4 samples.

**Figure 4.9** TEM image (a) and size distribution histogram (b) of CoFe<sub>2</sub>O<sub>4</sub> MNP5 prepared in the presence of TOPO and OlAm as surfactants. Red line – Gaussian fit.

**Figure 4.10** FTIR spectra (a) and TGA curve (b) of MNP5 versus MNP3.

**Figure 4.11** XPS spectra of CoFe<sub>2</sub>O<sub>4</sub> MNP5: wide scan spectrum (a); high-resolution C 1s spectrum (b); N 1s spectrum (count rate x10) (c); P 2p spectrum (count rate x10) (d); high-resolution Co 2p spectrum (e); high-resolution Fe 2p spectrum (f).

**Figure 4.12** TEM images (a,c,e) and size distribution histograms (b,d,f) of AgNP1 (a,b), AgNP2 (c,d) and AgNP3 (e,f) prepared by two-phase method using 1:1, 1:2 and 1:4 AgNO<sub>3</sub>/PSSH weight ratios, respectively.

**Figure 4.13** Schematics of synthetic route used for preparation of PS-covered silver nanoparticles (AgNPs) by reduction of silver precursor (Ag(acac) or AgAc) in the presence of oleylamine.

**Figure 4.14** TEM images (a,c,e) and size distribution histograms (b,d,f) of AgNP4 (a,b), AgNP5 (c,d) and AgNP6 (e,f) prepared by thermal decomposition of AgAc in the presence of OlAm.

**Figure 4.15** FTIR spectra (a) and TGA curves (b) of PS-modified AgNP4-AgNP6 samples.

**Figure 4.16** UV-VIS spectra of THF dispersions of AgNP4, AgNP5 and AgNP6b. C(Ag) = 0.05 mg/ml.

**Figure 4.17** AFM topography images of PS<sub>50</sub>-*b*-P2VP<sub>50</sub> (a) and PS<sub>56</sub>-*b*-P2VP<sub>21</sub> (b) thin film cast from THF. Film thickness ~50 nm (a) and ~30 nm (b).

**Figure 4.18** AFM height images of PS<sub>27</sub>-*b*-P4VP<sub>7</sub> (a), PS<sub>57</sub>-*b*-P4VP<sub>18</sub> (b), PS<sub>22</sub>-*b*-P4VP<sub>22</sub> (c) cast from THF and PS<sub>57</sub>-*b*-P4VP<sub>18</sub> cast from CHCl<sub>3</sub> (d). Film thickness ~30 nm (a,c) and ~50 nm (b,d).

**Figure 4.19** AFM height images of PS<sub>50</sub>-*b*-P2VP<sub>50</sub> thin films annealed in 1,4-dioxane for 30 min (a), 2 hrs (b), 3 hrs (c,d); d – zoomed part of image (c). Film thickness ~50 nm.

**Figure 4.20** AFM height image of PS<sub>50</sub>-*b*-P2VP<sub>50</sub> thin films annealed in 1,4-dioxane for 4 hrs (a) and cross-section profile (b) taken as it is shown on image a. Initial film thickness ~50 nm.

**Figure 4.21** AFM height images of PS<sub>56</sub>-*b*-P2VP<sub>21</sub> thin films annealed in 1,4-dioxane for 3 hrs (a,b) and after “slow” annealing in 1,4-dioxane for 48 hrs (c). Images (b) and (c) were taken after surface reconstruction step. Insets – FFT patterns and magnified image (c) with hexagonal lattice sketch.

**Figure 4.22** AFM height images of PS<sub>57</sub>-*b*-P4VP<sub>18</sub> ~50 nm thin films: as cast (a); after “slow” annealing in 1,4-dioxane for 48 hours (b,c); after “slow” annealing in CHCl<sub>3</sub> for 24, 48 and 96 hours, (d, e and f, respectively). Images (c) and (d) were taken after surface reconstruction step. Insets – FFT patterns of corresponding images.

**Figure 4.23** 2D GISAXS patterns of as-cast (a) and CHCl<sub>3</sub> annealed (b,c) PS<sub>57</sub>-*b*-P4VP<sub>18</sub> thin films obtained at incident angle  $\alpha_i=0.3^\circ$  (a,b) and  $0.2^\circ$  (c) and corresponding scattering profiles along  $q_y$  axis (out of plane cuts) taken at  $q_z=0.39\pm0.02\text{ nm}^{-1}$  and  $0.31\pm0.02\text{ nm}^{-1}$  for  $\alpha_i=0.3^\circ$  and  $0.2^\circ$ , respectively. For each pattern 10 min acquisition time was used.

**Figure 4.24** AFM height images of PS<sub>27</sub>-*b*-P4VP<sub>7</sub> ~30 nm thin films after “slow” annealing in CHCl<sub>3</sub> for 6 (a), 12 (b) and 24 (c) hours. Images were taken after surface reconstruction step. Insets show FFT patterns of corresponding images.

**Figure 4.25** AFM height images of PS<sub>22</sub>-*b*-P4VP<sub>22</sub> ~30 nm thin films after “slow” annealed in 1,4-dioxane for 12 (a), 24 (b) and 36 (c) hours.

**Figure 4.26** AFM height (a,c) and phase (b,d) images of MNP1/PS<sub>50</sub>-*b*-P2VP<sub>50</sub> composite thin films before (a,b) and after solvent vapour annealing in 1,4-dioxane for 3 hours (c,d). MNP1 content – 5.0 wt%. Film thickness ~50 nm.

**Figure 4.27** AFM height (a) and phase (b) images of THF-cast MNP3/PS<sub>50</sub>-*b*-P2VP<sub>50</sub> composite thin film containing 10.0 wt% of MNP3. Film thickness ~50 nm.

**Figure 4.28** AFM height (a,c,e), phase (b,d,f) and TEM (g,h,i) images of MNP3/PS<sub>50</sub>-*b*-P2VP<sub>50</sub> composites thin films containing 2.0 (a,b,g), 5.0 (c,d) and 10.0 wt% (e,f,h,i) of MNP3 after solvent vapour annealing in 1,4-dioxane. Film thickness ~50 nm.

**Figure 4.29** AFM height images of THF-cast (a) and 1,4-dioxane annealed (c) MNP4/PS<sub>50</sub>-*b*-P2VP<sub>50</sub> composite thin films; (b) – cross-sectional profile as shown on image (a); (d) – AFM height image of 1,4-dioxane annealed MNP5/PS<sub>50</sub>-*b*-P2VP<sub>50</sub> thin film. MNP content – 5.0 wt%. Film thickness ~50 nm.

**Figure 4.30** AFM height (a,c) and phase (b,d) images of THF (a,b) and CHCl<sub>3</sub> cast MNP3/PS<sub>56</sub>-*b*-P2VP<sub>21</sub> composite thin films containing 5.0 wt% of MNP3. Film thickness ~30 nm.

**Figure 4.31** AFM phase images of MNP3/PS<sub>56</sub>-*b*-P2VP<sub>21</sub> composite thin films containing 5.0 wt% of MNP3 after solvent vapour annealing in 1,4-dioxane (a) and CHCl<sub>3</sub> (b) for 10 min; (c,d) – TEM images of dioxane annealed MNP3/PS<sub>56</sub>-*b*-P2VP<sub>21</sub> composite thin films containing 2.0 (c) and 5.0 wt% (d) of MNP3. Film thickness ~30 nm.

**Figure 4.32** AFM height images of MNP3/PS<sub>57</sub>-*b*-P4VP<sub>18</sub> composite thin films: as-cast from THF (a) and CHCl<sub>3</sub> (b,c) and after ‘slow’ annealing in CHCl<sub>3</sub> for 24 hours (d,e,f) with MNP3 content of 2.0 (a,d), 5.0 (b,e) and 10.0 wt% (c,f). Film thickness ~50 nm.

**Figure 4.33** Plan view TEM images of unstained MNP3/PS<sub>57-b</sub>-P4VP<sub>18</sub> composite ~50 nm thin films containing 2.0 wt% of MNP3 (a,b); (c) – cross-sectional TEM image of unstained FIB lamella of MNP3/PS<sub>57-b</sub>-P4VP<sub>18</sub> ~160 nm thick film containing 5.0 wt% of MNP3 after solvent vapour annealing in CHCl<sub>3</sub>. The image (c) is presented as negative for better contrast: MNP3 are visualized as bright dots, P4VP cylinders – darker grey areas and PS matrix – brighter grey areas. Inset on image (a) – corresponding FFT pattern.

**Figure 4.34** AFM height images of THF-cast (a) and 1,4-dioxane annealed (b) MNP3/PS<sub>22-b</sub>-P4VP<sub>22</sub> composite thin films containing 5.0 wt% of MNP3; (c) – TEM image of annealed MNP3/PS<sub>22-b</sub>-P4VP<sub>22</sub> film loaded with 5 wt% of MNP3. Film thickness ~30 nm.

**Figure 4.35** AFM height images of THF-cast (a) and CHCl<sub>3</sub> annealed (b) MNP3/PS<sub>27-b</sub>-P4VP<sub>7</sub> composite thin films containing 5.0 wt% of MNP3; (c) – TEM image of annealed MNP3/PS<sub>27-b</sub>-P4VP<sub>7</sub> film loaded with 5 wt% of MNP3. Film thickness ~30 nm.

**Figure 4.36** 2D GISAXS patterns of THF-cast MNP3/PS<sub>57-b</sub>-P4VP<sub>18</sub> thin films containing of 0.0 (a) 2.0 (b), 5.0 (c) and 10.0 (d) wt % of MNP3 taken at  $\alpha_i=0.3^\circ$ ; (e) – corresponding scattering profiles along  $q_y$  axis at  $q_z=0.39\pm 0.02\text{ nm}^{-1}$ .

**Figure 4.37** 2D GISAXS patterns of CHCl<sub>3</sub>-annealed MNP3/PS<sub>57-b</sub>-P4VP<sub>18</sub> thin films containing of 0.0 (a), 2.0 (b), 5.0 (c) and 10.0 (d) wt % of MNP3 taken at  $\alpha_i=0.3^\circ$ ; (e) – corresponding scattering profiles along  $q_y$  axis at  $q_z=0.39\pm 0.02\text{ nm}^{-1}$ .

**Figure 4.38** 2D GISAXS patterns of MNP3/PS<sub>57-b</sub>-P4VP<sub>18</sub> thin films containing 5.0 wt % of MNP3 after “fast” (a) and slow (b) annealing in CHCl<sub>3</sub> taken at  $\alpha_i=0.20^\circ$ ; (c) – corresponding scattering profiles along  $q_y$  axis at  $q_z=0.31\pm 0.02\text{ nm}^{-1}$ . Scattering profile for neat PS<sub>57-b</sub>-P4VP<sub>18</sub> is included for comparison.

**Figure 4.39** MFM height (a,c,e) and phase (b,d,f) images of solvent annealed MNP3/PS<sub>50-b</sub>-P2VP<sub>50</sub> (a,b) and MNP3/PS<sub>56-b</sub>-P4VP<sub>18</sub> (c-f) composite thin films containing 10.0 wt% and 5.0 wt% of MNP3, respectively, obtained with magnetized (a-d) and non-magnetized (e,f) cantilever in dynamic lift mode at lift height of 30 nm.

**Figure 4.40** Magnetization curves of MNP3 and MNP3/PS<sub>57-b</sub>-P4VP<sub>18</sub> composite bulk samples with MNP3 loading of 2.0, 5.0 and 10.0 wt% taken at 5K (a,b) and 300K (c,d): (a) – raw data, (b,c) – data normalized to the content of pure Fe<sub>3</sub>O<sub>4</sub> (based on TGA measurements), (d) – magnified part of graph (c).

**Figure 4.41** AFM height (a,d), phase (b,e) and corresponding TEM images (c,f) of MNP3/PS<sub>50-b</sub>-P2VP<sub>50</sub> composites containing 10.0 wt% of MNP3 annealed in 1,4-dioxane for 3 hours in the presence of external magnetic field oriented perpendicular (a,b,c) and parallel (d,e,f) to the film surface. Film thickness ~50 nm.

**Figure 4.42** AFM height images of THF-cast AgNP4/PS<sub>50-b</sub>-P2VP<sub>50</sub> (a), AgNP6a/PS<sub>50-b</sub>-P2VP<sub>50</sub> (b) and AgNP6b/PS<sub>50-b</sub>-P2VP<sub>50</sub> (c) composite thin films containing 2.0 wt% of AgNP4, 5.0 wt% of AgNP6a and 5.0 wt% of AgNP6b, respectively. Film thickness ~50 nm.

**Figure 4.43** AFM height (a), phase (b) and corresponding TEM (c) images of 1,4-dioxane annealed AgNP4/PS<sub>50-b</sub>-P2VP<sub>50</sub> composite thin films containing 5.0 wt% of AgNP4. Film thickness ~50 nm.

**Figure 4.44** AFM height (a,d), phase (b,e) and corresponding TEM images (c,f) of 1,4-dioxane annealed AgNP5/PS<sub>50-b</sub>-P2VP<sub>50</sub> (a-c) and AgNP6a/PS<sub>50-b</sub>-P2VP<sub>50</sub> (d-f) composite thin films containing 2.0 wt% of AgNPs. Film thickness ~50 nm.

**Figure 4.45** TEM images of AgNP6a/PS<sub>50-b</sub>-P2VP<sub>50</sub> composite thin film after staining with I<sub>2</sub>. AgNPs appear nonuniform (marked with red circles) due to the reaction with I<sub>2</sub>.

**Figure 4.46** Intentionally defocused TEM image of 1,4-dioxane annealed AgNP5/PS<sub>50</sub>-*b*-P2VP<sub>50</sub> composite thin film containing 2.0 wt % of AgNP5 (a) and nitrogen map image of the same area obtained using EFTEM (b); (c) – an overlap of image (a) and inverse FFT of image (b): red-contoured areas depict PVP-rich regions.

**Figure 4.47** TEM (a) and AFM height (b) images of 1,4-dioxane annealed AgNP5/PS<sub>50</sub>-*b*-P2VP<sub>50</sub> (a) and AgNP6b/PS<sub>50</sub>-*b*-P2VP<sub>50</sub> (b) composite thin films containing 5.0 wt% of AgNPs. Circle and arrow point out AgNPs clusters formed atop of thin film after solvent vapour annealing. Film thickness ~50 nm.

**Figure 4.48** Different magnification TEM images 2D lattice formed of AgNP5 nanoparticles along the holes perimeter after annealing of AgNP5/PS<sub>50</sub>-*b*-P2VP<sub>50</sub> composite thin film in 1,4-dioxane vapour for 4 hours. Inset on image (c) – FFT with multiple order 6-fold symmetry peaks. Initial film thickness ~50 nm, AgNP5 content – 5.0 wt%.

**Figure 4.49** UV-VIS spectra of THF-cast (a) and annealed in 1,4-dioxane vapour for 3 hours (b) AgNP5/PS<sub>50</sub>-*b*-P2VP<sub>50</sub> composites thin films with different AgNP5 content. Film thickness ~50 nm.

**Figure 4.50** UV-VIS spectra of as-cast and 1,4-dioxane annealed AgNP5/PS<sub>50</sub>-*b*-P2VP<sub>50</sub> composites containing 5 wt% of AgNP5. Initial film thickness ~50 nm.

**Figure 4.51** AFM height (a) and TEM images (b,c) of 1,4-dioxane annealed AgNP6b/PS<sub>50</sub>-*b*-P2VP<sub>50</sub> composite thin films containing 5.0 (a,b) and 10.0 wt% of AgNP6b. Film thickness ~50 nm.

**Figure 4.52** UV-VIS spectra of THF-cast (a) and solvent annealed (b) AgNP6b/PS<sub>50</sub>-*b*-P2VP<sub>50</sub> composites thin films. For (b) all samples were loaded with 5.0 wt% of AgNP6b. Film thickness ~50 nm.

**Figure 4.53** AFM topography image of ternary MNP3/AgNP5/PS<sub>50</sub>-*b*-P2VP<sub>50</sub> (a) composite thin films (a) versus binary MNP3/PS<sub>50</sub>-*b*-P2VP<sub>50</sub> (b) and AgNP5/PS<sub>50</sub>-*b*-P2VP<sub>50</sub> (c) composites after annealing in 1,4-dioxane for 3 hours. Loading rate of each MNP3 and AgNP5 were 2.0 wt% . Film thickness ~50 nm.

**Figure 4.54** TEM images of MNP3/AgNP5/PS<sub>50</sub>-*b*-P2VP<sub>50</sub> composite thin films after annealing in 1,4-dioxane for 3 hours, containing 2.0 wt% (a) and 10 wt% (b) of MNP3 and 2.0 wt% of AgNP5 (a,b). Image (a) was taken after sample staining with I<sub>2</sub> for 1 hour. Film thickness ~50 nm.

**Figure 4.55** AFM phase images of MNP3/AgNP5/PS<sub>50</sub>-*b*-P2VP<sub>50</sub> ternary composites with different content of nanoparticles: (a) – 2.0 wt% of MNP3 and 2.0 wt% of AgNP5; (b) – 10.0 wt % of MNP3 and 2.0 wt % of AgNP5; (c) – 10.0 wt % of MNP3 and 5.0 wt% of AgNP5. All samples were annealed in 1,4-dioxane for 3 hours. Film thickness ~50 nm.

**Figure 4.56** Schematic representation of step-wise approach used for fabrication of ternary NP1/NP2/BCP composites.

**Figure 4.57** TEM image of citric acid stabilized MNP6 prepared by co-precipitation method with application of ultrasound cavitations.

**Figure 4.58** AFM height images of 1,4-dioxane annealed AgNP6b/PS<sub>50</sub>-*b*-P2VP<sub>50</sub> composite thin films before (a) and after exposure to an aqueous solution of MNP6 (b), PtNP (c) and PdNPs (d) for 24 hours.

**Figure 4.59** SEM image of AgNP6b/PdNP/PS<sub>50</sub>-*b*-P2VP<sub>50</sub> ternary composites prepared by step-wise approach. Appearance of different types of NPs in different phases is evident due to the difference of NPs size.

**Figure 4.60** TEM images of (a) AgNP6b/AuNP/PS<sub>50</sub>-*b*-P2VP<sub>50</sub>, (b) AgNP6b/PdNP/PS<sub>50</sub>-*b*-P2VP<sub>50</sub> and (c) AgNP6b/Pd/PS<sub>57</sub>-*b*-P4VP<sub>18</sub> ternary composites prepared using step-wise approach: AgNP6b content – 2.0 w%. Exposure time–24 h.

**Figure 4.61** SEM images of AgNP6b/AuNP/PS<sub>50</sub>-*b*-P2VP<sub>50</sub> ternary composites prepared by step-wise approach after (a) 60 minutes and (b) 24 hours of AuNPs deposition.

**Figure 4.62** UV-VIS spectra of binary AgNP6b/PS<sub>50</sub>-*b*-P2VP<sub>50</sub> and ternary AgNP6b/AuNP/ PS<sub>50</sub>-*b*-P2VP<sub>50</sub> composite thin films prepared by step-wise approach. Spectra were recorded after different deposition time of gold NPs.



## List of Tables

**Table 2.1** Summary of magnetic parameters of different materials

**Table 2.2** Summary comparison of synthetic methods for preparation of MNPs

**Table 3.1** Peak positions of Bragg reflections for various BCP morphologies

**Table 4.1** List of PS-*b*-PVP BCPs used for fabrication of NP/BCP composites

**Table 4.2** The summary of preparation conditions used for synthesis of MNP1÷MNP5

**Table 4.3** The solubility parameters, vapour pressure and calculated polymer-solvent interaction parameters for pairs of PS, P2VP and P4VP and solvents of different polarity

**Table 4.4** Summary of morphologies observed for as-cast and solvent annealed thin films of PS-*b*-PVP BCPs of various composition



# ***Chapter 1 Introduction and motivation***

## **1.1 Introduction**

From the invention of first transistor in 1947, the microelectronics and integrated circuits (IC) industry started its intensive growth giving the driving force to continuous development of new technologies intended for fabrication of systems and devices with new dimensional limits. As a result, size of many devices used in a modern industry has already approached a nanometer scale. For the last 50 years such minimization well fits famous Moore's law which predicts a doubling of the number of transistors could be placed into silicon IC within a period of approximately every two years.[Moo65]

From the other side, the interest in nanomaterials aroused also from the fact that new properties are acquired by the matter at the length scale between 1 and 100 nm ( $10^2$  to  $10^7$  atoms). For example, as noble metals particles are reduced in size to tens of nanometers, strong absorption band is observed as result of collective oscillation of electrons within conduction band from one side of the particle surface to another. This oscillation has a frequency comparable with the visible light and induces phenomenon called "surface plasmon resonance". Another example of fundamental changes of properties could be observed in magnetic materials, where the superparamagnetic properties become evident if lateral dimensions of ferro- or ferrimagnetic particles are reduced below certain critical value. Magnetic properties of such small particles are strongly influenced by thermal energy fluctuations, which lead to their spins disorientation. Therefore, they demonstrate magnetization behaviour whereas neither remanence nor coercivity exists.

The mentioned above and a number of other aspects of modern technological requirements gave a powerful stimulus to fast growth of scientific effort toward synthetic approaches of fabrication of nanomaterials themselves as well as of methods of their organisation into the nanoscale periodic structures. As a logical result, this exertion finally developed into a solitary scientific discipline known as "nanotechnology", which, in recent years, has become the hottest pursued technology over the world.

There are many subject areas under the banner of "nanotechnology": nanoelectronics, nanomechanics, nanophotonics, nanobiology, nanomedicine, ect. Yet

what is common for the vast variety of nanotechnology disciplines is a dimensional scale. Among other, fabrication of nanoobjects belongs to the one of the most important technological aspects, aiming the building of nanoscale structures, which can act as components, devices or even whole systems in general areas of engineering and science.

Thus, lithographic techniques (i.e. “top-down” approach) enable producing of periodic and irregular features with high accuracy down 20 nm.[Gri09] However, these methods, often restricted to 2D fabrication, also require expensive and sophisticated instrumentation with long processing times. Consequently, such limitations pushed scientists and manufacturers to search for an alternative, more effortless and reasonably cheap ways to produce devices in nanodimensional scale.

The alternative way which could be also applied in order to produce the nanometer scale structures is so called “bottom-up” approach. The main attraction of this method lies in its simplicity in structures formation, based on self-assembling behaviour of variety of materials. The approach exploits natural tendency of matter to minimize its energy and, in case of two-component system, due to the balance between attractive and repulsive forces within a system, to form most favourable arrangement of components with separated well-ordered domains. Among others, block copolymers (BCP) have attract much attention as a powerful and promising tool for the fabrication of such nanoscale ordered structures.[Kim10a,Ban09] Under certain conditions BCPs can self-assemble to form various periodic structures built of phase separated polymer blocks, called microdomains. The microdomain spacing in such structures primary depends on molecular weight, segment size and the strength of interaction between the blocks and typically varies in the range of 10-100 nm.[Bat90]

The self-assembling ability of BCP behaviour offers a simple and cost efficient way to create a periodic surfaces or matrices, whilst the additional selective incorporation of specific nanoadditives (e.g. metal or semiconductor nanoparticles (NPs), nanorods (NRs), quantum dots (QDs) or carbon nanotubes (CNTs) into the one of BCP phases leads to the formation of polymer composites with discrete target properties. Such BCP templates with ordered arrays of nanoadditives are attractive features for potential application in high-density data storage, optoelectronic materials and sensor devices.[For98,Ham03a,Boc05,Har06,Ham09] Therefore, a numerous experimental and theoretical works published recently were dedicated to attempts of realization and investigation of various NP/BCP composites.

## 1.2 Goal of the work

In present work our attention was focused on fabrication of functional BCP-based composites containing nanoparticles, selectively assembled within one of the blocks of BCP matrix.

Magnetic nanoparticles (MNPs) were selected among others since, as for today, there is the least number of successful results reported in literature on their selective incorporation into one of the phases of a BCP matrix, in contrast, for example, to noble metals NPs or QDs. From the application point of view fabrication of periodic arrays of “magnetic domains” with periodicity on nanometer scale is also of interest for potential use in high-density magnetic data storage devices. Therefore, one part of the present work was dedicated to a fabrication of nanocomposites of BCP and pre-synthesized magnetic nanoparticles ( $\text{Fe}_3\text{O}_4$ ,  $\text{CoFe}_2\text{O}_4$ ), selectively incorporated into one of the BCP domains. Magnetic nanoparticles, having apparent affinity toward polyvinylpyridine (PVP) phase were prepared using one-pot synthesis and did not required any additional surface modification. Highly selective nanoparticles segregation into PVP domain of microphase segregated polystyrene-*block*-polyvinylpyridine (PS-*b*-PVP) BCP was achieved upon owing to the presence of sparse stabilizing organic shell on the nanoparticles surface, maintaining at the same time their sufficient dispersive stability during the processing. Experiments were performed with thin films samples.

The second task of present work was fabrication of ternary NP1/NP2/BCP hybrid composites with two different types of nanoparticles, which were selectively localized in different microdomains of phase segregated block copolymer matrix. So far as only few studies have been reported on developing of approaches toward ternary composites,[Boc03,Soh03,Ach09,Kan10,Koh10] creation of an alternative and more straight forward routes toward such systems is still a challenge.

Silver nanoparticles (AgNPs) covered with polystyrene shell were prepared in the frame of this work with the purpose to be incorporated into PS-*b*-PVP matrix as a second additive, which would be selectively localized in the polystyrene block.

Two different approaches were tested to achieve desired three-component system. First, supposed simple blending of block copolymer and two kinds of nanoparticles having specific affinity toward different blocks of BCP in common solvent. After preparation of MNP/AgNP/BCP composite thin film and subsequent solvent vapour

annealing, different domains of microphase segregated PS-*b*-PVP BCP were filled with different type of nanoparticles.

Alternatively, step-wise approach for nanoparticles incorporation was developed and implemented for successful selective nanoparticles incorporation. For this purpose polystyrene stabilized AgNPs were initially mixed with PS-*b*-PVP BCP to produce composite thin films having nanoparticles selectively located within PS microdomains, while second type nanoparticles were deposited from their aqueous solutions into PVP domains of AgNP/PS-*b*-PVP composites. By partition of nanoparticles incorporation procedure into two distinct steps it was also possible to increase effective loading of each type of NPs into BCP matrix.

### **1.3 Thesis outline**

Chapter 1 (current) includes an overall introduction to the topic of the thesis, highlights the aim of the work and briefly presents our achievements, giving also an idea about thesis content and structure.

Chapter 2 contains theoretical overview of properties of magnetic and noble metal nanoparticles, summarizes synthetic methods of their preparation, details theoretical background of phase behaviour of block copolymers and gives a short introduction to the methods of fabrication of BCP-based nanocomposites described in literature.

Chapter 3 presents main experimental techniques used for preparation and characterisation of pre-synthesized nanoparticles and NP/BCP composites and denotes main characteristics of materials used during this work.

Chapter 4 is basically referred to experimental results, including analysis and discussion: It is subdivided into several parts concentrating separately on nanoparticles syntheses, fabrication of composites and investigation of their morphologies. Results on preparation and characterisation of ternary NP1/NP2/BCP composites are also presented in this part.

Chapter 5 presents the summary of the present work and outlook of further research. The list of references and list of publications and contributions to the conferences are given in Chapter 6, at the end of the thesis.

## ***Chapter 2 Theoretical background and literature overview***

### **2.1 Magnetic nanoparticles**

Magnetic nanoparticles (MNPs) are of great interest for researchers from a wide range of disciplines, including magnetic fluids,[Ode04] catalysis,[Tsa04] magnetic resonance imaging,[LiZ05] biotechnology/biomedicine,[Gup05] data storage[Hon10] or environmental remediation.[Tak04]

In order to design nanoparticles for specific application one has to consider many factors, such as size, size distribution, surface functionality, magnetic properties, chemical and dispersion stability, etc. Among other factors, which should be taken into account during MNPs preparation, are their magnetic properties since they significantly differ from that of bulk material having the same chemical composition and crystal structure. These properties are size-dependant and, therefore, could be tuned during particles preparation.

An unavoidable problem associated with particles in nanometer size is their intrinsic dispersion instability over longer periods of time. Such small particles tend to form agglomerates to reduce the energy associated with the high surface area to volume ratio of the nanosized particles. In addition, naked metallic nanoparticles are chemically highly active and easily oxidize in air, resulting generally in loss of magnetism and dispersibility. In most of cases, it is very crucial to protect and stabilize them against degradation during or after the synthesis.

For certain applications small magnetic particles perform best when their size is below a critical value, which is dependent on the material but is typically in a range of 10 to 20 nm. Below this critical size the nanoparticles behave as superparamagnetic. Such individual nanoparticles have a large constant magnetic moment and behave like a giant paramagnetic atom with a fast response to applied magnetic fields with negligible remanent magnetization and coercivity. These features make SPM nanoparticles very attractive for a broad range of biomedical applications, such as magnetic resonance imaging or controlled drug delivery.

On the other hand, the superparamagnetic behaviour of small MNPs is a challenge in the current design of magnetic data storage. Fabrication of MNPs with high

anisotropy constants[Wan07] or with magnetic exchange coupling effects [Sku03] represent some of the possible ways to circumvent this problem. It is also thought that fabrication of small MNPs with high coercivity and anisotropy could lead to significant improvements for the next generation of permanent magnets.[Zen08]

### 2.1.1 Magnetism of materials. Superparamagnetism

The response of a material to an applied external magnetic field is quantified by two parameters: the *susceptibility*,  $\chi_m$ , e.g. the variation of magnetisation  $\mathbf{M}$  with applied field,  $\mathbf{H}$ :

$$\chi_m = \frac{\mathbf{M}}{\mathbf{H}} \quad (\text{Eq. 2.1})$$

and the *permeability*  $\mu$ , the variation of magnetic induction,  $\mathbf{B}$ , with applied field  $\mathbf{H}$ :

$$\mu = \frac{\mathbf{B}}{\mathbf{H}} = \frac{\mu_0 (\mathbf{H} + \mathbf{M})}{\mathbf{H}} \quad (\text{Eq. 2.2})$$

where  $\mu_0 = 4\pi \times 10^{-7} \text{ N/A}^2$  is magnetic constant or magnetic permeability of vacuum.

The relative permeability,  $\mu_r$ , is the ratio of the permeability of a specific medium to the permeability of vacuum. The relation between magnetic susceptibility and relative permeability is expressed by

$$\chi_m = \mu_r - 1 \quad (\text{Eq. 2.3})$$

When a material is placed within a magnetic field, the materials' atomic magnetic moments will be affected. This effect is known as Faraday's the Law of Magnetic Induction. However, materials can behave quite differently in the presence of an external magnetic field. This behaviour is dependent on a number of factors, such as the atomic and molecular structure of the material, and the net magnetic field associated with the atoms. The magnetic moments associated with atoms originate from three different sources. These are the electron orbital motion, the change in orbital motion caused by an external magnetic field, and the spin of the electrons.



In many substances electrons occur in pairs only which spin in opposite directions. So, when electrons are paired together, their opposite spins cause their magnetic fields to cancel each other. Therefore, no net magnetic field exists. Such materials are known as *diamagnetic*. This is a type of magnetism occurring in substances with a small negative magnetic susceptibility ( $\chi_m$ ) and a relative permeability ( $\mu_r$ ) of less than unity. In this case, the individual induced magnetic moments oppose the external field, so there is no overall magnetic moment. Diamagnetic materials are very weakly repelled by external magnetic field and the material does not retain the magnetic properties when the external field is removed. Examples of diamagnetic materials include elements with filled electron shell (i.e., all noble gases), molecular hydrogen, copper, bismuth, water, sodium chloride, and all ions of alkali metals or halogens. Magnetic susceptibility of diamagnetics remains constant with changes of temperature.

Alternatively, materials having unpaired electrons possess a certain magnetic moment and, therefore, stronger react to an external magnetic field. Most of materials with at least one unpaired electron can be classified as *paramagnetic*, having a small and positive susceptibility to magnetic fields. These materials are slightly attracted by a magnetic field and do not retain the magnetic properties when the external field is removed.

The magnetic susceptibility for paramagnetic materials is small and positive. It is inversely related to the temperature and follows *Curie's law* (Eq. 2.4):

$$\chi_m = \frac{C}{T} \quad (\text{Eq. 2.4})$$

where  $C$  is a material specific Curie constant and  $T$  is the absolute temperature. Curie's law is valid under the commonly encountered conditions of low magnetisation, but does not obey in the high-field/low-temperature regime where saturation of magnetisation occurs and magnetic dipoles are all aligned with the applied field. Examples of paramagnetic materials at room temperature include aluminium, manganese, platinum, oxygen (gas and liquid), and rare earth ions.

In contrast to dia- and paramagnetics, *ferromagnetic* materials possess a large positive susceptibility with respect to external magnetic field. Similarly to paramagnetics, ferromagnetic materials have some unpaired electrons so their atoms

have a net magnetic moment. However, they get their strong magnetic properties due to the presence of *magnetic domains*. [Kit46] In these domains, large numbers of atom's moments ( $10^{12}$  to  $10^{15}$ ) are aligned parallel so that the magnetic force within the domain is strong. When a ferromagnetic material is in the unmagnetized state, the domains are nearly randomly organized and the net magnetic field for the part as a whole is zero. When an external magnetic field is applied, the domains become aligned to produce a strong magnetic field within the bulk of ferromagnets.

Even though electronic exchange forces in ferromagnets are very large, thermal energy eventually overcomes the exchange and produces a randomizing effect. This occurs at a particular temperature known as *Curie temperature* ( $T_C$ ). Thus, below the Curie temperature, the ferromagnet is ordered, while above  $T_C$  the material is paramagnetic so that magnetic moments are in a completely disordered state.

*Antiferromagnetic* materials, such as chromium, CoO or FeO, are similar to ferromagnetics, but the exchange interaction between neighbouring atoms leads to the anti-parallel alignment of the atomic magnetic moments. Therefore, the magnetic field cancels out and the material appears to behave in the same way as a paramagnetic. Like ferromagnetic materials antiferromagnetics become paramagnetic only above a transition temperature, known as the *Néel temperature*,  $T_N$ .

*Ferrimagnetism* is usually observed in compounds, which have more complex crystal structures than pure elements. Within these materials the exchange interactions lead to parallel alignment of magnetic moments in some of the crystal sites and anti-parallel alignment in others. The material breaks down into magnetic domains, just like a ferromagnetics so that magnetic behaviour is also very similar.

At an atomic level the magnetic properties depend upon interaction between the electrons associated with the metal ions. Here, adjacent atomic magnetic moments appear locked in anti-parallel with their neighbours. However, the magnitude in one direction is weaker than in opposite, leading thus to an overall magnetic moment. Thus, ferrimagnetic materials usually have lower saturation magnetisations compared to a ferromagnetics. An examples are most of ferrites  $MFe_2O_4$  ( $M=Fe, Co, Mg$ ) with the unit cell containing metal ions at different crystal sites.

The relationship  $\chi_m - T$  for ferro-, ferri- and antiferromagnetic materials is described by the *Curie-Weiss law*:

$$\chi_m = \frac{C}{T - \Theta} \quad (\text{Eq. 2.5})$$

where  $\Theta$  represents  $T_C$  or  $T_N$ , respectively.

Magnetic hysteresis loops are commonly used to describe the properties of ferromagnetic and ferrimagnetic materials. Figure 2.1 illustrates a typical hysteresis loop in which the magnetization of the material,  $M$ , is measured relative to the applied magnetic field,  $H$ . When a sufficiently large field is applied, the majority of magnetic domains within the material align with the field. The magnetization in this state is described by the saturation magnetization,  $M_S$ .

As the field is reduced, the domains in the material no longer align perfectly, however, they will partially remain aligned even when external field approaches zero. The magnetization at that point is denoted as the remanent magnetization,  $M_R$ . When the field is further decreased until a point when the magnetization becomes zero, that point is denoted as the coercive field,  $H_C$ , that is the magnitude of the field which must be applied to bring the net moment of the sample to zero.[Get08]

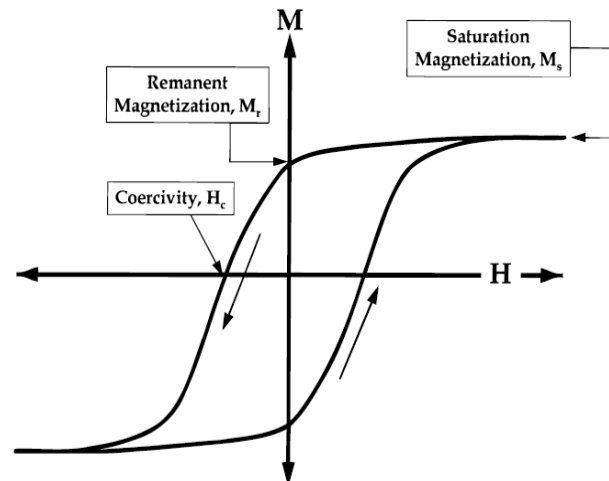


**Figure 2.1** Typical hysteresis loop of ferromagnetic material illustrating saturation magnetization  $M_S$ , remanent magnetization  $M_R$  and coercivity  $H_C$ . Reproduced from [Kla01].

Depending on a  $H_C$ , ferro- and ferrimagnetic materials are subdivided into two groups, so called ‘hard magnets’ having relatively high  $H_C$  values and, therefore, wide hysteresis loop, and ‘soft magnets’ with low coercivity and negligible or no hysteresis.

Another factor strongly affecting the shape of the materials’  $M-H$  curve (i.e. shape of hysteresis loop) is *magnetic anisotropy*. This term means that the magnetic properties of the material depend on the direction in which they are measured. When magnetic anisotropy exists the total magnetisation of a ferromagnet  $M_s$  will prefer to lie along one direction, called *easy axis*.

The energy per unit volume, associated with this alignment (i.e. anisotropy energy) is given by:

$$E_a(\theta) = K_a \sin^2 \theta \quad (\text{Eq. 2.6})$$

where  $K_a$  is the anisotropy constant, and  $\theta$  is the angle between  $M_s$  and easy axes. There are several causes of magnetic anisotropy, which could be pointed out, in particular, magnetocrystalline, shape, exchange anisotropy [Mei56] or anisotropy induced by magnetic annealing, irradiation or plastic deformation.

*Magnetocrystalline* anisotropy is an intrinsic property of a material, independent of grain size and shape. It could be determined by studying magnetization behaviour along different crystallographic axes. Depending on the crystallographic orientation of the sample in the magnetic field, the magnetization reaches saturation at different field strengths, defining in such a way easy and hard axes of magnetisation. For example, for *bcc* Fe crystals the easy magnetisation direction lies parallel to  $\{100\}$  crystallographic axis, for *fcc* Ni it is oriented along  $\{111\}$  direction, while for hexagonal  $\epsilon$ -Co crystals are magnetisation easiest in direction, that is parallel to  $\{0001\}$  axis.

If the magnetized sample is none-spherical then one or more specific directions occur which also represent easy magnetization axes, solely caused by the crystal shape. This phenomenon is known as *shape anisotropy*, which is an extrinsic property of material (e.g. history dependant). Its existence is caused by the presence of magnetic charges or poles at the surface of magnetized object. These surface charges themselves, acting in isolation, create induced demagnetizing field in direction opposite to the magnetization that produces them. Such demagnetisation field is stronger along a short axis, resulting, thus, in an easy magnetisation direction along the long anisotropic axis.

The arrangements of aligned spins in unmagnetized ferro- or ferrimagnetic materials are subdivided into domains throughout the material volume. The driving force for the formation of magnetic domains is the need to minimize the field energy of a magnetized material. The boundary between two neighbouring domains, the *domain wall*, suggests a smooth gradual rotation of the vector moment between domains in the absence of applied magnetic field.[Get08] Typically, the domain wall ranges in thickness from few to few hundreds of nanometres for most of the materials.[Den02]

The balance of the energy necessary to form a domain wall and the energy conserved by the existence of domains defines the lower limit of a domain size and, therefore, the formation of domains is a finite process. Frenkel and Dorfman first

theorized the single-domain nature of particles below certain critical size.[Fre30] In a large particles, energetic considerations favour the formation of domain walls and magnetization reversal, occurs through the nucleation and motion of these walls. As a particle size decreases, the number of magnetic domains per particle decreases down to the limit where it is energetically unfavourable for a domain wall to exist.[Kit46]

Starting from certain critical size ( $d_{SD}$ ) magnetic materials exist as *single-domain particles*. Thus, changes in the magnetization can no longer occur through domain wall motion but via the coherent rotation of spins (Fig. 2.2a) resulting in larger coercivity compared to multi-domain particles. Due to the high magnetic moment of each single domain particle compared

to that of individual atoms, saturation magnetization is reached at significantly lower strengths of an applied magnetic fields and, when the field is decreased, demagnetization is only dependent on coherent rotation of the spins, which results in large coercive forces.[Sto48]

The critical size for a magnetic particle to reach the single domain limit is defined as:

$$d_{SD} = \frac{18\sqrt{AK_a}}{\mu_0 M_s^2} \quad (\text{Eq. 2.7})$$

where  $A$  is the exchange constant,  $K_a$  is the effective anisotropy constant and  $M_s$  is the saturation magnetization.[Fre09] For most magnetic materials, this diameter is in the range 10–200 nm, though for some high-anisotropy materials the single domain limit can be several hundred nanometres (Table 2.1).

The amount of energy required to reverse the magnetization of single domain particle over the energy barrier from one stable magnetic configuration to the other is

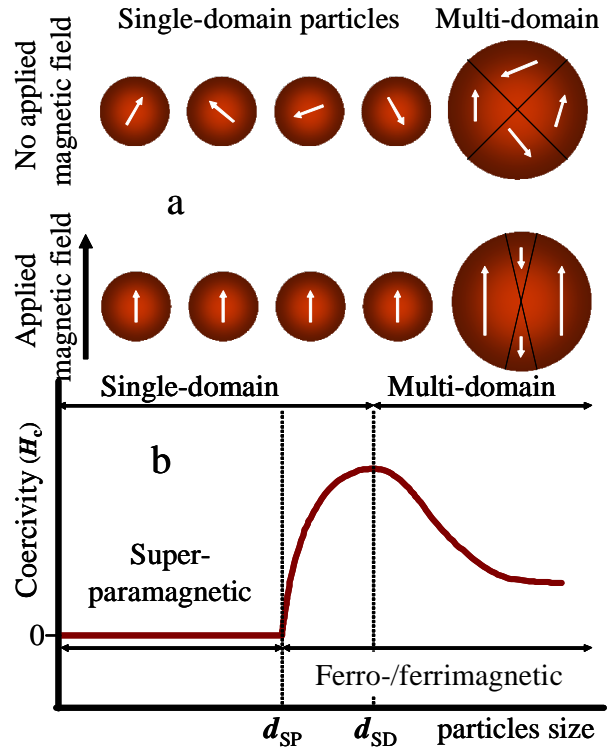


**Figure 2.2** Schematic representations of single-domain and multi-domain particles (a) and coercivity  $H_c$  as a function of particle size (b). Reproduced from [Kla01]

proportional to  $KV/k_B T$  where  $V$  is the particle volume,  $k_B$  and  $T$  are the Boltzmann's constant and temperature, respectively.[Nee49] Thus, as the particle size continues to decrease below the single domain dimension ( $d_{SD}$ ), the spins are increasingly affected by thermal fluctuations lowering remanent magnetization and coercivity gradually (Fig.2.2b).

**Table 2.1 Summary of magnetic parameters of different materials[Kla01, Lac05]**

Substance	Bulk saturation magnetization ( $M_s$ ) at 298 K (emu/cm <sup>3</sup> ) [Cul09]	$T_C$ (K) [Lac05]	Effective anisotropy constant $K_a$ (kJ cm <sup>-3</sup> ) [Lac05]	Single domain limit ( $d_{SD}$ ) for spherical particles, nm [Kla01]
Co (hcp)	1370[Lac05]	1394	530	70
Fe (bcc)	1714	1043	48	14
Ni	485 [Lac05]	631	-4.5	55
$\gamma$ -Fe <sub>2</sub> O <sub>3</sub>	364 [Tar03]	948	4.7 [Tar03]	166
Fe <sub>3</sub> O <sub>4</sub>	480	858	-13	128
CoFe <sub>2</sub> O <sub>4</sub>	425	793	180	70[Chi03]
MnFe <sub>2</sub> O <sub>4</sub>	400	573 [Cul09]	2.5 [Ron01]	
NiFe <sub>2</sub> O <sub>4</sub>	270	858	-6.9	

If the thermal energy is large enough to completely overcome the anisotropy energy, the magnetization approaches zero, and for particles with size below certain limit ( $d_{SP}$ ) no remanent magnetisation and coercivity is observed when external magnetic field is removed (Fig. 2.3). Such behaviour is referred as *superparamagnetic*. It is analogous to conventional paramagnetism, however, instead of individual electronic spins displaying this fluctuating response, it is the collective moment of the entire particle, hence is termed *superparamagnetism*. [Bea55]

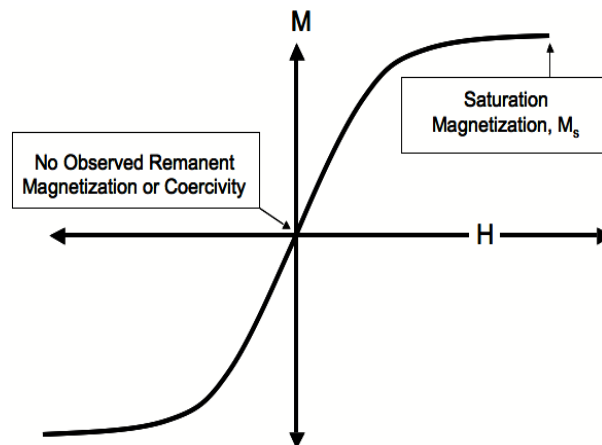


**Figure 2.3** Typical magnetization curve of superparamagnetic material with no coercivity and remanent magnetization. Reproduced from [Kla01].

The temperature at which the thermal energy can overcome the particles anisotropy energy is referred to as the blocking temperature,  $T_B$ . [Nee49] For an array of particles with a distribution in volume,  $T_B$  represents an average characteristic temperature and can be affected by inter-particle interactions as well as by timescale over which the measurement is performed due to the magnetic relaxation of the particles. [Maj06] Thus, in addition to  $d_{SP}$ , the blocking temperature defines the conditions for transition from ferromagnetism to superparamagnetism and ascribes the magnetic behaviour of an assembly of magnetic particles in nanometer length scale.

### 2.1.2 Synthetic routes for preparation of MNPs

Magnetic nanoparticles have been synthesized with a variety of different shape, [Par00] and composition, including pure metals, such as Fe and Co, [Sus96, Pun01] iron oxides, [Sun02, Bee95] spinel ferrites  $MFe_2O_4$  ( $M = Mn, Co, Ni$ ) [Sun04, Che01] as well as alloys, such as  $CoPt_3$  and  $FePt$ , [Par01, Sun00] ranging in size typically from 1 to 100 nm.

The pure metals, such as Fe and Co, have the highest saturation magnetisation and magnetic susceptibility (Table 2.1). The same is referred to the magnetic properties of these materials existing as nanoparticles. However, these transition metal nanoparticles are extremely sensitive to oxidation enhanced by their large surface area and under atmospheric conditions readily oxidize to form monooxides, which are antiferromagnetic. [Rot58] Currently, a lot of research effort is directed on the developing of ways to prevent oxidation of metal NPs, for instance, by covering them with inert toward oxidation shells. [Wan05a] Therefore, iron oxides (both  $\gamma-Fe_2O_3$  and  $Fe_3O_4$ ) as well as other ferrites  $MFe_2O_4$ , despite their initial lower magnetization, are of great potential as stable to oxidation nanomagnetic materials with diverse application possibilities in oxygen rich environments.

During the last decades, many studies have been carried out to establish efficient chemical synthetic routes toward highly monodisperse, composition- and shape-controlled magnetic nanoparticles. Several methods including co-precipitation, hydrothermal synthesis, microemulsion approach or thermal decomposition were applied to synthesize high-quality magnetic nanoparticles.

One of the oldest techniques for the synthesis of nanoparticles is the precipitation from solution. Classical aqueous precipitation allows the preparation of various oxide-based magnetic nanoparticles. The major advantage of precipitation methods is that large quantities of particles can be synthesized in a very simple way. The first controlled synthesis of magnetic nanoparticles based on alkaline precipitation of iron precursors was presented by Massart in 1981.[Mas81]  $\text{Fe}_3\text{O}_4$  nanoparticles were precipitated from  $\text{FeCl}_3$  and  $\text{FeCl}_2$  solution at basic pH using this synthetic procedure. The particles were roughly spherical, 10 nm in diameter, but showed high degree of polydispersity (more than 50% size distribution). Applying size selective titration it was possible to reduce the size distribution down to 5%.[Mas95] Later on, alkaline precipitation was also extended for preparation of other ferrite nanoparticles  $\text{MFe}_2\text{O}_4$ , where  $\text{M}=\text{Co},\text{Mn}$ ,[Tou90] ( $\text{Mn},\text{Zn}$ ) [Auz99] or ( $\text{Zn},\text{Ni}$ ).[Zin99]

Main characteristics (e.g. size, composition or crystal structure) of co-precipitated MNPs are strongly dependent on the reaction temperature, pH value, the type of precursor salts used and ionic strength of the media, as well as on the reactants ratio. An application of surfactants, such as fatty acids[She99] or polymeric materials[Lee96] as stabilizing (and/or reducing) agents, have been shown to be an efficient method to better control over the particles size distribution during precipitation, protecting them at the same time from oxidation. Nevertheless, co-precipitation methods do not ensure perfect control over the particle size distribution and, especially, particles shape if compared with other methods.

With the hydrothermal (or solvometal) approach a broad range of uniformly sized nanocrystals can be successfully produced, including noble metal, fluorescent, magnetic, semiconductor materials.[Wan05b] This strategy is based on phase transfer and separation mechanism occurring at the solid-liquid interface present during the synthesis. Hydrothermal reactions are typically carried out in reactors or autoclaves under high temperature and pressure and belong to the one of the efficient ways to grow dislocation free single crystal particles of different size. For examples, using solvometal approach, Li and coworkers were able to successfully synthesize both ferrite nanoparticles ( $\text{MFe}_2\text{O}_4$ ,  $\text{M}=\text{Fe},\text{Co}$ ) of 9-12 nm in diameter and single-crystalline microparticle with tunable size of 200-800  $\mu\text{m}$ . [SiS05,Den05] However, although hydrothermal technique is very versatile, the main drawbacks are the complicated equipment required and slow reaction kinetics.



Using the microemulsion technique metallic or metal alloys [Cap04] as well as iron oxide and ferrite-type magnetic nanoparticles of various size and shape have been synthesized.[Con99,Liu00a,Liu00b,Woo03] An inverse water-in-oil microemulsion is often used to run this type of synthesis where the micelles formed act as nanoreactors for particle formation. By mixing of two water-in-oil microemulsions each containing the one of the reactants, the reaction between them becomes possible and nanoparticles are formed inside the micelles. The size and shape of micelles, and, thus, of nanoparticles, can be controlled through variation of the surfactant and the water-to-surfactant molar ratio.[Cap04,Gan10] The inverse microemulsion method has been also proved as a robust one to produce core-shell particles having magnetic core and non-magnetic protective shell.[Lop03]

Although many types of magnetic nanoparticles have been synthesized in a controlled manner using the microemulsion method, the particle size and shape were still varying over a relative wide range. The diversity of compounds that could be synthesized in microemulsions is quite narrow and the yield of nanoparticles is low compared to other methods. Large amounts of solvents are usually necessary to synthesize appreciable amounts of material, thus, this method is not a very efficient one and also a rather difficult to scale-up.

Thermal decomposition of organometallic complexes is the next technique, which is widely used for the preparation of magnetic nanoparticles. Colloidal suspensions of metallic Co and Fe particles were prepared for the first time by decomposition of  $\text{Co}_2(\text{CO})_8$  and  $\text{Fe}(\text{CO})_5$  at elevated temperature in the presence of surfactants.[Tho66,Hes66] Decomposition of organometallic complexes accompanied by nanoparticles formation could be driven not only by temperature (thermolysis), but also by light (photolysis), or sound (sonolysis). Although acoustic cavitations applied to a metal precursor or their organic solutions typically induce formation of amorphous and porous nanomaterials, they could be further annealed to form crystalline phases.[Sus96] Through the years carbonyl decomposition was extended for fabrication of nanorods,[Pun01] alloy- and core-shell nanoparticles.[Par01] This method appears as extremely attractive due to its simplicity, reproducibility and scaling up potential. However, thermal decomposition of carbonyls has one serious drawback compared with other methods, namely, extremely high toxicity of reaction by-products.

Recently, S.Sun and co-workers have demonstrated that thermal decomposition of iron(III) acetylacetonate ( $\text{Fe}(\text{acac})_3$ ) in the presence of stabilizers, such as oleic acid and

oleylamine, leads to the formation of magnetite nanoparticles with narrow size distribution.[Sun02] This route also provides a good control over the shape, composition and crystallinity of produced nanoparticles. This procedure exhibits flexibility in the choice of metal precursor, enabling different NP compositions such as  $\text{Fe}_3\text{O}_4$ ,  $\text{CoFe}_2\text{O}_4$ ,  $\text{MnFe}_2\text{O}_4$ , etc., to be synthesized starting from a stoichiometric mixture  $\text{Fe}(\text{acac})_3$ ,  $\text{Co}(\text{acac})_2$ , and  $\text{Mn}(\text{acac})_2$  precursors.[Sun04] Decomposition of metal acetylacetonates and metal carbonyls mixtures was also used to synthesize an alloy-type MNPs such as FePt,[Sun00] CoPt,[Che02] core-shell nanoparticles [Wan05a] and nanorods with tuneable size and aspect ratio.[Pou09]

In most cases thermal decomposition of precursors containing cationic metal centers (e.g. metal acetylacetonates or carboxylate complexes [Jan04,Par04]) leads directly to the metal oxides, while, if the metal in the precursor is zero-valent, such as in carbonyls, pure metal nanocrystals are initially formed. In this case two-step procedure can be used to produce high-quality oxide nanoparticles as well.[Hye01] The ratio of the starting reagents including organometallic compounds, surfactant and solvent during thermal decomposition syntheses are the decisive parameters for the control of the size and morphology of magnetic nanoparticles. The reaction temperature, reaction time, as well as aging period may also be crucial for the precise control of size and morphology.

The advantages and disadvantages of the abovementioned synthetic methods are briefly summarized in Table 2.2. It is obvious, that in terms of composition, particles' size and morphology control, thermal decomposition routes seem to be the best methods developed to produce high quality MNPs with sufficient yield.

**Table 2.2 Summary comparison of synthetic methods for preparation of MNPs**

Synthetic method	Synthetic conditions	Reaction time	Reaction medium	Size distribution	Shape control	Yield
<b>co-precipitation</b>	ambient 20-90°C	minutes	water	relatively narrow	relatively poor	high scalable
<b>hydrothermal synthesis</b>	high T and pressure	hours – days	water /ethanol	very narrow	very good	medium
<b>microemulsion</b>	ambient	hours	organic solvents	relatively narrow	good	low
<b>thermal decomposition</b>	inert 100-350°C	hours – days	organic solvents	very narrow	very good	high scalable

In present work ferrite-type MNPs ( $\text{Fe}_3\text{O}_4$  and  $\text{CoFe}_2\text{O}_4$ ) were prepared using thermal decomposition of metal acetylacetonate precursors.[Sun02,Sun04] Synthetic

approach was modified in order to achieve affinity of as-prepared nanoparticles toward polyvinylpyridine domain of PS-*b*-PVP block copolymers.

## **2.2 Silver nanoparticles**

Noble-metal nanoparticles have fascinated scientists because of their colorful colloidal solutions long before semiconductors and their applications became an integral part of modern technology. It is well known, that gold colloids were used as a pigment of ruby-colored stained glass dating back to the 17th century.[Tur85] Faraday recognized that the red color is due to metallic gold in colloidal form.[Far57] The strong color of small particle colloidal solutions, which is, undoubtedly, the main characteristic feature of noble metal NPs, is caused by the phenomena, known as surface plasmon resonance (SPR).

SPR characteristics of metal nanoparticles are determined by a set of physical parameters that are particles size, composition, structure (e.g., solid or hollow) and dielectric constant of the surrounding medium. Moreover, anisotropic shaped NPs have SPR intensity that is stronger compared with nonanisotropic ones. In principle one can tailor and fine-tune the properties of metal nanocrystals by controlling any one of these parameters, but the flexibility and scope of change are highly sensitive to the specific parameter. Thus, the examination of the surface plasmon resonance absorption is part of a large ongoing research field to investigate properties on the nanometer scale.[Eus06,LuX09]

Of the three metals (Ag, Au, Cu) that display plasmon resonances in the visible spectrum, silver exhibits the highest efficiency of plasmon excitation.[Tan07] Silver nanoparticles interact with light more efficiently than particles of the same dimension composed of any known organic or inorganic chromophore. Silver is also the only material whose plasmon resonance can be tuned to any wavelength in the visible spectrum.[Eva05] The light-interaction cross-section for Ag can be about ten times that of the geometric cross-section, which indicates that the particles capture much more light than is physically incident on them.[Eva04]

Plasmonic materials are emerging as key platforms for applications that rely on the manipulation of light at small length scales. Metal nanoparticles generate enhanced

electromagnetic fields that affect the local environment. These electromagnetic fields are significantly stronger than observed from the bulk material. Therefore, rough metallic surfaces or metal nanoparticles under plasmonic excitation can act as antennae achieving scattering cross section enhancements of several orders of magnitude.[Cam98] This field enhancement is responsible for the host of extraordinary optical phenomena exhibited by metal nanostructures, such as surface-enhanced Raman scattering,[Kne97,Nie97,Cam98] superlensing,[Fan05] or light transmission through optically thick films.[Ebb04] Apart of material characteristics, also particle spatial arrangement determine the profile and intensity of the observed optical response.[Gao06,Mol04,Koe04] Nevertheless, exploiting the field enhancement offered by plasmonic materials for practical applications is still limited by lack of methods that can generate these nanostructures with geometric control and regularity in simple and reproducible manner. Therefore, a part of present work is concerned with the fabrication of ordered AgNPs arrays by exploiting block copolymer self-assembly (Chapter 4.6).

### 2.2.1 Origin of surface plasmon resonance (SPR)

*Plasmon resonance* is an optical phenomenon arising from the collective oscillation of conduction electrons in metals when the electrons are disturbed from their equilibrium positions. Such a disturbance can be induced by an electromagnetic wave (light), in which the free electrons of a metal are driven by the alternating electric field to coherently oscillate relative to the lattice of positive ions.

For a bulk metal of infinite size, the frequency of oscillation  $\omega_p$  is defined as:

$$\omega_p^2 = N_e e^2 / \epsilon_0 m_e \quad (\text{Eq. 2.8})$$

where  $N_e$  is the number density of conduction electrons,  $\epsilon_0$  is the dielectric constant of vacuum,  $e$  is the charge of an electron, and  $m_e$  is the effective mass of an electron.[Moo06] Thus, the bulk plasmon frequency of a particular material depends only on its free electron density and for most metals occurs in the UV range, while alkali and some transition metals such as Cu, Ag, and Au exhibit plasmon frequencies in the visible region.

Because the penetration depth of an electromagnetic wave inside of metal is limited (typically less than 50 nm), only plasmons caused by surface electrons are significant and are commonly referred to as *surface plasmons*. If a surface plasmon is associated with an extended metal surface, it is called a *propagating surface plasmon*. The frequency of a propagating surface plasmon is lower than the bulk frequency, with the theoretical frequency value of  $\omega_p / \sqrt{2}$  for the metal-vacuum interface boundary conditions.[LuX09]

If the collective oscillation of free electrons is confined to a finite volume as with small metal particle, the corresponding plasmon is called a *localized surface plasmon* with the theoretical frequency of  $\omega_p / \sqrt{3}$  for a metal sphere placed in vacuum.[Moo06]

Figure 2.4 shows the interaction between the electric field of incident light and the free electrons of a metal sphere whose size is smaller than the wavelength of light. The electric field of incident light displaces particles electrons from equilibrium in one direction, creating a dipoles, that can switch direction with the change in electric field. Generated restoring force tend to recombine charges, resulting thus in oscillatory motion of electrons. When the frequency of the dipole oscillation approaches that of an incident light, a resonance condition is reached, leading to constructive interference and the strongest signal for the plasmon. Such a condition is referred to as surface plasmon resonance (SPR), or localized surface plasmon resonance (LSPR).

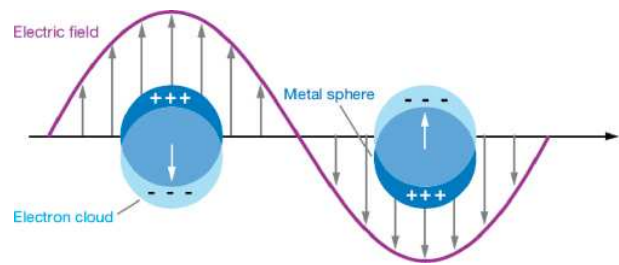


**Figure 2.4** Schematic illustration of a localized surface plasmon of a metal sphere. Reproduced from [Wil07].

Surface polarization (e.g. charge separation) is the most important factor that determines the frequency and intensity of plasmon peak for a given metal because it provides the main restoring force for electron oscillation. Thus, exact position and shape of SPR peak are primary defined by the material properties, namely, by materials electron density and dielectric constant.

Indeed, any variation in particle size, shape, or dielectric environment will change the surface polarization and, thus, position of resonance peak. Polarisation of the surrounding medium, which is induced by oscillation of metal electrons, reduces the restoring force for the electrons thereby shifting the SPR to a lower frequency. Thus, by

controlling the dielectric constant of the surrounding medium, the wavelength of the SPR can be fine-tuned to a desired position.

With increasing of particles size, plasmonic peak maximum shifts towards the red region of the visible spectrum. Moreover, for larger particles, higher order peaks (i.e. *quadrupole*, *octupole* SPR) become noticeable, arising from the existence of two or more polarization directions (Fig. 2.5).

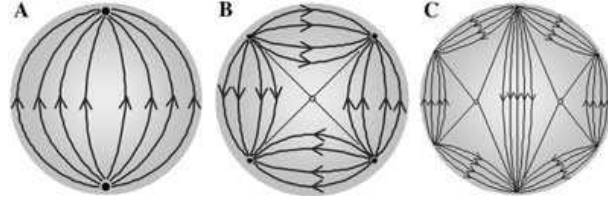


**Figure 2.5** Diagrams depicting the electric field lines for the (a) dipole, (b) quadrupole and (c) octupole resonances. Reproduced from [Eva05].

Gustav Mie [Mie08] was the first who theoretically explained the plasmon properties of metal colloids by solving Maxwell's equation for an electromagnetic light wave interacting with small spheres having the same frequency dependent dielectric constant as the bulk metal. The solution of this electro-dynamic calculation with appropriate boundary conditions for a spherical object leads to a series of multipole oscillations for the extinction cross-section of the particles ( $\sigma_{ext}$ ). For nanoparticles with radius  $r$  much smaller than the wavelength of light ( $r \ll \lambda$ ), where only the dipole oscillation dominates (*dipole approximation*), the solution of Maxwell equations results in the following relationship:

$$\sigma_{ext}(\omega) = \frac{12\pi\omega r^3}{c} \epsilon_m^{3/2} \frac{\epsilon_i(\omega)}{[\epsilon_r(\omega) + k\epsilon_m]^2 + \epsilon_i^2(\omega)} \quad (\text{Eq. 2.9})$$

where  $r$  is the particle radius,  $\omega$  is the angular frequency of the exciting light,  $c$  is the speed of light,  $\epsilon_m$  is dielectric constant of surrounding medium. While the  $\epsilon_m$  is assumed to be frequency independent, the dielectric function of material itself is complex and dependent on energy (i.e. frequency) of incident light:  $\epsilon(\omega) = \epsilon_r(\omega) + i\epsilon_i(\omega)$ , where  $\epsilon_r$  and  $\epsilon_i$  are the real and imaginary parts of dielectric function of material, respectively. The  $k$  factor is related to the particles shape anisotropy: it takes on a value of 2 for the case of a sphere, but increases to as large as 20 for the particle geometries with high aspect ratios.[Lin99]

For spherical particles the resonance condition is fulfilled when  $\epsilon_r(\omega) = -2\epsilon_m$  and  $\epsilon_i$  is small or weakly dependent on  $\omega$ :

$$\sigma_{ext}^{res}(\omega) = \frac{12\pi\omega r^3 \epsilon_m^{3/2}}{c \epsilon_i} \quad (\text{Eq. 2.10})$$

Since exact solutions for Maxwell's equations are known only for spheres, shells, spheroids, and infinite cylinders, a discrete dipole approximation (DDA) is applied to solve the equations for other geometries. In a DDA approach, the nanoparticle is discretized into an array of  $N$  polarizable points with each point representing the polarizability of a discrete volume of material. The presence of an electromagnetic field gives these points a dipole moment and each dipole is polarized by an electric field that includes contributions from the incident light and every other dipole in the array.

Wiley and coworkers provided a detailed overview of effect of particles shape on SPR.[Wil06] They applied Mie and DDA approximations to estimate SPR peaks of water dispersed silver nanoparticles having similar size but different shapes (Fig. 2.6). Calculations showed that 40 nm sphere-shaped silver particles primarily absorb blue light ( $\lambda_{max}=410$  nm), letting the red and green wavelengths combine to give silver sols their characteristic yellow color (Fig. 2.6 a).

In contrast, for a 40-nm cube (Fig. 2.6 b) DDA calculated spectra exhibits more peaks due to the several distinct symmetries for dipole resonance conditions compared with only one for the sphere.[Fuc75] Similar trends were observed for the tetrahedron (Fig. 2.6 c) and octahedron (Fig. 2.6 d), although they have reduced scattering cross-

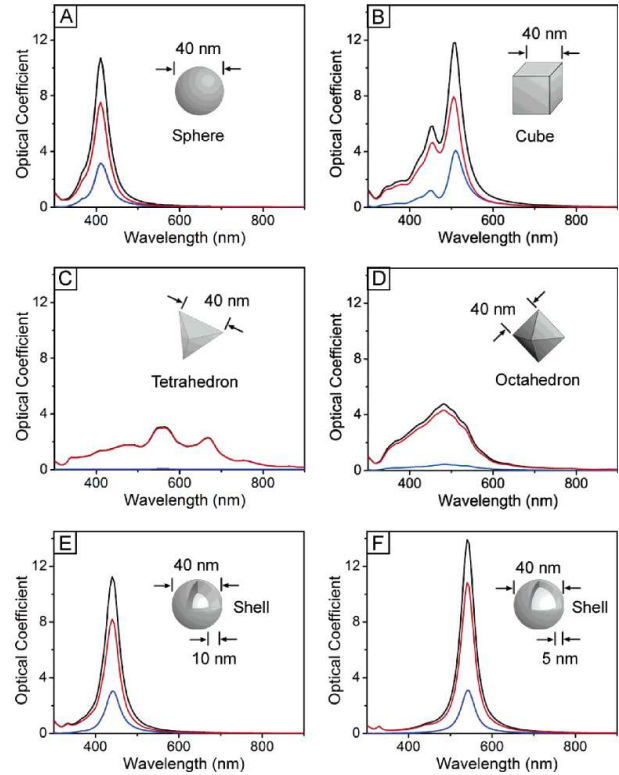


**Figure 2.6** Calculated UV-VIS spectra for silver nanocrystals of various shapes: black – extinction, red – absorption, blue – scattering. Reproduced from [Wil06].

sections because of different symmetries and smaller volumes. The tendency of surface charges to accumulate at sharp corners increases their separation distance and thereby reduces the restoring force for electron oscillation.[Aiz05] The weaker restoring force in turn manifests itself in a red-shift of the resonance peak compared with that of the sphere.

The calculated resonance peak of hollow spheres (or shells) is also red-shifted relative to that of a sphere (Fig. 2.6 e). In this case the incident electric field induces surface charges both inside and outside the shell. Under electromagnetic excitation it is energetically more favorable for charges to have the same sign on both inner and outer particles surface.[Pro03] As a consequence, for thinner shells, stronger coupling between charges inside and outside of the shell causes greater charge separation and further red-shift (Fig. 2.6 f).

The behaviour of metal/dielectric composite materials, where particles are embedded in an inert host medium and isolated from each other, could be ascribed with the Maxwell-Garnett theory (effective-medium concept).[Lin99] The particle dimension and interparticle distances are considered to be infinitely small compared with the wavelength of the interacting light. The relationship between dielectric constants of host medium  $\epsilon_m$ , metal particles  $\epsilon_p$  and composite itself  $\epsilon_c$  could be presented as:

$$\frac{\epsilon_c - \epsilon_m}{\epsilon_c + \kappa\epsilon_m} = f_p \frac{\epsilon_p - \epsilon_m}{\epsilon_p + \kappa\epsilon_m} \quad (\text{Eq. 2.11})$$

where  $f_p$  is the volume fraction of the metal nanoparticles in the composite material. Screening parameter  $\kappa$  is also related to the shape of the nanoparticles, similar to Mie theory and has a value of 2 for spherical particles. For long nanorods oriented with their axes of revolution parallel to the direction of the incident light  $\kappa = 1$ , while for flat discs oriented with their axes of revolution perpendicular to the incident light its value approaches infinity. However, in contrast with the Mie theory,  $\epsilon_m$  is also a complex function depending on the frequency of light.



## 2.2.2 Synthetic routes for preparation of silver NPs

Synthesis of noble metal nanoparticles can be performed using several methods, including reactions in microemulsions,[Pil00] solvometal synthesis,[Wan05b] thermal decomposition [Hir04] or reduction of metal precursor,[Bru94] which are commonly used also for fabrication of other types of colloids.

One of the most established methods involves aqueous reduction of Au or Ag salts in the presence of citrate anions.[Kim06a,Don09] Resulting colloids appear electrostatically stabilized due to the adsorption of citric ions to the particle surfaces during growth. Particles size distribution and shape could be tuned by gentle adjustment of reaction pH.[Pat08] However, since the flocculation of such colloids is irreversible, an application of chemisorbed organic ligands is essential to permit further handling.

A two-phase method, developed by Brust and co-workers, based on reduction of metal precursors, allows the preparation of metal organosols directly from water-soluble metal salts.[Bru94,HeS01] By stirring aqueous solutions metal salts (e.g.  $\text{HauCl}_4$ ,  $\text{AgNO}_3$ ,  $\text{AgClO}_4$ ) with toluene containing phase transfer agent, such as tetraoctylammonium bromide (TOAB), a two-phase system is initially formed, containing metal precursors on organic phase. Next, a measured quantity of capping agent, typically a long-chain alkanethiol, is added to the solution while stirring, and then a reducing agent (e.g.  $\text{NaBH}_4$  or hydrazine) is rapidly introduced to nucleate nanocrystals. The average particles size is coarsely tuneable by adjusting the ratio of the stabilizing agents to metal salt, whereas size-selective precipitation is employed to narrow the initial size distribution.

Similar to the magnetic nanoparticles synthesis, microemulsion [Pil00] and solvometal [Wan05b] approaches have been used to prepare silver NPs. The advantages and disadvantages of these methods are the same as in case of MNPs (discussed in Chapter 2.1.2).

High temperature decomposition of metal precursors in the presence of stabilizing agents has been widely used to produce noble metal NPs.[Par07a] In general, preparation scheme involves injection of metal precursors in high-boiling point inert solvents along with a combination of stabilizing ligands, such as alkanethiols, amines or carboxylic acids, at elevated temperature. Similar to other synthetic methods, NPs size

can be coarsely tuned by the ratio of capping groups to metal salt, while size-selective precipitation yields particles with polydispersity of ~5%.

Recently, Hiramatsu and Osterloh reported on simple and large-scale synthesis of gold and silver nanocrystals through mild reduction of metal precursors in the presence of oleylamine at elevated temperature.[Hir04] This method has been proved to produce nearly monodisperse particles with no need of time- and solvent-consuming size-selective precipitation steps. Here, oleylamine serves a function of both reducing and stabilizing agents, simplifying, thus, optimisation of reaction conditions significantly if compared to more complex multicomponent systems. Particles size and distribution could be tuned either by variation of reaction temperature (e.g. type of solvent) and/or by metal precursor/oleylamine ratio. Our experimental observation show, that apart of reaction temperature and components ratio, the protocol of precursor addition also significantly affects on particles size. Importantly, as-prepared nanoparticles could be easily modified with various thiol-containing molecules, including end-functionalized polymers, via ligand-exchange procedure due to stronger affinity of thiol moieties toward noble metal surfaces compared to amino groups. Taking into account all advantages, this method with some modifications was used in present work for the fabrication of polymer-coated silver nanoparticles.

## 2.3 Phase behaviour of block copolymers

Block copolymers (BCP) represent an important class of polymeric materials, consisting of two or more chemically dissimilar polymer subunits (blocks), covalently bond to each other.[Ham98] Depending on the number of blocks, they could be classified as *di*block (*di*BCP), *tri*block copolymers (*tri*BCP), etc. The blocks can be connected in a variety of ways (linear, star-shaped, etc). For example, if one of the constituting (blocks **A**) is bonded with either one or several types of side chains (block **B**), it is defined as of comb-shaped or graft-block copolymer. Examples of **A-b-B** *di*block, **A-b-B-b-A** *tri*block and *graft-BCP* **A-g-(B)<sub>n</sub>** structures are schematically shown on Figure 2.7:

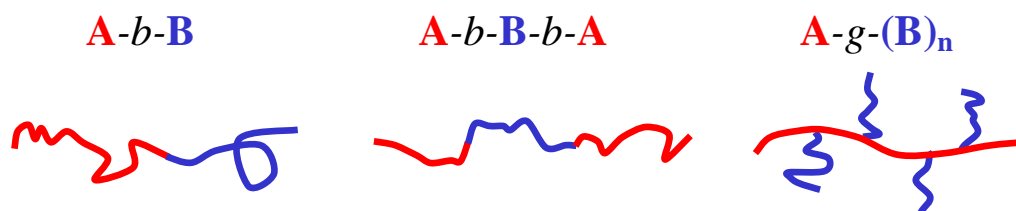


**Figure 2.7** Selected architectures of block copolymers.

The development in synthesis of block copolymers originates from the discovery of termination-free anionic polymerization, which made possible the sequential addition of monomers to various “living” polymer chains.[Szw56] As a consequence of the “living” nature of these reactions, the resulting block and overall molecular weight distributions are nearly ideal, i.e.  $M_w/M_n$  is close to 1.0, where  $M_w$  and  $M_n$  represent the weight and number-average molecular weight, respectively. Since the original studies of anionic block copolymerization in the 1950s, variety of new polymerization methods (e.g. condensation, Ziegler-Natta, RAFT, ATRP, etc.) have contributed to an expanding number of block copolymer classes (e.g. ABC) and novel architectures (e.g. *graft*BCP).[Had02]

### 2.3.1 Microphase separation of block copolymers. Phase diagram

A combination of two different homopolymers to form polymer blends is the simplest way to tune and improve desired properties and characteristic of

material.[YuL06, Bre04, Sie08] However, even a very slightly unfavourable interaction causes polymers to phase separate. The reason is in the entropy of mixing. Mixed polymers undergo phase separation by the same mechanisms as small molecule mixtures, that is, by nucleation and growth or by spinodal decomposition. Small molecule mixtures can have an unfavourable energetic interaction, but still mix, because their entropy of mixing overcomes it. In contrast, polymers are much larger molecules, and their entropy of mixing is correspondingly smaller, therefore most of the polymers do not mix. Thus, some additives, such as compatibilizers or plastisizers usually must be introduced in order to prevent undesired polymer demixing.

In this aspect BCPs are much attractive for material engineering purposes because of a presence of covalent linkage between blocks. Such joint between blocks create significant difference in behaviour of polymer blends and BCPs. Owing to their mutual repulsion but restricted by a covalent linkage, dissimilar blocks self-assemble into separate domains in such a way, that minimize a contact area of unlike components and form a periodic structure of defined morphology and dimensions, when oppositely acting driving forces are balanced. This is in contrast to macrophase separation process typically observed for immiscible homopolymer blends. As a consequence, a wide range of equilibrium morphologies are observed in BCP.[Fre96]

The resulting BCP morphology and symmetry are dependant on architecture, molecular weight and temperature, as well as on the volume fraction and chemical nature of individual blocks. Characteristic dimensions of domains are primary defined by  $R_g$  of corresponding individual blocks and lie in a range of 10-100 nm for most of BCP having molecular weight ranging 20-200 kg mol<sup>-1</sup>. [Bat90]

Phase behaviour of BCPs in bulk was systematically investigated in numerous experimental [Haj94,Bat94,Kha95,Sch96,Flo01] and theoretical [Mat94,Mat96,Gro98] works and could be ascribed by a Flory-Huggins theory.[Flo41,Flo42,Hug41]

Undisturbed polymer chain is characterized by Gaussian chain conformation having a radius of gyration  $R_g \sim N^{1/2}$ . However, when a covalently linked second block is introduced to a system, two competing processes simultaneously contribute to the equilibrium chain conformation. First of all, incompatibility of individual blocks drives them to phase separate and increase domain in size (positive enthalpy of demixing  $\Delta H_d$ ). This results in non-uniform density distribution within domain, lowered toward domain center. Therefore, stretching of the polymer chains takes place

to fulfil density fluctuations. Such stretching results in reduced number of possible chain conformations compared to unstretched one, in such a way decreasing the conformational entropy,  $\Delta S_c$ . The covalent junctions between individual blocks, localised within domain interface, additionally reduce entropy of the system  $\Delta S_i$ . Thus, the Gibbs free energy of demixing  $\Delta G_d$ , could be represented as:

$$\Delta G_d = \Delta H_d - T\Delta S_c - T\Delta S_i \quad (\text{Eq. 2.12})$$

The sign of  $\Delta G_d$  indicates if the transition from homogeneous mixing (disordered state) to a microphase separated structures (ordered state) is favourable or not. Thus, such transition occurs ( $\Delta G_d > 0$ ) when enthalpy contribution dominated over entropic one. For simplest *di*BCP, demixing enthalpy  $\Delta H_d$  is defined as a function of Flory-Huggins segmental interaction parameter  $\chi$ :

$$\chi = \left[ \epsilon_{AB} - \frac{1}{2}(\epsilon_{AA} + \epsilon_{BB}) \right] \quad (\text{Eq. 2.13})$$

where  $\epsilon_{AB}$ ,  $\epsilon_{AA}$  and  $\epsilon_{BB}$  represent segmental interaction energies (i.e. enthalpy) for **A-B**, **A-A**, and **B-B** monomer units, respectively. For most pairs of monomers the interaction parameter is positive and small, typically  $\chi = 0.001 - 0.1$ . By introducing entropic contribution dimensionless Flory-Huggins interaction parameter  $\chi$  could be presented in a form, which describes following temperature dependence:

$$\chi = C_1 / T + C_2 \quad (\text{Eq. 2.14})$$

where  $C_1$  and  $C_2$  are BCP specific parameters, representing an entropic and enthalpic terms, respectively.

Entropy change is inversely proportional to the total degree of polymerisation of BCP  $N = N_A + N_B$ , where  $N_A$  and  $N_B$  are degree of polymerisation of blocks **A** and **B**, respectively. On the other hand, it is also dependent on volume fraction  $f$  of each block in BCP:

$$f_A = N_A / N, f_B = N_B / N \quad (\text{Eq. 2.15})$$

Thus, in terms of parameters  $\chi$  and  $f$ , the Gibbs free energy of demixing,  $\Delta G_d$ , for *di*BCP could be presented as follows:

$$\frac{\Delta G_d}{kT} = \frac{f_A}{N_A} \ln(f_A) + \frac{f_B}{N_B} \ln(f_B) + \chi \cdot f_A \cdot f_B \quad (\text{Eq. 2.16})$$

The ability of BCP to microphase separate is primary determined by a product  $\chi N$ : an increasing of  $N$  or reducing of temperature (and thus increasing in  $\chi$ ) results in transfer from disordered to ordered state (or vice versa). This transition is known as *order-disorder transition* (ODT) (Fig. 2.8).

At values of  $\chi N < 10.5$  BCPs exist in disordered state with no interface between individual segments (Fig.2.9 a). [Lei80] Apart of small-chain BCP (low  $N$ ), disordered state is also realized at sufficiently high temperatures, for

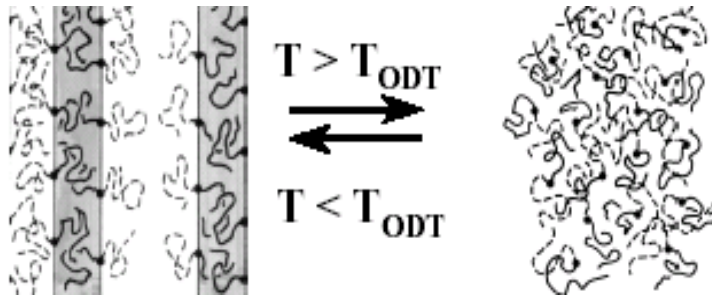


**Figure 2.8** Schematic representation of ODT induced by the change of temperature.

example in polymer melt, where an entropic contribution overcome an enthalpic one. The absence of composition gradients and low  $\chi$  values result in essentially unperturbed Gaussian coils with radius of gyration that scale as  $R_g \sim N^{1/2}$ .

For small  $\chi N$ , close to the order–disorder transition (up to  $\chi N \approx 12$  for symmetric *di*blocks), the composition profile (density of either component) is approximately sinusoidal. Such conditions are defined as *weak segregation regime* (WSR) (Fig. 2.9 b). At the region of high values ( $\chi N \gg 10.5$ ) *strong segregation regime* (SSR) occurs and is characterized by the presence of sharp interface between individual domains (Fig. 2.9 c). [Ham98]

Equilibrium is governed by a compromise between minimizing both interfacial area and coil stretching, while maintaining a constant density. The resulting ordered microstructures (microdomains) are characterized by periodicities that scale as  $D \sim N^{2/3}$ . Ordered-state symmetry, interfacial curvature and microdomain shape are primarily dictated by the BCP composition.

Finally, the region of  $\chi N$  between 10.5 and  $\sim 50$  is considered as the *intermediate segregation regime* (ISR).[Ham98] In this state phase behaviour is more complicated compared to WSR and SSR. Here, a delicate balance between entropic and enthalpic contributions to the overall

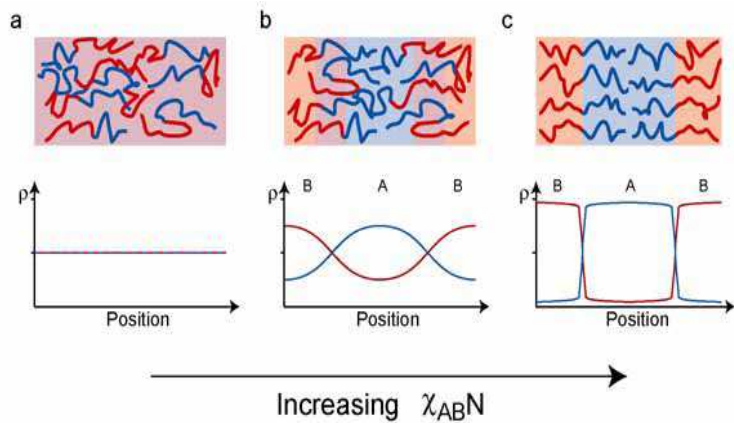


**Figure 2.9** Concentration profiles of **A** and **B** blocks at different conditions: disordered (a), WSR (b) and SSR (c). Reproduced from [Ham98].

free energy controls the phase behaviour. In addition to classical translational entropy, internal chain-stretching effects, that can be asymmetrically distributed within the microstructure are important.[Bat94]

The effect of block volume fraction  $f$  on the equilibrium morphology can be understood by considering the preferred curvature of domain interfaces. Figure 2.10 schematically shows an asymmetric block copolymer ( $f_A = 0.25$ ,  $f_B = 0.75$ ) with flat and curved domain interfaces. If the interface is flat (Fig. 2.10a), the thickness of the each of two domain is proportional to their volume fractions and the thickness of the **B** part ( $D_B$ ) is three times that of the **A** one ( $D_A$ ). Curving the domain interface towards the smaller **A** phase (Fig. 2.10 b) reduces chain stretching in the **B** domain but increases chain stretching in the **A**. Thus, the compromise between stretching in the **A** and **B** domains leads to an optimal interfacial curvature that depends on the block volume fractions and packing lengths. In the absence of segment asymmetry the optimal interface curves toward the smaller block and the curvature increases as the block volume fraction decreases.[Mat02,Gra06]

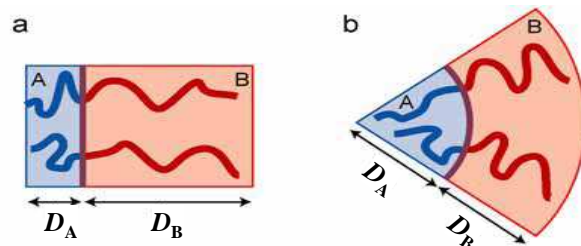


**Figure 2.10** Schematics of domain size versus interface curvature.

This trend in preferred domain curvature is reflected in the succession of “classical” *di*block copolymer bulk morphologies. Phase diagram (Fig. 2.11) graphically represent a variety of possible equilibrium phase morphologies for bulk *di*BCP, where the combination of two parameters ( $\chi N$  and  $f$ ) determines equilibrium phase morphology of BCP at certain conditions.[Mat94,Mat96]

In the simplest case of non-crystalline flexible coil *di*block copolymers lamellar, gyroid, cylindrical or spherical phases are formed, depending on the volume fractions of each block  $f$ , degree of polymerisation  $N$  and Flory-Huggins interaction parameter  $\chi$ . [Ham98,Had02]

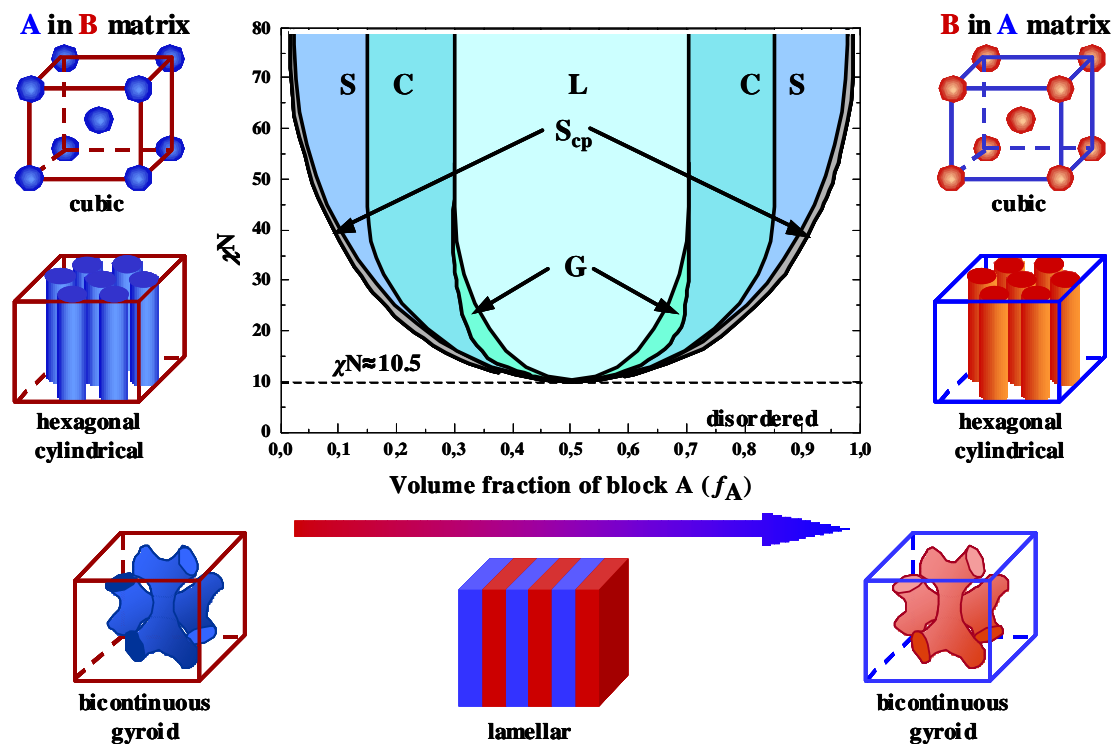


**Figure 2.11** Calculated phase diagram and equilibrium phase morphologies for bulk *di*block copolymer: *L* – lamellae, *C* – cylinders, *S* – spheres, *G* – gyroid, *S<sub>cp</sub>* – closely packed spheres. Modified from [Mat96].

For equal or nearly equal volume fractions ( $f_A = f_B$ ), the **A** and **B** blocks form lamellar (**L**) domains with flat interfaces. As  $f$  decreases, the morphologies with the minimum interfacial free energy changes from lamellar ( $0.34 < f < 0.50$ ) to bicontinuous double gyroid ( $0.28 < f < 0.34$ ) to cylindrical ( $0.13 < f < 0.28$ ) to spherical ( $f < 0.13$ ). [Liu94]



The double gyroid (**G**) morphology [Haj94] is consistent with trend in preferred interfacial curvature. In this three-dimensional bicontinuous network structure, the minority block forms tube-like struts that connect together at 3-fold nodes with an average curvature less than cylindrical and greater than lamellar domains.

At lower volume fractions of either A or B block, the minor block forms curved cylindrical (**C**) domains and for the lowest volume fractions the minority block forms even more tightly curved spherical (**S**) domains. Thus, the preferred curvature of domain interfaces is useful for a qualitative understanding the equilibrium morphologies formed in block copolymers.

As could be seen from Figure 2.11, phase boundaries are vertical in strong segregation regime, but become curved with lowering of  $\chi N$ . This assumes that for BCPs with volume fractions near the phase boundary between two morphologies, thermally induced order-to-order transition (OOT) may also occur since the Flory-Huggins interaction parameter  $\chi$  varies as the temperature changes.

Experimentally obtained *di*BCP phase diagrams, indeed, display certain dissimilarities compared to theoretically predicted.[Bat94,Kha95,Sch96,Flo01] These differences could be explained by effect of additional parameters that are not considered in theoretical simulations.

For example, phase diagrams, constructed by Bates et al.[Bat94] for a series of different linear *di*BCPs show analogous shifts of morphologies symmetry with respect to  $f = 1/2$  axis. Such shifts, in particular, are attributed to a segment conformational asymmetry parameter,  $\epsilon_{ca}$ , which gauges differences in the space-filling characteristics between blocks:

$$\epsilon_{ca} = \beta_A^2 / \beta_B^2 \quad (\text{Eq. 2.17})$$

$$\beta^2 = \frac{R_g^2}{V} = \frac{a^2}{6\nu} \quad (\text{Eq. 2.18})$$

where  $a$  is statistical segment length, and  $\nu$  – segment volume.

In addition to composition axis asymmetry, other morphologies, theoretically not predicted, were observed experimentally. For example, an intermediate between **L** and **C** perforated-lamellar (**PL**) phase similar to the classical **L** phase, but with a hexagonal arrangement of perforations in the thinner minority layers through which the majority layers are connected was found experimentally for PS-*b*-PI [Kha95] and PS-*b*-P2VP

[Sch96] *diBCP*. Interestingly, for PS-*b*-PI stability of **G** phase was observed only near the ODT with its further transformation to a **PL** at higher values of  $\chi N$ . In contrast, Hajduk et al. reported that **PL** phase was only metastable and eventually converts to the **G** phase after sufficient annealing.[Haj97,Vig98]

Hexagonally modulated lamella (**HML**) and layered hexagonally packed channels (**HPC**) as additional intermediate phases have been observed in asymmetric poly(ethylenepropylene)-*b*-poly(ethylethylene) (PEP-*b*-PEE) *diblock* copolymer near the order-disorder transition.[Ham93,Ham94] Phase transitions between ordered morphologies were indicated by the temperature dependence of the dynamic shear modulus and identified using small angle neutron scattering experiments.

The transition from amorphous to crystalline lamella ( $\mathbf{L}_{am} \Rightarrow \mathbf{L}_{cr}$ ) with increasing of  $\chi N$  was reported by Floudas *et al* for PI-*b*-PEO *diblock* copolymer system.[Flo01] Another structure observed for *starBCP* is the double-diamond (**D**) phase similar to **G**, but where the interweaving lattices are four-fold coordinated. However, this structure is absent for a *diBCP* systems.[Haj97]

For linear *triBCPs*, in particular, for ABC types, the variety of possible bulk morphologies becomes much wider compared to *diBCPs*. Here, in addition to all ‘classical’ *diBCP* symmetries, a reach variety of morphologies that often combine individual ones from *diBCP* systems, are observed.

An example of resumptive phase diagram for PS-*b*-PB-*b*-PMMA *triBCP* with schematic representation of different experimentally observed morphologies is presented on Figure 2.12.[Abe00] If the volume fractions of all three components are

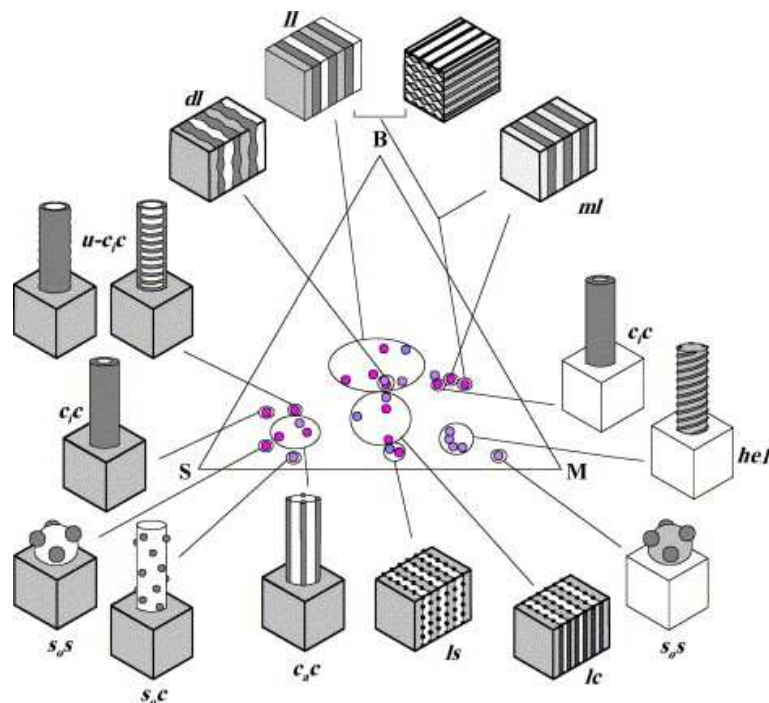


**Figure 2.12** Resumptive phase diagram and equilibrium phase morphologies for bulk PS-*b*-PB-*b*-PMMA *triBCP*. Reproduced from [Abe00].

nearly the same, alternating or modulated lamella are formed ( $ll$ ,  $ml$ ). On the other hand, if two blocks dominate over the third one, they form lamella with interfacial arrangement of minor-block cylinders or spheres ( $lc$  and  $ls$ ). However, if one of the blocks dominates, it typically forms a matrix perturbed by spheres, cylinders or even helices composed of minor blocks, combined in different manner ( $cc$ ,  $ss$ ,  $sc$ ,  $hel$ ), depending on the ratio of the volume fractions of individual blocks.

### 2.3.2 BCP morphology in thin films

Ordering in block copolymers induced by the presence of a surface has been of considerable interest both theoretically and experimentally. In contrast to a bulk behaviour, BCP thin films have an advantage of simultaneous microphase separation and domain orientation with respect to the solid substrate.[Rus89] Besides BCP composition and molecular weight, domain structure and orientation in thin films are dependent on the surface energies of the blocks and on geometrical constraints introduced by the confinement in a thin film.[Ham09] Consequently, the presence of a substrate and/or a free surface introduces additional driving forces for morphological development due to preferential segregation of one block to the substrate or surface.[Fas01]

For a lamellae-forming  $di$ block copolymer confined in a thin film, some of the possible configurations are shown in Figure 2.13. By convention, if the same block is found at each boundary, the BCP is said to have symmetric ‘wetting’. However, if one block preferentially ‘wets’ the interface with the substrate or air, ‘wetting’ is described

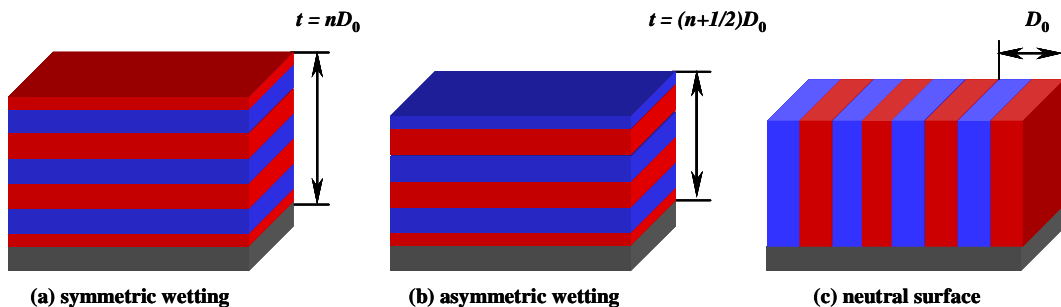


**Figure 2.13** Possible configurations of lamellae ordering in BCP films confined at one surface: parallel lamellae with symmetric (a) and asymmetric wetting (b) and perpendicular lamellae (neutral surface) (c).

as asymmetric. At equilibrium, symmetric films are stable at a total film thickness  $t = nD_0$ , whereas asymmetric films are stable at  $t = (n+1/2)D_0$ , where  $n$  is integer ( $n=1,2,3,4..$ ) and  $D_0$  is the lamellae domain spacing of BCP. When the thickness of the film is not commensurate to the equilibrium lamellar spacing, either holes or islands are nucleated on the film surface to adjust the local film thickness to the preferred quantized values.[Maa92]

The influence of the confinement and the interfacial interactions on the morphology of *di*block copolymers in thin films have been extensively studied theoretically within mean field theories [Pic97,Mat97,Hui00] and Monte Carlo simulations.[Gei99a,Gei99b,Wan00] The films are assumed to be confined between two surfaces thus, preventing formation of terraces. The calculations suggest that if there is no preference for blocks to wet the confining surfaces (neutral surface), the microdomains adopt perpendicular orientation having lower free energy, independently of gap between the confining surfaces.[Hui00]

However, for *di*BCP thin films an appearance of more complex (hybrid) morphologies was experimentally observed [Mor97,Fas00] and predicted theoretically.[Mat97,Fas00] Using self-consistent mean-field (SCF) calculations applied to the two-dimensional model (e.g. substrate-supported films) phase diagram of symmetric *di*BCP thin film morphologies was constructed by Fasolka and co-workers.[Fas00, Fas01] Stable morphologies calculated in these studies, assigned to the regions of their appearance on phase diagram are schematically presented on Figure 2.14. The ordinate gives the reduced film thickness,  $t / D_0$ , while abscissa represents the measure of the asymmetry of the surface energies:  $R = S_2^B / S_1^B$ . The sign of  $R$  distinguish symmetric (+) or asymmetric (-) boundary conditions.

Compositionally symmetric *di*block copolymers were modelled on a lattice as chains  $N$  statistical segments in length, each segment occupying one lattice space, with an **A/B** segmental repulsion quantified by the Flory-Huggins interaction parameter  $\chi_{AB}$ . The substrate boundary ( $S_1$ ) was energetically selective of the **B** segments with an interaction energy of  $S_1^B$ , whereas the (impenetrable) free surface boundary ( $S_2$ ) was selective for either **B** (symmetric boundary conditions,  $S_1^B = S_2^B$ ) or **A** segments (asymmetric boundary conditions,  $S_2^A = -S_2^B$ ), but always with an interaction energy of lower magnitude than the substrate interaction, i.e.  $|S_1| > |S_2|$ .

For symmetric surface energies ( $R = 1$ ) a single morphological transition occurs from **FL** (symmetric surface-parallel full lamella) to **PL** (perpendicular lamella) when film thickness decreases below  $t/D_0 \approx 0.3$ .

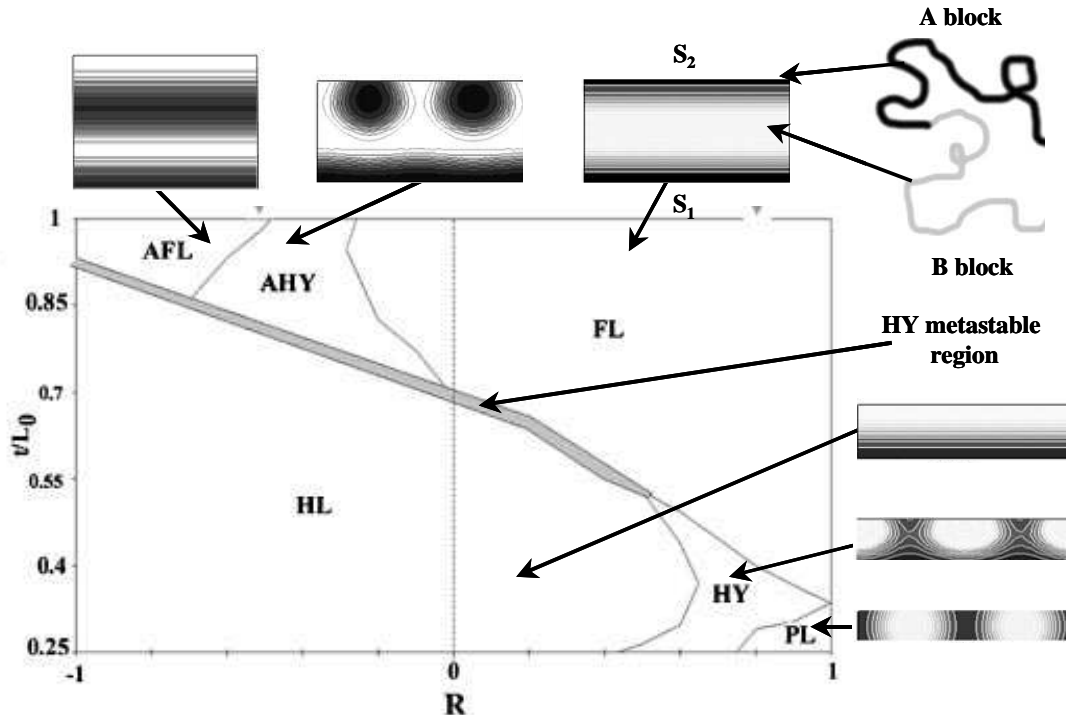


**Figure 2.14** Theoretical phase diagram and predicted morphologies for *di*BCP films confined between two surfaces: **FL** – symmetric surface-parallel full lamella, **AFL** – asymmetric surface-parallel full lamella, **PL** – surface-perpendicular lamella, **HL** – half lamella, **HY** – symmetric hybrid structure, **AHY** – asymmetric hybrid structure. Adopted from [Fas01].

With increasing energetic asymmetry ( $0 < R < 1$ ), the **PL** phase field splits, giving way first to a region in which the symmetric hybrid structure (**HY**) gains stability, then to another new phase field, the surface-parallel half-lamella morphology (**HL**). Thus as the surface interactions become more asymmetric, morphologies that lack a horizontal plane of symmetry (i.e., **HY** and **HL**) are favoured. On the whole, the system behaviour can be divided into two regimes based upon the existence of a stable **HL** phase. For more asymmetric values of  $R$ , a stable **HL** phase intervenes in the transition from **FL** to the perpendicular structures (**HY** and **PL**). As  $R$  becomes larger, a direct transition from **FL** to **HY** (or **PL**) occurs. The **HY** phase field is typically situated between the surface parallel morphologies (**FL** or **HL**) and the **PL** phase. With both surface-parallel and surface-perpendicular elements, this structure may be seen as a compromise morphology that serves as an intermediate between fully parallel and fully

perpendicular states. Moreover, the metastable existence of the **HY** morphology between the **FL** and **HL** phase fields suggests that such hybrids are possible intermediates between parallel-symmetric and asymmetric morphologies as well.

Different behaviour was noted for the asymmetric ( $R < 0$ ) part of the phase diagram. Here, no perpendicular phases were found in the sub- $D_0 = 2$  thickness region. Indeed, thinner films were all predicted to have the **HL** morphology, consistent with the classical view of asymmetric systems. Overall, three regimes of behaviour were observed in the morphology of the film near  $L_0$ , which were based on the degree of surface-energy asymmetry, i.e., the magnitude of  $R$ . For nearly equal A and B affinities for the surface and substrate, respectively ( $R \approx -1$ ), the asymmetric surface-parallel full-lamella morphology (**AFL**) is stable. When  $R$  is negative but small, there exists a region of **FL** stability for  $t/D_0 \geq 0.5$ . In this case, the entropic drive toward  $D_0$  periodicity overcomes the penalty of localizing **B** segments at the  $S_2$  surface. For intermediate values of  $R$ , a window of stability appears for the asymmetric hybrid structure (**AHY**). Similarities exist between this morphology and the **HY** structure found for  $R > 0$ . First, the **AHY** appears, like the **HY**, to be dependent upon boundary condition asymmetry. Also, like the **HY**, the **AHY** morphology seems to be an energetic compromise but between surface-parallel states. The presence of **AHY** morphology bound above asymmetric surface-parallel lamella (**AFL**) was also predicted for thicker films (e.g.  $t > D_0$ ) by Matsen et al.[Mat97] Furthermore, the position of the **AHY** phase field between the **AFL** and **FL** indicates its status as intermediary between asymmetric and symmetric structures as  $R$  is changed. Indeed, the mixed composition of **AHY** at the free surface ( $S_2$ ) provides a plausible transition between the surface wetting with **B** block (**FL**) and **A** block wetting (**AFL**).

Theoretical predictions of Fasolka et al. were compared with experimental observations on a series of PS-*b*-poly(*n*-alkyl methacrylate) BCPs supported on silicon substrates.[Fas00] AFM studies of BCP morphologies were performed at the edges of microdroplets, formed after thermal annealing step due to the film quantisation effect. These microdroplets exhibit a profile of film thickness (from 0 nm at the edges to 200 nm at the apex) which allowed to chart the thickness dependence of copolymer morphology in a precise manner via AFM. Investigations revealed gradual transition **PL**  $\Rightarrow$  **HY**  $\Rightarrow$  **HL**  $\Rightarrow$  **FL** with increasing of film thickness. However, for BCPs containing

methacrylates blocks with longer side alkyl chain, such as poly(hexyl methacrylate) or poly(lauryl methacrylate), the presence of **HL** morphology was not observed.

Co-existence of different theoretically predicted morphologies was experimentally observed by Morkved and Jaeger for gradient thin films of symmetric PS-*b*-PMMA on silicon nitride substrate.[Mor97] Film thickness was varied in a range  $\frac{1}{2}D_0 \leq t \leq \frac{3}{2}D_0$ . Applying different thermal annealing conditions authors were able to change BCP morphology from parallel lamella (annealed at higher temperatures) to a **PL** and **HY** structures (annealed at lower temperature).

### 2.3.3 Long range ordering of BCPs

The BCP microphase separation results in a regular microdomain structures, but the size of the pattern with high regularity is dependent on both thermodynamic and kinetics parameters of the system. Usually, BCPs reveal regions called *grains* that typically have dimensions from tens of nanometers to few microns in size and are randomly oriented with respect to each other. Individual grains are separated by different types of *grain boundaries* that are formed during sample preparation and/or treatment. For example, for lamella-forming block copolymers *tilt* and *twist* types of grain boundaries are typically observed,[Gid93,Gid94,Gid97] while in cylinder-forming 6-fold symmetry structures defects occur when the number of neighbours surrounding each microdomain differs from six.

Well-ordered structures, especially for high molecular weight BCP, are difficult to obtain directly or by application of thermal annealing. This is mainly due to kinetic and thermodynamic barriers (chain entanglements, diffusion restrictions), therefore, unassisted BCP self-assembly is not sufficient for most of nanofabrication. However, a combination of self-assembly with long-range ordering methods could potentially lead to the nanostructures possessing sufficiently high degree of order over the macroscopic lateral scale. Thus, in recent years a lot of efforts has been done on development so-called field-assisted alignment methods, that could be applied to a block copolymer systems.[Ham09,Dar07] Among of others flow (or shear) alignment, alignment in external electric field and surface field alignment belong to the most intensively studied and widely used approaches.

### 2.3.3.1 Effect of surface field. Solvent vapor annealing

In case of BCP thin films, the interfacial interactions of the blocks with free surface and the underlying substrate play crucial role. The surface energies of the blocks, and the commensurability between the film thickness and the BCP equilibrium periodicity dictate the BCP morphology and orientation of the microdomains,[Hua98,Fas01] as was discussed in Chapter 2.3.2. In general, such physicochemical constraints conditioned by the presence of interfaces are categorically referred to as *surface fields*, that imply control over the microdomain orientation through controlling a substrate property or/and an atmosphere.

Introduction of lithographic techniques to modify the substrate surface properties provides the way to better control the BCP microdomain orientation and order.[Che06] The placement of microdomains has so far been controlled by pre-patterning the substrate with either topographical guiding patterns (graphoepitaxy) [Seg01,Sund02,Sund04,Par07b] or surface chemical patterns (chemoepitaxy) [Hie97,Yan00,Rok01] combining in such a way ‘top–down’ (lithography) and ‘bottom–up’ (BCP self assembly) approaches.

Graphoepitaxy has been successfully employed to direct the self-assembly of microdomains of various morphologies. As one of the way, a pair of ridges is prepared by the lithography and surface energy of the sidewalls and bottom surface is carefully controlled before coating with the block copolymer film. Segalman et al. [Seg01] were the first to apply this technique to spherical phase block copolymers. In this study, the substrate was pre-patterned with 4.5  $\mu\text{m}$  square-wave channels that effectively directed the long-range ordering of 27 nm polystyrene-*block*-poly(2-vinylpyridine) (PS-*b*-P2VP) spheres. For lamella-forming polystyrene-*block*-poly(methyl methacrylate) (PS-*b*-PMMA) BCP, microdomains were found to align parallel to the sidewalls, thus subdividing the distance between the ridges, when the sidewalls had selective interaction with one phase of the block copolymer while the bottom surface was nonselective.[Par07b] In contrast, the alignment of lamellae perpendicular to the sidewalls has been realized when the surfaces of both the sidewalls and the bottom surface were modified with brush layer of random PS-*r*-PMMA to be nonselective for both BCP components.[Par09a] Under topographical confinement conditions also



cylinder-forming block copolymers have been aligned both perpendicular[Sund02] and parallel[Sund04] to the sidewall of silicon nitride gratings.

The effect of a chemically-patterned surface on the orientation of microphase separated *di*block copolymer was first reported by Rockford et al.[Roc99] The surface pattern, composed of an alternating stripes of SiO<sub>2</sub> and Au, induced normal to the substrate orientation of PS-*b*-PMMA lamellae due to selective wetting of gold by PS and silicon oxide by PMMA, respectively. The commensurability window for ultrathin films was found as much as 25%, while for thick films (>500nm) a mismatch in length scale of only 10% was sufficient to lose control over the microdomain orientation.[Roc01] Later, Nealey et al. have successfully directed the assembly of PS-*b*-PMMA BCPs of various compositions on chemically patterned striped substrates to fabricate defect-free arrays of either perpendicular lamella [Kim03,Edw04] or surface-parallel cylinders [Edw06] when the stripes periods were commensurate or near commensurate with the bulk block copolymer intercylinder repeat period,  $D_0$ .

The *solvent vapour annealing* is one of the most effective ways for fabricating both highly ordered structures and vertically oriented lamellar and cylindrical microdomains in thin BCP films. Because solvent can escape from a polymer film only at the surface, solvent evaporation is a strong and highly directional field. The concentration of solvent through the film thickness is not uniform, with the solvent concentration being lowest at the surface and highest in the interior of the film (solvent concentration gradient). With time, as solvent evaporates, this gradient solvent field propagates into the film until the solvent has evaporated (Fig. 2.15).

Despite a lack of complete understanding of mechanisms underlying structure development during solvent annealing step, certain aspects of solvent effect are discussed below. The presence of solvent in a block copolymer films performs several important functions, when the orientation and lateral ordering of the microdomains are of interest:

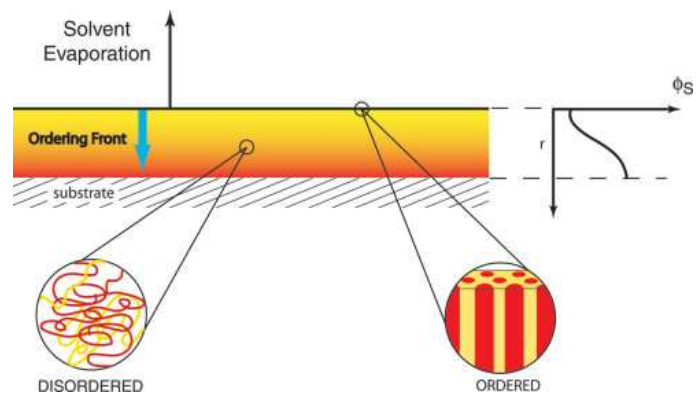


**Figure 2.15** Schematic representation of the solvent evaporation rate effect on the ordering of BCP thin film. Reproduced from [Kim04].

1) The presence of solvent mediates surface energies and, hence, tends to orient the microdomains normal to the surface, as long as there is no strong preferential interaction of the solvent with one of the blocks. If this is the case, the solvent will tend to orient the domains parallel to the surface.[Xua04]

2) Solvent affects the interactions between blocks and the relative volume fractions, potentially leading to changes in morphology.

3) In solution block copolymer is dissolved with no ordering while, in the solid state the BCPs microphase separate. Consequently, the gradient in the solvent concentration corresponds to a gradient in the ordering of the BCP with phase separation occurring initially at the film surface. As the solvent evaporates, subsequent microphase separation of the BCP is templated by the ordered structure at the surface of the film.

4) The presence of solvent imparts significant mobility to the BCP chains, remarkably reducing the glass transition temperature.[Mar03] Consequently, the grains of the microdomains formed initially can rapidly coarsen.

Thus, during solvent evaporation, multiple processes occur simultaneously and the resultant order and orientation of the BCP thin film will depend upon a balance of the kinetics associated with each process. As a consequence, the morphology of the film generated by solvent casting or solvent annealing is, in general, far from the equilibrium morphology of the BCP in the bulk.

Kim et al. first reported that solvent evaporation rate could be used to induce the ordering and orientation of BCP microdomains.[Kim98] Cylindrical PS microdomains of PS-*b*-PB-*b*-PS triblock copolymer were vertically aligned with respect to the substrate at low evaporation rates (5 nl/s) but underwent in-plane orientation at solvent evaporation as high as 200 nl/s. The same effect was also observed for polystyrene-*block*-poly(ethylene oxide) (PS-*b*-PEO) [Lin02] and polystyrene-*block*-poly(L-lactide) [HoR05] BCP thin films. This orientation was found to be independent of the substrate and was attributed to a copolymer/solvent concentration gradient normal to the film surface as discussed above. However, the lateral ordering of the cylindrical microdomains was poor. Hahm et al. and later, Kim et al. showed that evaporation-induced flow in solvent cast BCP films produced arrays of nanoscopic cylinders oriented normal to the surface with a high degree of ordering.[Hah00, Kim04]

Fukunaga et al. studied the effect of the solvent removal speed on the resulting microdomain morphology of lamella-forming PS-*b*-P2VP-*b*-PtBA triblock copolymer

films supported by a solid substrate.[Fuk00] Slow solvent extraction rates led to a parallel alignment of lamellar microphases within the plane of the film, while on fast drying, a perpendicular orientation of the lamellae was found.

By controlling the rate of solvent evaporation and solvent annealing time of PS-*b*-PEO thin films, Kim et al. achieved nearly defect-free arrays of cylindrical microdomains oriented normal to the film surface that spanned from the surface to the substrate.[Kim04] Moreover, the use of a co-solvent enabled further control over the length scale of lateral ordering. More recent results show that cylindrical microdomains oriented normal to the film surface could be obtained directly by spin-coating PS-*b*-P4VP BCPs from a mixture of toluene and THF of particular volume ratio and arrays of highly ordered cylindrical microdomains are formed over large areas after exposing the films to vapor of a toluene/THF mixture. This process was independent on substrate, but strongly dependent on the quality of the solvents for each block and the solvent evaporation rate.[Par07c]

Harant et al. demonstrated that vapour annealing of polystyrene-*block*-polyisoprene (PS-*b*-PI) block copolymer thin film in different solvents leads to a different domain orientation, maintaining substrate-perpendicular hexagonal structure in methyl ethyl ketone (MEK) atmosphere, while yielding a fingerprint texture (in-plane orientation) after vapor treatment with toluene.[Har05] Moreover, it was demonstrated, that the solvent choice for spin coating dramatically changes the initial thin film morphology: MEK provides a useful hexagonal structure without annealing, while toluene yields a disordered morphology.

The effect of the initial morphology on the evolution of topographical structures at the free surface of an asymmetric PS-*b*-P2VP block copolymer upon solvent vapour annealing in chloroform was also investigated.[LiX07] For a micellar film of the block copolymer prepared from toluene solution, the surface morphology developed via a nucleation and growth mechanism, while it evolved via spinodal and dewetting route for thin films prepared from THF solution. However, identical final morphologies were observed for the both kinds of the films after a long time solvent vapour annealing. These results reveal that the initial morphology also influences the process of the pattern evolution that develops at the free surface of BCP thin films during solvent vapour annealing.

### 2.3.3.2 Shear- and electric-field induced ordering of block copolymers

An application of shear field, in particular, *large amplitude oscillation shear* (LAOS) has been widely used to obtain uniaxial domain orientation either for BCP melts or solutions, allowing to control and switch orientation direction by means of variation experimental parameters, such as temperature,[Kop92] shearing frequency [Zha96] or amplitude.[Gup96] For lamellae-forming BCPs three possible domain orientations are distinguished with respect to the applied shear direction: parallel, perpendicular and transverse, as shown on Figure 2.16.

Parallel and perpendicular orientations are fairly observable experimentally. Koppi et al. observed both of them in dynamically sheared poly(ethylene-propylene)-*block*-poly(ethylene) (PEP-*b*-PEE) BCP melts using small-angle neutron scattering (SANS).[Kop92] Near the  $T_{ODT}$  and at low shear frequencies ( $\omega_0$ ), the lamellae arrangement adopted parallel orientation (Fig. 2.16 a), while at higher processing frequencies and at temperatures further away from the ODT ( $T \ll T_{ODT}$ ) lamellae with unit normal perpendicular to both the flow and velocity gradient directions was observed (perpendicular orientation, Fig. 2.16 b). The crossover from low to high frequency behaviour occurred at  $\omega_0$  close to  $\tau^{-1}$ , where  $\tau$  is the relaxation time for local domain deformations.

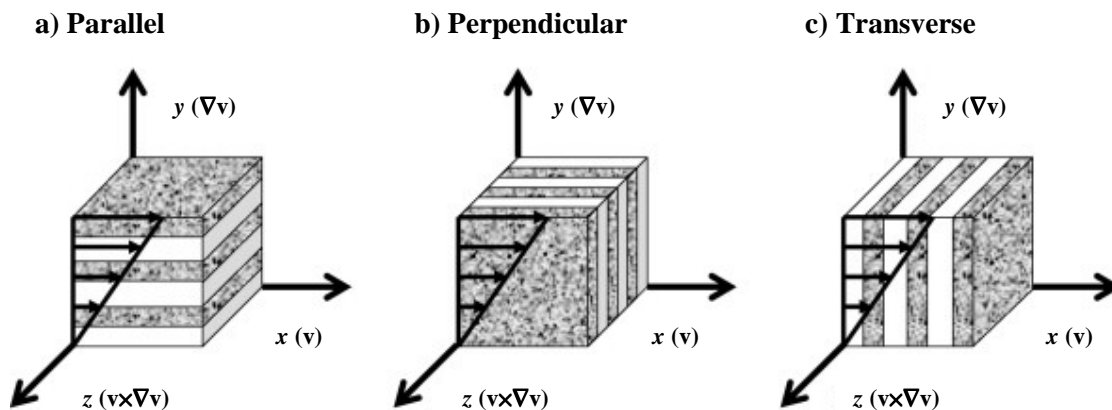


**Figure 2.16** Schematics of orientation of lamellar microdomains in the orthogonal coordination with velocity ( $\mathbf{v}$ ) (or shear) direction along  $x$  axis, velocity gradient ( $\nabla \mathbf{v}$ ) direction along  $y$  axis and vorticity ( $\mathbf{v} \times \nabla \mathbf{v}$ ) direction along  $z$  axis. The BCP domain orientation with the lamellar normal parallel to  $y$  is referred to as “parallel” orientation (a), parallel to  $z$  – as “perpendicular” orientation (b), and parallel to  $x$  – as “transverse” orientation (c). Adopted from [Gup96].

Regarding transverse orientation (Fig. 2.16 c), it is much less favourable compared to parallel and perpendicular ones. However, Okamoto et al. have reported co-existence of parallel and transverse orientations under LAOS conditions for polyethylene-*block*-poly(ethylene-propylene) (PE-*b*-PEP), [Oka94] while Pople et al. [Pop99] found it for concentrated aqueous solution of poly(oxyethylene-*b*-oxybutylene) BCP under steady shear flow. The latter case involved transition to perpendicular orientation by increasing the shear rate.

The potential of electric fields for microdomain alignment has attracted interest in the recent past as it may also be of considerable technical interest. [Thu00a] The driving force for the reorientation of microdomain structures under an electric field is the electrostatic free energy penalty associated with the dielectric interfaces, which are not parallel to the field vector. This force is proportional to  $(\Delta\epsilon E)^2$  [Mor96] where  $\Delta\epsilon$  is the differences in the dielectric constants of the blocks and  $E$  is the strength of electric field. Thus, the microdomains tend to orient parallel to the electric field vector, thereby lowering the free energy of the system.

It has been shown that both lamellar and cylindrical structures could be oriented macroscopically with an application of electric field. [Amu93, Amu94, Mor96, Thu00a] In lamellar structures all microdomain orientations containing the electric field vector within the lamellar planes are energetically equivalent. Therefore, the applied electric field induces domain alignment in such a way, that lamellar normal appear perpendicular to the field direction. [Amu93, Amu94]

Instead, cylindrical microdomains can be aligned along the field vector, resulting in a single domain (i.e. a block copolymer “single crystal”). For example, Thurn-Albrecht et al. achieved orientation of PMMA cylinders of asymmetric PS-*b*-PMMA BCP along the direction of applied electric field, that was oriented normal to the surface. [Thu00a] An existence of electric field strength threshold  $E_t$ , that allows to overcome interfacial interactions, was denoted: above  $E_t$  complete orientation of the cylindrical domains was achieved, while at field strengths below  $E_t$  a coexistence of the domains parallel and perpendicular to the electrode surface was observed.

Boker et al. have shown that concentrated block copolymer solutions can also be aligned in *dc* electric fields during solvent evaporation, leading to a highly anisotropic microdomain structures in the resulting films. [Bok02a] In contrast to melt alignment, the method is applicable to polymers with higher melt viscosities such as high molecular weight copolymers and copolymers of more complex architectures, which

cannot be aligned by electric field in molten state. With in-situ SAXS measurements authors were able to distinguish between two different underlying mechanisms, dominating in orientation process at different experimental conditions.[Bok02b] Close to the ODT, (e.g. at low concentrations and/or high temperatures) aligned parallel to the electric field microdomains grown at the expense of those aligned parallel to the electrodes, while intermediate orientations were not observed.

Such behaviour was attributed to the migration of grain boundaries mechanism, that was previously assigned for microdomain alignment under shear [Pol99] and assumed to play predominant role in previous electric-field alignment experiments.[Amu94] In contrast, for high concentrations and low temperatures (e.g. further away from the ODT) the scattering patterns were found preserved and merely shifted into the new orientation, pointing out the rotation of entire grains as an alternative orientation mechanism.

Another interesting aspect of electric field application is concerned phase behaviour of BPCs having cubic symmetry morphology (e.g. gyroid and spheres). As was mentioned above, when electric field is applied to lamellar or hexagonal phases, it exerts a torque which approaches zero when the lamellae or cylinders are oriented parallel to the field. However, the free energy penalty cannot be eliminated in cubic phases, such as the gyroid or BCC, which always have dielectric interfaces that are not parallel to the field, and their free energy under the influence of the electric field is higher than without. Nevertheless, it can be reduced by distorting the phase: the structures elongate in the applied field direction, to an extent at which electrostatic and elastic forces are in equilibrium. The free energy of distorted phase with reduced symmetry, increases with respect to the other phases, and, thus can lead to an *order-order transition* (OOT).[Tso03,Tso06]

The mechanism of electric-field induced order-order phase transition was studied theoretically[LyD07,Pin08] and experimentally.[XuT04,XuT05] For example, Xu et al. found that the spherical microdomains of an asymmetric *di*block copolymer were deformed into ellipsoids under an electric field and, with time, interconnected to cylindrical microdomains oriented in the direction of the applied electric field.[XuT04] Moreover, it was demonstrated that under effect of electric field the reorganization of cylindrical domains from surface-parallel to surface-perpendicular orientation is realized via electric field induced cylinder-to-sphere-to-cylinder transitions.[XuT05] Starting from an ordered state with cylinders parallel to the surface, the applied electric

field enhanced fluctuations at the interfaces of the microdomains. The growth of the fluctuations continued until the cylindrical microdomains broke up into spherical microdomains. With time, the spheres were deformed into ellipsoidal domains that reconnected into tilted with respect to the applied electric field cylindrical microdomains. Further annealing aligned the tilted cylinders along the applied field direction. Recently, gyroid-to-cylinder transition was also reported for concentrated BCP solutions.[Sch10]

## **2.4 Block copolymers as templates for patterning of nanomaterials**

Modern lithographic techniques, for example extreme ultraviolet interference lithography (EUVIL) or electron beam lithography (EBL) enable processing of periodic and aperiodic features with high accuracy below 25 nm.[Fuk10] However, these methods are often restricted to 2D fabrication, require complicated instrumentation or long processing time, and thus increase cost efficiency dramatically with lowering of the feature size.

In this aspect BCPs have been recognized as an attractive systems for pattern fabrication, in particular, for patterning of various types of nanomaterials, e.g. nanoparticles, nanorods, etc.[Har06] offering a reach variety of morphologies with a widely tuned periodicities,[Bat90] comparable with current lithographic requirements. In addition, fabrication of 3D-ordered hybrid organic/inorganic nanostructured materials become possible in a relatively simple and cost effective way.[Cro09] Thus, much attention has been paid toward developing of methods for selective incorporation nanoadditives into one of the BCP domains.

Depending on the final application, BCP-based nanohybrids could be prepared either as thin films or bulk samples, while their final target properties, arising from the presence of nanoadditives, could be tuned via different methods available for their incorporation. An “in-situ” and “ex-situ” approaches are the two most established up to now. However, some recent achievements in this area gave rise to development of more advanced and sophisticated routes to produce nanopatterns and nanohybrids with complex and multifunctional properties.

The chemical nature of constituent blocks often plays crucial role on a possibility to specifically incorporate inorganic additives into one of the BCP microdomains. Consequently, block copolymers comprised of certain ‘active’ blocks, which are able to directly interact (or complex) with a guest inorganic material (either pre-synthesized nanoparticles or precursors) via hydrogen bonding, electrostatic interaction, metallocene complexation, etc., are the most attractive ones. Among of other, BCPs containing blocks of poly(vinylpyridine) (either P2VP or P4VP), poly(ethylenoxide) (PEO), poly(methacrylic acid) (PMMA), poly(acrylic acid) (PAA), poly(styrenesulphonic acid) (PSSA), etc., are widely explored for fabrication of a variety of nanocomposites.

### 2.4.1 In-situ approach

“In-situ” approach toward polymer-based nanocomposites is being in focus of many research groups for several last decays of years. It implies formation of inorganic particles within the host BCP matrix starting from the polymeric materials consisting of monomer units bearing metal-functionalized counterparts. Such functionalization could be achieved either by polymerization of organometallic monomers or by complexing of appropriate inorganic precursors (e.g., salts) with reactive polymer moieties (e.g. functional groups, backbone polymer chains or particular blocks in BCPs). In latter case the mutual affinity between nanoparticles precursor and polymer functionality is desired.

Applied to the block copolymers, this method was first demonstrated by R.Cohen group.[Cha92a,Cha92b] They prepared functional block copolymers containing noble metal nanoparticles polymerizing norbornene-derivative monomers, complexed with appropriate organometallic compounds. Afterwards precursors were reduced under mild conditions by treatment with molecular hydrogen, leading to the formation of NPs/BCP composites with selective localization of metal clusters within BCP microdomain.

Later on, BCP-templated in-situ synthesis of nanoparticles has been extended for many other types of inorganic materials, including QDs,[Zha01, Lee10] magnetic nanoparticles,[Yun05,Abe03a] or intermetallic alloys.[Abe03b]

Since controlled polymerization of monomers coordinated with metal ions is rather hardly achievable, for “in-situ” NPs synthesis it is more common to bind precursors to preformed block copolymers. Such method has been widely explored for



different NPs/BCP systems and has been proved as highly efficient, especially for fabrication of hybrids with high NPs loading ratios.

Fabrication of highly oriented 3D-periodic arrays of gold nanoparticles in block copolymer bulk matrix starting from symmetric PS-*b*-P4VP BCP pre-loaded with gold precursor (HAuCl<sub>4</sub>) was reported.[Men08] In addition to a highly selective nanoparticles localization within P4VP domains, the macroscopic uniaxial orientation of the BCP lamellae was achieved by application of shear alignment under LAOS conditions.

Cobalt nanocrystals, selectively located in P2VP domains of PS-*b*-P2VP BCPs were obtained upon thermal treatment of appropriate complex of Co precursor with P2VP block of PS-*b*-P2VP BCPs.[Abe03a] However, the size distribution of Co nanocrystals was relatively broad (typically in the range of 5-50 nm) and became wider as the precursor loading rate increased. This method was then extended for fabrication of iron, iron-cobalt and cobalt-nickel alloy nanoparticles.[Abe03b]

Deshmukh et al. presented a one-step assembly process that describes simultaneous in-situ formation of silver NPs, directed assembly of block copolymers into a perpendicular lamellar morphology and NP organization into patterned arrays.[Des07] PS-*b*-PMMA was preloaded with silver precursor and thermally annealed after deposition onto the substrate. In this case nanoparticles, selectively localized in PMMA phase, were shown to decorate surface of thin film and, in the same time, promote normal to the substrate orientation of topmost layered lamellae.

Deposition of micellar monolayer films onto a substrate also offers a possibility to prepare arrays of polymer-embedded or free-standing hexagonally packed inorganic nanodots. As an example, iron oxide nanoparticles were generated in-situ on the solid substrate with the aid of micellar block copolymer template by means of oxygen plasma treatment.[Yun05] Since the plasma treatment also eliminates polymer matrix, pure patterns of iron oxide nanoparticles were obtained. Moreover, easy control over the size of nanoparticles by simple tuning of precursor/BCP composition allowed authors to create either ferrimagnetic or superparamagnetic patterns of nanoparticles without altering of preparation protocol.

Despite high efficiency of “in-situ” approach for selective incorporation of nanoadditives, certain disadvantages still could be pointed out. An important drawback of this method is that the reaction conditions occurring during the synthesis of the nanoparticles inside BCP are not always the optimal ones for achieving desired

properties of nanoadditives (e.g., size distribution, crystallinity, etc.). In many cases, an introduction of inorganic precursor makes the functionalized block poorly or insoluble in common organic media, resulting in rather poor control over the final morphology.

### 2.4.2 Ex-situ approach

“Ex-situ” approach overcomes some limitations of “in-situ” methods. In this case pre-synthesized nanoadditives, e.g. nanoparticles (NP), nanorods (NR), nanoplates (NP) etc., are added to the BCP in solution or in melt. The advantage is obvious if the size- and shape-dependant properties of nanoadditives are particularly important for the final application. This is evident since the possibility to precisely control important parameters of nanoparticles such as size, size distribution, shape, aspect ratio, etc., that are not always achievable for “in-situ” methods through the control of synthetic conditions.

To ensure sufficient stability against agglomeration during the processing, particles are usually surface-modified with certain stabilizing agents. Apart of conventional low molecular weight surfactants an application of polymer molecules for particles stabilization is also widely implemented.[Gru07,Lat08] For this purpose polymer chains could be chemically anchored to the nanoparticles surface via ‘*grafting-from*’ [Rag06,Gar07a,Gar07b] or ‘*grafting-to*’ approaches [Cor04] or adsorbed on a highly energetic particle surface via multiply particle-chain interaction.

Modification of nanoparticles with polymer shell has been shown efficient to compatibilize them with corresponding block of BCP.[Chi05,Kim05,Kim06b, Gar07a,Gar08] For example, Kramer and co-workers reported on selective segregation of gold NPs bearing PS or PVP stabilizing shell within appropriate phase of PS-*b*-P2VP BCP, respectively.[Chi05,Kim05,Kim06b] Similarly, magnetite nanoparticles, modified with PMMA or PS brushes were selectively localized within corresponding domains of P2VP-*b*-PMMA [Gar08] or PS-*b*-PI-*b*-PS [Gar07a] BCPs.

Spontaneous formation of hierarchical patterns of PS-covered CdSe nanorods was observed at the surface of PS-*b*-PMMA films during a cooperative phase separation process.[Plo10] In these two-dimensional surface patterns the nanorods selectively segregate to PS domains, where they orient preferentially perpendicular to the interfaces

between the domains. The ratio between the hosting domain width and the nanorod length dictates the number of nanorods that can be accommodated across the domains.

Nanoparticles stabilized with low molecular weight surfactants were also shown selectively segregate to one of the BCP domains. For example, TOPO-covered CdSe QDs (TOPO – tri-*n*-octylphosphineoxide) decorate surface-etch areas of P2VP cylinders of PS-*b*-P2VP promoting normal to the substrate domain orientation.[Lin05]

Oleic acid-stabilized Fe<sub>3</sub>O<sub>4</sub> NPs were shown to self assemble within PMMA domains of PS-*b*-PMMA thin film upon thermal annealing.[Kas09] After thermal annealing clustering of NPs was observed even at relatively low particles volume fraction (0.4 vol %), limiting thus a possibility to achieve ordered composites with high loading of MNPs.

Low molecular weight additives (LMA) are known to organize into supramolecular assemblies (SMA) within domains of BCPs through the formation of hydrogen bonds.[Sid03,Ikk04] A possibility to direct nanoparticles location within microphase segregated BCP, mediated by LMA/NPs interaction was demonstrated recently.[Zha09]

Authors showed that LMA, in particular, PDP or its derivatives, in addition to the formation of SMA, could serve also a function of nanoparticles compatibilizers through the hydrophobic interactions of alkyl part of LMA with the same originating form particle-stabilizing ligands. This method is quite overall and has been proved to be efficient for a wide range of nanoparticles, including QDs, magnetic NPs, metallic NPs and NRs, etc.

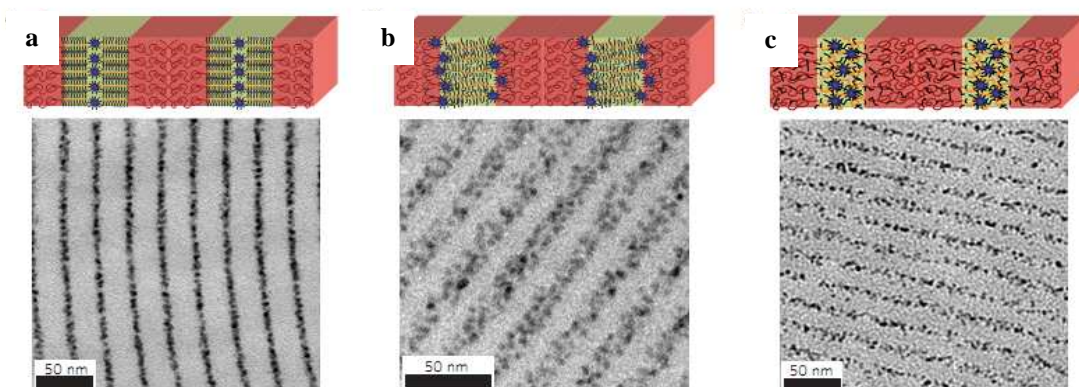


**Figure 2.17** Reversible thermal responsiveness of PS-*b*-P2VP(PDP) SMA loaded with alkyl-stabilized CdSe QDs. Adopted from [Zha09].

Moreover, reversible spatial distribution of the nanoparticles was shown to be thermo-responsive due to migration of LMA through the BCP phases upon heating/cooling steps and, thus, altering (perturbing) local distribution of NPs through domain section (Fig. 2.17).

### 2.4.3 Step-wise approaches

Pre-formed block copolymer patterns could be used for subsequent deposition of inorganic materials either by in-situ or ex-situ methods. This so-called step-wise approach has an advantage that lateral characteristics of BCP pre-patterned substrate usually are preserved upon particles deposition or precursor loading and, thus, could be pre-estimated by selection of appropriate block copolymer.

Implemented to the substrate-supported thin films this method was used for in-situ fabrication of nanoparticles arrays and nanowires starting from PS-*b*-P2VP pattern loaded with metal precursor.[Cha07,Cha08] Metal ions (Au, Pt, Pd) were introduced selectively into PVP domains of self-assembled BCP thin film by soaking in aqueous solution of anionic metal complexes. Subsequent plasma treatment results in simultaneous removal of BCP matrix and formation of metal nanostructures.

Alternatively, PS-*b*-P4VP templates with minor cylinder-forming P4VP block were used for deposition of pre-synthesized metal nanoparticles (Au, Pt, Pd) from their aqueous dispersions (ex-situ method).[Nan09,Gow10] In this case nanoparticles affinity toward P4VP phase was ensured by the presence of citric ions stabilizing the nanoparticles. This method has been proved effective for either perpendicular or in-plane P4VP cylinders formed after solvent annealing of BCP as well as for nanoporous BCP templates obtained after selective removal of LMA, such as HABA (2-(4'-hydroxybenzeneazo) benzoic acid), from the PS-*b*-P4VP(HABA) SMA.

Topographical features of PS-*b*-PMMA thin films were exploited for deposition of two kinds of NPs via simple spin-coating of nanoparticles dispersions.[Son09] Primary particles were selectively trapped within either PS or PMMA groves depending on the selectivity of solvent used during annealing, while secondary particles were deposited into a channels formed after removal of PMMA part by electron beam irradiation (Fig.2.18).

Starting from PS-*b*-PMMA patterns, ultra-dense cobalt nanowires [Thu00b] or polypyrrole nanorods [Lee08] were prepared by electrodeposition of appropriate precursors into channels after selective UV-etching of PMMA part of BCP.

Following a step-wise approach, bicontinuous morphologies were also prepared in bulk starting from gyroid-forming polyfluorostyrene-*block*-polylactic acid (PFS-*b*-PLA) BCP.[Cro09] After selective etching of

PLA phase, TiO<sub>2</sub> was electrodeposited into a porous PFS residue. After removal of PFS gyroid morphology of BCP was finally replicated into free-standing semi-conducting TiO<sub>2</sub> nodes.

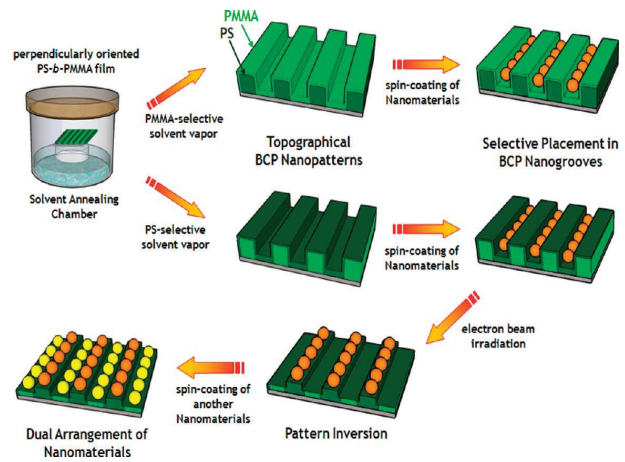


**Figure 2.18** Schematic representation of protocol implemented for fabrication of bi-nanoparticles arrays using topographical features of PS-*b*-PMMA BCP thin film. Reproduced from [Son09].



## Chapter 3 Experimental techniques

### 3.1 Atomic force microscopy (AFM)

Atomic force microscopy (AFM) [Bin86] or scanning force microscopy (SFM) is an experimental method, which, in particular, is widely used for investigation of surface morphologies of various materials in nanometer scale. During AFM experiments investigated surface is scanned with a cantilever-mounted sharp tip (probe) having a radii of curvature down to a few nm and tip-sample interaction is monitored by an electronic circuit to produce two-dimensional image of the sample surface (Fig. 3.1).[1]

In AFM experiments vertical resolution could be lowered down to a few angstroms, while lateral one is strongly dependent on the tip sharpness. With ultra-sharp [2] or carbon nanotube probes [Wil09] sub-nanometer lateral resolution could be achieved.

Most of AFM experiments rely on measuring of forces between the tip and sample. However, the force is not measured directly, but estimated from the cantilever deflection, which is detected with the aid of laser beam, focused on its surface. The tip-sample interaction force  $F$  is proportional to the tip deflection  $x$  (according to Hook's law  $F = -kx$ , where  $k$  is the stiffness of the cantilever).

The interaction force between the surface and the tip could be ether attractive, reaching maximum value at certain sample-to-tip distance, or repulsive, razing to infinity when this distance approaches zero.

Figure 3.2 schematically shows dependence of such interaction force versus sample-to-tip distance.

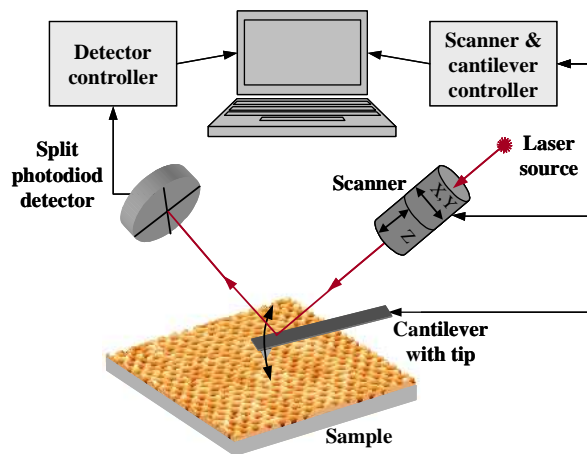


**Figure 3.1** Schematic representation of AFM principle. Adopted from [1].

[1] [www.nanoscience.com/education/AFM.html](http://www.nanoscience.com/education/AFM.html)

[2] [www.nanosensors.com](http://www.nanosensors.com)

Here, the region of negative force values corresponds to an attractive interaction regime, while repulsive interaction lies in a positive value region. Depending on the type of interaction several AFM operating modes are distinguished:

(a) In **contact mode** the tip scans the sample in close contact with the surface. The repulsive force between tip and sample is set to be constant by pushing the cantilever against the sample surface with a piezoelectric positioning element. Deflection of the cantilever is sensed and compared with setpoint value by feedback controller. If the measured deflection is different from setpoint value, the feedback amplifier applies a voltage to piezo to raise or lower the sample relative to the cantilever to restore the

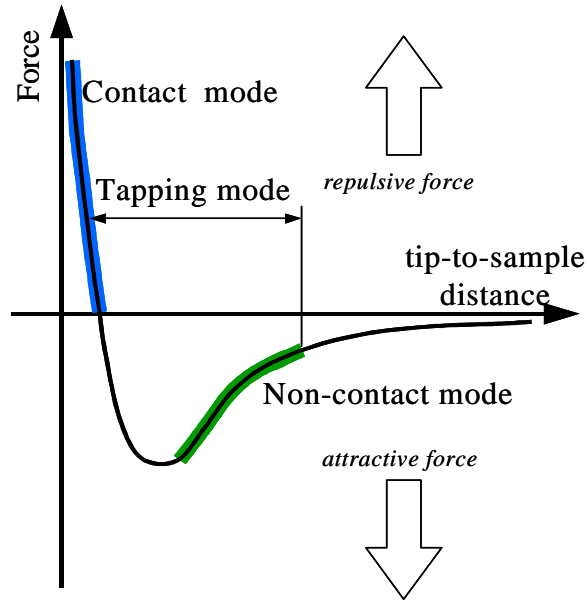


**Figure 3.2** Force versus distance curve and AFM operating modes. Adopted from [1].

desired value of deflection. By repeating of such protocol at every scan point sample topography map is constructed, having lateral resolution down to 1 nm and height resolution of less than 1 Å. However, due to the presence of adsorbed gas or moisture layer the contact mode imaging is heavily influenced by frictional and adhesive forces that pull the scanning tip toward the surface. These effects can damage samples and/or distort the image data.

b) **Non-contact mode** is one of several vibrating cantilever techniques in which AFM cantilever is oscillated over the sample surface at the distances of 50-150 Å and attractive Van der Waals forces are detected and transformed into a corresponding topographic image during scanning procedure.

Since the attractive forces are substantially weaker than forces involved in contact mode, small oscillation must be applied to the tip, so that changes in amplitude, phase or frequency of the oscillating cantilever in response to force gradients from the sample could be detected using alternating current detection methods.

Non-contact mode does not suffer from the tip or sample degradation effects, thus, it is preferable for studying soft or easy damageable samples. However, the resolution of non-contact mode is lower compared to contact mode. It is reasoned by the presence



of adsorbed fluid layer on the sample surface, which is substantially thicker than the range of the Van der Waals force gradient. Therefore, attempts to image the true surface with non-contact AFM fail as the oscillating probe becomes trapped in the fluid layer or hovers beyond the effective range of the forces.

(c) **Tapping mode (TM<sup>®</sup> AFM)** allows high resolution topographic imaging of the samples, that are loosely hold to their substrate, difficult to image by contact or non-contact AFM techniques or could be easily damaged during the scanning procedure. It overcomes problems associated with friction, adhesion or electrostatic forces by alternately placing the tip in contact with the surface to provide high resolution and then lifting the tip off the surface to avoid dragging the tip across the surface. Tapping mode imaging is implemented by oscillating the cantilever at or near the cantilever's resonant frequency using a piezoelectric crystal. The piezo motion causes the cantilever to oscillate with a high amplitude (typically greater than 20 nm) when the tip is not in contact with the surface. The oscillating tip is then moved toward the surface until it starts to lightly touch, or tap the surface. During scanning the vertically oscillating tip alternately contacts the surface and lifts off, generally at frequencies in a range of 50 – 500 kHz. As the cantilever begins to intermittently contact the surface, its oscillation is necessarily reduced due to energy loss caused by the contact with the surface. The reduction in oscillation amplitude is used to identify and measure surface features.

In tapping mode, unlike contact and non-contact regimes, the tip is prevented from sticking to the surface and causing damage during scanning, since high oscillating amplitude is sufficient to overcome adhesive forces. Also, the surface material is not pulled sideways by shear forces since the applied force is always vertical.

An extension of tapping mode AFM is a phase imaging, where the material-dependent phase shift of cantilever oscillation is detected simultaneously with tip deflection. This allows performing mapping of the components in composite materials with different chemical composition, stiffness, adhesion, etc.

Several other modes, such as lateral force microscopy (LFM), force modulation, conductive AFM, tunnelling AFM (TUNA), electric and magnetic force microscopy (EFM, MFM) are also possible with the most of modern AFM instruments.

In present work tapping mode AFM was used to study surface morphology of the samples of both neat BCPs and NPs/BCP composites. Phase and topography images were obtained simultaneously using single silicon tips with resonant frequency of 45-65 kHz and spring constant of 1.5-3.7 N·m<sup>-1</sup> having tip radius in the range of 10-20 nm.

MFM images were obtained in dynamic lift mode at lift height of 30 nm using Co/Cr coated magnetized cantilevers having resonant frequency 60-100 kHz and nominal tip radius of ~25 nm.

All the experiments were performed using Dimension 3100 microscope (*Digital Instruments, Inc.*, Santa Barbara, USA.). AFM images were treated and analysed with WSxM 5.0 open-source software.[3]

## 3.2 Transmission electron microscopy (TEM)

The transmission electron microscope (TEM) operates on the same basic principles as the light microscope but uses electrons instead of light. Due to the significantly shorter wavelength of electrons (~2.5 pm at 200 kV) compared to a visible light (400-700 nm) the angstrom resolution is reached, which is thousand times higher than in conventional light microscopes.

Schematic view of transmission electron microscope [4] and the principle of image formation (bright field imaging) are shown on Figure 3.3.[Rei08] Most of modern transmission electron microscopes consist of two principle parts, namely, illumination system (the upper part of microscope above the sample holder) and imaging system (below sample holder).

Electrons are emitted from a biased V-shaped electron gun and accelerated with high-tension (HT) electric field. Accelerated electrons pass through the system of electromagnetic condenser lenses and condenser aperture. Condenser aperture (user-selectable) restricts high-angle electrons (those far from the optic axis) and so electrons reach the specimen in a form of monochromatic electron beam of well defined shape. The electrons are scattered by the specimen and those that are scattered beyond certain angle are blocked by the objective aperture.

These blocked electrons are then missing in the beam and give rise to darker areas in the image. The image formed by the objective lens is magnified by the projector lenses and displayed on a fluorescent viewing screen or recorded with a CCD camera.

Depending on electron-specimen interaction, transmitted electrons could be subdivided into three types:

[3] [www.nanotec.es](http://www.nanotec.es)

[4] <http://barrett-group.mcgill.ca/teaching/nanotechnology/nano02.htm>

(a) *Unscattered electrons.* These are incident electrons that are transmitted through the thin specimen without any interaction inside the specimen.

Thus they do not carry any information about the specimen and form only the background intensity in the image.

(b) *Elastically scattered electrons.* Those are electrons that are scattered (deflected from their original path) by cores of the atoms in the specimen in an elastic fashion (no loss of energy). The elastically scattered electrons carry information mainly about the structure and morphology of the specimen.

For scattering in amorphous specimens relatively simple rules apply. The probability of scattering of the electron to a certain angle increases with the increasing atomic number of the scattering atom, density of the scattering atoms and specimen thickness. In this way a so-called mass-thickness contrast arises. Areas of the specimen that are thicker or contain atoms with larger atomic numbers scatter more electrons beyond the orifice of the objective aperture and thus appear darker.

For crystalline specimens much more complicated rules apply. The probability of scattering of the electron to a certain angle sensitively depends on the orientation of the crystal lattice with respect to the incoming electron beam.

The simplest form of this dependence is the Bragg law ( $n\lambda = 2d \sin \theta$ ), e.g. all incidents that are scattered by the same atomic crystallographic plane will be scattered by the same angle. This allows performing diffractive imaging and analysing crystal structures of the sample.

For crystalline specimens much more complicated rules apply. The probability of scattering of the electron to a certain angle sensitively depends on the orientation of the crystal lattice with respect to the incoming electron beam. The simplest form of this

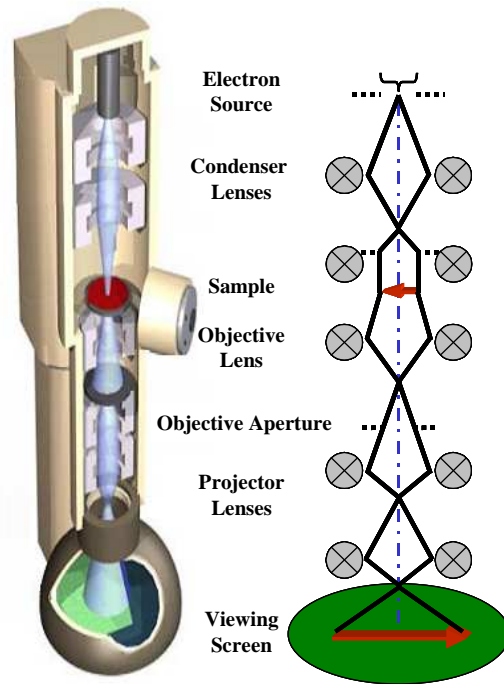


**Figure 3.3** Schematic view of transmission electron microscope (left) and electron beam path with the image formation diagram (bright field imaging) (right). Modified from [4] and [Rei08].

dependence is the Bragg rule ( $n\lambda = 2d \sin \theta$ ), e.g. all incidents that are scattered by the same atomic crystallographic plane will be scattered by the same angle. This allows perform diffractive imaging and analyse crystal structures of the sample.

(c) *Inelastically scattered electrons.* Such incident electrons that loose their energy by excitation of the electrons in the specimen during the interaction are called inelastically scattered. Inelastically scattered electrons can be utilized for Electron Energy Loss Spectroscopy (EELS) experiments. The inelastic loss of energy of the incident electrons is characteristic for the elements that were interacted with, known as element absorption edge. These energies are unique to each bonding state of each element and thus inelastically scattered electrons can be used to extract both compositional and bonding (i.e. oxidation state) information on the specimen region being examined.

Depending on thickness of the specimen, a single primary electron may interact several times with the atoms of the specimen (both elastically and inelastically), which leads to a quite complicated ways of image formation. Thus very thins specimens (10 nm – 100 nm) are favourable for an easier image interpretation.

In present work conventional bright field (BF) TEM images as well as electron diffraction patterns (DP) were recorded with Libra 200 and Libra 120 (Carl Zeiss AG, Germany) transmission electron microscopes operated at 200 kV and 120 kV, respectively. Nanoparticles specimens for TEM imaging were prepared by drying a droplet of nanoparticles dispersion in  $\text{CHCl}_3$  on amorphous carbon-coated copper grids (200-mesh, Plano GmbH, Wetzlar, Germany). To perform TEM imaging of NPs/BCP composites, thin films were etched from Si wafers by immersion into a 1M NaOH solution and transferred onto 200-mesh copper grid.

A Libra 200 TEM with integrated Omega-type energy filter was used to perform energy-filtered transmission electron microscopy (EFTEM) imaging with a purpose to determine position of nanoparticles within certain block of PS-*b*-PVP BCP matrix. Nitrogen elemental map was created in accordance with the “three-window power law” method,[Rei95] where the first EF image just above the element absorption edge is acquired as image containing element-specific information as well as background. The background is extrapolated from two images acquired below the absorption edge. This background image is subtracted from the element-specific image, resulting in elemental-map image.

### 3.3 Grazing incidence small-angle X-ray scattering (GISAXS)

Grazing incidence small-angle X-ray scattering (GISAXS) introduced by Levine and Cohen [Lev89] emerged to a versatile and frequently used analytical technique in the field of investigation of micro- and nanostructured materials, in particular microphase separated block copolymer system.[Gom09,Mue03] In GISAXS experiments, transmission geometry, used for conventional small-angle X-ray scattering (SAXS), is replaced by reflection one. This yields a surface sensitivity, which allows to perform investigation of surfaces and thin films with thicknesses from few to few hundreds of nanometers. Following the same principles as in the transmission SAXS geometry, larger length scales could be reached by an increase of the sample to detector distance (GIUSAXS). GISAXS method is complementary to TEM or AFM techniques, because images obtained, for example, by AFM are still tip-dependent, especially for densely packed systems, when the distance between two neighbouring objects is of the same order as the tip curvature. In addition, due to the shallow incident angle, the footprint of the X-ray beam on the sample surface in GISAXS is few millimetre long, increasing thus, the statistics of the structures information by a factor of  $>10^3$  compared to AFM or TEM.

The geometry of GISAXS experiment is illustrated in Figure 3.4. A monochromatic X-ray beam with the wave vector  $k_i$  is directed on a surface with a very small incident angle ( $\alpha_i < 1^\circ$ ) with respect to the surface. The z-axis is the normal to the surface plane. The x-axis is the direction along the surface parallel to the beam and the y axis perpendicular to it. The X-rays are scattered along  $k_f$

in the direction  $(2\theta, \alpha_f)$  by any type of electron density fluctuations at the illuminated portion of the surface. For exit angles equal to incident critical angle ( $\alpha_i = \alpha_f$ ) there is an

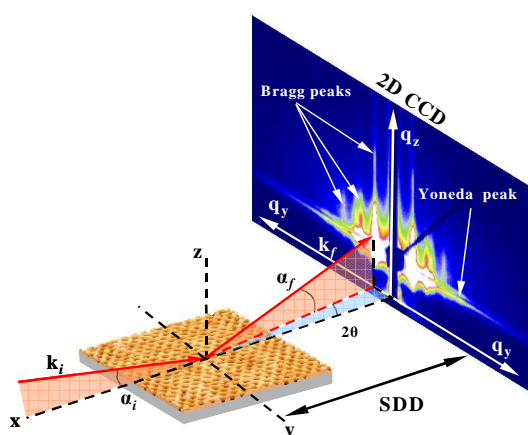


**Figure 3.4** Schematics of GISAXS geometry used for thin film investigation. Modified from [5].

enhancement in the scattering intensity due to the refraction effects, which is also known as Yoneda peak.[Yon63]

The appearing scattering wave vectors  $q_x$ ,  $q_y$  and  $q_z$  for the three spatial directions are defined as [Haz00]:

$$\begin{aligned} q_x &= (2\pi / \lambda) \cdot (\cos(\alpha_f) \cdot \cos(2\theta) - \cos(\alpha_i)) \\ q_y &= (2\pi / \lambda) \cdot \sin(2\theta) \cdot \cos(\alpha_f) \\ q_z &= (2\pi / \lambda) \cdot (\sin(\alpha_i) + \sin(\alpha_f)) \end{aligned} \quad (\text{Eq. 3.1})$$

2D GISAXS patterns are typically analyzed in two mutually perpendicular directions:

(a) along  $q_y$  axis, e.g. the scattering intensity is plotted *versus*  $q_y$  at constant  $q_z$ . Such plots are known as *out-of-plane scans* and provide the information about structure correlations in lateral direction;

(b) along  $q_z$  axis, when the scattering intensity is plotted *versus*  $q_z$  at certain  $q_y$  value. These are known as *detector scans*, representing the correlations in direction normal to the sample surface, such as layer thickness, surface roughness.

Figure 3.5 schematically represent 2D GISAXS patterns of lamellae forming block copolymer films having parallel, perpendicular or mixed (disordered) orientation of microdomains.[5]

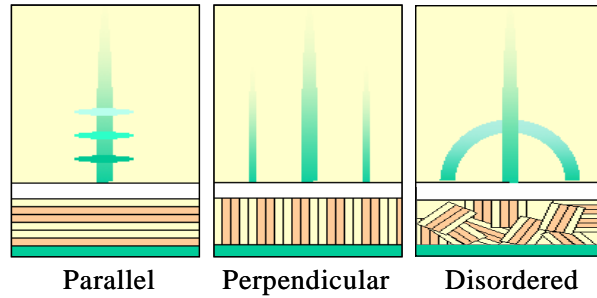


**Figure 3.5** Schematics of GISAXS patterns of lamella forming BCP film with different lamellae orientation. Reproduced from [5].

Similar to SAXS, in GISAXS geometry position of first order Bragg reflection comprise the information

about domain spacing (or interdomain distance) while appearance of multiply order peaks ( $2^{\text{nd}}$ ,  $3^{\text{rd}}$ ,  $4^{\text{th}}$ , ...) rely on degree of ordering of BCP domains.

The domain spacing  $D_0$  could be determined from the Equations 3.2 and 3.3:

$$D_0 = 2\pi / q \quad (\text{Eq. 3.2})$$

$$q = (4\pi / \lambda) \sin \theta \quad (\text{Eq. 3.3})$$

where  $q$  is scattering vector,  $\lambda$  is a X-ray wavelength and  $\theta$  is scattering angle.

[5] [www.chess.cornell.edu](http://www.chess.cornell.edu), GISAXS webpage of Dr. Detlef Smilgies

In case of block copolymers, multiple orders of Bragg reflection can be observed for strongly segregated ordered samples. For a specific morphology multiple order peaks appear at certain position with respect to a first order peak. The correlation between expected Bragg peak positions for various BCP morphologies are listed in Table 3.1:

**Table 3.1 Peak positions of Bragg reflections for various BCP morphologies [Ham04]**

Structure	Ratio $q_i / q^*$
Lamellar	1, 2, 3, 4, 5, 6.....
Cylindrical (Hex)	$1, \sqrt{3}, \sqrt{4}, \sqrt{7}, \sqrt{9}, \sqrt{12}$ .....
Gyroid	$1, \sqrt{3/4}, \sqrt{7/3}, \sqrt{8/3}, \sqrt{10/3}, \sqrt{11/3}$ .....
Spherical (BCC)	$1, \sqrt{2}, \sqrt{3}, \sqrt{4}, \sqrt{5}, \sqrt{6}$ .....
Spherical (FCC)	$1, \sqrt{3/4}, \sqrt{8/3}, \sqrt{11/3}, \sqrt{12/3}, \sqrt{16/3}$ .....

In present work GISAXS experiments were performed at the beamline BW4 (HASYLAB, Hamburg, Germany). The X-ray beam ( $\lambda = 0.138$  nm) was focused to the size of  $60 \mu\text{m} \times 30 \mu\text{m}$  ( $H \times V$ ). The sample was placed horizontally on a goniometer and tilted to an incident angle ( $\alpha_i$ ). MARCCD 2D detector (2048 x 2048 pixels, pixel size  $79.1 \mu\text{m}$ ) was mounted at sample-to-detector distance (SDD) of 1747.7 mm. A beam stop was used to block the direct beam in front of the detector. In addition, a second moveable beam stop was used to block the high-intensity specular peak on the detector.

The incident angles ( $\alpha_i$ ) used were  $0.20^\circ$  and  $0.30^\circ$ , which are above the critical angle of the PS-*b*-P4VP BCP ( $\alpha_c(\text{PS-}b\text{-P4VP}) = 0.16^\circ$ )[Par09b] as well as for estimated critical angle of MNP/BCP composites at the highest MNP loading ( $\omega_{\text{max}}(\text{MNP}) = 10.0$  wt%). At  $\alpha_i = 0.20^\circ$  which is below the critical angle of Si ( $\alpha_c(\text{Si}) = 0.22^\circ$ )[Par09b], X-rays were totally reflected from the Si substrate, enhancing the scattering observed for the film. At such conditions the scattering data replicate structural information of the whole depth of the film. Out-of-plane cuts were made at the Yoneda maximum  $q_z = 0.31 \pm 0.02 \text{ nm}^{-1}$  for  $\alpha_i = 0.20^\circ$  and  $q_z = 0.39 \pm 0.02 \text{ nm}^{-1}$  for  $\alpha_i = 0.30^\circ$ .

### 3.4 Other analytical methods

#### *Fourier transform infrared spectroscopy (FTIR)*

Fourier Transform Infrared (FTIR) spectroscopy is an analytical technique that uses infrared (IR) radiation to identify functional groups and types of chemical bonds in materials.[Sil88,Gri07] Photon energy associated with the IR region is absorbed by organic molecules and converted into energy of molecular vibration, either stretching or bending. Different types of bonds and, thus, different functional groups absorb infrared radiation of different wavelengths giving rise to characteristic absorption peaks. In FTIR spectroscopy, there are three frequency regions, which are attributed to different vibration modes: near-infrared (10000-4000  $\text{cm}^{-1}$ ), middle (4000-200  $\text{cm}^{-1}$ ) and far-infrared (200-10  $\text{cm}^{-1}$ ).

FTIR spectrum is plotted as transmittance (or absorbance) versus wavenumber ( $\text{cm}^{-1}$ ) and for particular compound is unique and, therefore, can be used as its fingerprint. Liquids are usually examined as thin films sandwiched between two polished NaCl plates that display no absorbance in IR region. Alternatively, solids may either be incorporated into thin KBr disk, prepared under high pressure, or mixed with non-volatile liquid and ground to a paste (or mull) that is smeared between salt plates.

In this work, FTIR spectroscopy was used to study the nature of stabilizing shell of nanoparticles and efficiency of particles modification reaction during ligand exchange steps. IR spectra were recorded with Vertex 80v spectrometer (Bruker, Germany) in transmission mode using KBr technique.

#### *Thermogravimetric analysis (TGA)*

Thermogravimetric analysis (TGA) was used to determine the amount of organic stabilizing layer on the surface of synthesized and chemically modified nanoparticles. The number of surfactant molecules or polymer chains attached to a nanoparticles core was calculated, that allowed to estimate their areal density. TGA measurements were performed using TA Q 5000 thermal analyser (TA Instruments) at heating rate of 10 K/min in nitrogen flow.



*X-ray photoelectron spectroscopy (XPS)*

X-ray Photoelectron Spectroscopy (XPS) is experimental technique that involves analysis of kinetic energy distribution of electrons knocked out from inner electron shells of atoms by a monochromatic beam of soft X-rays.[Mou95] Due to the softness of X-rays free electrons passes small distances in a material without scattering, therefore, only electrons ionized close to the sample surface (max 10 nm) could be detected.

The kinetic energy of the emitted electrons,  $E_k$ , could be presented as a difference between the energy of X-ray photons ( $E_p = hc / \lambda$ ) and the electron binding energy,  $E_b$ :

$$E_k = hc / \lambda - E_b \quad (\text{Eq. 3.4})$$

The core electrons of each element have unique binding energy, thus by its measuring the elemental composition could be determined. The electron binding energy also depends on the chemical environment of the element. This variation of the binding energy assists to study the chemical status of the element (oxidation state, functional groups, etc.).

In present work, XPS spectra were recorded by an AXIS ULTRA spectrometer (Kratos Analytical, UK) equipped with monochromatic Al  $K_\alpha$  source of 300 W at 20 mA. The hemispheric analyzer was set to pass energy of 160 eV for wide scan spectra and 20 eV for high-resolution spectra, respectively. During all measurements electrostatic charging of the sample was over-compensated by means of a low-energy electron source working in combination with a magnetic immersion lens. All recorded peaks were shifted by the same amount which was necessary to set the C 1s peak to 285.00 eV for saturated hydrocarbons.

*Ultraviolet-visible spectroscopy (UV-VIS)*

Nanoparticles of noble metals exhibit strong ultraviolet-visible absorption bands due to the surface plasmon resonance (SPR). The position, width and symmetry of these absorption bands, which lies in UV-VIS region, provide useful information about the

size, size distribution and inter-particle distances of NPs. In present work UV-VIS spectroscopy was used to record the SPR absorption spectra of nanoparticle (in solutions) and NP/BCP composites in thin films geometry. Spectra were measured in the range of wavelength  $\lambda = 300\div 1100$  nm with step width 1 nm by using Lambda 900 spectrophotometer (Perkin-Elmer). The UV-VIS spectra of thin films prepared from NP/BCP composites were measured on glass substrates using similar substrate without thin films as a reference.

#### *Scanning electron microscopy*

Scanning electron microscopy was performed using NEON 40 FIB-SEM workstation (Carl Zeiss AG, Germany) operated at 3 kV. In order to resolve nanoparticles position within BCP matrix thin films of NP/BCP composites supported on Si or glass substrates were studied with SEM without any metal coverage.

### **3.5 Materials used and sample preparation**

#### *Polymers used*

Block copolymers of polystyrene-*block*-poly(2-vinylpyridine) (PS-*b*-P2VP) and polystyrene-*block*-poly(4-vinylpyridine) (PS-*b*-P4VP) as well as thiol-terminated polystyrene homopolymers (PSSH) with number-average molecular weight  $M_n=1100$  g·mol<sup>-1</sup>, PDI=1.12 (further denoted as PSSH1) and  $M_n=5300$  g·mol<sup>-1</sup>, PDI=1.10 (further denoted as PSSH5) were purchased from Polymer Source Inc, Canada and used without any further purification. For convenience, all BCP parameters (molecular weight, PDI, composition, etc.) are presented in Chapter 4.1.

#### *Chemicals used*

Iron (III) acetylacetonate (Fe(acac)<sub>3</sub>, 99.95%), cobalt (II) acetylacetonate (Co(acac)<sub>2</sub>, 99.99%), silver acetate (AgAc, 99%), sodium borohydride (NaBH<sub>4</sub>, 99%), tetraoctylammonium bromide (TOAB, 98%), 1,2-hexadecanediol (1,2-HDD, 90%),

1,2-decanediol (1,2-DD, 98%), dibenzyl ether (DBE, 99%), oleylamine (OlAm, 70%), oleic acid (OlAc; 90%), tri-*n*-octylphosphine oxide (TOPO, 99%), 1,2-dichlorobenzene (1,2-DCB, 99%), citric acid (99%), Iron (II) chloride tetrahydrate ( $\text{FeCl}_2 \cdot 4\text{H}_2\text{O}$ , 99%) and Iron (III) chloride hexahydrate ( $\text{FeCl}_3 \cdot 6\text{H}_2\text{O}$ , 97%) were purchased from Aldrich and used as received.

Milli-Q water (cleaned with Purelab Plus® ultra-pure purification system) was used throughout the work. Ammonium hydroxide (25%, Acros) and hydrogen peroxide (30%, Merck) were used as received. Organic solvents, such as acetone, chloroform, 1,4-dioxane, toluene, tetrahydrofuran (THF) (purchased from Acros), ethanol and methanol (VWR chemicals) were of analytical grade and used as received.

#### *Substrates preparation*

Highly polished silicon (Si) wafers with <100> orientation and a native silicon oxide layer of ~1.5 nm thickness purchased from Si-Mat Silicon Materials (Kaufering, Germany) were used as substrates. Before use, they were cut into an appropriate size and cleaned three times with dichloromethane in an ultrasonic bath for 15 minutes and afterwards in a mixture of ammonia solution (29%), hydrogen peroxide (30%) and deionised water in volume ratio (1:1:4) at 75°C for 1 h. Substrates were rinsed several times with Milli-Q water, stored in the same overnight and dried with nitrogen flow before film deposition. Glass substrates were purchased from Manzel GmbH & Co (Braunschweig, Germany) and cleaned similar to Si wafers before film deposition.

#### *Thin film preparation and annealing*

Thin films were deposited onto pre-cleaned Si or glass wafers by spin or dip-coating from BCP or NP/BCP composite solutions. Film thickness was adjusted with rotation / withdrawing speed during spin / dip-coating and/or polymer concentration.

The SENTECH SE-402 microfocus null-ellipsometer equipped with He/Ne laser ( $\lambda = 632.8 \text{ nm}$ ,  $70^\circ$  angle of incidence) was used to measure the thickness of block copolymer thin films. The refractive indices  $n_{\text{Si}} = 3.858 - i0.018$  for silicon substrate and  $n_{\text{SiO}_2} = 1.4598$  for native silicon dioxide were used for the calculations. For the PS-*b*-PVP block copolymers, a weight average refractive indices were estimated using  $n_{\text{PS}} = 1.589$ [Wan06],  $n_{\text{P}_2\text{VP}} = 1.595$ [Wan06] and  $n_{\text{P}_4\text{VP}} = 1.590$  values.[Sid03] The film

thickness of NP/BCP composites was controlled by scratch test on three different places of the sample using AFM instrument.

Solvent vapour annealing [Nan09] of the thin films was performed in a glass chamber (80(*d*)×30(*h*) mm, V~80 ml), saturated with solvent vapour. In all experiments (except solvent annealing in the presence of magnetic field), thin films supported on Si or glass substrates were horizontally placed on the bottom of annealing glass chamber. 0.5 ml of solvent was added into a Petri dish placed inside the annealing chamber. Then, the chamber was tightly closed with grinded lid and left for annealing for certain time at RT. Two different ways of solvent annealing were used: “fast” annealing when sample was placed directly into a chamber saturated with a solvent vapour (annealing time 10÷360 min), and “slow” annealing, when sample was additionally enclosed into a small glass vessel connected with solvent saturated chamber through the needle (annealing time 1÷96 hrs). Particular samples were also thermally annealed in vacuum for 48 hours at temperatures above  $T_g$  of both PS and PVP blocks.

*Preparation of lamella for cross-sectional TEM imaging with focused ion beam (FIB)*

Lamellae for cross-sectional TEM imaging were prepared using NEON 40 FIB-SEM workstation (Carl Zeiss AG, Germany) equipped with a Ga ion beam and operated at 30 kV. The sample was initially sputter-coated with 60 nm thick gold layer and then a localized 15 nm thick platinum protective film was deposited with ion beam over the area selected for lamella preparation. The sample was milled and polished with the FIB to give a 100 nm thick lamella and than transferred and attached lift-out grid (Plano GmbH, Wetzlar, Germany).

## Chapter 4 Results and discussion

### 4.1 Choice of block copolymers

In present work, polystyrene-*block*-polyvinylpyridine block copolymers, namely, PS-*b*-P2VP and PS-*b*-P4VP (Fig. 4.1) have been used for fabrication of NPs/BCP composites.

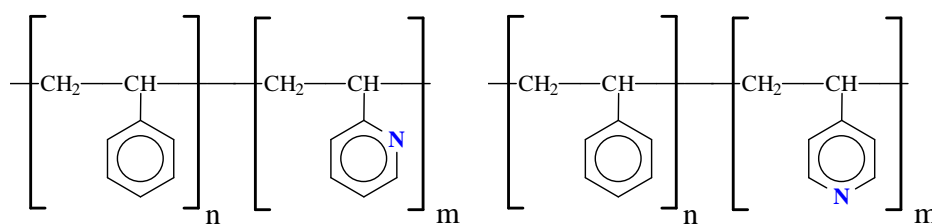


**Figure 4.1** Schematics of chemical structure of PS-*b*-P2VP and PS-*b*-P4VP block copolymers.

Several reasons determined this choice of this BCP system for particular application. First of all, polyvinylpyridine (PVP) is known as universal immobilizer of various types of nanoparticles including metals, semiconductors or dielectrics.[Mal02] Such ability is attributed to the ability of the pyridine groups to undergo various types of interactions with different surfaces. Those interactions could be realized either via hydrogen bonding or through coordination of electron pair of nitrogen with some electron acceptor species, for example metal or metal ions. Therefore, PVP-based block copolymers have been widely used for fabrication of ordered nanostructures containing different types of nanoparticles. [Lin05,Cha07,Cha08,Men09,Nan09]

The value of Flory-Huggins interaction parameter for PS/P4VP pair ( $\chi(PS/P4VP) = -1.370 \cdot 10^{-3} + 2.091/T$ ) is larger than that for PS/P2VP ( $\chi(PS/P2VP) = -1.791 \cdot 10^{-4} + 0.478/T$ ) [Zha07] allowing thus to achieve microphase separation conditions for PS-*b*-P4VP of lower molecular weight and fabricate structures with smaller domain periodicity and size.

P4VP-containing BCPs also could be coordinated with low-molecular weight organic molecules such as pentadecylphenol (PDP) [Zoe08] 1-pyrenebutyric [Kui10] or 2-(4,4'-hydroxybenzeneazo)benzoic acid (HABA) [Tok05], leading to supramolecular

structures. This complexation could be exploited to regulate domain orientation and periodicity. Moreover, these additives could be further washed out, resulting in porous structures with tuneable pore size and pore-to-pore distances, suitable for filling with nanoparticles.[Nan09]

Up to now, fabrication of well ordered composites containing magnetic nanoparticles using PS-*b*-PVP or any other types BCPs still remains challenging. In present work we intended to exploit coordinating properties of PVP to prepare MNPs/PS-*b*-PVP composites with pre-synthesized magnetic NPs, selectively arranged within PVP domains. Using two kinds of nanoparticles bearing different surface functionalities we were also able to prepare ternary NP1/NP2/PS-*b*-PVP composites with either kind of nanoparticles segregated within different BCP microdomains.

PS-*b*-PVP block copolymers of different molecular weight and compositions with polydispersity indexes in a range 1.05-1.15 were used. The variation of BCP composition allowed us to prepare templates of different morphology (i.e. cylinders or lamellae) and domain periodicity.

Main characteristics of PS-*b*-P2VP and PS-*b*-P4VP block copolymers used in this work are summarized in Table 4.1:

**Table 4.1 List of PS-*b*-PVP BCPs used for fabrication of NP/BCP composites**

BCP assignment	$M_n \times 10^3$ g mol <sup>-1</sup>	$M_w/M_n$	Composition: PS- <i>b</i> -PVP $M_n \times 10^3$ , g mol <sup>-1</sup>	$\phi(\text{PVP})$ vol %	Expected morphology
PS <sub>50</sub> - <i>b</i> -P2VP <sub>50</sub>	100.0	1.16	50.0- <i>b</i> -50.0	48.8	Lamellae ( <i>L</i> )
PS <sub>56</sub> - <i>b</i> -P2VP <sub>21</sub>	77.0	1.06	56.0- <i>b</i> -21.0	26.4	Cylinders ( <i>C</i> )
PS <sub>57</sub> - <i>b</i> -P4VP <sub>18</sub>	76.0	1.14	57.5- <i>b</i> -18.5	23.3	Cylinders ( <i>C</i> )
PS <sub>22</sub> - <i>b</i> -P4VP <sub>22</sub>	44.0	1.09	22.0- <i>b</i> -22.0	48.5	Lamellae ( <i>L</i> )
PS <sub>27</sub> - <i>b</i> -P4VP <sub>7</sub>	34.0	1.15	27.0- <i>b</i> -7.0	23.3	Cylinders ( <i>C</i> )

## 4.2 Preparation of magnetic nanoparticles (MNPs)

The first task of the present work was synthesis of magnetic nanoparticles (MNPs), with the aim to be selectively incorporated into PVP domains of PS-*b*-PVP BCP matrix. To accomplish this task several requirements with respect to the MNPs properties have to be ensured:

- mutual affinity between NP surface and PVP moieties of BCP;
- good dispersion stability in common with BCP organic solvent(s);
- appropriate particles size and narrow size distribution;
- particles stability towards oxidation and degradation.

Among the various types of MNPs, ferrite-type magnetic nanoparticles (i.e.  $MFe_2O_4$ ,  $M=Fe, Co, Mn, Ni$ ) are attractive since they can be prepared in relatively easy way and could be handled at ambient conditions without additional precautions. In present work, two kinds of ferrite-type MNPs, namely,  $Fe_3O_4$  and  $CoFe_2O_4$ , were prepared and used as nanoadditives.

### 4.2.1 Synthesis of $Fe_3O_4$ MNPs by thermal decomposition route and their characterisation

Taking into account all advantages of thermal decomposition routes of MNPs preparation,[Wil04] series of  $Fe_3O_4$  MNPs were synthesised from iron(III) acetylacetonate precursor[Sun02,Sun04] in the presence of combination of different surfactants, as schematically presented on Figure 4.2.:

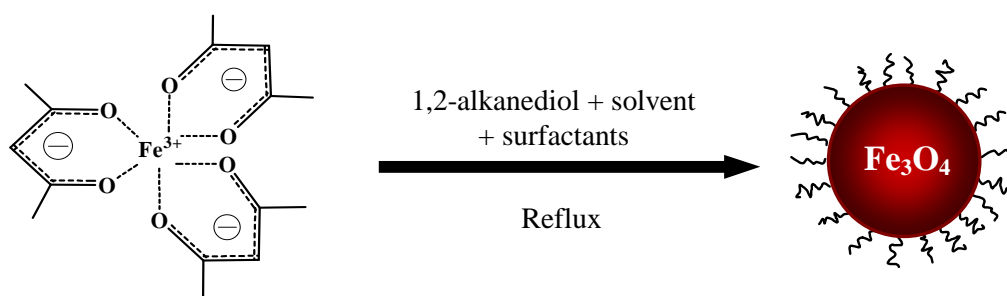


**Figure 4.2** Schematic representation of synthetic route used for preparation of  $Fe_3O_4$  magnetic nanoparticles by thermal decomposition of iron (III) acetylacetonate precursor. Modified from [Sun02].

In typical synthesis, 1 mmol of iron (III) acetylacetonate ( $Fe(acac)_3$ ) was dissolved in 5 ml of dibenzyl ether (DBE) and mixed with another 5 ml of DBE containing corresponding amount of reducing agent and surfactants (Table 4.2). The

mixture was transferred into a three-neck round-bottom flask, equipped with gas inlet, reflux condenser and thermometer and flushed three times with argon. Next, reaction mixture was heated to 200°C and kept at this temperature for 2 hours, followed by refluxing (~290°C) for another 60 min. During the heating, the colour of mixture turned from red-orange to a black, indicating the formation of Fe<sub>3</sub>O<sub>4</sub> MNPs. Particles were precipitated into ~100 ml of ethanol and collected over the permanent magnet. Black-brown supernatant was discarded and particles were purified repeatedly (4 times) by precipitation/redispersion procedure, using chloroform as solvent (~5 ml) and ethanol as flocculating agent (~100 ml).

Table 4.2 summarize preparation conditions applied for MNPs syntheses.

**Table 4.2 Summary of preparation conditions used for synthesis of MNP1–MNP5**

Sample name	Precursor used	Solvent used*	Reducing agent used	Surfactants used	Molar ratios of reactants used during MNPs syntheses
MNP1	Fe(acac) <sub>3</sub>	DBE	1,2-HDD	OIAc/OIAm	Fe(acac) <sub>3</sub> :1,2-HDD:OIAc:OIAm 1 : 2 : 3 : 3
MNP2	Fe(acac) <sub>3</sub>	DBE	1,2-HDD	TOPO	Fe(acac) <sub>3</sub> :1,2-HDD:TOPO MNP2a– 1 : 2 : 3; MNP2b– 1 : 2 : 6
MNP3	Fe(acac) <sub>3</sub>	DBE	1,2-HDD	TOPO/OIAm	Fe(acac) <sub>3</sub> :1,2-HDD:TOPO:OIAm 1 : 2 : 3 : 3
MNP4	Fe(acac) <sub>3</sub>	DBE	1,2-DD	TOPO/OIAm	Fe(acac) <sub>3</sub> :1,2-DD:TOPO:OIAm 1 : 2 : 3 : 3

\* – in all syntheses metal precursor-to-solvent ratio was kept as 1:10 mmol/ml.

Fe(acac)<sub>3</sub> – iron (III) acetylacetonate; DBE – dibenzyl ether; 1,2-HDD – 1,2-hexadecane diol; 1,2-DD – 1,2-decanediol, OIAc – oleic acid; OIAm – oleylamine; TOPO – tri-*n*-octylphosphine oxide

After each precipitation/redispersion step small amount of nanoparticles was collected, dried in vacuum overnight at 50°C and analysed with TGA in order to determine the amount of remained reactants on NPs surface. Notably, TGA experiments showed that all reactants and excess of surfactants were almost completely removed after first two precipitation/redispersion steps, resulting in almost no additional weight lost after the next purification cycles (Fig. 4.3).

All TGA curves possessed two distinct weight lost regions: the first was observed in the temperature range from 100 °C to ~500 °C, which is usually attributed to degradation of organic stabilizing shell, and second, above 600 °C, was reasoned by the phase transition from Fe<sub>3</sub>O<sub>4</sub> to FeO, which is thermodynamically more stable above 570 °C.[Zhao06]



As the first sample, oleic acid (OlAc) capped  $\text{Fe}_3\text{O}_4$  MNPs (further denoted as MNP1) were prepared in the presence of 1,2-hexadecanediol (1,2-HDD) as reducing agent and a mixture of OlAc and oleylamine (OlAm) as surfactants, according to a protocol reported elsewhere.[Sun02]

Resulted MNP1 were found to be readily dispersible in low-and moderate polarity organic solvents (e.g. THF,  $\text{CHCl}_3$ , toluene) but rapidly precipitate in ethanol, indicating, therefore, monolayer type of stabilising shell.

Determination of particles size and size distribution was done by analysis of TEM images of correspondent MNPs. For MNP1 an average particles diameter  $d_{\text{MNP1}} = 5.9 \text{ nm}$  with standard deviation  $\text{SD} = 1.0 \text{ nm}$  (17.2%) was found (Fig. 4.4).

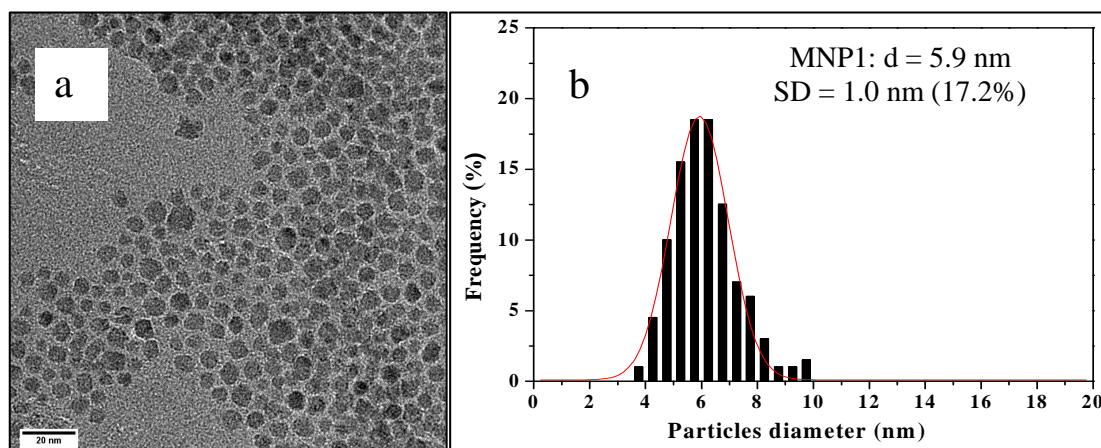


**Figure 4.3** TGA curves of MNP1 after 1<sup>st</sup>, 2<sup>nd</sup>, 3<sup>rd</sup> and 4<sup>th</sup> purification cycles.

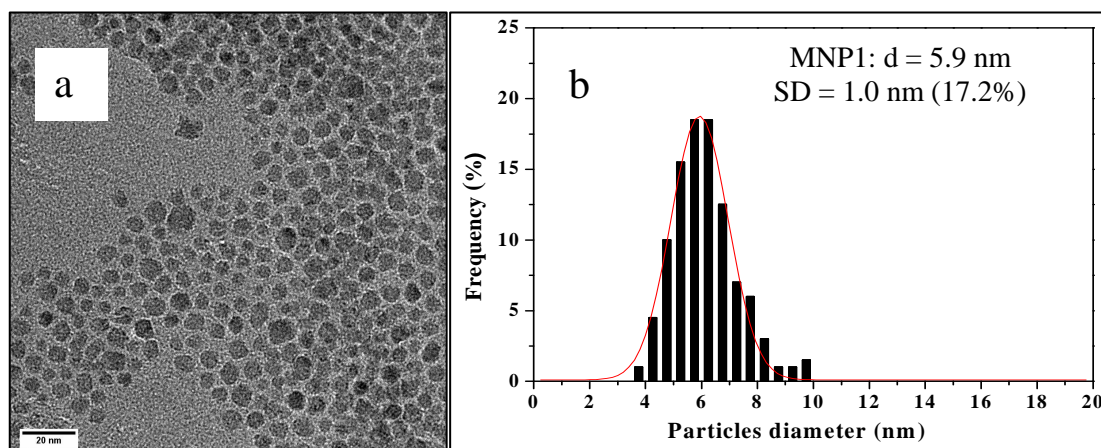


**Figure 4.4** TEM image (a) and size distribution histogram (b) of MNP1 prepared in the presence OlAc/OlAm as surfactants. Red line – Gaussian fit.

For preparation of next sample (denoted as MNP2), tri-n-octylphosphine oxide (TOPO) was used as surfactant instead of OlAc and OlAm. From correspondent TEM images (Fig. 4.5 a,b) it was found that MNP2, prepared in the presence of TOPO had larger size ( $d_{\text{MNP2}} = 8.1 \text{ nm}$ ) and displayed broader particles size distribution ( $\text{SD}=27.2\%$ ) compared to MNP1, independently on the  $\text{Fe}(\text{acac})_3/\text{TOPO}$  ratios used during the reaction. One of the reasons of such broad size distribution could be

explained considering geometry of TOPO molecule: three C8-alkyl chains, which are bound to a single P atom, sterically repel each other, thus, making the TOPO molecule more bulky and less effective for NPs nucleation and growth control, compare to the OIAc and OIAm.[Hou05]

Therefore, as a next sample, MNP3 were synthesized in the presence equimolar ratio of both TOPO and OIAm as surfactants. It was found that such combination of surfactants results in nanoparticles of almost same size and polydispersity as MNP1 ( $d_{\text{MNP3}} = 6.1 \text{ nm}$ ,  $\text{SD} = 17.1\%$ ) (Fig.4.5 c,d).

Additionally, MNP4 were prepared as a reference sample in the way similar to MNP3, but instead of 1,2-HDD, 1,2-decanediol (1,2-DD), which has a shorter alkyl chain length was used during the synthesis.

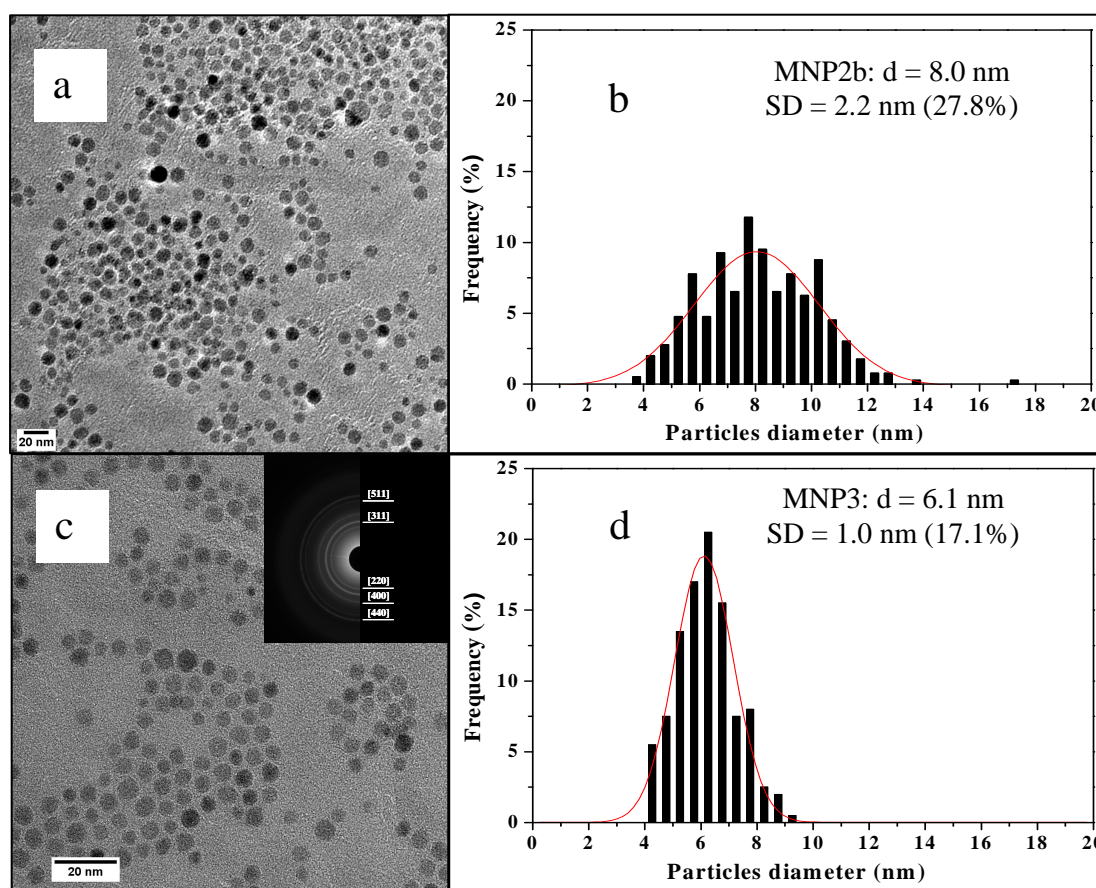


**Figure 4.5** TEM images (a,c) and size distribution histograms (b,d) of MNP2b (a,b) and MNP3 (c,d). Inset on (c) – electron diffraction pattern of MNP3. Red lines – Gaussian fits.

From electron diffraction pattern (EDP) of MNP3 (Fig. 4.5c, inset) it was revealed formation of BCC spinel lattice structure, which is typical for magnetite. (JCPDS, card No 79-0418).

All preparation and purification steps in MNP2÷MNP4 syntheses were performed similar to MNP1 synthesis, with only one difference that after reflux (i.e. before purification), reaction mixture was left for stirring for another 12 hours at room temperature. It should be mentioned, that such stirring overnight was crucial for long-term dispersal stability of particles in organic solvent.

For longer periods of time, after purification particles were stored under ethanol saturated with argon to prevent undesirable oxidation and agglomeration. Such conditions ensured perfect MNPs dispersability in organic solvents even after several months of storage.

All synthesized MNPs were characterized with FTIR in order to clarify the nature of stabilizing shell formed on the particles surface by surfactants. Figure 4.6 shows FTIR spectra of MNP1÷MNP4 series, as well as spectra of reactants used during the particles syntheses.

Several characteristic spectral features common for all MNP samples were observed. First, there are three characteristic peaks at  $\sim 2956$ ,  $\sim 2924$  and  $\sim 2854$   $\text{cm}^{-1}$ , which correspond to  $\nu_a(\text{CH}_3)$ ,  $\nu_s(\text{CH}_2)$  and  $\nu_a(\text{CH}_2)$  bands, respectively.[Klo07] Second, two strong absorptions at  $\sim 592$   $\text{cm}^{-1}$  and  $\sim 626$   $\text{cm}^{-1}$  were attributed to  $\nu_2(\text{Fe-O})$  and  $\nu_1(\text{Fe-O})$  vibrations, respectively.[Klo07]

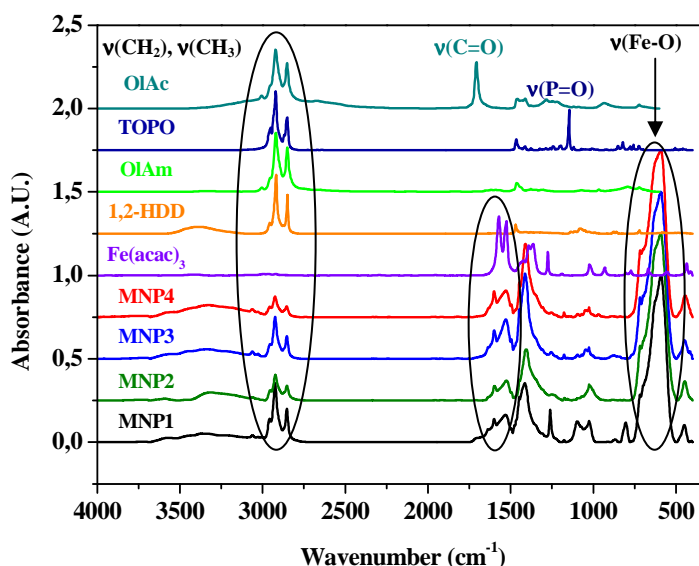


**Figure 4.6** FTIR spectra of MNP1-MNP4 samples prepared by thermal decomposition of  $\text{Fe}(\text{acac})_3$  and reactants used during their syntheses.

As was expected, for MNP1 appearance of intense C=O signal at  $\sim 1707$   $\text{cm}^{-1}$ , was not detected. In contrast, on spectrum of pure oleic acid such peak is clearly visible, indicating that after purification no free oleic acid is present in MNP1 sample and only chemisorbed molecules remain on MNPs surface.[Lan07,Zhan06]

However, nearly identical peaks in the  $1400\text{-}1700$   $\text{cm}^{-1}$  region, which are often assigned to symmetric and asymmetric stretching of chemisorbed carboxylic

groups,[Klo07,Zhan06] were observed in FTIR spectra of all MNP samples. Since neither oleic nor other carboxylic acids were used in the synthesis of MNP2, MNP3 and MNP4 samples, these spectral features were attributed to the presence of carboxylic species coming from acetylacetonate precursor.

On the other hand, characteristic  $\nu(\text{P}=\text{O})$  band at  $1146\text{ cm}^{-1}$ ,[Sta08] which was

observed for pure TOPO, was not detected for any MNP samples prepared in the presence of TOPO, supposing thus, its complete removal during particles purification. In order to assay the origin and nature of stabilizing shell formed on particles, prepared in presence of TOPO and OlAm, MNP3 sample was studied by XPS (Fig. 4.7). Indeed, as it was supposed above, from XPS results it became evident, that rather small amounts of TOPO and OlAm remain on MNP3 surface after purification. As can be seen, the signal intensity in regions of N 1s and P 2p peaks (399.4 and 133.0 eV, respectively) only slightly overcomes background level.

On the other hand, an appearance of intense C 1s peak (285.0 eV) assumes the presence of saturated hydrocarbons. The atomic ratios of nitrogen/carbon and phosphorus/carbon pairs obtained from XPS ( $\text{N}:\text{C}_{\text{XPS}} = 1:63.2$ ,  $\text{P}:\text{C}_{\text{XPS}} = 1:108.6$ ) were found substantially lower

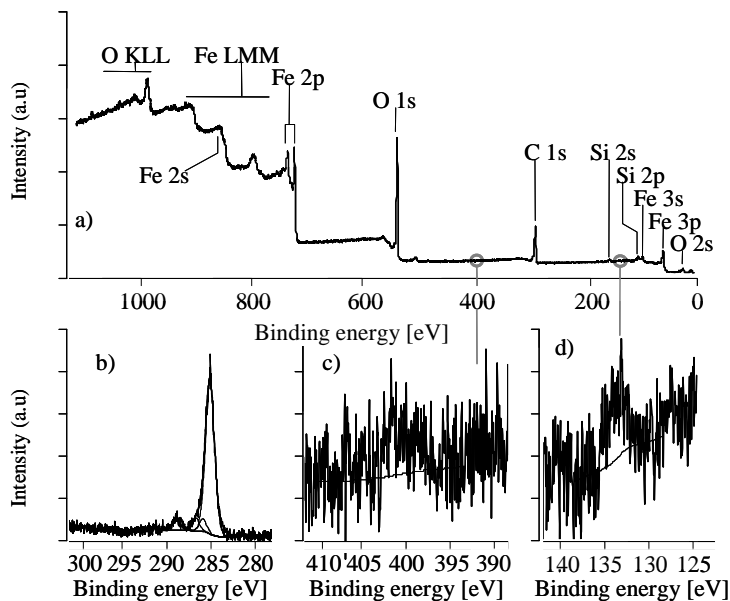


**Figure 4.7** XPS spectra of MNP3: wide scan spectrum (a); high-resolution C 1s spectrum (b); N 1s spectrum (count rate  $\times 10$ ) (c); P 2p spectrum (count rate  $\times 10$ ) (d).

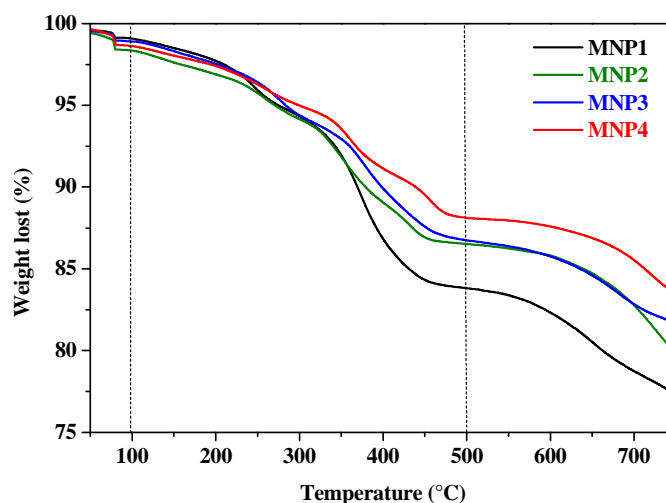


**Figure 4.8** TGA traces of MNP1-MNP4 samples.

compared to predicted ones for TOPO and OIAm molecules ( $N:C_{OIAm,calc} = 1:18$ ,  $P:C_{TOPO,calc} = 1:24$ ). Thus, it was assumed that organic layer in case of MNP3 was formed predominantly *via* 1,2-hexadecanediol adsorption.[Bin08]

TGA data obtained from different samples were compared in order to obtain the amount of surfactants on the particles surface. From TGA results (Fig. 4.8) it was found that the amount of the adsorbed surfactants differs in different MNP samples with the highest content in MNP1 and lowest in MNP4 cases. From the TGA data (weight lost at the temperature region  $100^{\circ}\text{C} \pm 500^{\circ}\text{C}$ ) the content of organic part in MNP1, MNP2, MNP3 and MNP4 samples was found to be 18.3, 13.7, 14.1, 12.1 wt%, respectively (considering iron oxide content as 100%).

It was also observed, that dispersion stability of MNP1, MNP2, MNP3 and MNP4 was substantially different and case-dependent on the polarity of solvent. MNP1 were readily dispersible in organic solvent of low and moderate polarity (such as toluene, THF,  $\text{CHCl}_3$ ) and they remained stable in dispersion for a long period time (i.e. up to 6 months), while MNP2 and MNP3 produced stable dispersions only in solvents of moderate polarity like THF or chloroform and had a strong tendency to aggregate in toluene or toluene/THF mixture containing even small fraction of toluene (i.e. less than 20 vol%). Regarding MNP4, it was noted that they were much less stable even in such polar solvents like THF and tend to agglomerate irreversibly already after 24 hours of storage.

#### 4.2.2 Synthesis and characterization of $\text{CoFe}_2\text{O}_4$ NPs (MNP5)

Cobalt ferrite  $\text{CoFe}_2\text{O}_4$  NPs (further denoted as MNP5) were also prepared by thermal decomposition, using  $\text{Fe}(\text{acac})_3$  and  $\text{Co}(\text{acac})_2$  as precursors.[Sun04] Synthetic procedure was performed similarly to MNP3 case. Initially,  $\text{Co}(\text{acac})_2$  and  $\text{Fe}(\text{acac})_3$  precursors with molar ratio of 1:2 to give the total amount of 1 mmol were mixed with the rest of reactants and then preparation and purification were carried out as for the MNP3.



First, investigation of as-prepared MNP5 by TEM imaging was performed (Fig. 4.9) and it was found that particles had an average diameter of 6.0 nm, similar to MNP3, however, displayed slightly broader size distribution.

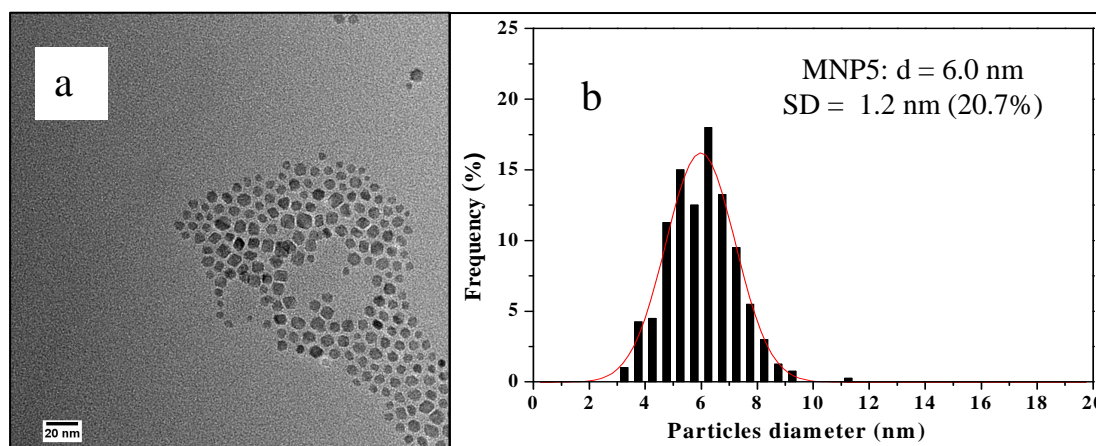


**Figure 4.9** TEM image (a) and size distribution histogram (b) of  $\text{CoFe}_2\text{O}_4$  MNP5 prepared in the presence of TOPO and OIAm as surfactants. Red line – Gaussian fit.

FTIR, TGA and XPS (Fig. 4.10 and 4.11) analyses were also performed and it was revealed that the nature of stabilising layer (i.e. 1,2-HDD) was the same as in the case of MNP3 with organic layer content 12.9 wt% (considering  $\text{CoFe}_2\text{O}_4$  as 100%).

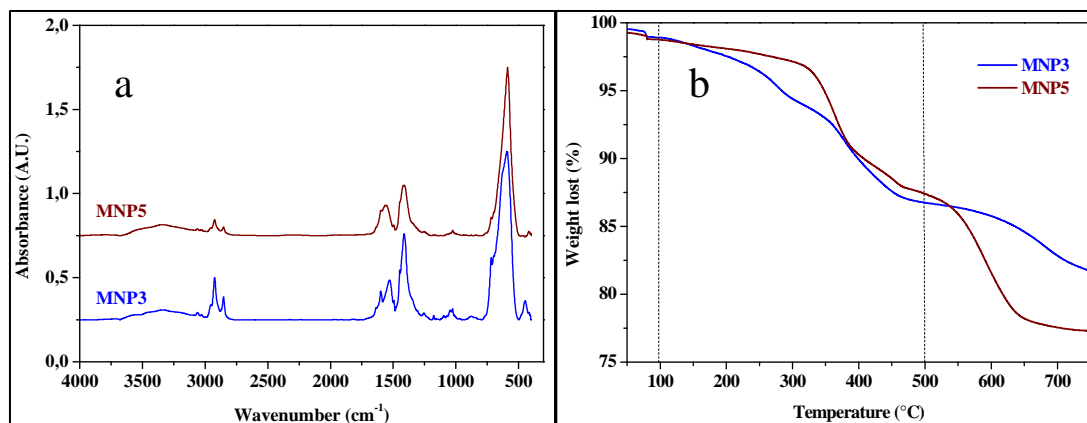


**Figure 4.10** FTIR spectra (a) and TGA curve (b) of MNP5 versus MNP3.

From XPS measurements the presence of Co in the particles was revealed (Fig. 4.11 e). Quantitative analysis of Fe 3p and Co 3p signals (56.025 eV and 60.455 eV, respectively) resulted in Co:Fe atomic ratio of 2.26, which differs significantly from expected value of  $\sim 0.5$ . Since XPS mostly detects signals from very topmost layer of the sample (max. 10 nm), it is rather difficult to conclude about real composition of the whole sample.

MNP5 particles appeared moderately stable toward agglomeration in THF dispersion and irreversibly precipitated after 2-3 weeks of storage.

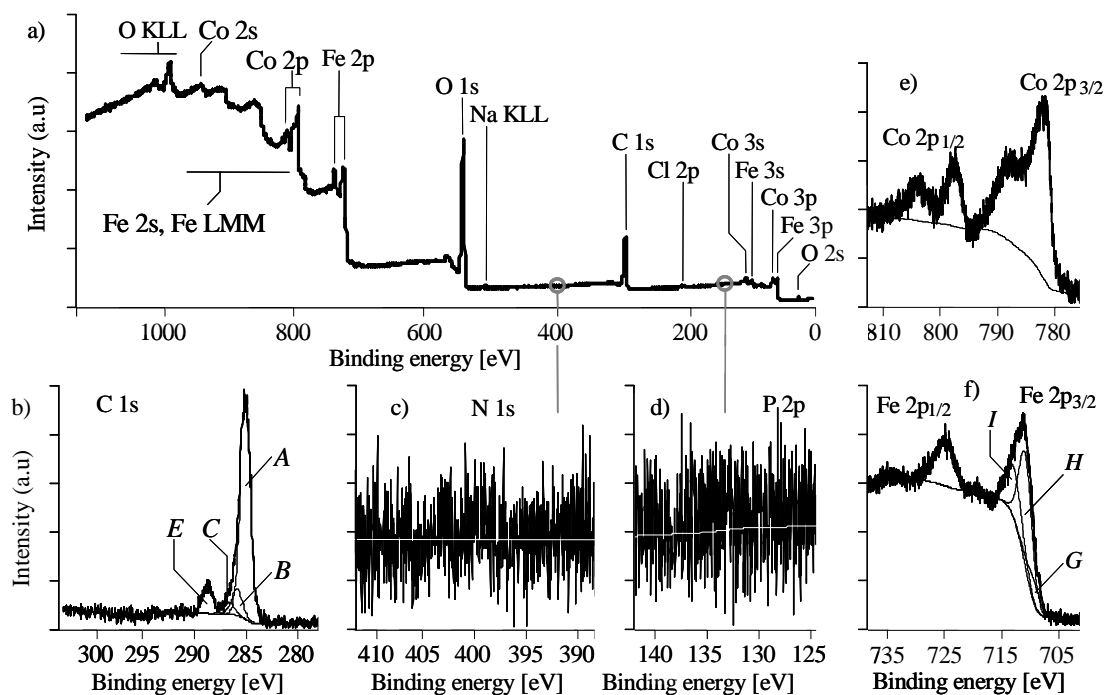


**Figure 4.11** XPS spectra of  $\text{CoFe}_2\text{O}_4$  MNP5: wide scan spectrum (a); high-resolution C 1s spectrum (b); N 1s spectrum (count rate x10) (c); P 2p spectrum (count rate x10) (d); high-resolution Co 2p spectrum (e); high-resolution Fe 2p spectrum (f).

Summarizing all experimental results on preparation and investigation of  $\text{Fe}_3\text{O}_4$  and  $\text{CoFe}_2\text{O}_4$  MNPs (i.e. MNP1–MNP5) and observations discussed above it could be stated the following. The densest stabilizing layer on MNP1 is reasonable due to the distinct affinity of oleic acid carboxylic groups towards  $\text{Fe}_3\text{O}_4$  surface. In case of MNP2, MNP3 and MNP5, thinner, but still sufficient for particles stabilization organic shell was formed, that is an important prerequisite for efficient binding of particles to PVP. In latest cases, nanoparticles stabilization was achieved due to coordination with 1,2-HDD instead of OIAc. An application of TOPO, in combination with OIAm ensured relatively good control over MNPs nucleation and grows during the synthesis. However, due to their weak affinity toward iron oxide surface, these molecules were washed out during particles purification, as was proved by IR and XPS experiments and only 1,2-HDD remained on particles surface. When 1,2-decanediol with shorter chain length was used during MNP synthesis (MNP4), it led to further reduction of stabilizing layer content and poor particles stability in most of organic solvents and, thus made them less suitable for particular application.

### 4.3 Synthesis and characterization of AgNPs

As a second type, silver NPs (AgNPs), covered with polystyrene stabilizing shell, were prepared with an aim to be incorporated into PS block of PS-*b*-PVP block copolymer. Namely modification of AgNPs surface with PS layer has to ensure their dispersion stability of such particles in organic solvents and their PS-selective segregation in PS-*b*-PVP BCP matrix.

For preparation of PS-covered AgNPs two methods (with certain modifications) were used. As a first, two-phase Brust method [Bru94,HeS01] was performed in the presence of thiol-terminated polystyrene (PSSH). As a second method, two-step synthesis was adopted from approach, reported by Hiramatsu and Osterloch [Hir04] starting from preparation of OIAm covered AgNPs followed by ligand-exchange step afterwards.

Two-phase hydride reduction method using AgNO<sub>3</sub> as metal precursor was used for fabrication of series of silver NPs, denoted as AgNP1÷AgNP3. The preparation procedure was followed as described by He and co-workers [HeS01] with a difference that thiol-terminated polystyrene (PSSH1, M<sub>n</sub>=1100 g·mol<sup>-1</sup>, Polymer Source Inc.) was used during the syntheses as stabilizing shell-forming ligand instead of alkanethiol.

As it can be seen from corresponding TEM images and size distribution histograms (Fig. 4.12), the average particles size was gradually lowered with an increase of AgNO<sub>3</sub>/PSSH1 weight ratio, as it was expected. However, such modification of synthetic procedure (i.e. application of PSSH instead of alkanethiol) resulted in nanoparticles with broad size distribution, independently on AgNO<sub>3</sub>/PSSH1 weight ratios used.

Such broad nanoparticles size distribution compared to results reported by He et al. [HeS01] could be assumed to be an effect of stabilizing ligand, used during the reaction. It is possible that the steric bulk of the PS polymer chains influences the growing mechanism of the silver cores significantly, since effective capping of the silver cores is lessened by a bulky ligand, leading to more polydisperse nanoparticles compared to that made in presence of alkanethiol. Similar effect of size of stabilizing polymer ligand on nanoparticles polydispersity (SD in order of 27 %) was also observed



for gold nanoparticles prepared via Brust method in the presence of low-molecular weight PSSH.[Cor04]

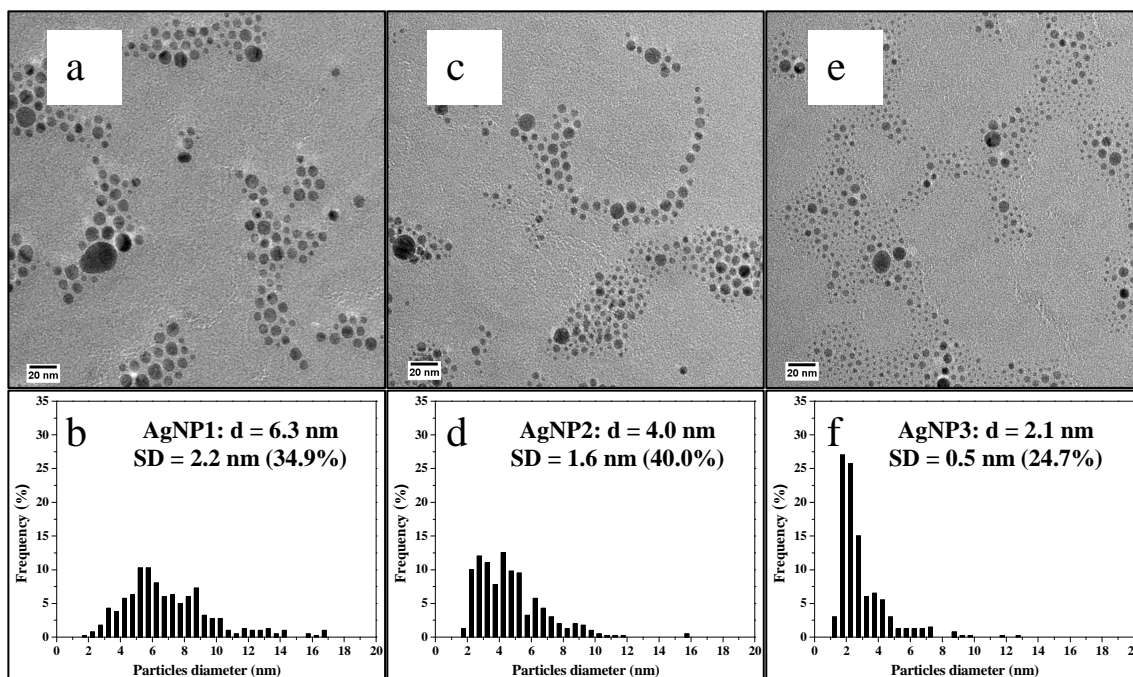


**Figure 4.12** TEM images (a,c,e) and size distribution histograms (b,d,f) of AgNP1 (a,b), AgNP2 (c,d) and AgNP3 (e,f) prepared by two-phase method using 1:1, 1:2 and 1:4  $\text{AgNO}_3/\text{PSSH}$  weight ratios, respectively.

One of the possible ways to circumvent polydispersity problem could involve the synthesis of AgNPs in the presence of alkanethiols followed by ligand-exchange reaction with PSSH molecules. However, kinetic studies of the ligand exchange mechanism suggest that such reactions belong to diffusion limited process.[Car08] In addition, ligand exchange process is reversible and due to the same chemical nature of capping end-groups in alkanethiol and PSSH, the large excess of PSSH and long time of reaction would be required. In contrast, if the initial capping agent will possess weaker affinity toward silver surface compared to thiol moieties, such ligand exchange step should be more effective and faster.

Therefore, thermal decomposition of silver precursor in the presence of solely oleylamine as reducing and stabilizing agent [Hir04] was pointed out as an alternative way to prepare AgNPs. It was also shown that weakly adsorbed oleylamine on the nanoparticles could be readily replaced with thiol-containing molecules. Schematically, synthetic procedure is presented on Figure 4.13.

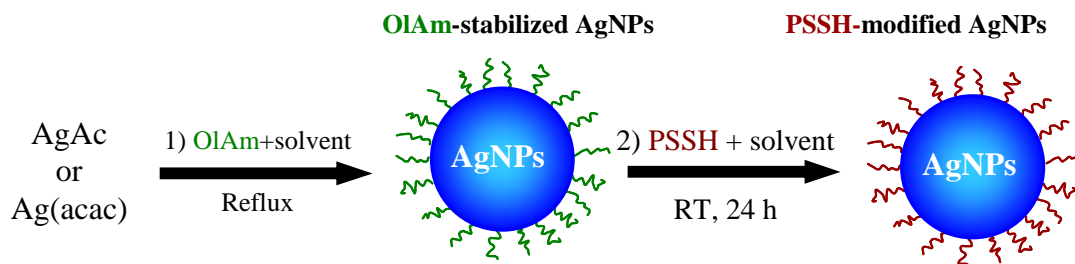


**Figure 4.13** Schematics of synthetic route used for preparation of PS-covered silver nanoparticles (AgNPs) by reduction of silver precursor (Ag(acac) or AgAc) in the presence of oleylamine.

For preparation of AgNPs (denoted as AgNP4), 3 mmol of silver acetate (AgAc) was mixed with 25 ml of OlAm and 500 ml of toluene. The reaction mixture was heated to 110°C under inert argon atmosphere (heating rate 10°C/min) and then refluxed for 24 hours. The colour of the mixture gradually changed from colourless to yellow and then – to dark-yellow, indicating formation of silver colloids. As it was mentioned before, in such reaction OlAm simultaneously serves function of both mild reducing and particles stabilizing agent. After 24 hours of reflux, reaction mixture was cooled down to RT and toluene was removed on rotary evaporator to give a viscous AgNP4/OlAm mixture.

As a next step, AgNP4/OlAm mixture was mixed with 50 ml of CHCl<sub>3</sub> containing 300 mg of PSSH1 and stirred at room temperature for the next 24 hours. Thereafter, PS-modified AgNPs were precipitated in *ca.* 100 ml of ethanol and centrifuged at 5000 RPM for 10 min. To remove the rest of OlAm and excess of PSSH, repeated (5-6 times) centrifugation/redispersion steps were performed by adding chloroform as a solvent (*ca.* 5 ml) and acetone as flocculating agent (*ca.* 100 ml for each step). At such conditions, PS-modified AgNP precipitate while PSSH1 remains soluble. Final product was collected and dried overnight in vacuum at 50°C to give *ca.* 100 mg of metal-like powder readily dispersible in organic solvents.

TEM investigation of AgNP4 sample (Fig. 4.14 a,b) revealed formation of 4.1 nm nanoparticles with uniform spherical shape and narrow size distribution (SD = 0.6 nm, 14.5%).

8.5 nm AgNP5 (Fig. 4.14 c,d) were also prepared in toluene, similar to AgNP4, with the only difference that the mixture of AgAc and OlAm was injected into a boiling toluene under inert conditions and then refluxed for 24 hours. The other reaction conditions, including ligand exchange and purification, were kept similar to AgNP4 synthesis.

Finally, 12.8 nm AgNP6 (Fig.4.14 e,f) were prepared in 1,2-dichlorobenzene (1,2-DCB) as reaction medium. For this purpose 3 mmol of AgAc and 25 ml of OIAM were dissolved in 500 ml of 1,2-DCB and refluxed under inert atmosphere for 12 hours. After reaction mixture was cooled down to RT, ligand exchange steps were performed. Two kinds thiol-terminated polystyrene homopolymers of different molecular weight were used to modify AgNP6 surface, namely PSSH1 ( $M_n=1100 \text{ g}\cdot\text{mol}^{-1}$ ) and PSSH5 ( $M_n=5300 \text{ g}\cdot\text{mol}^{-1}$ ). For this purpose reaction mixture was split into two parts and PS-modification step was done by addition to each part of 10 ml of 1,2-DCB containing 150 mg of either PSSH1 or PSSH5 followed by stirring for next 24 hours at RT. To purify AgNP6, ~100 ml of ethanol was added and PS-modified particles were collected by centrifugation (15000 RPM for 30 min). Nanoparticles were washed with chloroform/acetone mixture 5-6 times, similarly to AgNP4 and AgNP5. For convenience, AgNP6 modified with PS of different molecular weight are further denoted in text as AgNP6a (PSSH1) and AgNP6b (PSSH5).

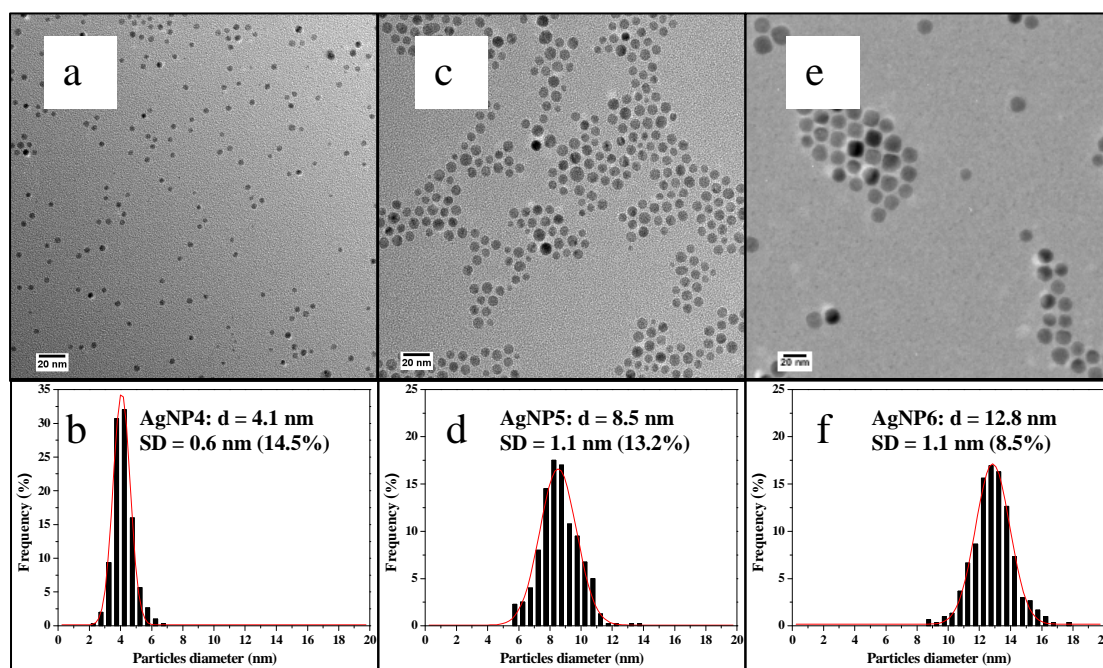


**Figure 4.14** TEM images (a,c,e) and size distribution histograms (b,d,f) of AgNP4 (a,b), AgNP5 (c,d) and AgNP6 (e,f) prepared by thermal decomposition of AgAc in the presence of OIAM.

FTIR spectra (Fig. 4.15 a) confirmed success of ligand exchange step for all series of AgNPs prepared, independently on reaction medium (i.e. chloroform and 1,2-DCB) and molecular weight of PSSH used for particles modification: characteristic peaks of PSSH are replicated in spectra of all PS-modified AgNP4–AgNP6 samples.

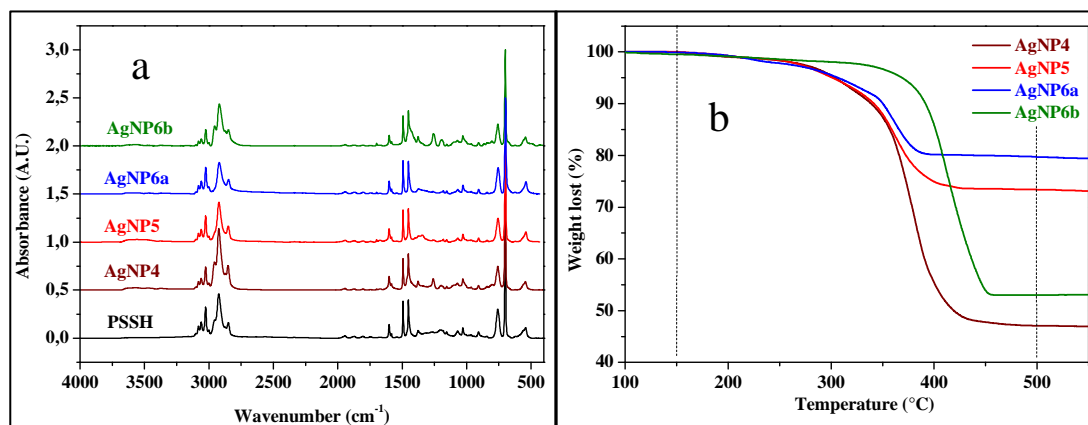


**Figure 4.15** FTIR spectra (a) and TGA curves (b) of PS-modified AgNP4-AgNP6 samples.

As was expected, TGA data (Fig. 4.15 b) revealed reduction of PSSH1 content with an increase of particles size due to the lower surface-to-volume ratio for larger-size particles. Calculated PS grafting densities, determined from TEM and TGA experiments, resulted in values of 4.4, 3.0 and 3.1 PS chains/nm<sup>2</sup> for AgNP4, AgNP5 and AgNP6a, respectively, considering spherical particles shape. Significant increase of organic layer content was observed for AgNP6b covered with longer chain polystyrene (PSSH5) compared to AgNP6a, stabilized with shorter-chain PS (PSSH1). Polymer grafting density calculated for AgNP6b sample was found lower (2.2 PS chains/nm<sup>2</sup>) compared to AgNP6a, which is in agreement with expectations due to larger  $R_g$  of PSSH5 polymer.

Importantly, densely grafted polymer layers (i.e. above 2 chains/nm<sup>2</sup>) were formed on the surface of all PS-modified AgNPs samples, which is important requirement to screen possible particles interaction with PVP chains and achieve their PS-selective segregation within PS-*b*-PVP BCP matrix.[Kim06b] Formation of such dense polymer layer, which is rather hardly achievable for flat surfaces *via* “grafting-to” approach, nevertheless, was reported for PS-modified gold nanoparticles.[Cor04]

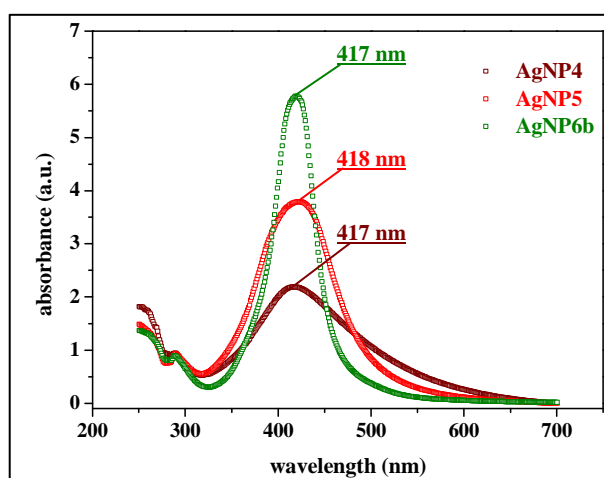


**Figure 4.16** UV-VIS spectra of THF dispersions of AgNP4, AgNP5 and AgNP6b.  $C(\text{Ag}) = 0.05 \text{ mg/ml}$ .

UV-VIS spectra of PS-modified AgNP4, AgNP5 and AgNP6b nanoparticles dispersed in THF (0.05 mg/ml of Ag content) are shown on Figure 4.16. SPR peak maxima of nanoparticles THF dispersions appeared at 417 (AgNP4 and AgNP6b) and 418 nm (AgNP5), indicating almost no influence of particles size and polystyrene stabilizing shell nature on position of SPR peak maxima for particular samples. With reduction of AgNPs size broadening of SPR band was observed, which might be explained by the effect of an increase in nanoparticles size distribution (i.e. 8.5% for AgNP6 vs. 14.5% for AgNP4). In addition, UV-VIS spectrum of AgNP4 was of asymmetric shape that might be reasoned by particles clustering due to their high surface energy. In contrast, both AgNP5 and AgNP6b spectra were of well defined symmetric shape, revealing monodisperse character of nanoparticles, as was also observed by TEM.



## 4.4 Morphology of neat PS-*b*-PVP BCPs

Incorporation of nanoadditives into a block copolymer matrix could significantly affect both morphology and behaviour of the composite system compared to native BCP. Several different effects, which were experimentally observed and theoretically predicted, [Tho01, Bal03, Liu06] could be pointed out as principal. Among them swelling of BCP microdomains, stabilisation of grain boundaries, [Lis06] order-disorder [LoC07] or phase transition of a system, induced by the presence of nanoparticles, [Kim05] directional reorientation of microdomains, [Lin05] are the most cited.

Thus, in order to recognize possible influence of nanoadditives, the morphology of neat BCPs was studied before they were used for composites preparation. Most of experiments on block copolymers and NP/BCP composites morphology investigation were performed on thin films. The thin films were prepared on Si/SiO<sub>2</sub> substrates by spin- or dip-cast from correspondent solutions (0.5-2.5 wt%). The choice of cast solvent was conditioned by the requirement of both block copolymers solubility and dispersion stability of both magnetic and silver NPs used for NP/BCP composite preparation. Among the solvents that provide sufficiently good solubility for PS and PVP, THF was considered as the most suitable one since it ensured also the best dispersion stability of nanoparticles, and used as casting solvent in most of experiments. Alternatively, for particular samples also CHCl<sub>3</sub> was used as a solvent for thin film preparation. Before film deposition, cast solutions were mechanically stirred for 24 hours at RT to ensure homogeneous system and filtered through 0.2 µm pore-sized membrane filter just before film deposition to remove particulate impurities. The film thickness, measured afterwards by ellipsometry, was adjusted by variation of polymer concentration and/or rotation (withdrawing) speed.

Morphologies of BCPs thin films are primary dependant on polymer structure and composition, as well as on casting conditions, such as substrate chemistry, solvent, film thickness etc. Therefore, dependence of morphology on type of BCP (i.e. PS-*b*-P2VP or PS-*b*-P4VP) in “as-cast” samples was analyzed first.

#### 4.4.1 Morphologies of “as-cast” PS-*b*-P2VP thin films

An effect of block copolymer molecular weight and blocks ratio on resulting morphology of “as-cast” PS-*b*-P2VP BCPs thin films could be seen on Figure 4.17. Worm-like morphology was observed for symmetric PS<sub>50</sub>-*b*-P2VP<sub>50</sub> BCP thin film cast from THF (Fig. 4.17 a), while surface covered with PS<sub>56</sub>-*b*-P2VP<sub>21</sub> was featureless (Fig. 4.17 b).

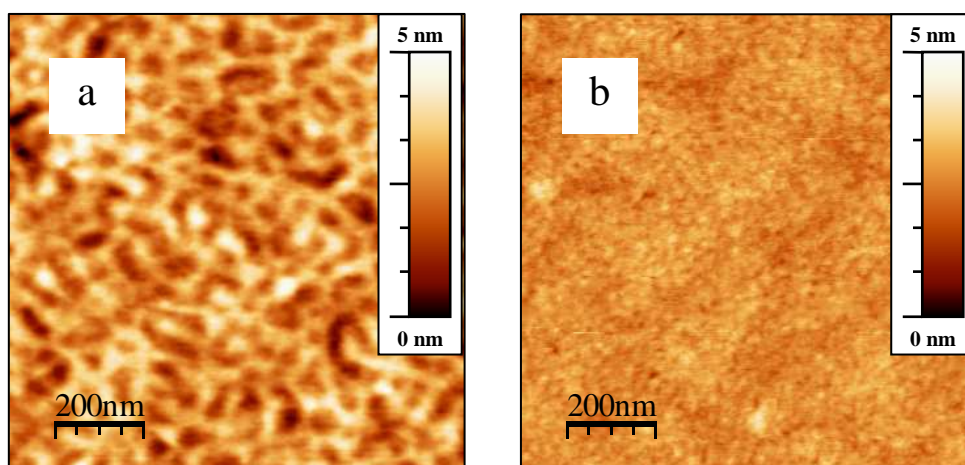


**Figure 4.17** AFM topography images of PS<sub>50</sub>-*b*-P2VP<sub>50</sub> (a) and PS<sub>56</sub>-*b*-P2VP<sub>21</sub> (b) thin film cast from THF. Film thickness ~50 nm (a) and ~30 nm (b).

It is obvious, that for both PS-*b*-P2VP BCPs, THF-cast samples show no evidence of any ordered structures formation. Similarly, no ordered structure formation was found for chloroform-cast PS-*b*-P2VP thin films. Since THF and CHCl<sub>3</sub> are non-selective solvents for both PS and P2VP,<sup>[LiX07]</sup> the “as-cast” thin films of PS-*b*-P2VP BCPs showed disordered morphology.

#### 4.4.2 Morphologies of “as-cast” PS-*b*-P4VP thin films

In contrast to PS-*b*-P2VP, all BCPs containing P4VP block display dimple-type (dried micelles) structures when cast from THF solutions (Fig. 4.18 a-c). The reason of such difference lies in a fast evaporation rate of the solvent during film casting process, which causes the polymer molecules to appear in a ‘frozen’ state after deposition. Thus, “as-cast” morphology could be considered as strongly influenced by the polymer chain



conformation in solution, i.e. by solvent polarity and different selectivity towards particular block.

Therefore, when more polar P4VP block, compare to P2VP, is present in block copolymer, THF appears more selective to PS block and less selective to P4VP block.[Par07c] This results in core-shell conformation of PS-*b*-P4VP molecules in THF solution, with P4VP chains forming collapsed core and PS chains extending shell. Such micellar morphology is preserved during fast drying and, indeed, was clearly observed on corresponding films after deposition (Fig. 4.18 a-c).

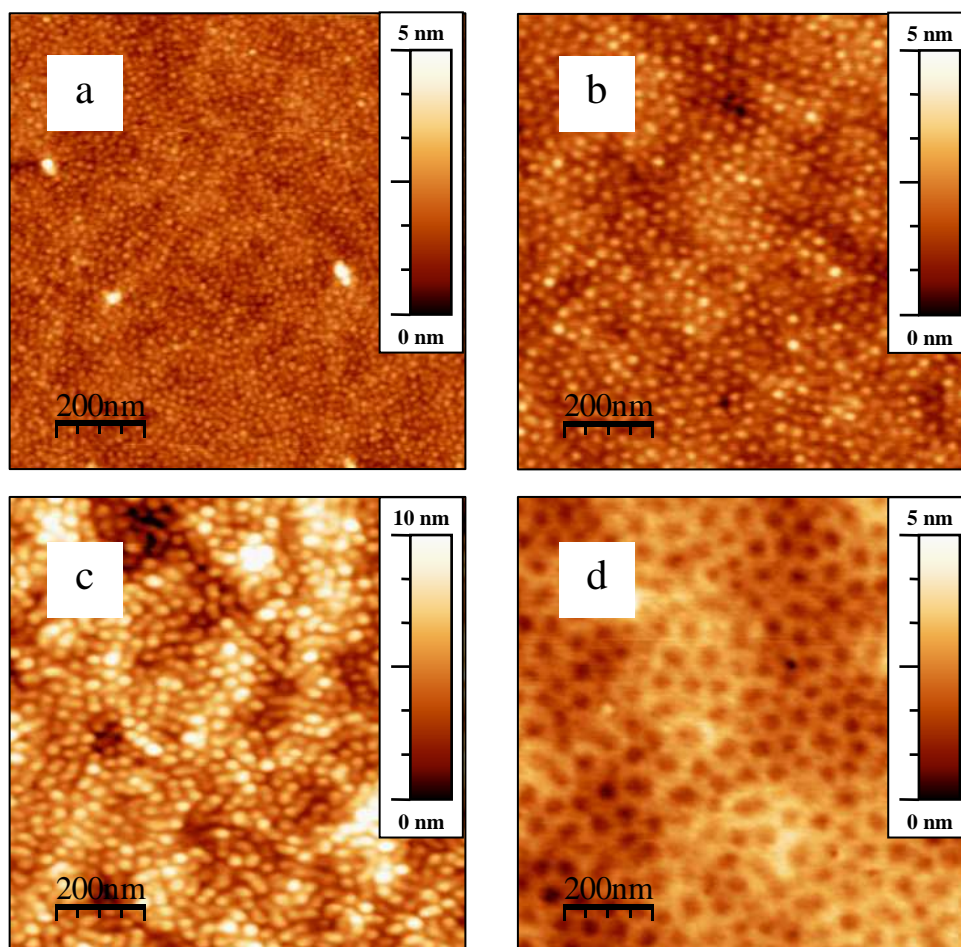


**Figure 4.18** AFM height images of PS<sub>27</sub>-*b*-P4VP<sub>7</sub> (a), PS<sub>57</sub>-*b*-P4VP<sub>18</sub> (b), PS<sub>22</sub>-*b*-P4VP<sub>22</sub> (c) cast from THF and PS<sub>57</sub>-*b*-P4VP<sub>18</sub> cast from CHCl<sub>3</sub> (d). Film thickness ~30 nm (a,c) and ~50 nm (b,d).

As was also revealed from AFM images of THF-cast PS-*b*-P4VP BCP thin films, the size of surface features varied depending on change of molecular weight and PS/P4VP blocks ratio. As it was expected, short-chain PS<sub>27</sub>-*b*-P4VP<sub>7</sub> ( $M_n=34000 \text{ g mol}^{-1}$ ) resulted in smallest micelle size, with mean intermicellar distances of about 18 nm

revealed from analysis of corresponding PSD plot. Consequently, for PS<sub>57</sub>-*b*-P4VP<sub>18</sub> ( $M_n = 76\ 000\ \text{g mol}^{-1}$ ) having longer polymer chains, such distance was found to be significantly larger and was in a range of 31 nm. However, such dependence was not strongly obeyed, whereas when thin film morphology of PS<sub>22</sub>-*b*-P4VP<sub>22</sub> with an intermediate molecular weight ( $M_n = 44\ 000\ \text{g mol}^{-1}$ ) was analyzed. In this case, the structures with size in order of 33 nm were found, which even exceed the structure size of PS<sub>57</sub>-*b*-P4VP<sub>18</sub>. Nevertheless, such results become reasonable from the point of view that at such condition the size of surface features is strongly dependent on the lengths of solely P4VP block that forms micelle cores. Therefore, it is no wonder that PS<sub>22</sub>-*b*-P4VP<sub>22</sub>, which has the largest P4VP block, displayed also the largest feature size compare to the shorter-PVP chain PS<sub>57</sub>-*b*-P4VP<sub>18</sub> for THF-cast thin films.

It was also interesting to observe, that at similar deposition conditions, micelles appear more uniformly packed for asymmetric PS<sub>27</sub>-*b*-P4VP<sub>7</sub> and PS<sub>57</sub>-*b*-P4VP<sub>18</sub> block copolymers than for symmetric PS<sub>22</sub>-*b*-P4VP<sub>22</sub> one. Such difference in micelles spatial arrangement was intuitively attributed to the micelles separation distances that are, in turn, dependent on PS chain lengths which is the lowest in case of PS<sub>22</sub>-*b*-P4VP<sub>22</sub> BCP.

An effect of solvent used for PS-*b*-P4VP dissolution on resulted polymer thin film morphology could be seen from comparison of two AFM images of PS<sub>57</sub>-*b*-P4VP<sub>18</sub> BCP, deposited from THF and CHCl<sub>3</sub> (Fig. 4.18 b and d). When chloroform was used as cast solvent, cylindrical morphology with normal to the substrate domains orientation was observed, while in case of films cast from THF, only dried micelles displaying almost no lateral order were found. The mean interdomain distance between cylinders, determined from AFM images analysis, was in range of 56 nm, which is approximately two times larger compared to the intermicellar distances on THF-cast films.

From experimental results presented above the possible morphologies of thin films of both PS-*b*-P2VP and PS-*b*-P4VP after deposition of them on the substrate were analyzed. Depending composition and molecular weight of BCP and film preparation conditions, different surface morphologies were obtained, which displayed, however either no structure formation, like in case of PS-*b*-P2VP, or structures displaying poor lateral order. However, initial morphology of “as-cast” polymer films can be significantly changed after applied annealing procedure, which is often used and a method to orient and laterally order BCP microdomains. Therefore, additional sample annealing step was necessary to achieve required structure formation in block copolymer films.

### 4.4.3 Evolution of polymer films morphology upon solvent vapour annealing

To bring the BCP system to its equilibrium state, annealing procedure must be applied to the solvent-cast BCP thin films. However, for block copolymers having constituent blocks of different surface energies, like PS-*b*-PVP, in thin film both the substrate and free surface strongly influence on equilibrium morphology. Thus, thermal annealing above  $T_g$  often results in parallel to the substrate domains orientation because of the preferential interaction of one of the blocks (e.g. PVP) with substrate surface. To orient BCP microdomains perpendicularly to the substrate and also improve the lateral order, that is important for practical application, thermal annealing is often replaced by solvent vapour annealing procedure.[Alb10]

Orientation of the microdomains normally to the surface is generally dependent on the solvent evaporation conditions and the solubility of the constituted blocks in annealed solvent.[Kim04] The selectivity of solvent to the correspondent polymer/solvent system can be described by the value of interaction parameter between the solvent and polymer, which, can be calculated from Equation 4.1:

$$\chi_{p/s} = \chi_p + \chi_s = V_m (\delta_s - \delta_p)^2 / RT + 0.34 \quad (\text{Eq. 4.1})$$

where  $V_m$  is the molar volume of polymer and  $\delta_s$  and  $\delta_p$  are the solubility parameters of solvent and of particular block of polymer, respectively.

On the base of Equation 4.1 the interaction parameters for PS, P2VP and P4VP blocks and different solvents ( $\chi_{p/s}$ ) were calculated and summarized in Table 4.3. For calculations, solubility parameters of correspondent block copolymers constituents P2VP, P4VP and PS were taken as 20.4, 22.2 and 18.6 (MPa)<sup>0.5</sup>, respectively.[Lud03,Par07c]

The polymer will be soluble in a particular solvent at particular temperature if the polymer/solvent interaction parameter  $\chi_{p/s}$  is below 0.5.[Par07c] From the  $\chi_{p/s}$  values calculated for different polymer/solvent pairs it could be concluded that increasing of solubility parameter of solvent leads to increase of interaction parameter and, therefore, to decrease of selective solubility of PS, while the highest selectivity towards P2VP and P4VP could be achieved by solvents having moderate values of  $\delta_s$ . The comparison of

$\chi_{p/s}$  obtained for P2VP and P4VP shows that in case of P4VP polymer chain mobility will be more hindered (higher  $\chi_{p/s}$  values) in low and moderate polar solvent (e.g. in toluene, THF or chloroform), while solubility of both P4VP and P2VP in polar solvents, such as ethanol or nitromethane will be impeded.

**Table 4.3 The solubility parameters, vapour pressure and calculated polymer-solvent interaction parameters for pairs of PS, P2VP and P4VP and solvents of different polarity**

Solvent	$V_m^*$ cm <sup>3</sup> /mol	$\delta_s^*$ (MPa) <sup>0.5</sup>	Vap. pressure** mmHg (20°C)	$\chi$ PS-solv	$\chi$ P2VP-solv	$\chi$ P4VP-solv
<b>Toluene</b>	106.3	18.2	28[Par07c]	0.35	0.55	1.04
<b>THF</b>	81.1	18.5	176[Par07c]	0.34	0.46	0.80
<b>Chloroform</b>	80.5	18.7	158	0.34	0.44	0.75
<b>Acetone</b>	73.3	20.1	184	0.41	0.34	0.47
<b>Dichloromethane</b>	63.8	20.3	430	0.42	0.34	0.43
<b>1,4-Dioxane</b>	85.3	20.5	37	0.47	0.34	0.44
<b>Nitromethane</b>	53.7	25.1	27	1.27	0.83	0.53
<b>Ethanol</b>	58.4	26.2	44	1.73	1.15	0.72

\* – Handbook of Solubility Parameters, *CRC Press, 1983*

\*\* – Handbook of Chemistry and Physics, *CRC Press, 1999*

The calculated polymer-solvent interactions were further used in order to find the best conditions of solubility of correspondent polymer in particular solvent as well as in explanation of differences in morphologies of thin films after deposition.

In present work several solvents having different selectivity towards BCP constituent blocks were tested for vapour annealing procedure. In all cases annealing of polymer films was performed at RT by sealing the samples into a glass chamber saturated with solvent vapour for the time periods from 10 minutes up to 6 hours. Alternatively, “slow” annealing procedure was implemented in particular cases in order to achieve better effect of solvent treatment for lateral ordering of BCP microdomains. For this, solvent vapour was allowed to saturate glass chamber with the sample gradually through a needle and, therefore, annealing time was extended up to 96 hours.

During the solvent annealing procedure, the colour of polymer thin film was changed with time, which undoubtedly was caused by increase of thickness due to the swelling. This effect was used in order to perform visual control over the annealing process by estimation of degree of swelling (DS). It was important because the solvent

induced swelling of polymer thin film is usually limited by dewetting phenomena, which usually took place when polymer DS does beyond the value of 3.

#### 4.4.4 Morphology of solvent annealed PS-*b*-P2VP thin films

For symmetric PS<sub>50</sub>-*b*-P2VP<sub>50</sub> thin films the best results were obtained after annealing in atmosphere of 1,4-dioxane which led to the formation of areas with perpendicular to the substrate orientation of lamellae (Fig. 4.19). Such polymer orientation, which is not favourable for PS-*b*-PVP BCP on polar substrates with strong affinity of PVP toward silicon oxide surface, however, become possible after annealing in 1,4-dioxane due to its selectivity toward P2VP block. It is suggested that interaction between P2VP block and SiO<sub>2</sub> surface is diminished and screened due to its solvation by with 1,4-dioxane molecules.

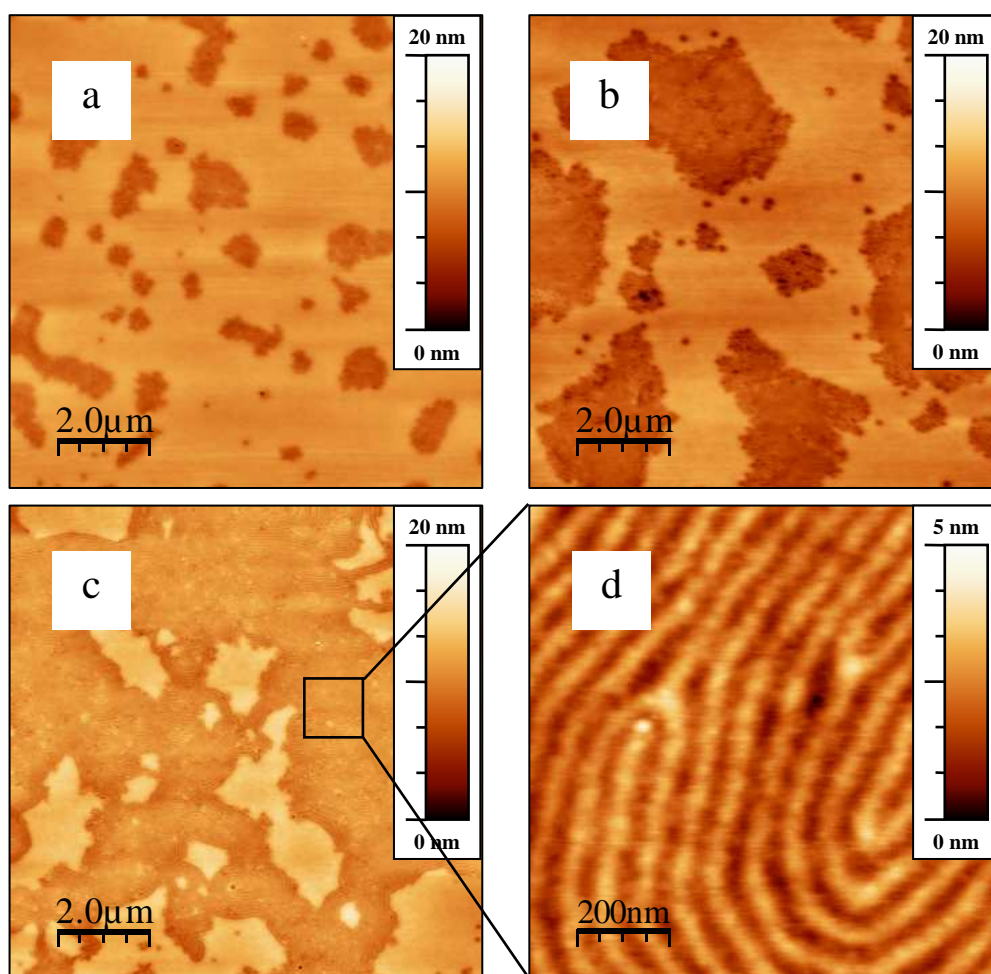


**Figure 4.19** AFM height images of PS<sub>50</sub>-*b*-P2VP<sub>50</sub> thin films annealed in 1,4-dioxane for 30 min (a), 2 hrs (b), 3 hrs (c,d); d – zoomed part of image (c). Film thickness ~50 nm.

As the increase of time of annealing from 0.5 to 3 hours, the surface fraction covered with perpendicularly oriented lamellae were gradually increased from 0.23 to 0.82 (Fig. 4.19 a-c), as it was determined from analysis of AFM topography images.

Lamella period  $D_{0(L)}$  calculated from PSD plot of AFM image (Fig. 4.19 d), was found to be around 75 nm.

It was also observed that further extension of annealing time led to the formation of terraces (Fig. 4.20 a) (islands or holes, depending on film thickness), driven by film thickness quantisation. Cross-sectional profile of such holes revealed height drop of ca. 25 nm that is approximately 1/3 of lamellae period for a given PS-*b*-P2VP BCP (Fig. 4.20 b).

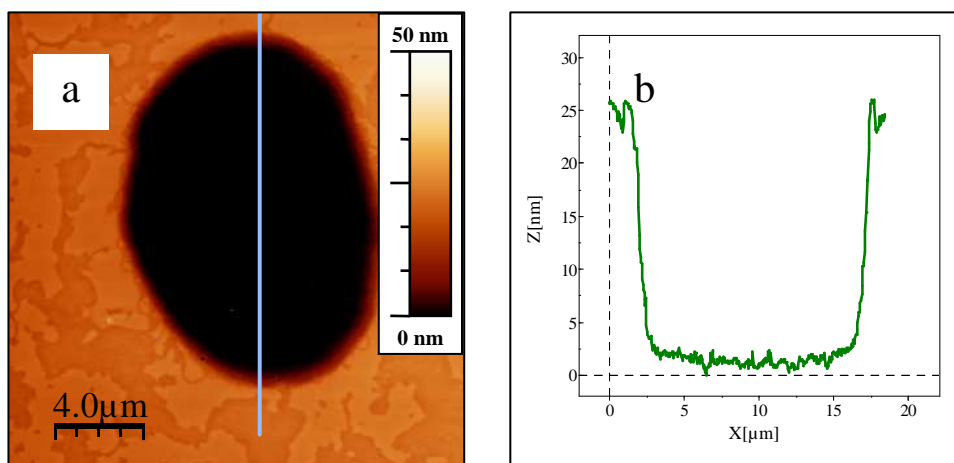


**Figure 4.20** AFM height image of PS<sub>50</sub>-*b*-P2VP<sub>50</sub> thin films annealed in 1,4-dioxane for 4 hrs (a) and cross-section profile (b) taken as it is shown on image a. Initial film thickness ~50 nm.

Annealing of PS<sub>50</sub>-*b*-P2VP<sub>50</sub> in THF vapour was also tested. Similarly to 1,4-dioxane annealing, treatment with THF vapour resulted in film morphology containing mixed perpendicular and parallel lamellae. The drawback of THF annealing for particular BCP was much higher vapour pressure of THF compared to 1,4-dioxane. As a result, in THF atmosphere film swelling was very fast (after 30 minutes dewetting started), thus, making the control over the polymer film behaviour more difficult. In contrast, annealing of PS<sub>50</sub>-*b*-P2VP<sub>50</sub> in chloroform led to worm-like morphologies, similar to THF-cast samples.

Next, the influence of solvent annealing on the morphology of thin films of asymmetric PS<sub>56</sub>-*b*-P2VP<sub>21</sub> was studied. Thus, annealing of PS<sub>56</sub>-*b*-P2VP<sub>21</sub> in 1,4-dioxane vapour resulted in formation of cylindrical morphology with normal to the



substrate domain orientation (Fig. 4.21 a). No difference in morphology was observed for this sample with increasing of time of annealing from 0.5 to 5 hours and rather low degree of lateral ordering of cylindrical P2VP microdomains was achieved, independent on annealing time. An extension of annealing time for more than 5 hours caused the thin films dewetting, similarly to case of PS<sub>50</sub>-*b*-P2VP<sub>50</sub>.

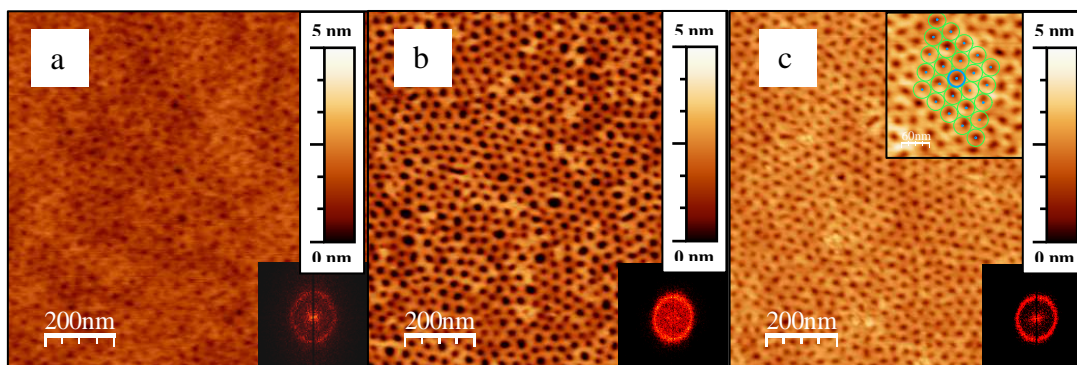


**Figure 4.21** AFM height images of PS<sub>56</sub>-*b*-P2VP<sub>21</sub> thin films annealed in 1,4-dioxane for 3 hrs (a,b) and after “slow” annealing in 1,4-dioxane for 48 hrs (c). Images (b) and (c) were taken after surface reconstruction step. Insets – FFT patterns and magnified image (c) with hexagonal lattice sketch.

To enhance topography contrast, so-called “surface reconstruction” procedure was applied, when after solvent annealing step samples were shortly (for 2-3 minutes) exposed to ethanol vapour and then rapidly dried with nitrogen flow. This method is based on the preferential solvation of the PVP block with ethanol, which causes its selective swelling and further collapse upon drying, resulting in formation of porous morphology (Fig. 4.21 b). The “surface reconstruction” is usually applied in cases when the surface features formed by the thin films right after annealing could not be visualized clearly and helps to specify the film morphology.

With a purpose to improve lateral order, attempts to apply “slow annealing” procedure were performed. Indeed, AFM height images (Fig. 4.21 c) and FFT patterns (inset) of resulted polymer film showed more uniform distribution of interdomain distances (less diffuse FFT spectrum) and partial improvement of hexagonal order on the local scale (upper inset). The interdomain distance was found to be in a range of 30-31 nm (PSD) for both “fast” and “slow” annealed samples. However, such order is still far away from desired perfection due to the presence of multiply dislocation defects. Attempts to achieve the better order by application of other solvents (e.g. CHCl<sub>3</sub>, THF) in annealing procedure were even less successful.

#### 4.4.5 Morphology of solvent annealed PS-*b*-P4VP thin films

In case of asymmetric PS<sub>57</sub>-*b*-P4VP<sub>18</sub> perpendicularly oriented cylinders have been formed upon annealing in 1,4-dioxane vapours independently on annealing time until films remain stable against dewetting. Remarkably, both “as-cast” (Fig. 4.22 a) and 1,4-dioxane annealed samples (Fig. 4.22 b) displayed similar topography features, e.g. closely-packed PVP domains, but with significantly larger domain size and interdomain spacing in case of annealed samples. Such results were attributed to a solvent-induced transition from dried micelles (in THF-cast samples) to vertically oriented cylinders (in annealed samples) with interdomain distance of ca. 45 nm (found from PSD). However, almost no improvement of lateral ordering of cylindrical P4VP domains upon annealing in 1,4-dioxane was achieved, similarly to PS<sub>56</sub>-*b*-P2VP<sub>21</sub> case.

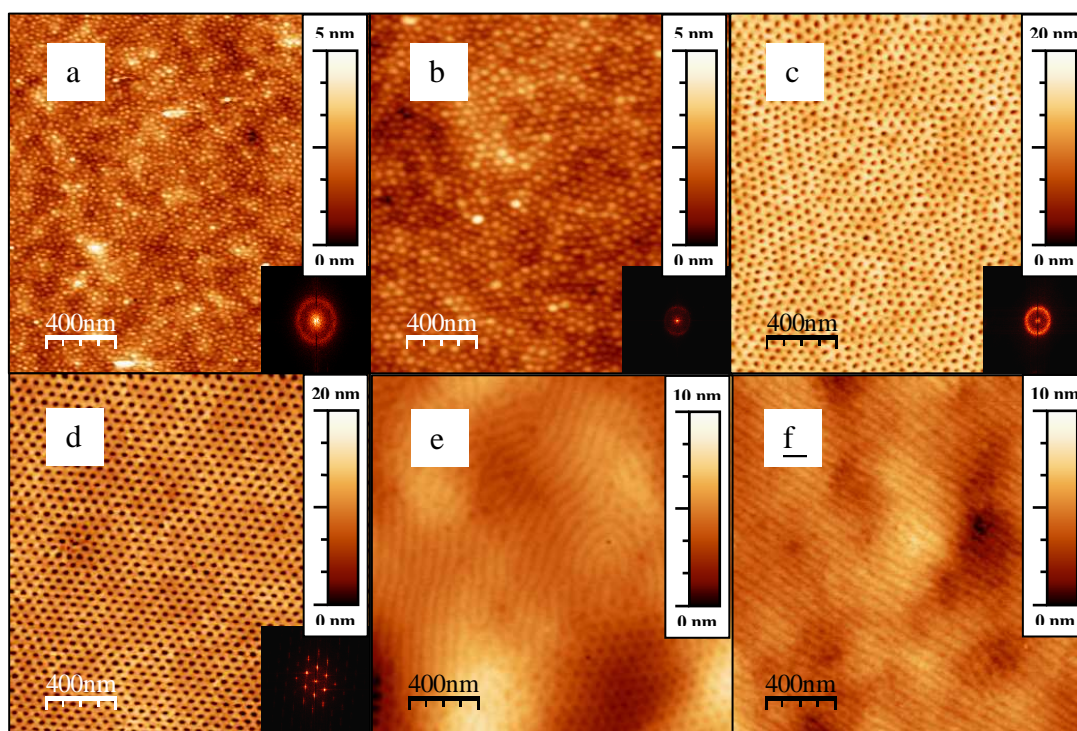


**Figure 4.22** AFM height images of PS<sub>57</sub>-*b*-P4VP<sub>18</sub> ~50 nm thin films: as cast (a); after “slow” annealing in 1,4-dioxane for 48 hours (b,c); after “slow” annealing in CHCl<sub>3</sub> for 24, 48 and 96 hours, (d, e and f, respectively). Images (c) and (d) were taken after surface reconstruction step. Insets – FFT patterns of corresponding images.

Significantly better hexagonal order of P4VP microdomains was obtained when chloroform was used as annealing solvent, instead of 1,4-dioxane. Nearly defect-free hexagonal patterns of P4VP cylinders, oriented normal to the substrate, were obtained under “slow” annealing conditions by quenching of annealing after 24 hours



(Fig. 4.22 d). Further increase of annealing time in chloroform led to in-plane (e.g. parallel to the substrate) re-orientation of P4VP domains (Fig. 4.22 e,f).

From the analysis of AFM images of 1,4-dioxane and chloroform annealed samples with perpendicular P4VP domain orientation almost similar interdomain distances equal to 48 and 47 nm, respectively were found. In both cases, P4VP domain diameter was found to be in order of 13 nm.

The influence of annealing conditions on ordering effect might be explained by different degree of solvent selectivity towards each block. In case of 1,4-dioxane, which interact almost unselectively with both blocks, annealing lead to a simultaneous swelling of both PS and P4VP, while in chloroform, which is selective for PS and non-selective for P4VP, PS swells more intensively in contrast to less swollen PVP. Such conditions could results rather in micelles formation during annealing in chloroform. Upon fast solvent drying, such micelles coalescence in vertical direction forming thus vertically oriented cylinders.

To get more details about the structures present in thin films, samples of neat PS<sub>57</sub>-*b*-P4VP<sub>18</sub> BCP were also investigated with GISAXS. GISAXS experiments provide information about internal structure of thin films and also probe the sample at laterally large areas compared to AFM or TEM, increasing thus the statistic of experimental data.

2D GISAXS patterns obtained at incident angle  $\alpha_i = 0.3^\circ$  for a 50 nm thick PS<sub>57</sub>-*b*-P4VP<sub>18</sub> films and correspondent 1D plots along  $\mathbf{q}_y$  axis at constant  $\mathbf{q}_z$  (i.e. out-of plane scans) for THF-cast and annealed in chloroform are presented in Figure 4.23, a and b, respectively. For comparison, 2D pattern of annealed film was also taken at  $\alpha_i = 0.2^\circ$  (Fig. 4.23 c). Correspondent out-of plane scans are shown on Figure 4.23 (d,e). As can be seen, for THF-cast (not annealed) sample only first order Bragg peak ( $\mathbf{q}_y^*$ ) is clearly visible. The position of peak maxima (Fig. 4.23 d) was found at  $\mathbf{q}_y = 0.192 \pm 0.023 \text{ nm}^{-1}$ , which correspond to interdomain distance  $D_0 = 32.7 \pm 4.2 \text{ nm}$ . This value is in a good agreement with values obtained from analysis of AFM PSD plots of THF-cast samples (32-34 nm). However, no higher order peaks were observed for THF cast films, indicating no or very poor lateral ordering.

Both 2D patterns of chloroform annealed PS<sub>57</sub>-*b*-P4VP<sub>18</sub>, taken at two different incident angles ( $\alpha_i = 0.20^\circ$  and  $0.30^\circ$ , Fig. 4.23, b and c, respectively), represent laterally ordered structures, which is evident from the appearance of higher order peaks along  $\mathbf{q}_y$  axis. Such scattering pattern confirms the alignment of the structures

perpendicularly to the substrate. For annealed samples the position of first order peak was found to be shifted to a lower  $q_y^*$  values ( $q_y^* = 0.132 \pm 0.018 \text{ nm}^{-1}$ ) compared to as-cast sample, that indicates an increase of domain spacing up to  $47.6 \pm 6.5 \text{ nm}$ . The positions of 2<sup>nd</sup>, 3<sup>rd</sup> and 4<sup>th</sup> order peaks, those occur at  $q_y$  values of 0.227, 0.252 and  $0.350 \text{ nm}^{-1}$ , were rated to the position of first order peak as  $\sqrt{3}$ ,  $\sqrt{4}$  and  $\sqrt{7}$ , respectively. Such peaks ratio is characteristic for hexagonally organized structures, composed of cylindrical BCP microdomains and correlate with AFM results shown in Figure 4.22. At incident angle  $\alpha_i = 0.20^\circ$  the intensities of observed peaks appear higher than in case of  $\alpha_i = 0.30^\circ$ , since at such conditions  $\alpha_i$  is set below the critical angle of silicon ( $\alpha_c(\text{Si}) = 0.22^\circ$  [Par07c]), and incident beam was totally reflected from the substrate, resulting in enhancement of scattering intensity. Nevertheless, peak positions at both incident angles for the same sample remain unchanged.

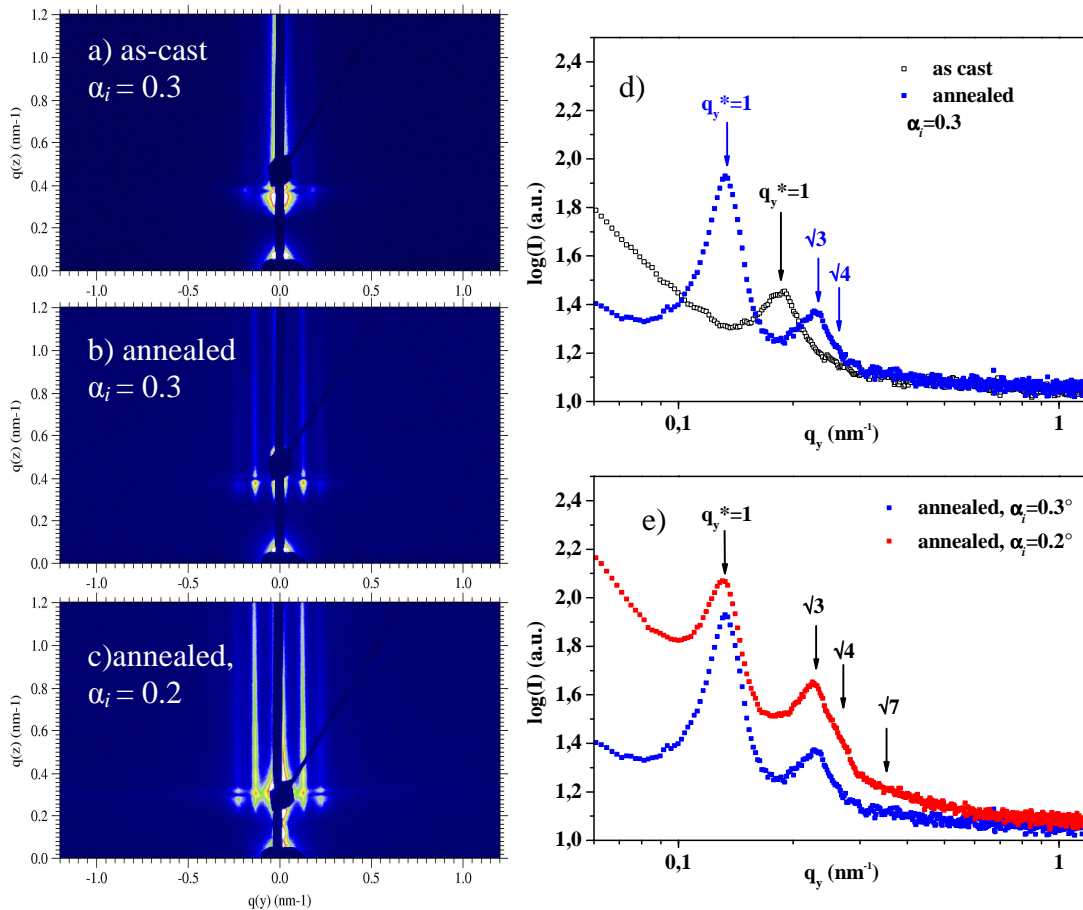


**Figure 4.23** 2D GISAXS patterns of as-cast (a) and CHCl<sub>3</sub> annealed (b,c) PS<sub>57</sub>-*b*-P4VP<sub>18</sub> thin films obtained at incident angle  $\alpha_i = 0.3^\circ$  (a,b) and  $0.2^\circ$  (c) and corresponding scattering profiles along  $q_y$  axis (out of plane cuts) taken at  $q_z = 0.39 \pm 0.02 \text{ nm}^{-1}$  and  $0.31 \pm 0.02 \text{ nm}^{-1}$  for  $\alpha_i = 0.3^\circ$  and  $0.2^\circ$ , respectively. For each pattern 10 min acquisition time was used.

As a next PS-*b*-P4VP BCP, asymmetric but of smaller molecular weight PS<sub>27</sub>-*b*-P4VP<sub>7</sub> was subjected to annealing procedure in order to obtain ordered cylindrical morphology. It was found that, similarly to PS<sub>57</sub>-*b*-P4VP<sub>18</sub>, the best-ordered structures for PS<sub>27</sub>-*b*-P4VP<sub>7</sub> BCP were obtained after “slow” annealing in CHCl<sub>3</sub> vapours. It should be mentioned that our attempts to perform “fast” annealing of such low molecular weight BCP in CHCl<sub>3</sub> were not successful due to high vapour pressure of solvent and, therefore, fast polymer film dewetting. In order to obtain perpendicularly oriented cylinders (Fig. 4.24 a), annealing was quenched after 6 hours. Further extension of annealing time led to successive reorientation of cylinders parallel to the substrate. As a result, after 24 hours of annealing, almost complete in-plane orientation of microdomains was achieved. Notably, annealing time required for achievement of particular domain orientation for PS<sub>27</sub>-*b*-P4VP<sub>7</sub> was significantly reduced compare to PS<sub>57</sub>-*b*-P4VP<sub>18</sub> BCP, which is reasonable, taking into account lower molecular weight of PS<sub>27</sub>-*b*-P4VP<sub>7</sub> BCP.

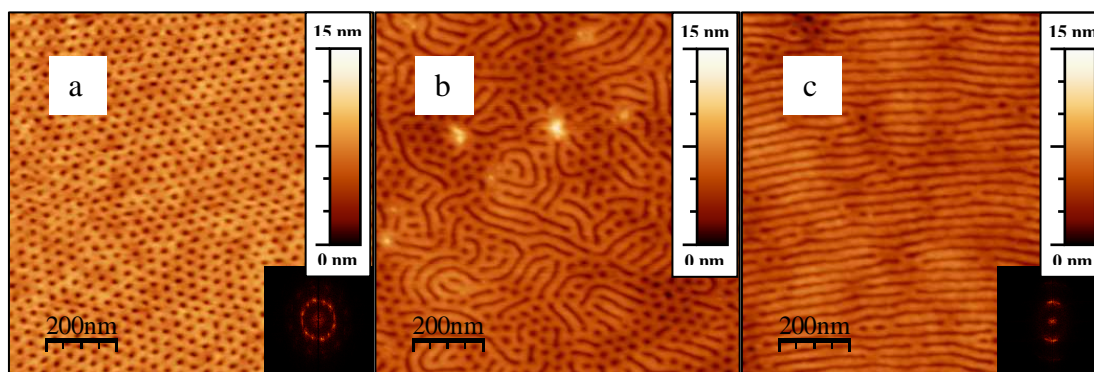


**Figure 4.24** AFM height images of PS<sub>27</sub>-*b*-P4VP<sub>7</sub> ~30 nm thin films after “slow” annealing in CHCl<sub>3</sub> for 6 (a), 12 (b) and 24 (c) hours. Images were taken after surface reconstruction step. Insets show FFT patterns of corresponding images.

Interdomain distance for annealed PS<sub>27</sub>-*b*-P4VP<sub>7</sub> samples was also calculated from the analysis of AFM images and was found in order of 30 nm. This value was higher compare to intermicellar space of as-cast film (18 nm). P4VP domain diameter for PS<sub>27</sub>-*b*-P4VP<sub>7</sub> after annealing was found to be equal to 8 nm.

Examination of symmetric PS<sub>22</sub>-*b*-P4VP<sub>22</sub> BCP morphology after annealing revealed that preformed in THF micellar structure after vapour annealing in 1,4-dioxane led to perpendicularly oriented lamellae, similar to symmetric PS<sub>50</sub>-*b*-P2VP<sub>50</sub>, as can be seen in Figure 4.25. With an increase of annealing time, the fraction of P4VP micelles, which were formed after film casting, gradually decreased finally resulting in perpendicular lamella morphology.

From comparison of THF “as-cast” and 1,4-dioxane annealed samples of neat PS<sub>50</sub>-*b*-P2VP<sub>50</sub> and PS<sub>22</sub>-*b*-P4VP<sub>22</sub> BCPs different mechanism of lamellae formation could be suggested. In case of PS<sub>50</sub>-*b*-P2VP<sub>50</sub> perpendicular lamella are, most probably, formed via reorientation mechanism, caused by decrease of interaction of P2VP with polar substrate due to the screening effect upon solvent uptake. At the initial stage of annealing, microdomains are predominantly oriented parallel to the substrate, with P2VP part lying at the bottom of the film. With time, due to the increased amount of selective to P2VP solvent inside the film, its domains tend to orient normally to the substrate.

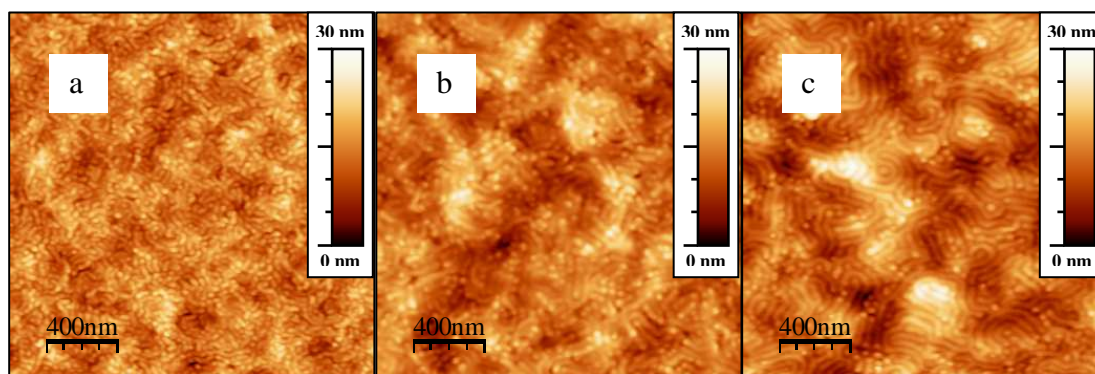


**Figure 4.25** AFM height images of PS<sub>22</sub>-*b*-P4VP<sub>22</sub> ~30 nm thin films after “slow” annealed in 1,4-dioxane for 12 (a), 24 (b) and 36 (c) hours.

In contrast, in PS<sub>22</sub>-*b*-P4VP<sub>22</sub> case, because the selectivity of 1,4-dioxane was almost similar for both PS and P4VP blocks, as-cast formed micelles progressively swelled and interconnected in lateral direction, forming in such a way perpendicularly oriented lamella microdomains. These observations are in agreement with results published in literature on dependency of structure evolution mechanism for BCP thin films having different initial morphology.[LiX07]

Morphology of PS-*b*-P4VP BCPs after annealing in THF vapour remained unchanged with respect to as-cast samples, that is, quasi-hexagonally packed dried micelles. It is also important to mention, that variations in initial morphology of thin films, cast from different solvents, as well as type of substrate used (i.e. Si/SiO<sub>2</sub> or glass) did not affect on resulting structure observed after solvent annealing, which is in agreement with observations reported elsewhere.[Boh10]

Considering experimental results, obtained from investigation of morphologies of as-cast and solvent annealed PS-*b*-PVP block copolymers of various compositions, it can be stated following:

– THF-cast thin films of neat BCP display either disordered or micellar morphology, depending of position of nitrogen in pyridine ring (i.e. PS-*b*-P2VP and PS-*b*-P4VP, respectively). For all types of BCPs used, rather poor degree of lateral order was achieved due to fast evaporation rate of solvent during sample preparation step;

– desired morphology (e.g. perpendicular or parallel orientation of BCP microdomains) and significant improvement of lateral order could be achieved with an application of solvent vapour annealing step, however, in case of PS-*b*-P2VP BCPs complete perpendicular microdomain orientation is hardly achievable due to film dewetting;

– for cylinder-forming BCP, switching of domain orientation could be realized by means of different annealing conditions, such as nature of solvent, annealing time.

Table 4.4 summarize thin film surface morphologies that were observed for PS-*b*-PVP BCPs of various composition and different preparation condition.

**Table 4.4 Summary of morphologies observed for as-cast and solvent annealed thin films of PS-*b*-PVP BCPs of various composition**

<b>BCP Solvent</b>	<b>as-cast</b>	<b>CHCl<sub>3</sub></b>	<b>1,4-Dioxane</b>	<b>THF</b>
<b>PS<sub>50</sub>-<i>b</i>-P2VP<sub>50</sub></b>	worm-like	worm-like	<b>L<sub>⊥</sub>+L<sub>//</sub>*</b>	<b>L<sub>⊥</sub>+L<sub>//</sub></b>
<b>PS<sub>56</sub>-<i>b</i>-P2VP<sub>21</sub></b>	featureless	dewetting	<b>C<sub>⊥</sub></b>	dewetting
<b>PS<sub>57</sub>-<i>b</i>-P4VP<sub>18</sub></b>	dried micelles or C <sub>⊥</sub> **	C <sub>⊥</sub> or C <sub>//</sub> ***	<b>C<sub>⊥</sub></b>	dried micelles
<b>PS<sub>22</sub>-<i>b</i>-P4VP<sub>22</sub></b>	dried micelles	not tested	<b>L<sub>⊥</sub></b>	dried micelles
<b>PS<sub>27</sub>-<i>b</i>-P4VP<sub>7</sub></b>	dried micelles	C <sub>⊥</sub> or C <sub>//</sub> ***	<b>C<sub>⊥</sub></b>	dried micelles

\*-**⊥** and **//** indices denote perpendicular and parallel to the substrate domain orientation, respectively;

\*\* – THF cast / CHCl<sub>3</sub>-cast;

\*\*\* – depending on annealing time either perpendicular or parallel orientation.



## 4.5 Preparation and investigation of MNP/BCP composites

### 4.5.1 MNP/PS-*b*-P2VP composites: an effect of MNP stabilizing shell density

After the annealing conditions for perpendicular BCP domain orientation and ordering on the substrate were optimized, we attempt to incorporate the MNP selectively into the PVP domains of various PS-*b*-PVP BCPs. For preparation of MNP/BCP composites MNPs and BCP were separately dissolved in THF (or CHCl<sub>3</sub>) and then mixed together to give a number of MNPs concentrations from 0 to 10.0 wt% with respect to BCP weight. Then solutions, which contain MNP/BCP mixture were stirred mechanically for 24 hours, passed through 0.2 μm pore-sized membrane filter and thin films were deposited by spin- or dip coating. By variation of BCP concentration and/or rotation (withdrawing) speed, film thicknesses were established 30 or 50 nm depending on particular sample. AFM scratch tests were performed in order to confirm the accuracy of chosen conditions for resulted film thicknesses.

MNP1/PS<sub>50</sub>-*b*-P2VP<sub>50</sub> composites were examined first. AFM images of as-cast samples showed random distribution of MNP1 within PS<sub>50</sub>-*b*-P2VP<sub>50</sub> film (Fig. 4.26 a,b). Samples were first annealed in 1,4-dioxane atmosphere. From AFM images of annealed sample (Fig. 4.26 c,d) it is obvious the presence of perpendicularly oriented lamellar structure, similar to neat PS<sub>50</sub>-*b*-P2VP<sub>50</sub>. However, after solvent annealing MNP1 underwent phase segregation atop of BCP film surface, showing no evidence of affinity toward any of BCP phases (Fig. 4.26 c,d). Such tendency of MNP1 to phase segregate atop of the film was also observed for all MNP1/PS<sub>50</sub>-*b*-P2VP<sub>50</sub> composition studied, independently on MNP1 content. Moreover, MNP1 macrophase segregate similarly also upon samples exposure to other solvents (e.g. THF or CHCl<sub>3</sub>).



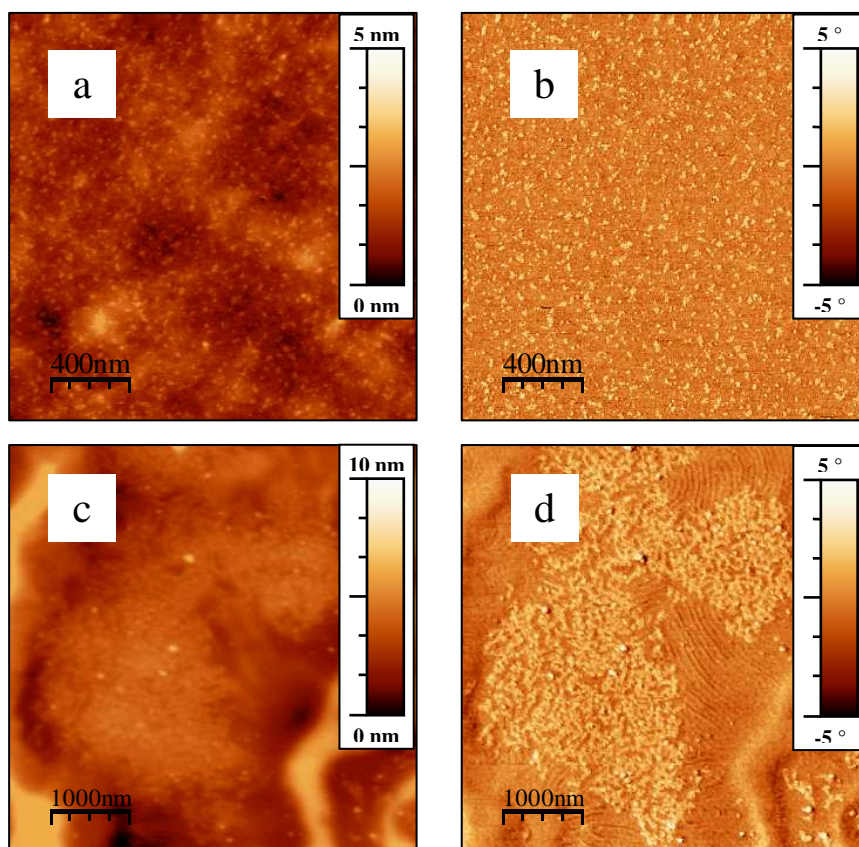


**Figure 4.26** AFM height (a,c) and phase (b,d) images of MNP1/PS<sub>50</sub>-*b*-P2VP<sub>50</sub> composite thin films before (a,b) and after solvent vapour annealing in 1,4-dioxane for 3 hours (c,d). MNP1 content – 5.0 wt%. Film thickness ~50 nm.

In contrast, selective MNPs segregation within one of the BCP domains was achieved when MNP3 were used instead of MNP1. As it was assumed and later confirmed by other experiments, MNP3 were selectively segregated into P2VP domains due to their mutual affinity.

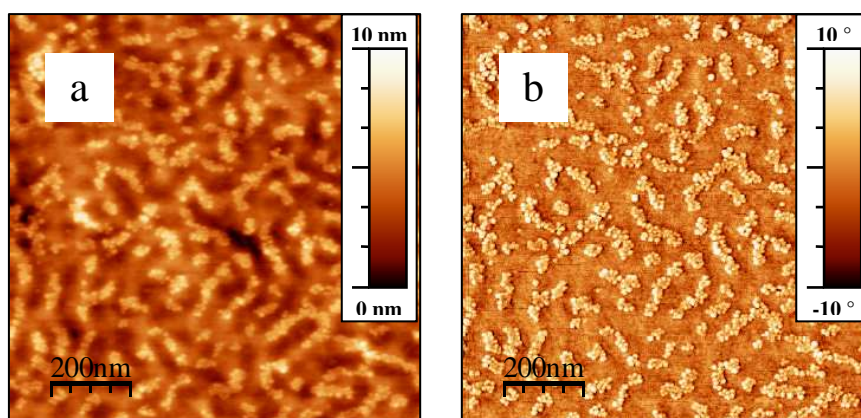


**Figure 4.27** AFM height (a) and phase (b) images of THF-cast MNP3/PS<sub>50</sub>-*b*-P2VP<sub>50</sub> composite thin film containing 10.0 wt% of MNP3. Film thickness ~50 nm.



It was found from AFM images that THF-cast MNP3/PS<sub>50</sub>-*b*-P2VP<sub>50</sub> composite thin films displayed already pre-formed discontinuous lamella-like structures with normal to the substrate domain orientation. Moreover, MNP3 were found selectively located at such disordered short-length lamellae (Fig. 4.27). Such enhanced structuring effect compare to the as-cast neat polymer is attributed to the presence of MNP3 in BCP matrix and, most probably, was conditioned by diminution of surface tension of P2VP phase due to presence of nanoparticles in the system. Such effect was already reported for other PS-*b*-PVP systems, containing, for example CdSe QDs.[Lin05]

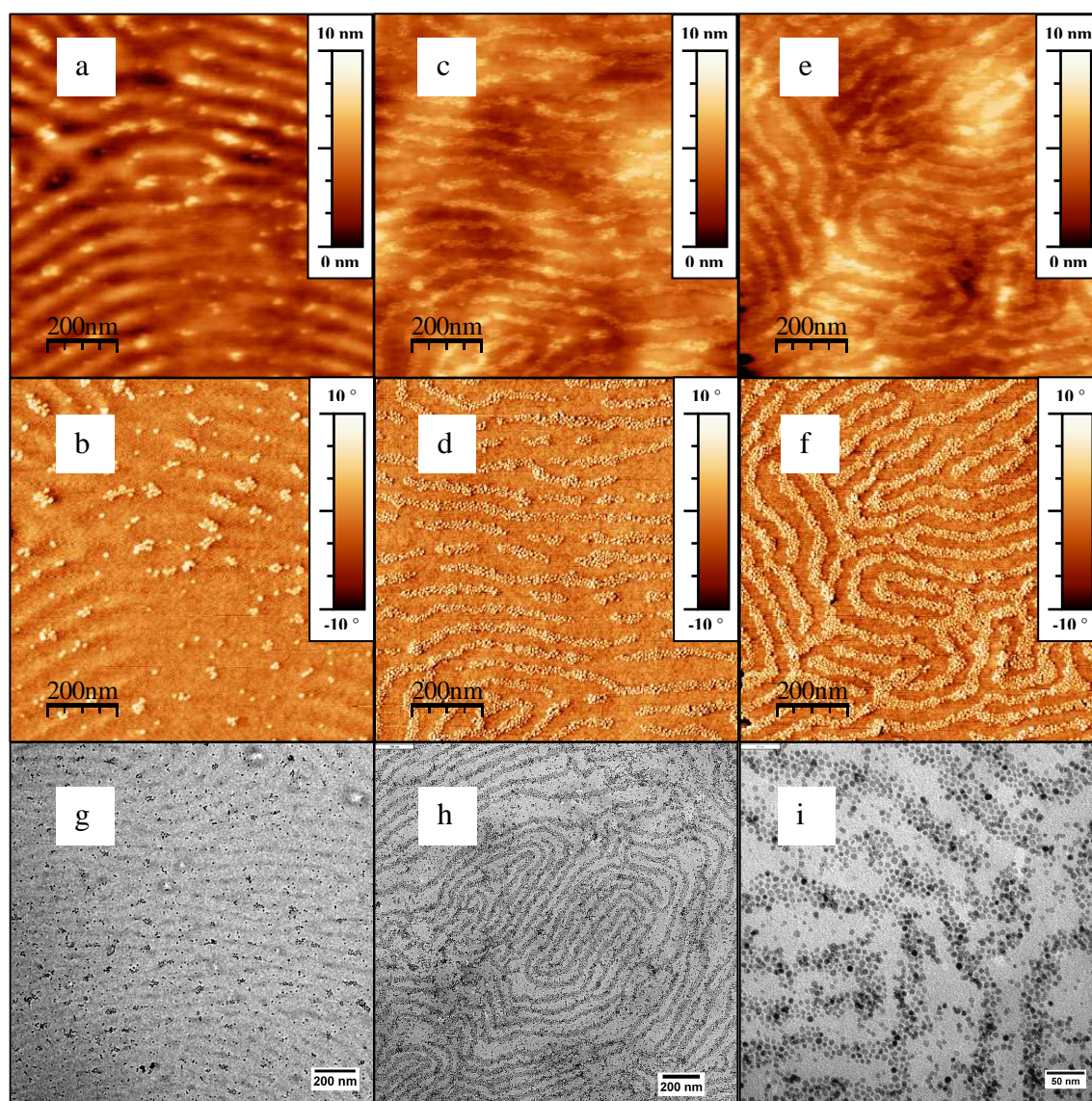


**Figure 4.28** AFM height (a,c,e), phase (b,d,f) and TEM (g,h,i) images of MNP3/PS<sub>50</sub>-*b*-P2VP<sub>50</sub> composites thin films containing 2.0 (a,b,g), 5.0 (c,d) and 10.0 wt% (e,f,h,i) of MNP3 after solvent vapour annealing in 1,4-dioxane. Film thickness ~50 nm.

It should be mentioned that for particular system (i.e. MNP/PS-*b*-P2VP composites) such effect was observed only if nanoparticles possessed affinity towards one of the block, like in case of MNP3/PS<sub>50</sub>-*b*-P2VP<sub>50</sub> composites. It seems that such MNP3/polymer interaction was sufficient to ensure their cooperative assembly already during sample preparation step. Annealing of MNP3/PS<sub>50</sub>-*b*-P2VP<sub>50</sub> samples in 1,4-dioxane vapour led to perpendicularly oriented continuous lamellae morphology formation, similar to neat BCP. Moreover, MNP3 were found selectively arranged within single (as was supposed – P2VP) phase (Fig. 4.28, a-f). Perpendicularly oriented microdomains were found for all MNP/BCP compositions studied independently on MNP3-to-BCP ratio. No evidence of nanoparticles macrophase segregation neither before nor after annealing procedure was observed, unlike MNP1/PS<sub>50</sub>-*b*-P2VP<sub>50</sub> case.

It is also important to mention, that with an increase of MNP3 content in MNP3/PS<sub>50</sub>-*b*-P2VP<sub>50</sub> samples, substantial reducing of annealing time required to obtain larger areas of perpendicularly oriented lamellae was observed (i.e. for 5.0 x 5.0 μm AFM scans – 60 min for 10 wt% of MNP3 loading instead of 3 hours for neat PS<sub>50</sub>-*b*-P2VP<sub>50</sub>). Thus,

the presence of MNP3 nanoparticles gives an important profit in microdomains formation and orientation processes. The high degree of selectivity of nanoparticles location in one of the PS-*b*-P2VP domains was also confirmed by TEM imaging of thin films after their etching from the substrate (Fig. 4.28, g-i).

The next sample of MNPs used for preparation of composites with PS<sub>50</sub>-*b*-P2VP<sub>50</sub> BCP was MNP4 with stabilizing shell formed by

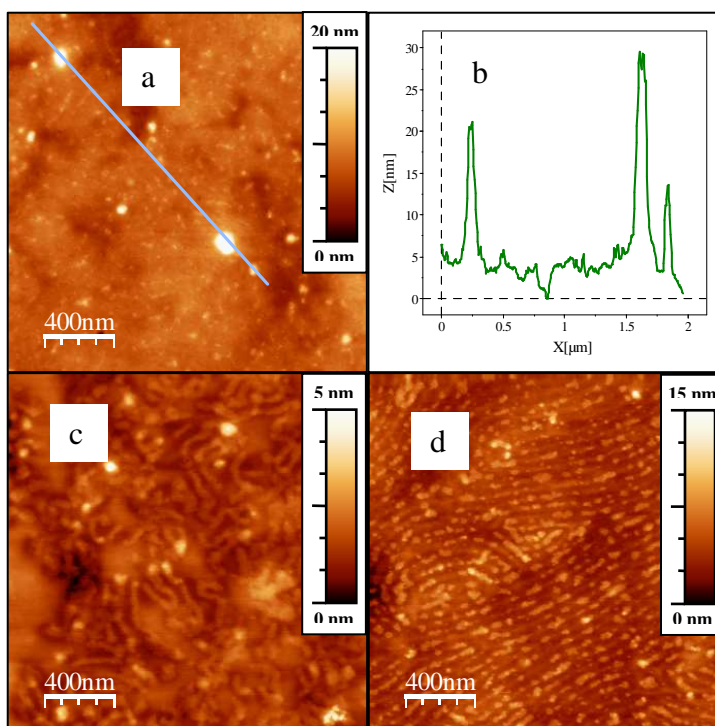


**Figure 4.29** AFM height images of THF-cast (a) and 1,4-dioxane annealed (c) MNP4/PS<sub>50</sub>-*b*-P2VP<sub>50</sub> composite thin films; (b) – cross-sectional profile as shown on image (a); (d) – AFM height image of 1,4-dioxane annealed MNP5/PS<sub>50</sub>-*b*-P2VP<sub>50</sub> thin film. MNP content – 5.0 wt%. Film thickness ~50 nm.

short-chain 1,2-decanediol. In contrast to MNP3, they were found to form aggregates already after thin film deposition (Fig. 4.29, a,b). In our opinion such tendency to aggregation could be reasoned by not sufficient steric stabilization of nanoparticles surface by short 1,2-decanediol molecules. Upon annealing, some selective segregation of MNP4 in P2VP domains was nevertheless observed, but obtained structures were found much less regular and uniform compare to MNP3/PS<sub>50</sub>-*b*-P2VP<sub>50</sub> composites.

Similarly to Fe<sub>3</sub>O<sub>4</sub> MNP3, CoFe<sub>2</sub>O<sub>4</sub> MNP5 were also found promising for particular application and their selective segregation in one of the PS<sub>50</sub>-*b*-P2VP<sub>50</sub> domains was observed, when sample preparation procedure and annealing conditions were replicated from MNP3/PS<sub>50</sub>-*b*-P2VP<sub>50</sub> to MNP5/PS<sub>50</sub>-*b*-P2VP<sub>50</sub> system (Fig. 4.29 d). However, enhanced tendency of MNP5 to agglomeration required further optimisation of particles preparation condition in order to ensure their dispersion stability for sufficient period of time.

From all given results become evident that among others MNP3 revealed themselves as the most attractive for in fabrication of polymer composites selectively filled with magnetic nanoparticles. Therefore all other experiments were performed based on MNP3/BCP composites.

#### **4.5.2 MNP/PS-*b*-P2VP composites: an influence of BCP composition**

From experimental results presented above it was not possible, however, to distinguish which block exactly, either PS or P2VP, was that selective for MNP3 incorporation. It was suggested, that mutual affinity between MNP3 nanoparticles and P2VP chains was the driving force underlying PVP selective nanoparticles segregation.

One possibility to prove or refuse such assumption was to use for composite preparation asymmetric PS-*b*-P2VP BCP, composed of minor P2VP block, which could form cylindrical morphology. In this case, presence or absence of nanoparticles within cylinders would argue their affinity toward P2VP phase, while their distribution within a matrix will indicate an opposite, namely, selectivity towards PS phase. For this purpose, composites of MNP3 and PS<sub>56</sub>-*b*-P2VP<sub>21</sub> BCP with were prepared and studied.

AFM investigations of MNP3/PS<sub>56</sub>-*b*-P2VP<sub>21</sub> cast form THF or CHCl<sub>3</sub> thin films gave an evidence of MNP3 selectivity toward P2VP phase, as it was expected (Fig. 4.30). Indeed, MNP3 were found located within cylinders, formed by P2VP block



with high degree of selectivity. From AFM phase image of  $\text{CHCl}_3$ -cast sample (Fig. 4.30 d) it becomes obvious that most of P2VP domains possessed either single particle or small particle clusters atop of them.

Similar to MNP3/PS<sub>50</sub>-*b*-P2VP<sub>50</sub> system, in case of MNP3/PS<sub>56</sub>-*b*-P2VP<sub>21</sub> composites the presence of MNP3 also affect the morphology of as-cast samples, changing it from smooth feature-less for THF-cast observed for neat PS<sub>56</sub>-*b*-P2VP<sub>21</sub> BCP to a dimple-type for MNP3/PS<sub>56</sub>-*b*-P2VP<sub>21</sub> (Fig. 4.17 b and Fig. 4.30 a, respectively).

Nevertheless, diminution of P2VP fraction in PS-*b*-P2VP composition was found to have a detrimental influence on the nanoparticles phase behaviour during solvent annealing if compared with MNP3/PS<sub>50</sub>-*b*-P2VP<sub>50</sub> system. In fact, even after short exposure (e.g. 5-10 min) of

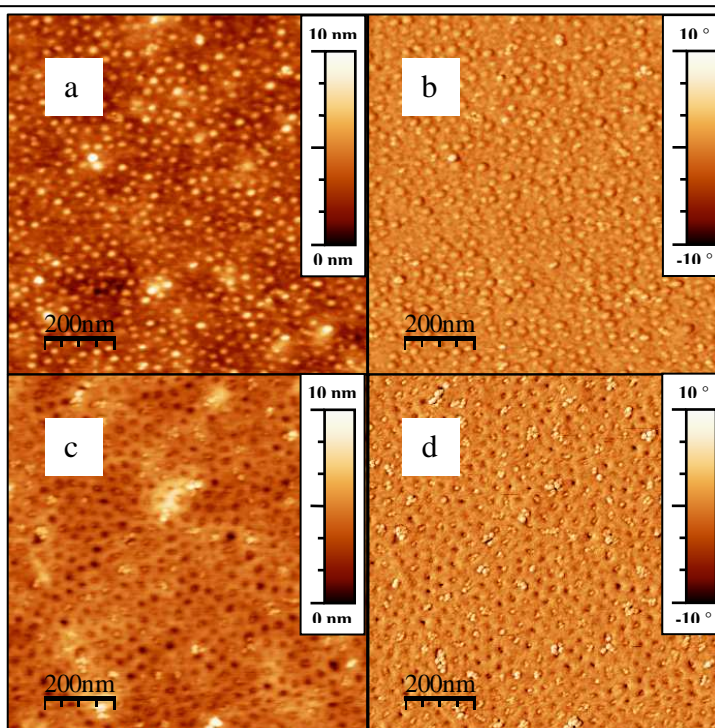


**Figure 4.30** AFM height (a,c) and phase (b,d) images of THF (a,b) and  $\text{CHCl}_3$  cast MNP3/PS<sub>56</sub>-*b*-P2VP<sub>21</sub> composite thin films containing 5.0 wt% of MNP3. Film thickness  $\sim 30$  nm.

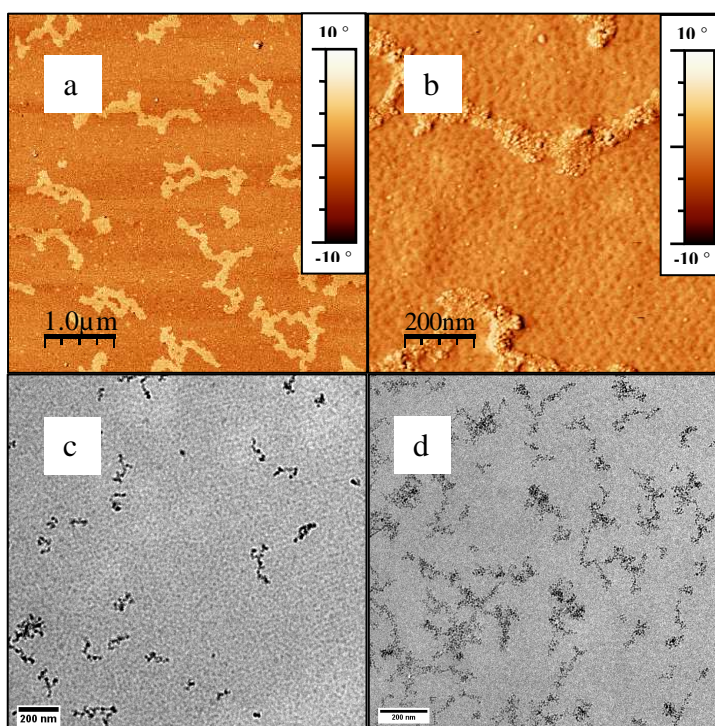


**Figure 4.31** AFM phase images of MNP3/PS<sub>56</sub>-*b*-P2VP<sub>21</sub> composite thin films containing 5.0 wt% of MNP3 after solvent vapour annealing in 1,4-dioxane (a) and  $\text{CHCl}_3$  (b) for 10 min; (c,d) – TEM images of dioxane annealed MNP3/PS<sub>56</sub>-*b*-P2VP<sub>21</sub> composite thin films containing 2.0 (c) and 5.0 wt% (d) of MNP3. Film thickness  $\sim 30$  nm.

MNP3/PS<sub>56</sub>-*b*-P2VP<sub>21</sub> thin film to a solvent vapour, segregation of nanoparticles atop of BCP film surface occurred as a major pathway even at low MNP3 concentration and independently on nature of solvents used (Fig. 4.31). Even so, after short-time vapour annealing, some of the NPs still remained trapped within P2VP cylinders (Fig. 4.31 b), further increase of annealing time led to complete MNP3 phase segregation, as it can be seen from corresponding TEM images of films after their etching from the substrate (Fig. 4.31 c,d).

Ineffective experimental results on preparation of laterally ordered MNP/PS-*b*-P2VP structures with cylinder-type morphology motivated us to shift our attention to another MNP/BCP system, namely to MNP3/PS-*b*-P4VP.

#### 4.5.3 MNP3/PS-*b*-PVP composites with P4VP block: an effect of nitrogen position

It was assumed, that among of the reasons, which caused the solvent-induced nanoparticles macrophase separation in MNP3/PS<sub>56</sub>-*b*-P2VP<sub>21</sub> system, too weak

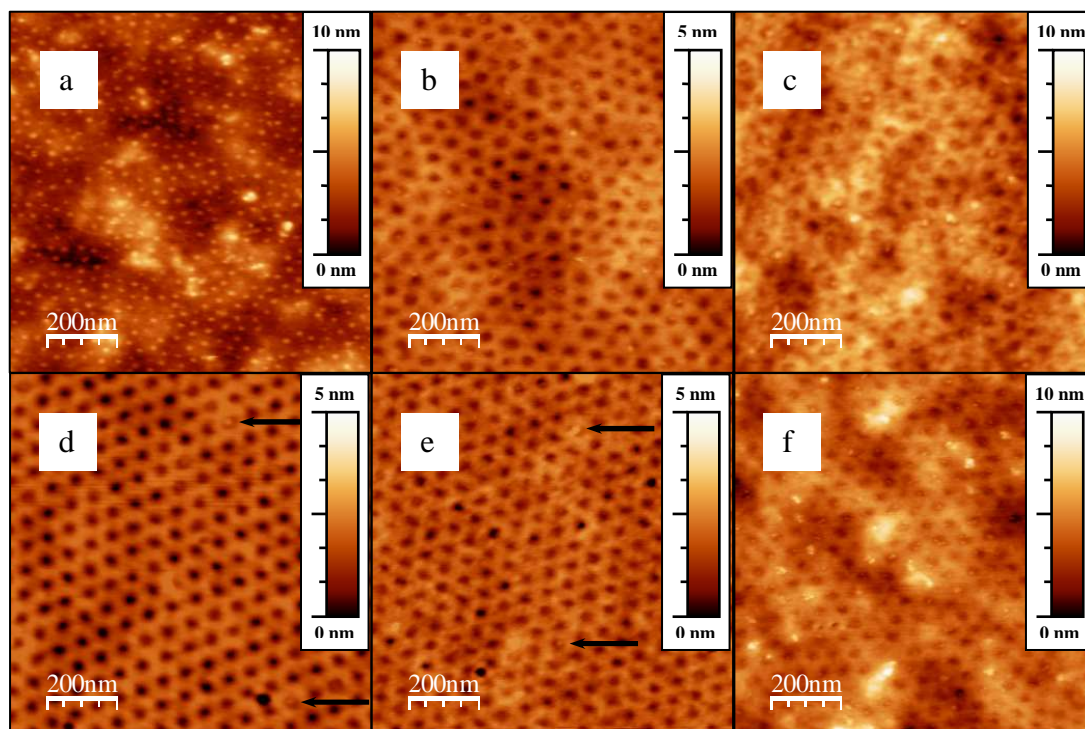


**Figure 4.32** AFM height images of MNP3/PS<sub>57</sub>-*b*-P4VP<sub>18</sub> composite thin films: as-cast from THF (a) and CHCl<sub>3</sub> (b,c) and after ‘slow’ annealing in CHCl<sub>3</sub> for 24 hours (d,e,f) with MNP3 content of 2.0 (a,d), 5.0 (b,e) and 10.0 wt% (c,f). Film thickness ~50 nm.

interaction between MNP and P2VP might be of crucial importance.



Such explanation is reasonable taking into account the steric hindrance of 2VP moieties having the nitrogen atoms in ortho-position. Thus, to overcome such problem, BCPs which contain P4VP blocks in the structure were used next instead of P2VP-containing ones.

Thin film morphology of as-cast MNP3/PS<sub>57-b</sub>-P4VP<sub>18</sub> film was found similar to that of neat PS<sub>57-b</sub>-P4VP<sub>18</sub> BCP, namely, dried micelles were observed for THF-cast samples (Fig. 4.32 a) and laterally disordered perpendicularly oriented P4VP cylinders were formed when CHCl<sub>3</sub> was used as casting solvent (Fig. 4.32 b,c). Moreover, in MNP3/PS<sub>57-b</sub>-P4VP<sub>18</sub> composites P4VP-selective MNP3 segregation was observed, similarly as it was observed for CHCl<sub>3</sub>-cast MNP3/PS<sub>56-b</sub>-P2VP<sub>21</sub> samples.

When MNP3/PS<sub>57-b</sub>-P4VP<sub>18</sub> samples were annealed in CHCl<sub>3</sub> atmosphere, P4VP cylinders became arranged into ordered hexagonal lattice, independently on MNP3 content (Fig. 4.32 d-f). At low MNP3 concentration (up to 5.0 wt%), the nanoparticles in P4VP cylinders (depicted with black arrows) was hardly observed by AFM (Fig. 4.32 d,e). However, at 10 wt% of MNP3 in BCP matrix almost all P4VP cylinders were found be filled with the nanoparticles (Fig.4.32 f) and, at the same time, the long-range order of the cylinders was still preserved. Most importantly, particles macrophase separation was not observed upon solvent annealing, in contrast to MNP3/PS<sub>56-b</sub>-P2VP<sub>21</sub> composites.

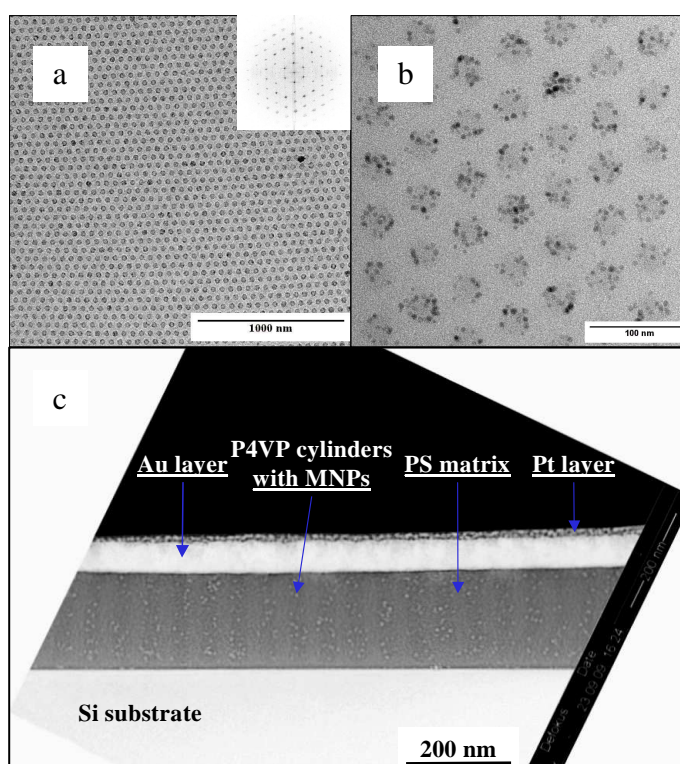


**Figure 4.33** Plan view TEM images of unstained MNP3/PS<sub>57-b</sub>-P4VP<sub>18</sub> composite ~50 nm thin films containing 2.0 wt% of MNP3 (a,b); (c) – cross-sectional TEM image of unstained FIB lamella of MNP3/PS<sub>57-b</sub>-P4VP<sub>18</sub> ~160 nm thick film containing 5.0 wt% of MNP3 after solvent vapour annealing in CHCl<sub>3</sub>. The image (c) is presented as negative for better contrast: MNP3 are visualized as bright dots, P4VP cylinders – darker grey areas and PS matrix – brighter grey areas. Inset on image (a) – corresponding FFT pattern.

Because AFM imaging only provides the information about the morphology of very topmost surface layer, TEM investigations were performed in order to study distribution of nanoparticles throughout the whole film as well as confirmation of orientation of P4VP cylinders along the film thickness. Figure 4.33 shows the plane view (a, b) and cross-sectional view (c) of TEM images of the MNP3/PS<sub>57-b</sub>-P4VP<sub>18</sub> films. From correspondent TEM images it became obvious that MNP3 nanoparticles are located exclusively in P4VP cylindrical microdomains of PS<sub>57-b</sub>-P4VP<sub>18</sub>. Moreover, the P4VP cylinders are also seen as packed in a highly ordered hexagonal lattice with almost no defects observed over lateral dimensions of more than 4  $\mu\text{m}^2$ .

The distribution of nanoparticles along the cylinders is best seeing on cross-sectional view of the thin films (Fig. 4.33 c). This image undoubtedly shows that the perpendicularly oriented P4VP cylinders expand from free surface down to the substrate interface, despite the film thickness was increased to  $\sim 160$  nm. Furthermore, MNP3 nanoparticles are seen to be homogeneously distributed along the whole length of the cylinders without any tendency to aggregation.

It is noteworthy to mention here that thin films of net PS<sub>57-b</sub>-P4VP<sub>18</sub> also demonstrate perpendicular oriented cylinders when annealed in chloroform vapours for 24 hours. However, after prolongation of annealing time up to 96 hours, in-plane reorientation of cylinders was observed (Fig. 4.22 f). In case of presence of MNP3 nanoparticles in PS<sub>57-b</sub>-P4VP<sub>18</sub>, the cylinders remained oriented normal to the substrate even after long-time annealing conditions when film overall remained stable against dewetting.

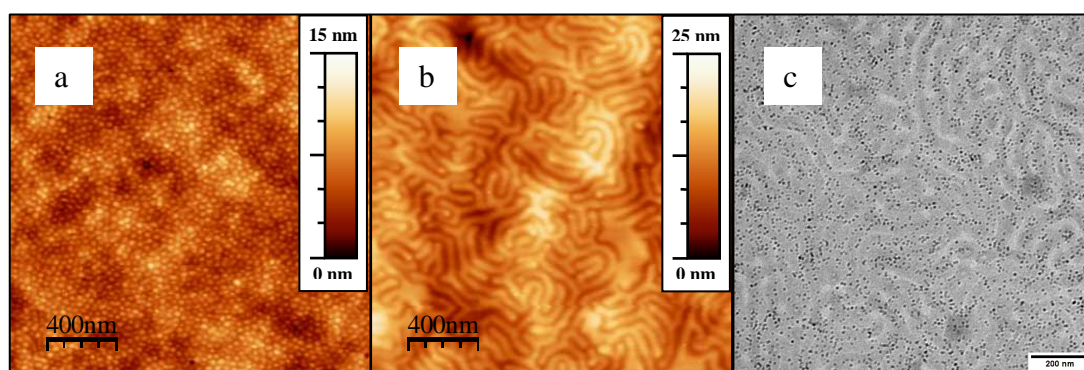


**Figure 4.34** AFM height images of THF-cast (a) and 1,4-dioxane annealed (b) MNP3/PS<sub>22-b</sub>-P4VP<sub>22</sub> composite thin films containing 5.0 wt% of MNP3; (c) – TEM image of annealed MNP3/PS<sub>22-b</sub>-P4VP<sub>22</sub> film loaded with 5 wt% of MNP3. Film thickness  $\sim 30$  nm.

When symmetric PS<sub>22</sub>-*b*-P4VP<sub>22</sub> BCP was used as a host matrix, P4VP-selective MNP3 segregation was also achieved. In this case, dried micelle morphology of THF-cast MNP3/PS<sub>22</sub>-*b*-P4VP<sub>22</sub> composite thin films was turned into perpendicularly oriented lamella upon solvent annealing in 1,4-dioxane vapour (Fig. 4.34). MNP3 were found microphase segregated within lamellar of P4VP domains, which are visualized as darker grey areas after iodine staining, with no evidence tendency toward macrophase segregation.

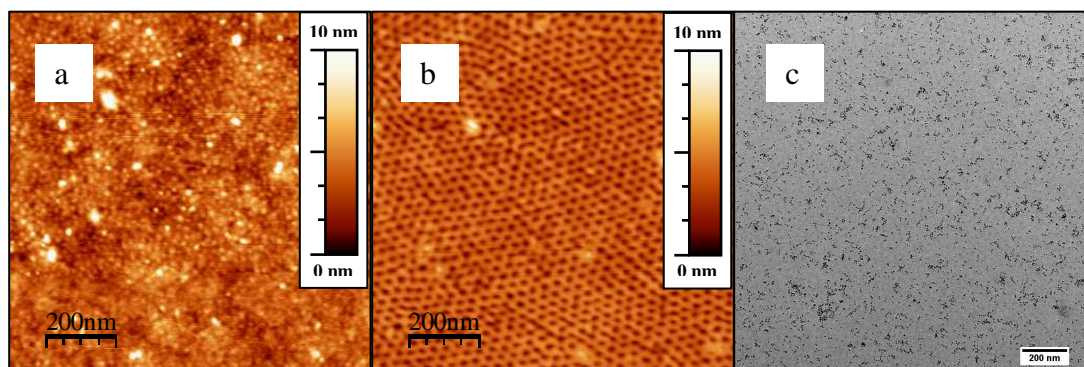


**Figure 4.35** AFM height images of THF-cast (a) and CHCl<sub>3</sub> annealed (b) MNP3/PS<sub>27</sub>-*b*-P4VP<sub>7</sub> composite thin films containing 5.0 wt% of MNP3; (c) – TEM image of annealed MNP3/PS<sub>27</sub>-*b*-P4VP<sub>7</sub> film loaded with 5 wt% of MNP3. Film thickness ~30 nm.

Finally, MNP3/PS<sub>27</sub>-*b*-P4VP<sub>7</sub> composites were examined. In this system AFM and TEM studies revealed no tendency toward particles macrophase segregation, which was found in other MNP3/PS-*b*-P4VP compositions (Fig. 4.35).

However, in case of such low molecular weight PS<sub>27</sub>-*b*-P4VP<sub>7</sub>, nanoparticles did not appear as selectively arranged solely within hexagonally packed P4VP cylinders, but was observed both as individual particles, trapped within P4VP cylinders and also as small aggregates overall inside the film, which led to a marginal disturbing of the order of microdomains.

#### 4.5.4 GISAXS investigation of MNP3/PS<sub>57</sub>-*b*-P4VP<sub>18</sub> composites

In addition to AFM and TEM investigation, MNP3/PS<sub>57</sub>-*b*-P4VP<sub>18</sub> composites were also studied with GISAXS at two different incident angles ( $\alpha_i$ ) of 0.20° and 0.30°. The value of critical angle for Fe<sub>3</sub>O<sub>4</sub> MNP was estimated using Equation 4.2 [To199]:



$$\alpha_c(\text{rad}) \approx \sqrt{2\delta} \quad (\text{Eq. 4.2})$$

where  $\delta$  represents dispersion term of material refractive index,  $n$ :

$$n = 1 - \delta(r) + i\beta(r) \quad (\text{Eq. 4.3})$$

Dispersion ( $\delta$ ) and absorption ( $\beta$ ) terms of refractive index can be expressed correspondently as:

$$\delta(r) = \frac{\lambda^2 e^2}{8\pi^2 c^2 m_e \epsilon_0} \rho(r) \sum_{j=1}^N \frac{f_j^0 + f_j'(E)}{Z} \quad (\text{Eq. 4.4})$$

$$\beta(r) = \frac{\lambda^2 e^2}{8\pi^2 c^2 m_e \epsilon_0} \rho(r) \sum_{j=1}^N \frac{f_j''(E)}{Z} \quad (\text{Eq. 4.5})$$

where  $\lambda$  is a wavelength,  $c$  is the light velocity,  $\epsilon_0$  is a dielectric constant,  $e$  and  $m_e$  are the electron charge and mass, respectively.  $Z$  represents the total number of electrons in one molecule of compound. The parameters  $f_j^0$  are  $\mathbf{q}$ -dependant, however, for small values of incident and exit angles it could be approximately assigned that  $f_j^0 = Z_j$ . Finally,  $f'(E)$  and  $f''(E)$  are the factors that take into account dispersion and absorption corrections depending on the irradiation energy.  $f'(E)$  values for elemental Fe and O at  $\lambda = 0.138$  nm are  $f'_{Fe} = -0.2442$  and  $f'_O = 0.0420$ , respectively.[6] Thus, dispersion term of refractive index, calculated for pure  $\text{Fe}_3\text{O}_4$  was found to be equal  $\delta(\text{Fe}_3\text{O}_4) = 1.261 \cdot 10^{-5}$ , resulting in  $\alpha_c(\text{Fe}_3\text{O}_4) = 0.2877^\circ$ , which is very close to the value reported in literature for maghemite ( $\alpha_c(\text{Fe}_2\text{O}_3) = 0.28^\circ$  [Kas09]).

For calculation of  $\alpha_c$  for MNP/BCP composites,  $\alpha_c(\text{Fe}_3\text{O}_4) = 0.2877^\circ$  and  $\alpha_c(\text{PS-}b\text{-P4VP})=0.160^\circ$ [Par09c] were used. Calculations showed that for MNP/BCP composites weight-average critical angle  $\alpha_c$  increases from  $0.162^\circ$  (2.0 wt% MNP) up to  $0.173^\circ$  (10.0 wt% MNP). Therefore, it was assumed that GISAXS patterns taken at both  $0.20^\circ$  and  $0.30^\circ$  incident angles could be interpreted as such that were obtained from whole depth of film thickness.

---

[6] [http://skuld.bmsc.washington.edu/scatter/AS\\_periodic.html](http://skuld.bmsc.washington.edu/scatter/AS_periodic.html)

2D GISAXS patterns and corresponding 1D plots of scattering intensity along  $q_y$  direction (out of plane cuts) obtained from as-cast films containing different amount of MNP3 are presented on Figure 4.36.

As was already mentioned, THF cast-samples of both net PS<sub>57</sub>-*b*-P4VP<sub>18</sub> and MNP3/PS<sub>57</sub>-*b*-P4VP<sub>18</sub> composites showed dimple-like (dried micelles) morphology. On GISAXS patterns intermicellar lateral distances (i.e. domain size  $D_0$ ) are reflected in position of first order Bragg peak.

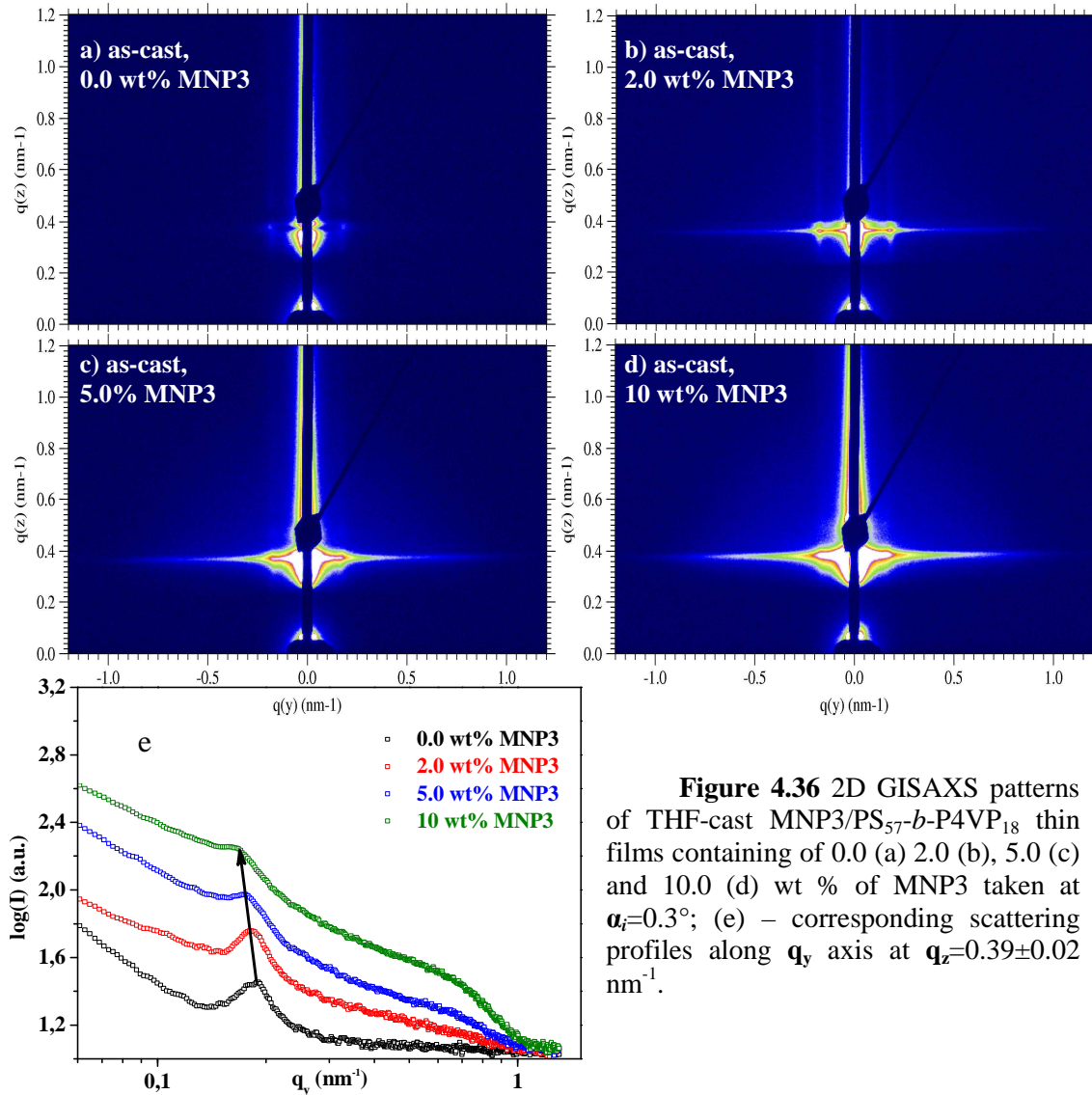


**Figure 4.36** 2D GISAXS patterns of THF-cast MNP3/PS<sub>57</sub>-*b*-P4VP<sub>18</sub> thin films containing of 0.0 (a) 2.0 (b), 5.0 (c) and 10.0 (d) wt % of MNP3 taken at  $\alpha_i=0.3^\circ$ ; (e) – corresponding scattering profiles along  $q_y$  axis at  $q_z=0.39\pm 0.02$  nm<sup>-1</sup>.

With an increase of MNP3 content from 0 to 10 wt%, the position of such peak gradually shifts to lower  $q_y$  values, as indicated by arrow on Figure 4.36 e. In real-space length this reflects an increase of distances between neighboring micelles, most probably due to trapping of nanoparticles inside of PVP micelles. The mean values of

$D_0$  calculated for composites with different nanoparticles content were found equal to 32.7, 34.0, 35.5 and 38.1 nm for 0.0, 2.0, 5.0 and 10.0 wt %, respectively.

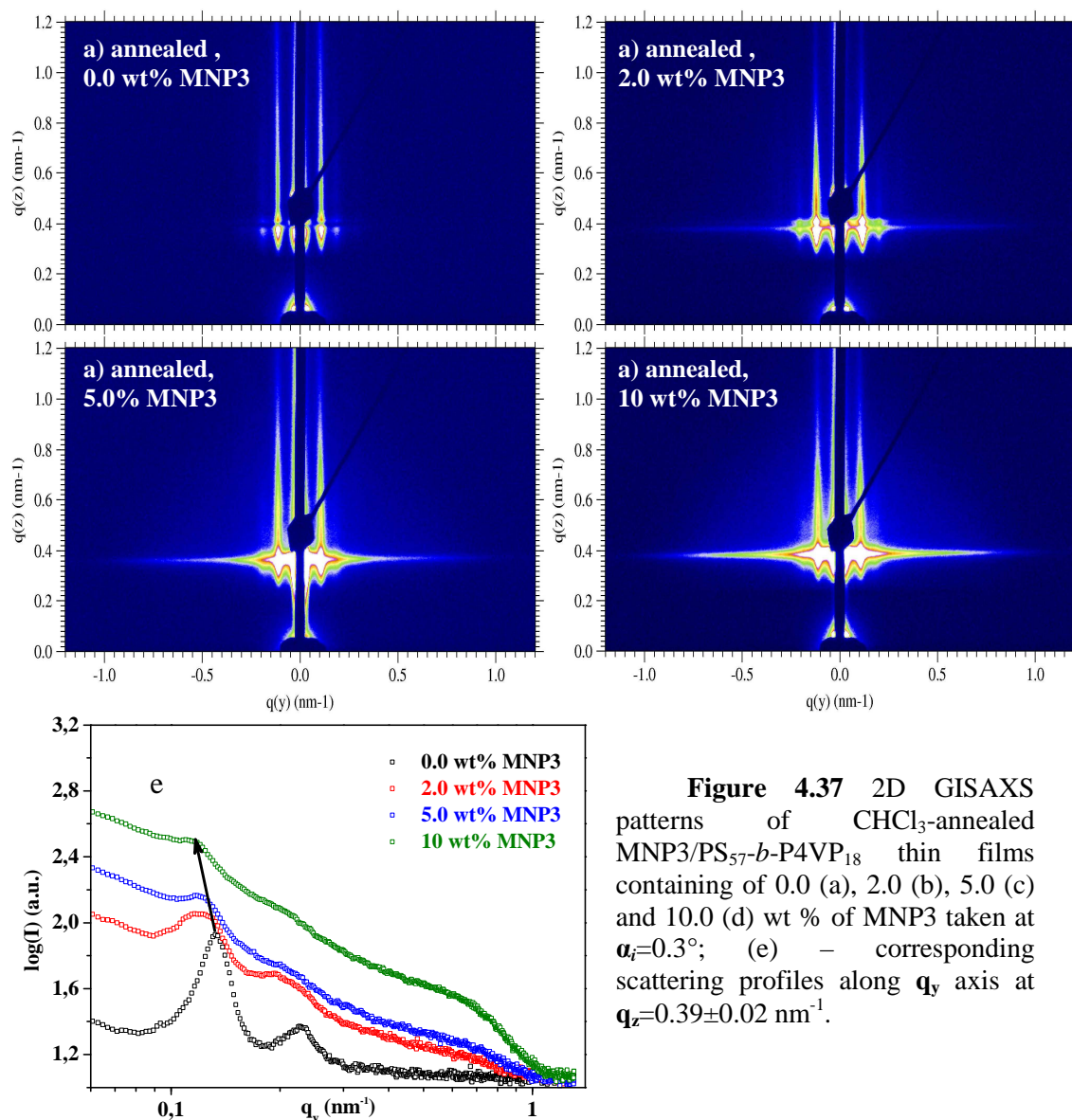


**Figure 4.37** 2D GISAXS patterns of  $\text{CHCl}_3$ -annealed MNP3/PS<sub>57</sub>-*b*-P4VP<sub>18</sub> thin films containing of 0.0 (a), 2.0 (b), 5.0 (c) and 10.0 (d) wt % of MNP3 taken at  $\alpha_i=0.3^\circ$ ; (e) – corresponding scattering profiles along  $q_y$  axis at  $q_z=0.39\pm 0.02$  nm<sup>-1</sup>.

In addition, an increase on particles content led to the broadening and less intensity of peaks, reflecting thus formation of less ordered structures. The second observed feature was an appearance of shallow diffuse scattering originating most probably from the presence of nanoparticles clusters inside the films. From comparison of  $q_y$  scan plots it is became clear that intensity of such diffuse scattering increase at higher particles loading.

2D GISAXS patterns and out of plane cuts taken from the samples after 30 minutes of “fast” annealing in  $\text{CHCl}_3$  are shown on Figure 4.37. For all investigated films perpendicularly oriented structures could be identified from the presence of

vertically oriented reflections, while ordering effect is clear from appearance of second and third order peaks.

However, it is also evident that higher order peaks could be well resolved only for neat BCP and for sample with 2.0 wt.% of MNP3, while at 5.0 and 10 wt% of MNP3 2<sup>nd</sup> and 3<sup>rd</sup> peaks appeared only as weak and broad shoulders over diffuse scattering. The  $q_y$  values of 1<sup>st</sup>, 2<sup>nd</sup> and 3<sup>rd</sup> order peaks were rated as  $1:\sqrt{3}:\sqrt{4}$ , indicating hexagonally packed cylinders, oriented normal to the substrate.

It should be mentioned, that above GISAXS patterns represent the structure of simultaneously annealed samples, where “fast” annealing procedure was used. Thus, above results do not reflect the best possible ordering effect of solvent annealing.

The significance of different ordering effect obtained after “fast” (30 min) and “slow” (24 hours) annealing of thin films MNP3/PS<sub>57</sub>-*b*-P4VP<sub>18</sub> composite loaded with 5 wt % of MNP3 could be revealed from Figure 4.38.

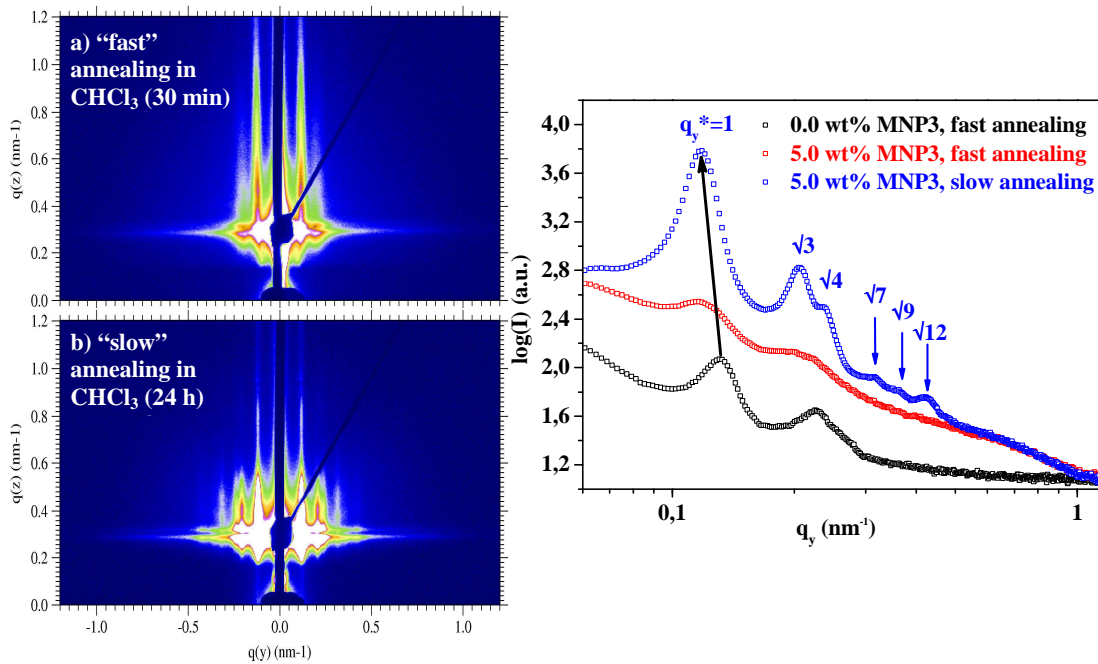


**Figure 4.38** 2D GISAXS patterns of MNP3/PS<sub>57</sub>-*b*-P4VP<sub>18</sub> thin films containing 5.0 wt % of MNP3 after “fast” (a) and slow (b) annealing in CHCl<sub>3</sub> taken at  $\alpha_i=0.20^\circ$ ; (c) – corresponding scattering profiles along  $q_y$  axis at  $q_x=0.31\pm 0.02 \text{ nm}^{-1}$ . Scattering profile for neat PS<sub>57</sub>-*b*-P4VP<sub>18</sub> is included for comparison.

Formation of highly ordered hexagonally packed cylinders after “slow” annealing is evident from the appearance of multiply order peaks at positions  $1:\sqrt{3}:\sqrt{4}:\sqrt{7}:\sqrt{9}:\sqrt{12}$  (Fig.4.38 b). Importantly, the presence on magnetic nanoparticles did not disturb morphology of BCP at conditions of slow annealing. An increase of domain period

from 47.6 nm for net BCP to 53.2 nm for composition with 5.0 wt % of MNP3 was attributed to the expansion of volume occupied by P4VP phase loaded with MNP3.

To shortly summarize this part, the results presented above show that the nature of nanoparticles shell as well as the nature and composition of block copolymers play the crucial role in ordering and selective localization of the nanoparticles in the composite systems.

As it was discussed, pyridine moieties in the PVP chains have the affinity towards metal and metal oxide surfaces. It was found that MNP1 particles stabilized by oleic acid underwent macrophase segregation and segregate out of BCP thin film during solvent vapour annealing. However, MNP3 having the same size of particles as MNP1 but thinner shell, were able to be selectively incorporate into the PVP domain of the BCP. The same behaviour was observed also for  $\text{CoFe}_2\text{O}_4$ , MNP5 sample. There could be two possible reasons for such change in behaviour. The first one might be linked to the fact that thicker shells increase the apparent size of the nanoparticles and thus might lead to macrophase segregation due to entropic energy factors as has been discussed by Balazs and co-workers.[Bal06] The second reason could be due to the fact that the thinner stabilizing shell allows the MNP3 to directly interact with the PVP chains due to the presence of some free binding sites available around the  $\text{Fe}_3\text{O}_4$  surface. In the case of MNP1, a thicker organic shell of oleic acid shields the  $\text{Fe}_3\text{O}_4$  nanoparticles better, thus precluding interaction with pyridine group and deriving their macrophase segregation.

The second important observation was that though MNP3 were successfully incorporated in symmetric  $\text{PS}_{50}\text{-}b\text{-P2VP}_{50}$  BCP, they macrophase segregate when the P2VP was used as the minor block (asymmetric  $\text{PS}_{56}\text{-}b\text{-P2VP}_{21}$ ). However, when  $\text{PS}\text{-}b\text{-P4VP}$  of similar asymmetric composition and chain lengths was used ( $\text{PS}_{57}\text{-}b\text{-P4VP}_{18}$ ), MNP3 were again found to exclusively locate within the P4VP cylinders. This suggests that the nature of PVP chains significantly influence on the interaction with the nanoparticles and can be rationalized in terms of different binding ability of the P2VP and P4VP blocks. In P2VP the nitrogen atoms in the 2VP units are present at “ortho”-position and, hence, they are not readily available for any physical interactions due to steric factors. Since the chemical interaction is weaker, the polymer chains try to stretch around the nanoparticles, and, as the radius of gyration is lower in the cylindrical BCP with P2VP, macrophase segregation of the nanoparticles takes place that was predicted by Ballazs et al.[Bal06] From this point of view, sufficiently strong MNP/PVP

interaction and the formation of well ordered structures with MNP3 is provided only when the fraction of P2VP in PS-*b*-P2VP BCP is high enough. Since in P4VP, the nitrogen atoms in 4VP units do not have such constraints for interaction with other species, P4VP interacts stronger with the nanoparticles that allows achieving of high loadings of MNP3 in nanocomposites even when P4VP is a minor block. The stronger chemical interactions between the nanoparticles and the polymer chains may overcome the entropic constraints cause by chain stretching around the nanoparticles, and lead to their selective segregation inside the P4VP phase.

When nanoparticles with even thinner stabilizing shell were used (i.e. MNP4 covered with 1,2-decanediol shell), they were found to form aggregates due to increased surface energy. Such aggregation was observed for MNP4 already for their dispersions in THF as well as in as-cast MNP4/BCP samples, retaining, however, their affinity towards PVP phase.

#### **4.5.5 Investigation of magnetic properties of MNP/PS-*b*-PVP composites**

Magnetic force microscopy (MFM) imaging of annealed MNP3/PS<sub>50</sub>-*b*-P2VP<sub>50</sub> and MNP3/PS<sub>57</sub>-*b*-P4VP<sub>18</sub> composites films was performed in dynamic lift mode using magnetized cantilevers. The ‘magnetic domains’ of P2VP lamellae (Fig. 4.39 a,b) and P4VP cylinders (Fig. 4.39 c,d) with incorporated magnetic nanoparticles were clearly observed on correspondent phase images when scans were performed with magnetized cantilever (Fig. 4.39 b,d) at lift height 30 nm.

As control experiment, AFM scans of MNP3/PS<sub>57</sub>-*b*-P4VP<sub>18</sub> sample were also performed in dynamic lift mode using the same but non-magnetized cantilever. As a result phase images without any contrast and correlation to topography image were obtained maintaining the same lift height (Fig. 4.39 f). This indicate that phase contrast obtained upon scanning of sample with magnetized tip was, in fact, reasoned by its interaction with nanoparticles and not by any other long-range forces, that could influence tip deflection at such distances.

Magnetisation behaviour of neat MNP3 and MNP3/PS<sub>57</sub>-*b*-P4VP<sub>18</sub> bulk composites with varied nanoparticles loading was studied using SQUID (Fig. 4.40). The magnetization data obtained for MNP3 showed their superparamagnetic nature, with no



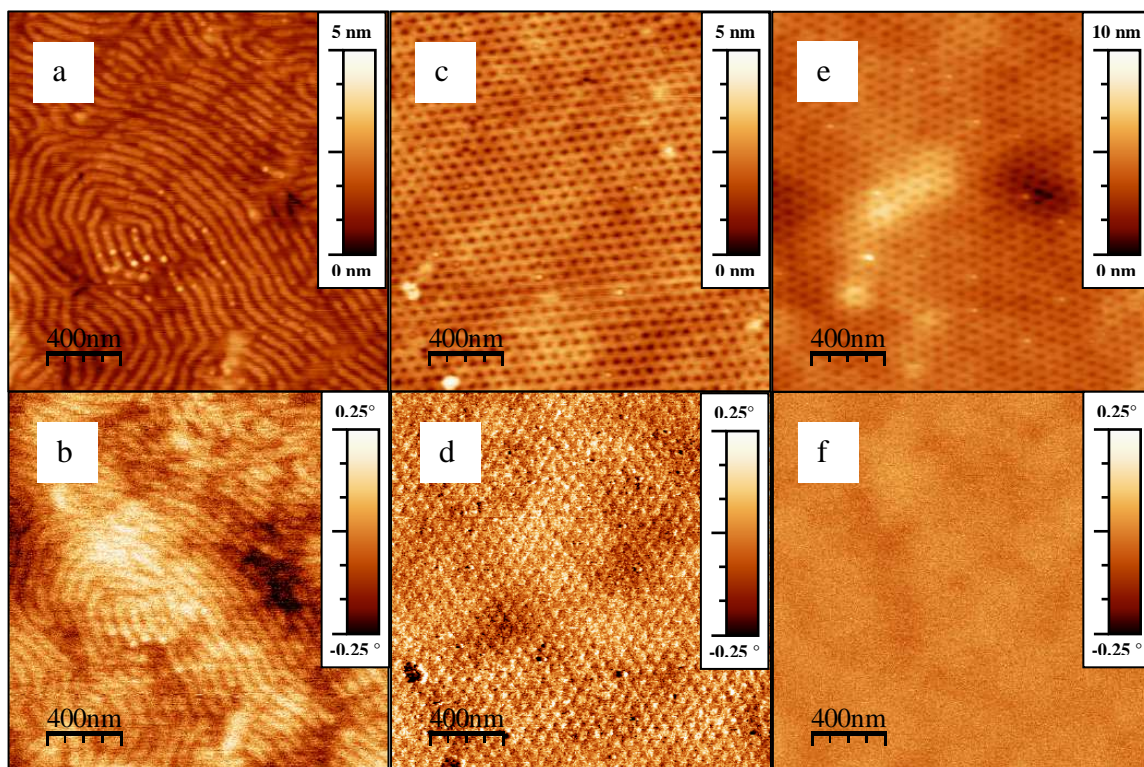


**Figure 4.39** MFM height (a,c,e) and phase (b,d,f) images of solvent annealed MNP3/PS<sub>50</sub>-*b*-P2VP<sub>50</sub> (a,b) and MNP3/PS<sub>56</sub>-*b*-P4VP<sub>18</sub> (c-f) composite thin films containing 10.0 wt% and 5.0 wt% of MNP3, respectively, obtained with magnetized (a-d) and non-magnetized (e,f) cantilever in dynamic lift mode at lift height of 30 nm.

remnant magnetisation and coercivity. The saturation magnetization, normalized to the magnetite content, was 83.7 and 69.3 emu/g of at 5K and 300K, respectively, which matches the corresponding values for ~6 nm magnetite particles reported elsewhere.[Sun02,Car07]

The comparison of magnetisation curves obtained for neat MNP3 and MNP/BCP composites shows that magnetisation ( $M$ ) reaches its saturation value at lower strength of external magnetic field, if particles are embedded into BCP matrix. Such effect could be explained as result of MNP3 dispersion within the host BCP matrix, when the nanoparticles clustering effect is diminished. On the other hand, as the strength of magnetic field increased, normalized magnetisation for composites gradually decreased below its maximum values as magnetic field strength was increased. This is in contrast to neat MNP3 case, where magnetisation plateau was observed at high values of applied external magnetic field. Such reduction of magnetisation with increase of magnetic field strength becomes more pronounced at lower MNP3 loadings (e.g. 2.0 wt%) and is explained as an increased contribution of diamagnetic nature of PS-*b*-PVP BCP, which becomes more significant at higher values of applied external magnetic field.

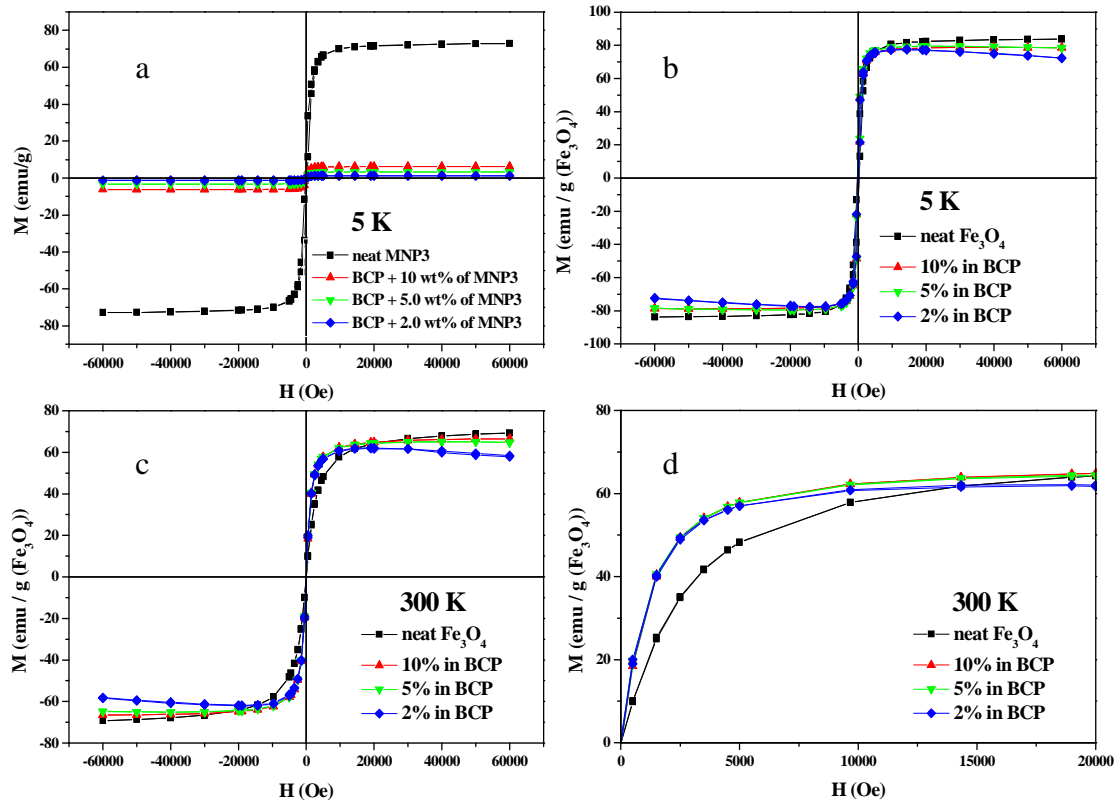


**Figure 4.40** Magnetization curves of MNP3 and MNP3/PS<sub>57</sub>-*b*-P4VP<sub>18</sub> composite bulk samples with MNP3 loading of 2.0, 5.0 and 10.0 wt% taken at 5K (a,b) and 300K (c,d): (a) – raw data, (b,c) – data normalized to the content of pure Fe<sub>3</sub>O<sub>4</sub> (based on TGA measurements), (d) – magnified part of graph (c).

#### 4.5.6 Annealing of MNP/PS-*b*-PVP composites in the presence of external magnetic field

In addition to shear and electric field induced alignment of BCPs, several reports on application of external magnetic field to orient block copolymer microdomains could be found in literature.[Gri05,Tao07] However, in most experiments, high-strength magnetic field, in order of several Tesla was required to achieve such orientation effect. Recently, Hammond et al. reported on application of magnetic field came out from conventional laboratory permanent magnet (~900 mT) to orient PS-*b*-P2VP cylinders, filled with rod-shaped magnetic nanoparticles.[Ham10] However, although orientation effect was achieved, resulted structures were strongly disturbed by the presence of nanorods having size significantly larger than BCP domains.



An effect of the presence of external magnetic field on MNP3/PS<sub>50</sub>-*b*-P2VP<sub>50</sub> morphology during solvent vapour annealing was also studied in present work. Samples were placed either parallel or perpendicular with respect to magnetic field, created by a disc-shaped permanent magnet (400 mT) and annealed in 1,4-dioxane. To eliminate possible effects of diverse annealing conditions compare to ordinarily used (chamber volume, sample position and orientation) another sample was placed inside the chamber as far as possible (*ca.* 10 cm) from the magnet edge and used as a reference. Importantly, the morphology of such reference samples did not show any significant difference compare to the samples annealed using ordinary annealing conditions without external magnetic field.

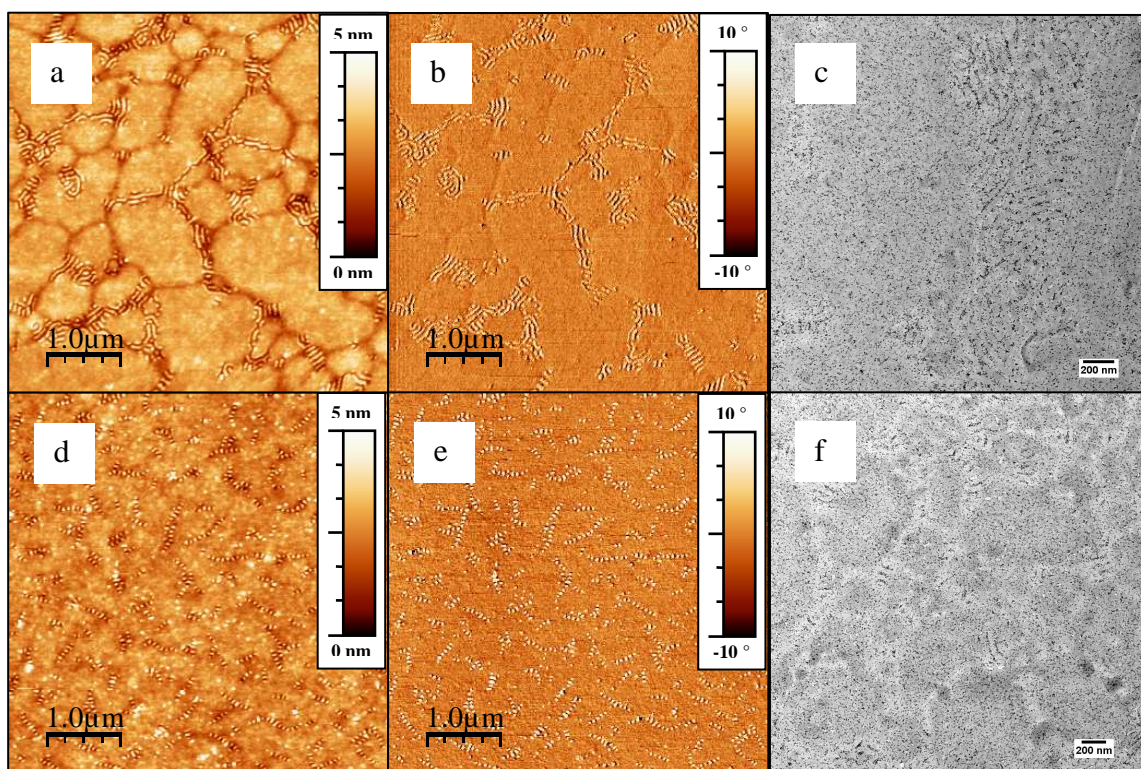


**Figure 4.41** AFM height (a,d), phase (b,e) and corresponding TEM images (c,f) of MNP3/PS<sub>50</sub>-*b*-P2VP<sub>50</sub> composites containing 10.0 wt% of MNP3 annealed in 1,4-dioxane for 3 hours in the presence of external magnetic field oriented perpendicular (a,b,c) and parallel (d,e,f) to the film surface. Film thickness  $\sim$ 50 nm.

AFM images of MNP3/PS<sub>50</sub>-*b*-P2VP<sub>50</sub> composite thin films containing 10 wt% of MNP3 annealed in the presence of external magnetic field are shown on Figure 4.41 a, b, d and e. As can be seen, the surface morphologies formed during annealing in magnetic field differ from the structures observed after vapour annealing without an application of magnetic field. Formation of flat featureless areas, separated by narrow

and periodically structured regions was observed instead of perpendicularly standing lamellae, formed on reference samples, similar to those shown on Figure 4.28. Such morphology could be interpreted as substrate parallel lamella perturbed by regions of microdomains being oriented normal to the substrate. The flat regions did not show any evidence of MNP presence at the surface reach area, suggesting being composed of PS block. Instead, structured areas were decorated with nanoparticles, similar to perpendicularly oriented lamellae. Further TEM investigation of above mentioned samples etched from the substrate (Fig. 4.41 c,f) confirmed such perturbed nature of substrate parallel lamellar domain orientation for both samples annealed with an application of external magnetic field.

From above mentioned it was suggested, that structure and morphology of BCPs loaded with magnetic NPs could be altered by an application of external magnetic field during annealing step. It seems that perpendicular orientation of lamellae, observed upon annealing in 1,4-dioxane atmosphere, is somehow prevented when additional magnetic forces are involved. Unfortunately, by simple variation of annealing conditions, such as annealing time, nature and amount of solvent used, our attempts to achieve uniform domain orientation in certain direction by action of applied magnetic field were not successful. This might be reasoned by several factors, in particular, low strength and non-uniformity of magnetic field, also due to the presence of substrate.

Since the morphology of solvent annealed thin films is also dependant on variety of factors, such as film thickness, annealing time, substrate properties, further experiments are required to better understand their contribution into structure formation in the presence of applied external magnetic field.

## 4.6 Preparation and investigation of AgNP/BCP composites

For preparation of AgNP/PS-*b*-PVP composites silver NPs having different core diameter, namely, AgNP4 ( $d_{av}=4.1$  nm), AgNP5 ( $d_{av}=8.5$  nm), AgNP6a ( $d_{av}=12.8$  nm) covered with polystyrene stabilizing shell (PSSH1,  $M_n=1100$  g·mol<sup>-1</sup>) were used. Additionally, AgNP6b of the same core diameter as AgNP6a, but covered with PS layer of larger molecular weight (i.e. PSSH5,  $M_n=5300$  g·mol<sup>-1</sup>) were also tested as nanoadditives. Composites were prepared in the way similar to MNP/BCP, i.e. by mixing of separately prepared AgNPs and BCP solutions in THF to give nanoparticles concentration varying in a range of 0.0-10.0 wt% and block copolymer concentration in a range of 0.5-2.5 wt%. Thin film preparation and annealing were performed on Si and glass substrates in the way similar to neat BCPs and MNP/BCP composites.

Due to the presence of PS shell AgNPs were expected to segregate selectively into polystyrene phase of BCP matrix. For AgNP/PS<sub>50</sub>-*b*-P2VP<sub>50</sub> composites thin films hole-like morphology was observed for THF-cast samples, independently on AgNP core size and molecular weight of polystyrene stabilizing shell (Fig. 4.42). No difference in surface morphology was observed for as-cast samples containing different amount of AgNPs in concentration range studied (i.e. up to 10.0 wt% of AgNPs loading).

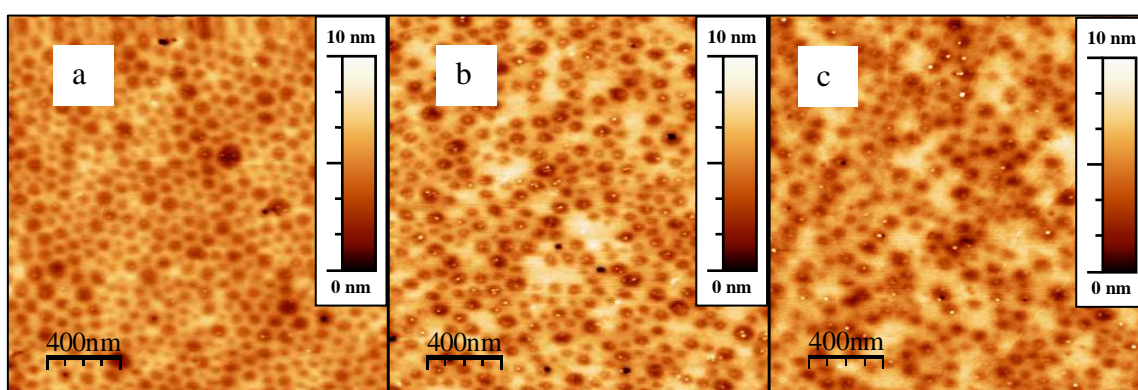


**Figure 4.42** AFM height images of THF-cast AgNP4/PS<sub>50</sub>-*b*-P2VP<sub>50</sub> (a), AgNP6a/PS<sub>50</sub>-*b*-P2VP<sub>50</sub> (b) and AgNP6b/PS<sub>50</sub>-*b*-P2VP<sub>50</sub> (c) composite thin films containing 2.0 wt% of AgNP4, 5.0 wt% of AgNP6a and 5.0 wt% of AgNP6b, respectively. Film thickness ~50 nm.



From the comparison of AFM images obtained for neat PS<sub>50</sub>-*b*-P2VP<sub>50</sub> BCP with MNP3/PS<sub>50</sub>-*b*-P2VP<sub>50</sub> and AgNP/PS<sub>50</sub>-*b*-P2VP<sub>50</sub> composites it becomes evident that morphology of as-cast thin films is influenced not only by the presence of nanoparticles, but also by their nature. For instance, worm-like morphology of THF-cast PS<sub>50</sub>-*b*-P2VP<sub>50</sub> neat BCP (Fig. 4.17) was changed into discontinuous perpendicular lamellae upon addition of MNP3 (Fig. 4.27), while an addition of PS-stabilized AgNPs resulted in hole-like structures (Fig. 4.42). In case of MNP3/PS<sub>50</sub>-*b*-P2VP<sub>50</sub> system, perpendicular orientation of BCP microdomains is enhanced upon increase of MNP3 loading due to their affinity towards PVP block.[Lin05] In contrast, for AgNP/PS<sub>50</sub>-*b*-P2VP<sub>50</sub> system, such microdomain orientation effect was not observed for any type of AgNPs added.

In order to generate formation and orient lamellar microdomains of BCP perpendicularly to the substrate, AgNP/PS<sub>50</sub>-*b*-P2VP<sub>50</sub> composite thin films were solvent annealed. It was observed, that annealing in 1,4-dioxane vapour of AgNP4/PS<sub>50</sub>-*b*-P2VP<sub>50</sub> composite thin films led to the transformation of hole-like morphology of as-cast samples to lamellar structures with domains oriented normally to the substrate plane (Fig. 4.43). However, from AFM imaging alone it was difficult to visualize the presence and distribution of AgNP4 due to their small size (Fig. 4.43 a,d). Consequently, composite thin films were etched from the substrate and transferred onto copper grid for TEM imaging. TEM studies revealed selective segregation of AgNP4 within one of the lamellar microdomains of microphase segregated PS<sub>50</sub>-*b*-P2VP<sub>50</sub>

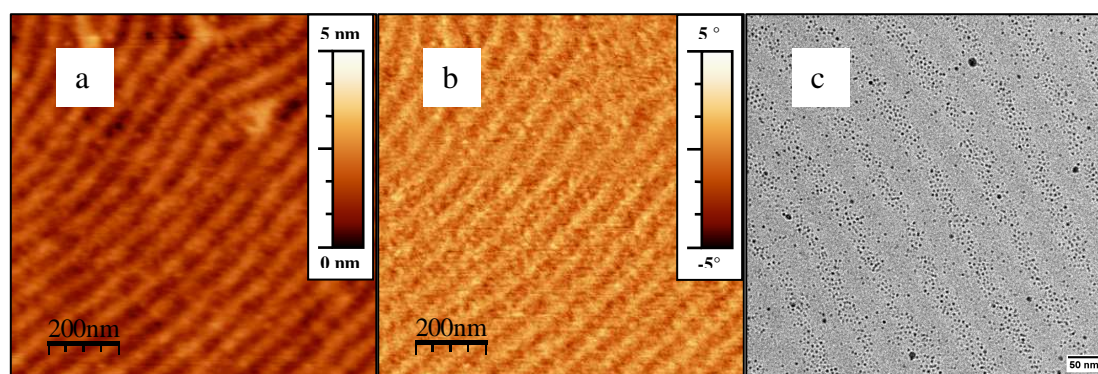


**Figure 4.43** AFM height (a), phase (b) and corresponding TEM (c) images of 1,4-dioxane annealed AgNP4/PS<sub>50</sub>-*b*-P2VP<sub>50</sub> composite thin films containing 5.0 wt% of AgNP4. Film thickness ~50 nm.

matrix (Fig. 4.43 c).

Similarly, for larger size AgNP5 and AgNP6 nanoparticles their selective segregation within one of the PS-*b*-P2VP microdomains was achieved after solvent vapour annealing, as it was observed on AFM height and phase images (Fig. 4.44 a,b,d,e) and further confirmed by TEM studies (Fig. 4.44 c,f).

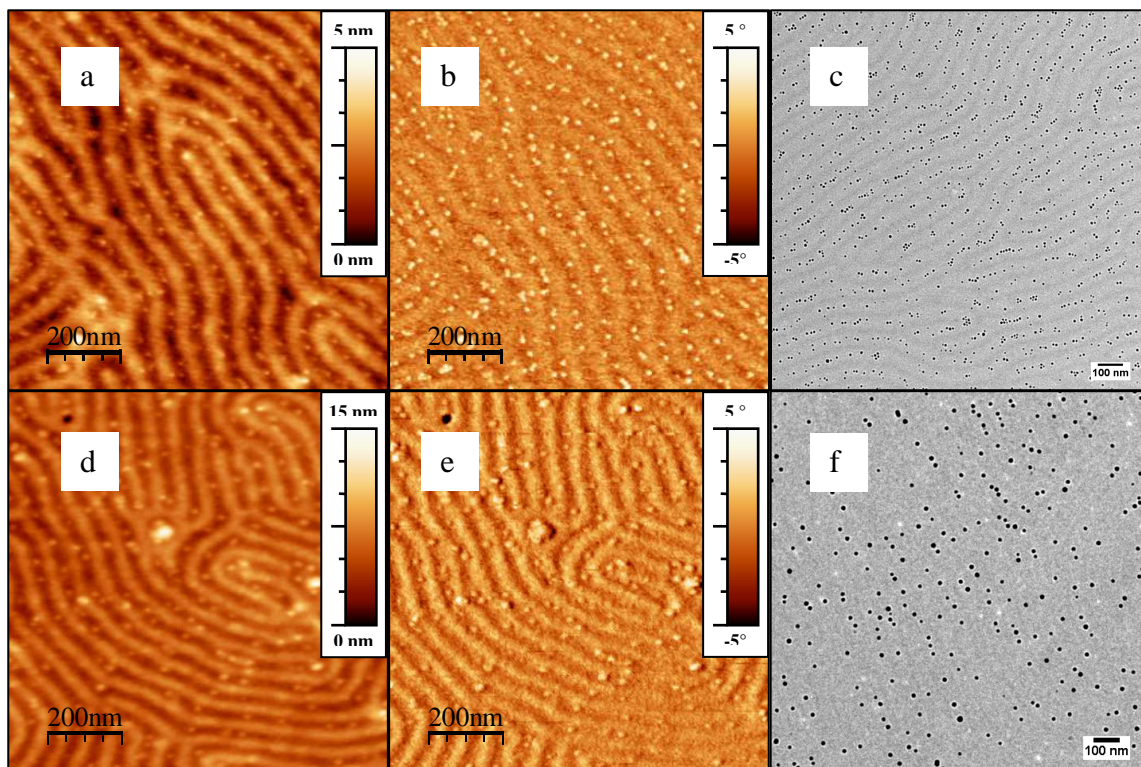


**Figure 4.44** AFM height (a,d), phase (b,e) and corresponding TEM images (c,f) of 1,4-dioxane annealed AgNP5/PS<sub>50</sub>-*b*-P2VP<sub>50</sub> (a-c) and AgNP6a/PS<sub>50</sub>-*b*-P2VP<sub>50</sub> (d-f) composite thin films containing 2.0 wt% of AgNPs. Film thickness ~50 nm.

Due to the lack of electron density contrast between PS and P2VP phases, it was not possible to distinguish them from bright-field TEM images. Even so the contrast between different BCP domains could be enhanced by defocusing (Fig. 4.44 c) it gives no evidence of particular domains position.

In order to ascertain AgNPs position within particular block, AgNP/PS<sub>50</sub>-*b*-P2VP<sub>50</sub> samples were treated with iodine, which is known as selective staining agent for PVP.[Par02] An example of iodine stained AgNP6a/PS<sub>50</sub>-*b*-P2VP<sub>50</sub> thin film is shown on Figure 4.45. From TEM images it is evident that most of the PS-covered AgNP6a are selectively located within brighter PS domains of PS<sub>50</sub>-*b*-P2VP<sub>50</sub>. However, iodine staining also affected silver nanoparticles inside the BCP film, which after staining were found nonuniform in size and electron density contrast (Fig. 4.45 b).



Such effect is attributed to the formation of AgI crystals as a result of reaction between  $I_2$  and silver during staining procedure.

Alternatively, selectivity of AgNPs position could be determined with the aid of

electron energy loss spectroscopy (EELS) and energy-filtered TEM imaging (EFTEM) (Fig. 4.46). Using EFTEM, it was possible to obtain nitrogen map of studied AgNP5/PS<sub>50</sub>-*b*-P2VP<sub>50</sub> thin film and, thus, to distinguish PS from P2VP phase. PS-rich (darker) and PVP-rich (brighter) areas were resolved on EFTEM image obtained at the nitrogen edge of electron spectra (Fig. 4.46 b). The location of AgNPs in BCP was mapped on image (c) which is an overlap of image (a) and inverse FFT of image (b) (Fig. 4.46). Therefore, both iodine staining and EFTEM imaging confirmed segregation of PS-covered AgNPs selectively into polystyrene domain of PS<sub>50</sub>-*b*-P2VP<sub>50</sub> BCP.

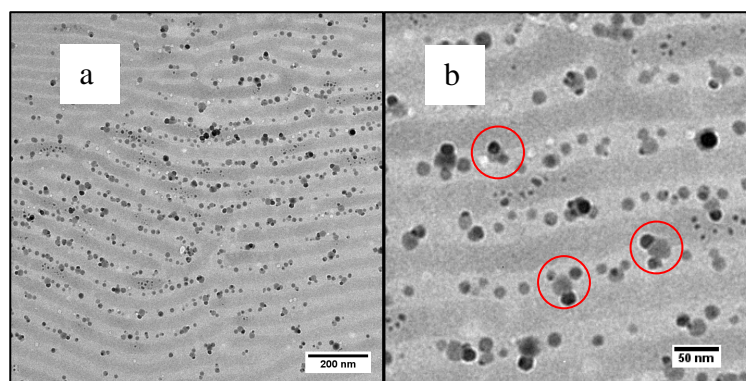


**Figure 4.45** TEM images of AgNP6a/PS<sub>50</sub>-*b*-P2VP<sub>50</sub> composite thin film after staining with  $I_2$ . AgNPs appear nonuniform (marked with red circles) due to the reaction with  $I_2$ .

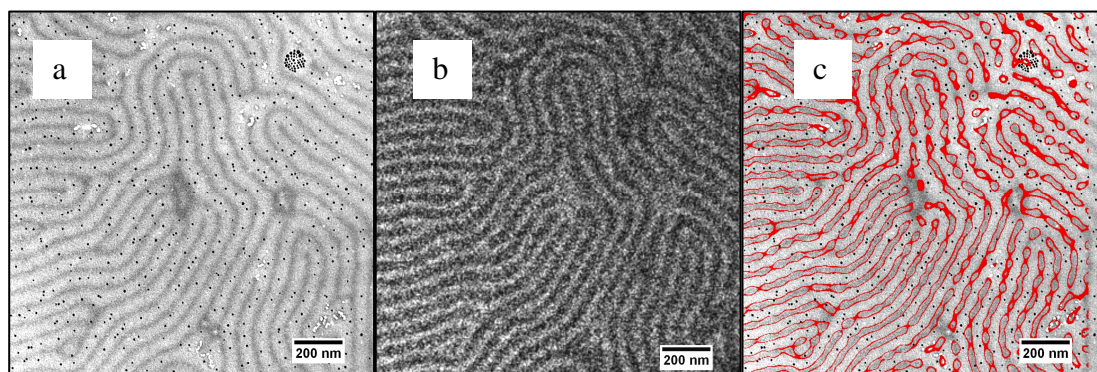


**Figure 4.46** Intentionally defocused TEM image of 1,4-dioxane annealed AgNP5/PS<sub>50</sub>-*b*-P2VP<sub>50</sub> composite thin film containing 2.0 wt % of AgNP5 (a) and nitrogen map image of the same area obtained using EFTEM (b); (c) – an overlap of image (a) and inverse FFT of image (b): red-contoured areas depict PVP-rich regions.

In contrast to AgNP4/PS<sub>50</sub>-*b*-P2VP<sub>50</sub> composites, attempts to further increase AgNP5 loading rate above 2.0 wt% led to partial particles phase segregation atop of thin film surface during solvent vapour annealing, as it was revealed from TEM studies (Fig. 4.47 a). Similar tendency was also observed for composites containing larger

AgNP6a particles: in this case even after 30 min of samples exposure to 1,4-dioxane vapour formation of AgNP6a clusters was observed atop of film surface (Fig. 4.47 b). Such tendency of AgNP5 and AgNP6a towards macrophase segregation is attributed to the increased entropy penalty arising from incorporation of nanoparticles into polymer matrix due to increased nanoparticles size compared to AgNP4.[Boc05] Another factor that might also affect AgNP5 and AgNP6a tendency toward phase segregation is the formation of stabilizing shell with lower PS grafting density

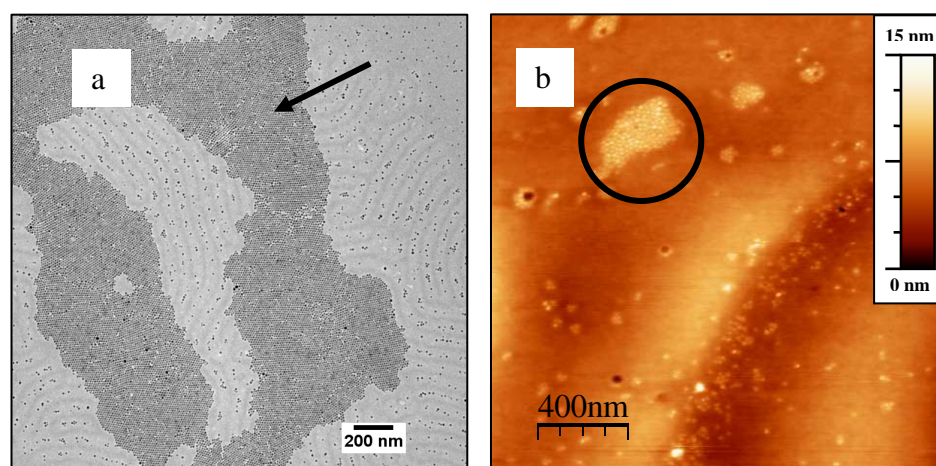


**Figure 4.47** TEM (a) and AFM height (b) images of 1,4-dioxane annealed AgNP5/PS<sub>50</sub>-*b*-P2VP<sub>50</sub> (a) and AgNP6b/PS<sub>50</sub>-*b*-P2VP<sub>50</sub> (b) composite thin films containing 5.0 wt% of AgNPs. Circle and arrow point out AgNPs clusters formed atop of thin film after solvent vapour annealing. Film thickness ~50 nm.

compared to that, which possess AgNP4 nanoparticles (Chapter 4.3).

As it was previously shown, upon prolonged vapour annealing of PS<sub>50</sub>-*b*-P2VP<sub>50</sub> BCP thin films formation of defects take place if the degree of film swelling exceeds ~3 (Chapter 4.4.3). These defects appear as holes or islands, depending on film thickness incommensurability with respect to BCP microdomain period. After addition of the AgNPs to the system, it was interesting to observe that AgNP5 in PS<sub>50</sub>-*b*-P2VP<sub>50</sub> thin films form regular ring-like structures along the holes perimeter (Fig. 4.48).

After closer look, it was found that the borders of these rings are composed of silver nanoparticle monolayer, which appear organized into well-ordered hexagonally packed 2D lattices, as it is shown on Figure 4.48 c. It is evident that PS-stabilized AgNP5 have a tendency to concentrate at the defect borders (i.e. holes edges). Similar tendency of nanoparticles to stabilize the BCP microdomain defects (i.e. grain boundaries) was also experimentally observed by Listak and Bockstaller [Lis06] and theoretically modelled by Thompson [Tho10] for bulk NP/BCP composites. Moreover,

our observations are in agreement with results recently shown for PS-*b*-PnBMA block

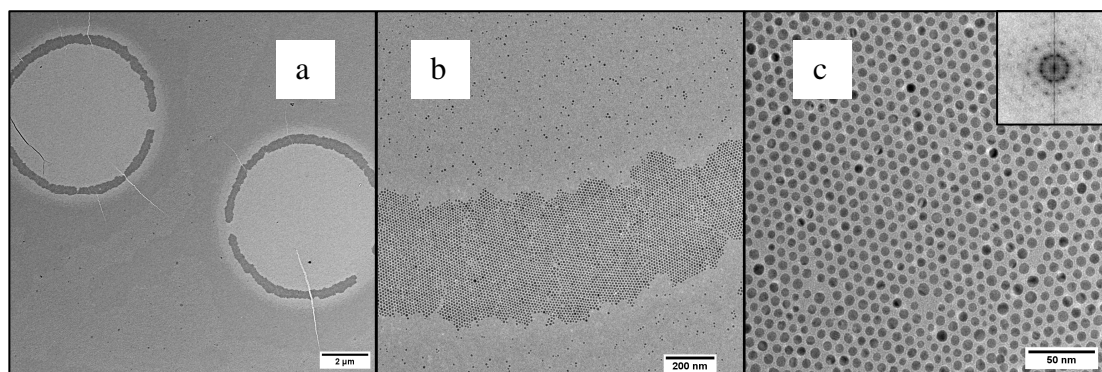


**Figure 4.48** Different magnification TEM images of 2D lattice formed of AgNP5 nanoparticles along the holes perimeter after annealing of AgNP5/PS<sub>50</sub>-*b*-P2VP<sub>50</sub> composite thin film in 1,4-dioxane vapour for 4 hours. Inset on image (c) – FFT with multiple order 6-fold symmetry peaks. Initial film thickness ~50 nm, AgNP5 content – 5.0 wt%.

copolymer thin films containing PS-coated gold nanoparticles,[Kim10b] where nanoparticles were found segregated at the edges of island and holes boundaries.

Formation of such particles monolayers, which represent significant drawback for obtaining of well-ordered NP/BCP nanostructures, might be useful as an approach for microstructure fabrication. From this point of view, an application of patterned substrates would be interesting for further investigation with the purpose to establish control over the defect formation.

Examination of optical properties of AgNP5/PS<sub>50</sub>-*b*-P2VP<sub>50</sub> composite thin films before and after solvent vapour annealing revealed the dependence of surface plasmon resonance (SPR) peak position from particles content and annealing time. For as-cast

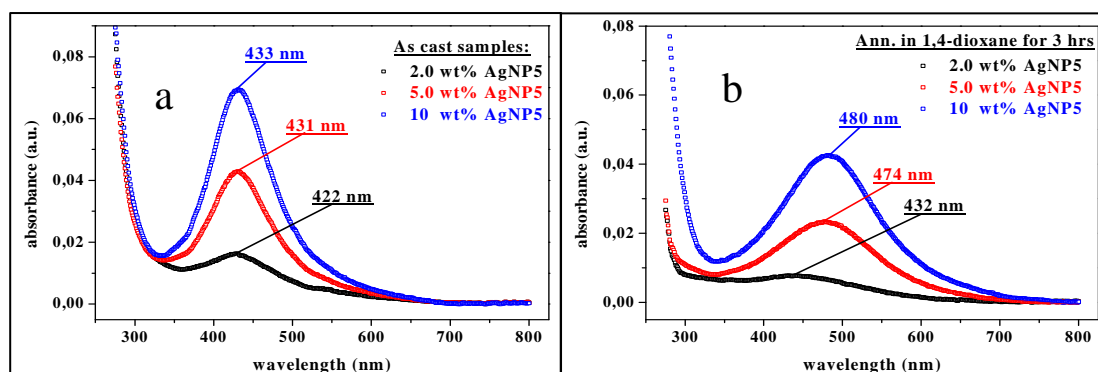


**Figure 4.49** UV-VIS spectra of THF-cast (a) and annealed in 1,4-dioxane vapour for 3 hours (b) AgNP5/PS<sub>50</sub>-*b*-P2VP<sub>50</sub> composites thin films with different AgNP5 content. Film thickness ~50 nm.



thin films, the position of SPR peaks underwent gradual shift toward longer wavelength (from  $\lambda=422$  to  $\lambda=433$  nm) with an increase of AgNP5 concentration (Fig. 4.49 a).

The appearance of red-shift with an increase of nanoparticles loading rate could be related to decrease of average interparticle distances.[Jai07,Zhe02] In addition the SPR peak maxima for as-cast composite films are also red-shifted relatively to the peak position observed for AgNP5 dispersed in THF on  $\Delta\lambda=5\div 15$  nm ( $\lambda_{\text{THF}} = 418$  nm, Fig. 4.16) due to the different nature of surrounding media (THF and PS-*b*-P2VP, respectively).

Much more prominent shift of plasmon peak was detected for the samples after annealed in 1,4-dioxane vapour. When the samples were exposed to 1,4-dioxane vapour for 3 hours, peak position was shifted towards longer wavelength values and in the same time appeared broader (Fig.4.49 b). For samples loaded with 2.0 wt % of AgNP5, after solvent annealing SPR peak maxima appeared at 432 nm, while for composites loaded with particles on 5.0 and 10.0 wt%, peak positions were shifted to 474 and 480 nm, respectively.

When annealing time of AgNP5/PS<sub>50</sub>-*b*-P2VP<sub>50</sub> composites films was extended up to 4 hours, resulted absorption peak appeared even broader (Fig.4.50). Interestingly, extension of annealing time led to the blue-shift of SPR peak maxima if

compare with the similar sample annealed for 3 hours. In addition, the peak acquired strongly asymmetric shape, indicating the presence of more than one constituent. Deconvolution of experimental data resulted in two individual peaks having maxima at 440 and 526 nm (Fig.4.50). An appearance of strongly red-shifted peak at 526 nm might be reasoned by the coupling effect of plasmon resonance of individual nanoparticles, closely packed into a lattice as it was shown on Figure 4.48.

Both the broadening and shift of SPR peaks maxima were attributed to a difference in spatial organisation of nanoparticles within thin film matrix before and

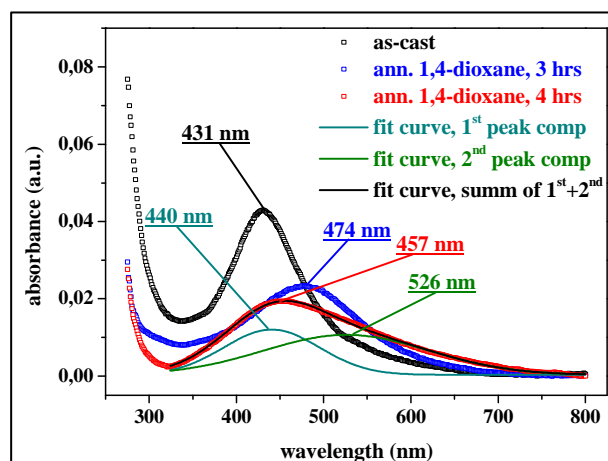


**Figure 4.50** UV-VIS spectra of as-cast and 1,4-dioxane annealed AgNP5/PS<sub>50</sub>-*b*-P2VP<sub>50</sub> composites containing 5 wt% of AgNP5. Initial film thickness  $\sim 50$  nm.

after vapour annealing. For as-cast samples nanoparticles appeared distributed randomly within BCP thin film, while 1,4-dioxane annealed samples were characterized by the presence of closely packed AgNP5 monolayers atop of the film surface (Fig.4.48 and Fig.4.49). Thus, reduced interparticles distances gave rise to a red shift of SPR peak,[Zhe02] while none-uniform particle distribution is reflected in a broadening of plasmon peak. From UV-VIS studies it is evident that for solvent annealed samples shift of SPR maxima becomes more significant with an increase of AgNP5 loading (e.g. 423 nm peak shifts to 432 nm for 2.0 wt% whereas 431 nm peak shifts to 475 nm for 5.0 wt%). This is attributed to an increase of particles fraction undergoing phase separation during solvent vapour annealing.

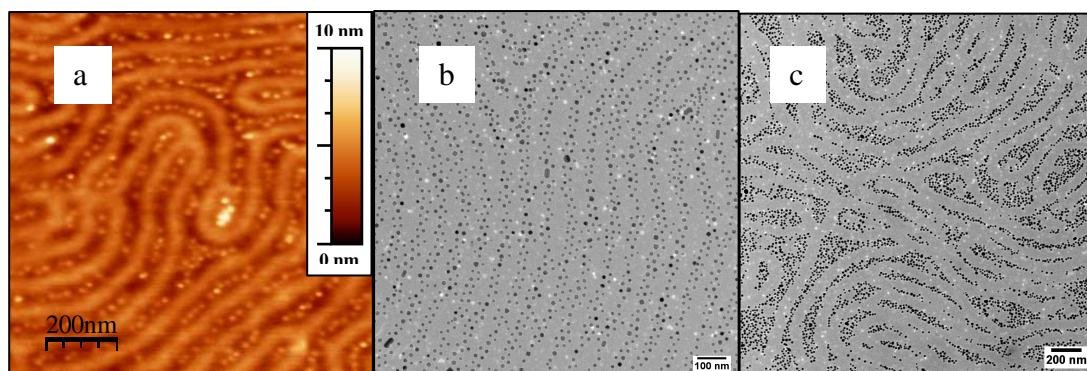


**Figure 4.51** AFM height (a) and TEM images (b,c) of 1,4-dioxane annealed AgNP6b/PS<sub>50</sub>-*b*-P2VP<sub>50</sub> composite thin films containing 5.0 (a,b) and 10.0 wt% of AgNP6b. Film thickness ~50 nm.

When AgNP6b, stabilized with longer PS chains (i.e. PSSH5,  $M_n=5300 \text{ g}\cdot\text{mol}^{-1}$ ), were used for preparation of AgNP/PS<sub>50</sub>-*b*-P2VP<sub>50</sub> composites instead of AgNP5 or AgNP6a, no evidence of particles macrophase segregation was detected after solvent annealing procedure. For up to 5.0 wt% of AgNP6b loading, regular lamellar structures with AgNP6b selectively arranged within PS phase were formed (Fig 4.51 a,b), while with further increase of AgNP6b loading (i.e. up to 10 wt%) formation of nonperiodic structures, strongly perturbed by the presence of nanoparticles, was observed (Fig 4.51 c).

Unlike AgNP5 and AgNP6a composites, AgNP6b did not form monolayer atop of film surface, but were trapped within PS microdomain, causing also their swelling within the regions of particles concentration (Fig 4.51 c).

UV-VIS studies of THF-cast AgNP6b/PS<sub>50</sub>-*b*-P2VP<sub>50</sub> composites thin films revealed small red shift of SPR peak with an increase of AgNP6b content (Fig 4.52 a),

similar to observed for AgNP5/PS<sub>50</sub>-*b*-P2VP<sub>50</sub> system. However, in contrast to

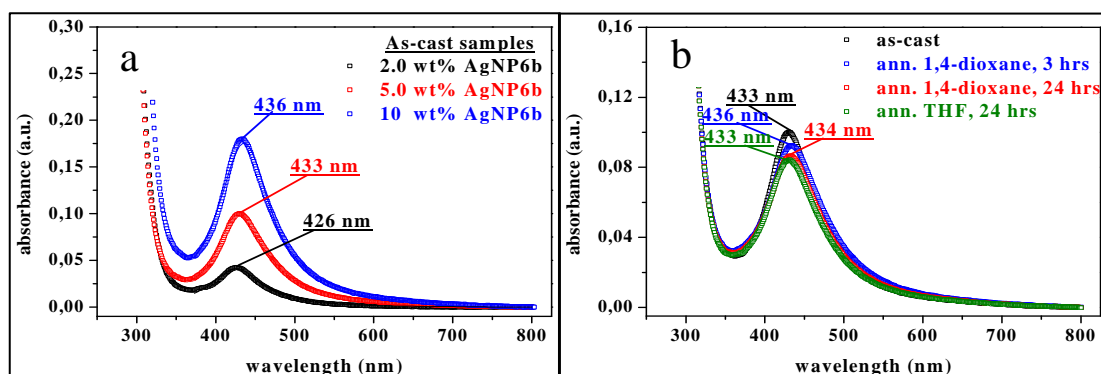


**Figure 4.52** UV-VIS spectra of THF-cast (a) and solvent annealed (b) AgNP6b/PS<sub>50</sub>-*b*-P2VP<sub>50</sub> composites thin films. For (b) all samples were loaded with 5.0 wt% of AgNP6b. Film thickness ~50 nm.

AgNP5/PS<sub>50</sub>-*b*-P2VP<sub>50</sub> system, position of SPR peak maxima after solvent vapour annealing in AgNP6b/PS<sub>50</sub>-*b*-P2VP<sub>50</sub> thin films remained almost the same as for as-cast samples, even when annealing time was increased up to 24 hours (Fig 4.52 a).

Such difference between AgNP5/PS<sub>50</sub>-*b*-P2VP<sub>50</sub> and AgNP6b/PS<sub>50</sub>-*b*-P2VP<sub>50</sub> composites behaviour during solvent annealing step is attributed to the effect of chain length of polystyrene molecules, which were used for nanoparticles surface modification. It is assumed, that in case of AgNP6b, the presence of PS shell formed from the longer-chain polymer molecules ( $M_n=5300 \text{ g}\cdot\text{mol}^{-1}$ ) ensures more effective particles compatibilization with polystyrene block of PS-*b*-P2VP BCP due to entanglement effects, compared to AgNP5 (or AgNP6a), stabilized with a short-chain PS shell ( $M_n=1100 \text{ g}\cdot\text{mol}^{-1}$ ).

To summarize, comparing the results obtained from the studies of MNP/PS-*b*-PVP and AgNP/PS-*b*-PVP composite systems certain similarities and diversities in nanoparticles assembling and phase segregation behaviour could be pointed out. For our opinion, it is obvious that appropriate nanoparticles surface functionality is crucial for their selective incorporation into particular microdomain of BCP matrix. Sufficiently strong enthalpic interactions between NPs and polymer host block, like in case of MNP3/PVP pair, allows to avoid macrophase segregation of nanoparticles during solvent annealing procedure. In this case entropic penalty due to reduced number of polymer chain conformations after accommodation of particulate inclusions could be overcome by energetically favourable MNP/PVP coordination. In

contrast, when only weak hydrophobic or Van der Waals interactions are involved to accommodate nanoparticles within host block, like in AgNP5/PS case, reduced stability of AgNP5 within PS phase is observed, resulting in nanoparticles macrophase segregation upon solvent vapour annealing. Phase segregation effect becomes more significant with an increase of particles loading rate and their core size (Fig. 4.47). However, it might be overcome by grafting of sufficiently long-chain polymer molecules to their surface that ensures nanoparticles stability within BCP matrix due to polymer entanglements, like in case of AgNP6b.





## 4.7 Fabrication of ternary NP1/NP2/BCP composites

### 4.7.1 Ternary NP1/NP2/PS-*b*-PVP composites by direct mixing approach

The final part of present work is devoted to the aim to fabricate ternary NP1/NP2/BCP composites composed of two different types of pre-synthesized nanoparticles selectively segregated within different block copolymer domains. As a first, supposable simplest way towards NP1/NP2/BCP hybrids preparation, direct mixing approach, which was based on simple mixing of two different kinds of nanoparticles with BCP in common solvent followed by composite thin film casting and annealing, was applied.

To obtain the ternary NP1/NP2/BCP composite system, MNP3 having distinct affinity towards PVP phase (NP1) and PS-coated AgNP5, which have been proved to selectively segregate into polystyrene microdomains (NP2), have been chosen. PS<sub>50</sub>-*b*-P2VP<sub>50</sub> was used as a block copolymer host matrix, while all steps of composites and thin films preparation and annealing were kept identical to previously described protocols applied for MNP3/PS<sub>50</sub>-*b*-P2VP<sub>50</sub> and AgNP5/PS<sub>50</sub>-*b*-P2VP<sub>50</sub> composites.

After thin film solvent annealing of MNP3/AgNP5/PS<sub>50</sub>-*b*-P2VP<sub>50</sub> in 1,4-dioxane vapour, the presence of nanoparticles was observed in either microdomain of lamellar BCP matrix (Fig. 4.53 a). From AFM height image (Fig. 4.53 a) it is evident that the grains (P2VP phase) are decorated with small clusters of nanoparticles, similar that was observed for MNP3/PS<sub>50</sub>-*b*-P2VP<sub>50</sub> composites (Fig. 4.53 b), while the grooves (PS phase) contained singularly dispersed particles, likewise in AgNP5/PS<sub>50</sub>-*b*-PVP<sub>50</sub> composite samples (Fig. 4.53 c).



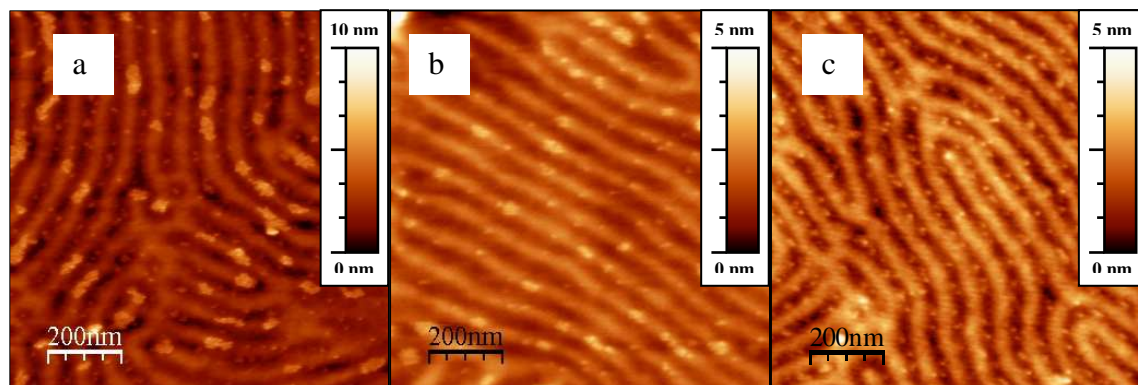


**Figure 4.53** AFM topography image of ternary MNP3/AgNP5/PS<sub>50</sub>-*b*-P2VP<sub>50</sub> (a) composite thin films (a) versus binary MNP3/PS<sub>50</sub>-*b*-P2VP<sub>50</sub> (b) and AgNP5/PS<sub>50</sub>-*b*-P2VP<sub>50</sub> (c) composites after annealing in 1,4-dioxane for 3 hours. Loading rate of each MNP3 and AgNP5 were 2.0 wt%. Film thickness ~50 nm.

From TEM images (Fig. 4.54) it could be also resolved the presence of both small particles clusters (i.e. MNP3), and uniformly distributed individual particles (i.e. AgNP5), oriented along the lamellar microdomain direction. Unfortunately, all attempts to resolve position of each type of nanoparticles using EELS and EDX methods were not successful due to sample drift and low resolution caused by charging effect (metal spattering was not implemented).

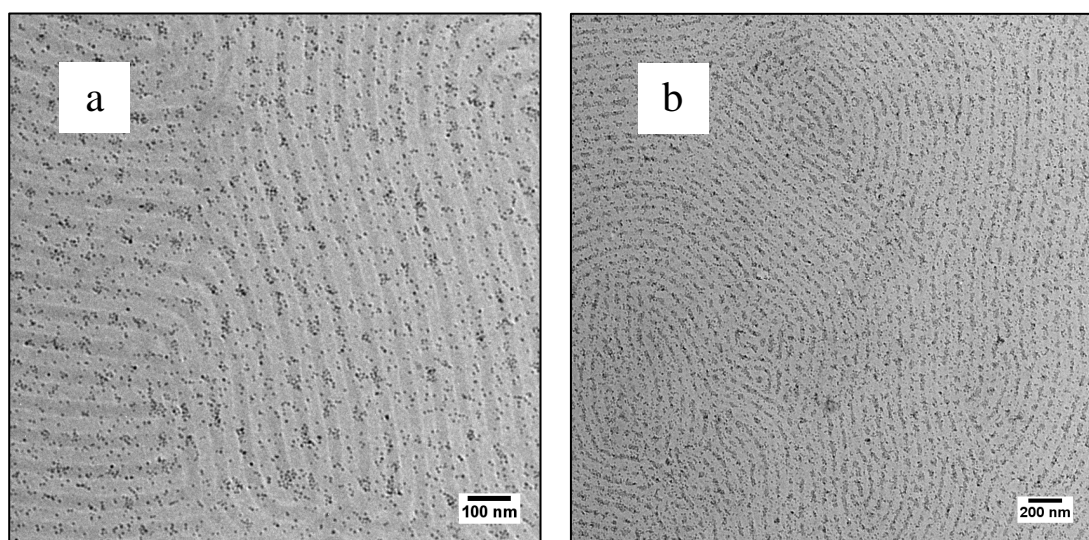


**Figure 4.54** TEM images of MNP3/AgNP5/PS<sub>50</sub>-*b*-P2VP<sub>50</sub> composite thin films after annealing in 1,4-dioxane for 3 hours, containing 2.0 wt% (a) and 10 wt% (b) of MNP3 and 2.0 wt% of AgNP5 (a,b). Image (a) was taken after sample staining with I<sub>2</sub> for 1 hour. Film thickness ~50 nm.

However, it was possible to prove (indirectly) that, indeed, different kinds of nanoparticles were selectively located in different phases by variation of content of one



of types of nanoparticles maintaining the second one constant. Figure 4.55 shows AFM phase images of ternary MNP3/AgNP5/PS<sub>50</sub>-*b*-P2VP<sub>50</sub> composites loaded with 2.0/2.0 wt% (a), 10.0/2.0 wt% (b) and 10.0/5.0 wt% (c) of MNP3/AgNP5, respectively. As it can be seen, with increase of MNP3 content from 2.0 to 10.0 wt%, perpendicular lamella appear progressively filled with particles, being at 10 wt% of MNP3 content almost fully loaded (Fig. 4.55 a and b, respectively). Similar tendency was previously observed for binary MNP3/PS<sub>50</sub>-*b*-P2VP<sub>50</sub> composite thin films (Fig. 4.28). But when the concentration of AgNP5 was increased from 2.0 to 5.0 wt% at MNP3 loading rate of 10 wt%, silver nanoparticles were found phase segregated atop of film surface, forming closely packed arrays, following the typical behaviour of AgNP5, maintaining P2VP domains filled up with MNP3 (Fig. 4.55 c).

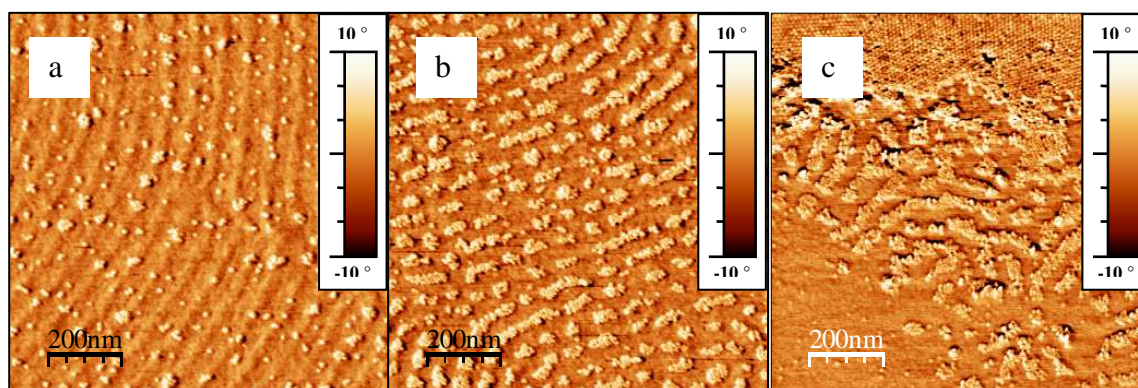


**Figure 4.55** AFM phase images of MNP3/AgNP5/PS<sub>50</sub>-*b*-P2VP<sub>50</sub> ternary composites with different content of nanoparticles: (a) – 2.0 wt% of MNP3 and 2.0 wt % of AgNP5; (b) – 10.0 wt % of MNP3 and 2.0 wt % of AgNP5; (c) – 10.0 wt % of MNP3 and 5.0 wt% of AgNP5. All samples were annealed in 1,4-dioxane for 3 hours. Film thickness ~50 nm.

To overcome the problem associated with nanoparticles phase separation with an increase of their loading rate, an application of AgNP stabilized with longer-chain PS molecules (e.g. AgNP6b) looks reasonable. In addition, with an application of larger size AgNP6b ( $d_{av}=12.8$  nm, which is twiced compared to 6.1 nm of MNP3) it might be possible to directly distinguish position of each type of nanoparticles within BCP matrix. Further investigations in this direction are currently in progress.

#### 4.7.2 Step-wise approach towards ternary NP1/NP2/BCP composites

Alternatively to direct mixing approach, step-wise approach was also used in present work to fabricate ternary NP1/NP2/BCP composites. Recently, very simple and robust way for fabrication of ordered arrays of noble metal nanodots and nanowires by direct nanoparticles deposition from their aqueous solutions over the preliminary formed P4VP domains of ordered PS-*b*-P4VP templates was published.[Nan09] In present work this method was extended and applied for fabrication of ternary NP1/NP2/BCP composites. Because of successive order of preparation procedure the method is pointed out as step-wise approach.

The approach includes several preparation steps, as schematically shown on Figure 4.56. At the first step, BCP was mixed with a primary-type of nanoparticles (NP1) in common solvent (THF) and deposited onto the substrate. NP1/BCP thin films were then annealed in solvent vapour in order to induce desired perpendicular orientation of microdomains. As a next step, obtained BCP patterns, containing NP1 particles were immersed into a water dispersion of secondary type of nanoparticles (NP2) for certain time. After exposure, samples were rinsed with deionized water and dried in nitrogen flow for further investigation.

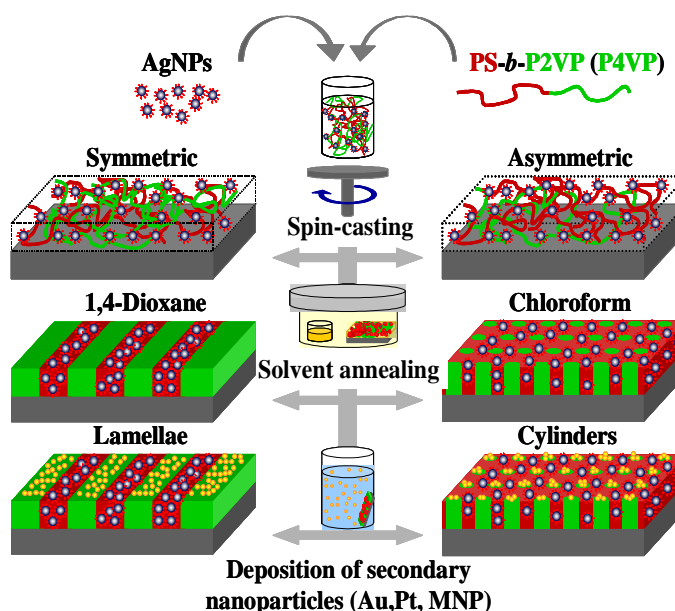


**Figure 4.56** Schematic representation of step-wise approach used for fabrication of ternary NP1/NP2/BCP composites.

For preparation of NP1/NP2/BCP composites, PS-coated silver nanoparticles, namely AgNP6b, were used as a primary type (NP1), while citrate-stabilized noble metals (Au, Pt, Pd) and Fe<sub>3</sub>O<sub>4</sub> nanoparticles were decided to use as secondary ones (NP2).

The water dispersions of noble metal nanoparticles for these experiments have been prepared and kindly provided by the group of Prof. A. Eychmüller, Technical University of Dresden. To synthesize gold, platinum and palladium nanoparticles with average particle diameter of  $3.5\pm 0.5$ ,  $2.5\pm 0.5$  and  $3.8\pm 0.5$  nm, respectively (further denoted as AuNPs, PtNPs and PdNPs), protocols similar to the synthetic route described by Brown et al.[Bro00] were applied. The details of nanoparticles preparation could be also found elsewhere.[Nan09]

Citric acid stabilized water-soluble  $\text{Fe}_3\text{O}_4$  MNPs were prepared by co-precipitation method, using  $\text{FeCl}_3$  and  $\text{FeCl}_2$  as iron precursors and ammonia hydroxide as precipitant, according to the protocol described elsewhere.[Rac05] From TEM studies (not shown here) the average size and polydispersity of  $\text{Fe}_3\text{O}_4$  nanoparticles obtained by co-precipitation method were found to be relatively large ( $d_{\text{av}} = 15.3$  nm,  $\text{SD} = 3.6$  nm or 23%) compare to MNP obtained by thermal decomposition method. Recently it was also shown that co-precipitation of Fe(II) and Fe(III) salts from their aqueous solutions under the influence of ultrasound power yields in smaller  $\text{Fe}_3\text{O}_4$  NPs with a narrow size distribution.[Mor08] Thus, the next batch of  $\text{Fe}_3\text{O}_4$  magnetic nanoparticles (denoted further MNP6) was prepared by co-precipitation reaction performed in the presence of ultrasound cavitations. Ultrasonic processor UP200S (200 W, 24kHz, Hielscher Ultrasonics GmbH, Germany) equipped with titanium sonotrod (tip diameter 3 mm) was used to generate cavitations. The sonotrod was immersed into acidified water solution (50 ml,  $\text{pH}=2.5$ ) containing the mixture of 5 mmol of  $\text{FeCl}_2$  and 10 mmol of  $\text{FeCl}_3$  salts through the tightly adjusted hole in Teflon cup. The mixture was purged with argon for 30 minutes and then heated to 80 °C. 10 ml of concentrated ammonium hydroxide aqueous solution (25 vol.%) was quickly injected into a ferric salt mixture under ultrasound agitation, resulting in a rapid formation of black product. The mixture was sonicated for next 10 minutes under gentle argon flow and then cooled to room temperature. Black precipitate was collected over the permanent magnet and washed three times with 50 ml of deoxygenated ethanol. In a next step, 1.5 g of citric acid dissolved in 50 ml of deionized and deoxygenated water was added to black precipitate. The mixture was heated to 80 °C and left under mechanical stirring for next 30 minutes. Finally, the major part of water was removed by evaporation on rotovapour and nanoparticles were flocculated and washed with acetone to remove excess of citric acid and dried in vacuum at 50 °C overnight.

Analysis of TEM images of MNP6 (Fig. 4.57) revealed an average nanoparticles size of  $6.5 \pm 1.4$  nm. However, in contrast to nanoparticles prepared by thermal decomposition route (e.g. MNP3), MNP6 appeared non-uniform in shape, namely, as a mixture of spherical and cubic-shaped particles, which is one of the main drawbacks of co-precipitation method.

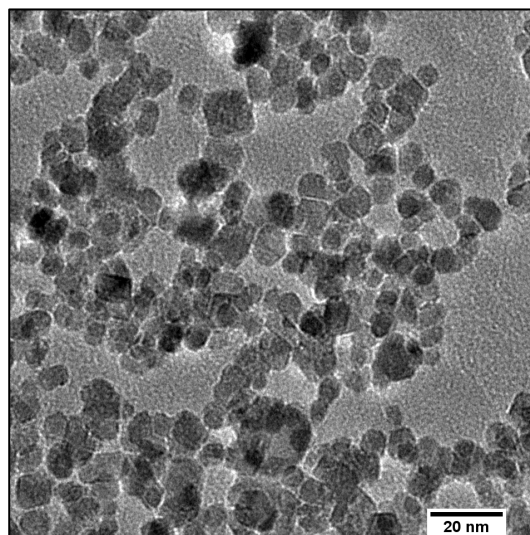


**Figure 4.57** TEM image of citric acid stabilized MNP6 prepared by co-precipitation method with application of ultrasound cavitations.

To prepare ternary NP1/NP2/BCP hybrids, AgNP6b/PS-*b*-PVP thin films were deposited onto the substrate and solvent annealed to give structures with BCP domains oriented normal to the substrate, as it was detailed in previous chapters. Afterwards, the substrates with AgNP6b/PS-*b*-PVP thin films were immersed into aqueous solutions of various types of NPs (secondary NP2) for their deposition.

For deposition of Fe<sub>3</sub>O<sub>4</sub> nanoparticles, pre-synthesized MNP6 were dispersed in deionized water to give NPs concentration 0.05 wt%. All other types of citrate-stabilized NPs (Au, Pt and Pd) were used in forms of their aqueous dispersions obtained directly during their syntheses. Before immersion of substrates, aqueous dispersions of secondary NPs were filtered through the hydrophilic 0.22 μm pore-

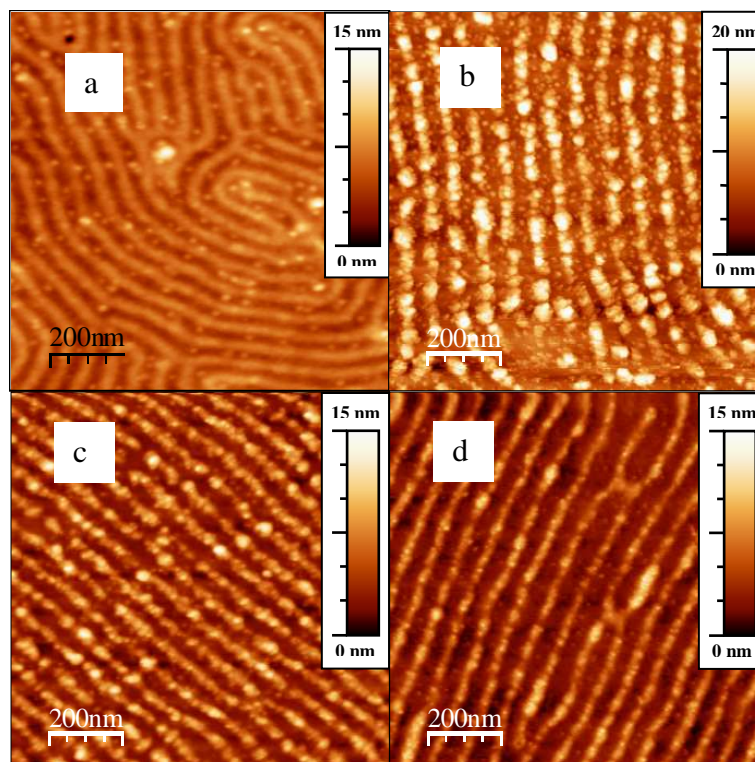


**Figure 4.58** AFM height images of 1,4-dioxane annealed AgNP6b/PS<sub>50</sub>-*b*-P2VP<sub>50</sub> composite thin films before (a) and after exposure to an aqueous solution of MNP6 (b), PtNP (c) and PdNPs (d) for 24 hours.



size membrane filter to remove the aggregates and particulate impurities.

AFM studies (Fig. 4.58) confirmed success of deposition step of second type of particles, as it was revealed from enhanced topography contrast of the samples before (Fig. 4.58 a) and after immersion into aqueous solution of various types of NPs (Fig. 4.58 b-d). However, due to the sharp topographic contrast after deposition of secondary NPs, it was difficult to resolve position of each type of nanoparticles with AFM: even so those secondary NPs were clearly observed as arranged along BCP microdomains, primary AgNP6b appeared hardly detectable. Nevertheless, owing to the difference in nanoparticles size, it was possible to distinguish between larger primary (AgNP6b) and smaller secondary (e.g. PdNP) nanoparticles by performing electron microscopy imaging of NP1/NP2/BCP composites.

SEM imaging of ternary composites gave the evidence of selectivity of nanoparticles location within individual domains (Fig. 4.59). Due to the difference in size between nanoparticles used, location of each type of NPs (e.g. AgNP6b or PdNP) could be clearly visualized on corresponding SEM image.

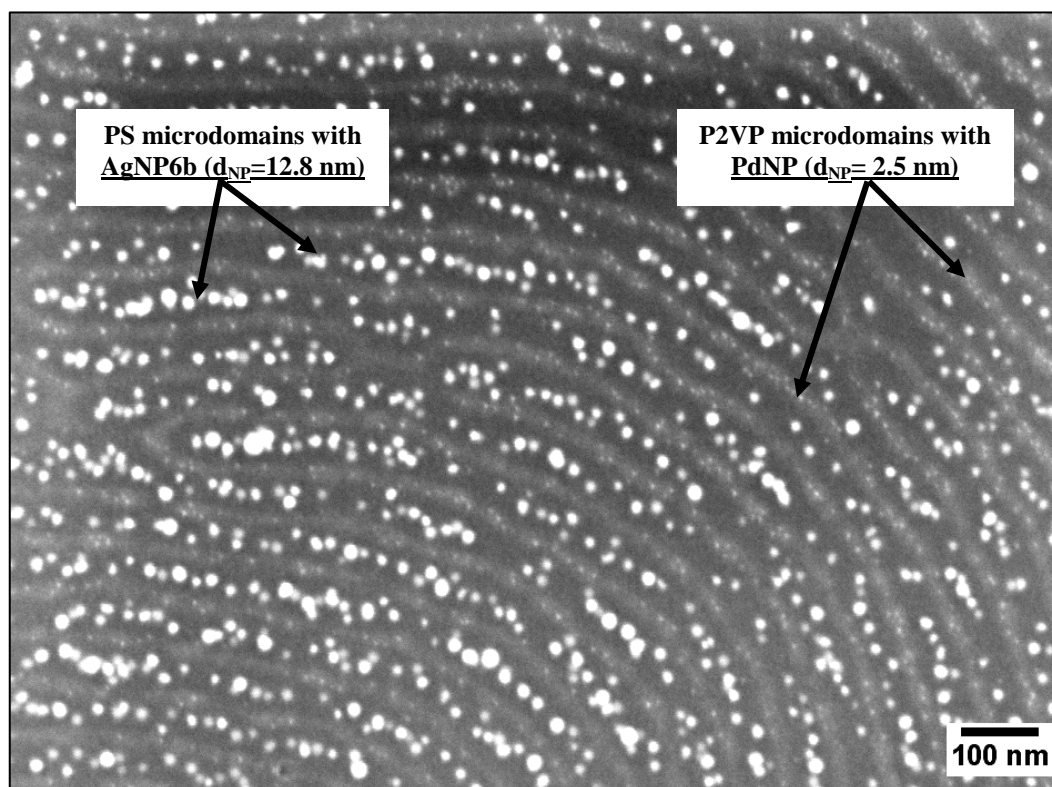


**Figure 4.59** SEM image of AgNP6b/PdNP/PS<sub>50</sub>-*b*-P2VP<sub>50</sub> ternary composite prepared by step-wise approach. Appearance of different types of NPs in different phases is evident due to the difference of NPs size.

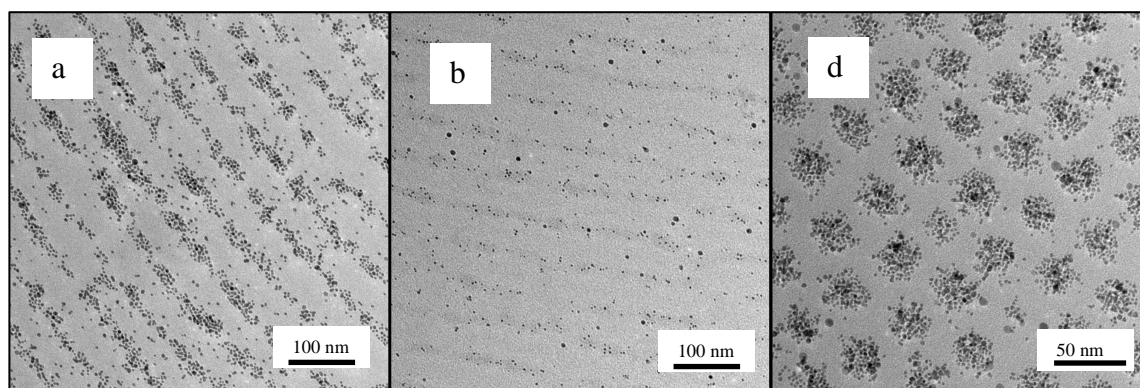


**Figure 4.60** TEM images of (a) AgNP6b/AuNP/PS<sub>50</sub>-*b*-P2VP<sub>50</sub>, (b) AgNP6b/PdNP/PS<sub>50</sub>-*b*-P2VP<sub>50</sub> and (c) AgNP6b/Pd/PS<sub>57</sub>-*b*-P4VP<sub>18</sub> ternary composites prepared using step-wise approach: AgNP6b content – 2.0 w%. Exposure time – 24 hours.

From AFM investigation it is obvious that after deposition of secondary NPs BCP domains appear highly loaded regardless of either type of NPs was used. Corresponding TEM images of composite films, etched from the substrate, however, show reduced content of nanoparticles remained after etching procedure (Fig. 4.60 b). Such dissimilarity, in our opinion, could be conditioned by etching procedure itself, which might affect particles stability within P2VP domain.

The best withstanding ability was observed for gold nanoparticles (Fig. 4.60 a), while only individual PdNPs (Fig. 4.60 b) and Fe<sub>3</sub>O<sub>4</sub> NPs (not shown) remained within BCP template after etching. The majority of secondary NP2 was, most probably, washed out during the contact with etching solution (1M NaOH). Position of pyridine nitrogen also influences on stability of citrate-stabilized NPs against washing. As it was expected, in contrast to PS-*b*-P2VP, for PS-*b*-P4VP BCP PdNPs remain densely filling the domains PVP domains even after etching as it could be observed on corresponding TEM image.(Fig. 4.60 c).

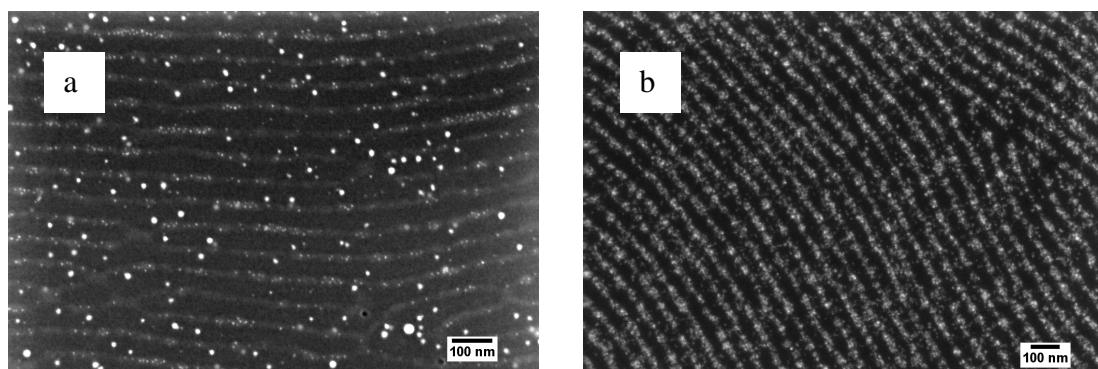


**Figure 4.61** SEM images of AgNP6b/AuNP/PS<sub>50</sub>-*b*-P2VP<sub>50</sub> ternary composites prepared by step-wise approach after (a) 60 minutes and (b) 24 hours of AuNPs deposition.

The amount of deposited secondary NPs could be also tuned by variation of deposition (exposure) time. Figure 61 shows SEM images of AgNP6b/AuNP/PS<sub>50-b</sub>-P2VP<sub>50</sub> ternary composites prepared varying the time of AuNP deposition.

As it was expected, UV-VIS spectra of ternary AgNP6b/AuNP/PS-*b*-P2VP composites display SPR peaks originated from both Ag and Au NPs (Fig.4.62). Since Au and Ag NPs display SPR maxima at different wavelength, they could be resolved as individual peaks: peak maxima of silver NPs were observed at 425-431 nm, while gold NPs absorb in a range of 520-560 nm for particular composites samples. With an

increase of AuNPs deposition time, position of maxima was observed to be gradually shifted from 524 nm (exposure time 60 min) to 558 nm (exposure time 24 hours), which was, most probably, reasoned by nanoparticles clustering.

On the other hand, position of AgNPs SPR peak was blue-shifted when AgNPs were deposited (i.e. from 431 nm for AgNP6b/PS<sub>50-b</sub>-P2VP<sub>50</sub> to 425-427 nm for AgNP6b/AuNP/PS<sub>50-b</sub>-P2VP<sub>50</sub>). However, no correlation between position of AgNPs SPR peak position and AuNPs deposition time was found. Therefore, at this point, it would be too unsubstantiated to argue that such blue shift of AgNPs SPR peak maxima is related solely to the presence of gold NPs in film structure.

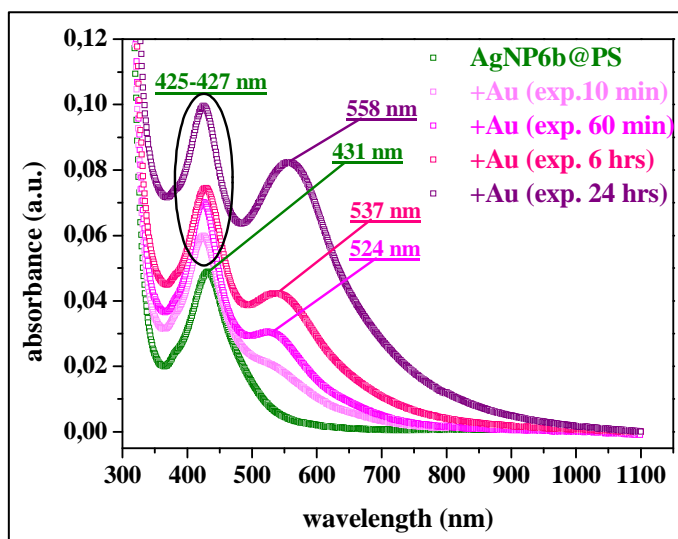


**Figure 4.62** UV-VIS spectra of binary AgNP6b/PS<sub>50-b</sub>-P2VP<sub>50</sub> and ternary AgNP6b/AuNP/PS<sub>50-b</sub>-P2VP<sub>50</sub> composite thin films prepared by step-wise approach. Spectra were recorder after different deposition time of gold NPs.





## Chapter 5 Conclusions and outlook

### 5.1 Conclusions

In present work, fabrication of ordered arrays of pre-synthesized nanoparticles (NPs) inside the block copolymers (BCP) thin films used as templates has been demonstrated. It was shown that self-assembling phenomena of BCPs could be exploited to fabricate both binary (i.e. NP/BCP) and ternary (i.e. NP1/NP2/BCP) nanocomposites containing nanoparticles selectively arranged within particular BCP microdomain. Different types of nanoparticles, such as magnetic  $\text{Fe}_3\text{O}_4$  or  $\text{CoFe}_2\text{O}_4$ , noble metal Ag, Au, Pt or Pd, have been used for preparation of nanocomposites.

For fabrication of NPs/BCP composites poly(styrene-*b*-vinylpyridine) (PS-*b*-PVP) block copolymers of various molecular weight and composition were used. This gave the opportunity to create BCP thin film structures with either lamellar or cylindrical morphologies. Coordinating ability of nitrogen in PVP blocks towards the surface of nanoparticles of various chemical nature was utilized to promote NPs selectively segregate inside the PVP domains. Alternatively, to provide the affinity of second type of NPs to the PS phase, polystyrene brush layer was grafted to their surface, supplying them compatibility with corresponding PS block of BCP.

The first task of present work was synthesis of ferrite type magnetic nanoparticles (MNPs), such as  $\text{Fe}_3\text{O}_4$  or  $\text{CoFe}_2\text{O}_4$ , suitable for their selective incorporation into polyvinylpyridine domains of PS-*b*-PVP BCP. To maximize the interactions between the iron oxide surface and PVP, it was required to obtain the MNPs surface accessible for such interaction, i.e. free from stabilizing molecules. On the other hand, the presence of the shell is required to avoid aggregation of the MNPs during nanocomposite preparation procedure. As was supposed, too densely grafted stabilizing shell might significantly screen the reactive surface of the MNPs, thus prohibiting their complexation with the PVP chains. It was suggested, therefore, that should be an optimum in the shell thickness and the shell nature for sufficient stabilization of the NPs without excessive screening of their surface.

Series of MNPs were synthesized by thermal decomposition of metal acetylacetonate precursors in presence of combination of various surfactants.

Depending on the type of surfactant used during nanoparticles synthesis, the nanoparticles appeared covered with organic layer of different nature and thickness.

Omitting of widely used oleic acid as stabilizing agent during MNP synthesis and application of TOPO/oleylamine as surfactants in combination with 1,2-hexadecanediol was found beneficial in terms of promoting interaction with PVP chains, whilst maintaining good control of MNPs size and polydispersity during their syntheses. Observed outstanding mutual affinity between PVP and MNPs was attributed to the formation of thinned, but still sufficient for particles stabilization organic shell. It was suggested that such thinned stabilizing layer allows the MNPs directly interact with the PVP chains due to the presence of some free binding sites available overall on the MNPs surface.

Consequently, prepared  $\text{Fe}_3\text{O}_4$  and  $\text{CoFe}_2\text{O}_4$  MNPs with sparse surfactant layer were successfully incorporated into lamellar and cylindrical PVP microdomains of PS-*b*-P2VP and PS-*b*-P4VP BCPs, displaying high degree of selectivity of MNPs location. From experimental results it was found that an efficiency of selective MNPs incorporation is dependent not only on the character and thickness of nanoparticles stabilizing shell, but also on the composition of BCP used. For example, it was possible to organize MNPs within lamellar structures of symmetric PS-*b*-P2VP, but failed in attempts to introduce them into cylinder-forming P2VP domains of asymmetric PS-*b*-P2VP having the shorter-chain P2VP block. Nevertheless, when asymmetric PS-*b*-P4VP of similar molecular weight and composition was used instead of PS-*b*-P2VP, MNPs were found being perfectly organized within P4VP cylinders. Such difference in results observed for similar molecular weight asymmetric PS-*b*-P2VP and PS-*b*-P4VP BCPs can be rationalized in terms of different binding ability of P2VP and P4VP blocks. In P2VP the nitrogen atoms in the 2VP units placed in “ortho”-position and, hence, they are not readily available for any physical interactions due to steric factors. In contrast, in P4VP chains, where nitrogen is located in “para”-position, pyridine units do not have such constrains and thus could more effectively interact with nanoparticles surface.

To achieve desired microdomain orientation and lateral ordering of both neat and loaded with nanoparticles BCPs, solvent vapour annealing was applied. An application of so called “slow” annealing procedure gave the possibility to create an arrays of well ordered hexagonally packed cylindrical PVP microdomains oriented normal to the substrate over relatively large sample areas (more than 4 sq  $\mu\text{m}$ ). Moreover, an

incorporation of MNPs did not alter the ability of BCPs to form highly ordered hexagonal structures, which is important prerequisite for their possible applications, for example in data storage.

As a second type of nanoparticles for fabrication of ternary NP1/NP2/BCP composites, with aim to be selectively incorporated into a polystyrene microdomains of PS-*b*-PVP matrix, silver nanoparticles (AgNPs) of various size and narrow size distribution were chosen. The suitable AgNPs were prepared using one-pot synthesis, which was based on mild reduction of silver precursor with oleylamine in organic medium. One of the ways to ensure selectivity of AgNPs towards PS is covering them with stabilizing shell composed of polystyrene molecules. For this purpose, polystyrene brush layer was grafted to the surface of AgNPs using ligand-exchange reaction with thiol-terminated polystyrene homopolymer. It was shown that PS brushes with high grafting density (i.e.  $\sim 3\text{-}4$  chains  $\text{nm}^{-2}$  depending on particles size), which were successfully formed on the AgNPs surface effectively prevent them from possible coordination with PVP, enabling simultaneously their selective incorporation into polystyrene phase.

Although PS-covered AgNPs appeared preferentially located within polystyrene phase of microphase separated PS-*b*-PVP matrix, in contrast to MNP/PS-*b*-PVP system, with an increase of AgNPs loading, they displayed a tendency to segregate atop of BCP film surface. Moreover, AgNPs revealed propensity to be localized along the edges of hole-like defects formed on BCP film surface upon prolonged solvent annealing. The reason of such diversity in phase behaviour of MNPs and AgNPs could be explained as resulted from difference in enthalpic interaction contributions involved required for accommodation of each type of NPs within corresponding block of BCP matrix.

Revealed ability of nanoparticles to macrophase segregation forming in the process ring-like structures of hexagonally packed nanoparticles monolayer, which is undesired for preparation of highly-loaded AgNP/BCP composites, might be interesting for other applications, for example, for fabrication of two-dimensional metal structures of regular shape and size on substrate surface. In this direction, further investigations are in progress.

Preparation of NP/BCP composites having two kinds of nanoparticles selectively segregated within different BCP microdomains was pointed out as a next task of current work. To the best of our knowledge, as for today only few reports of successful fabrication of such ternary NP1/NP2/BCP composites are presented in literature.

Direct mixing approach was used first to obtain MNP/AgNP/BCP composite. Here the both MNP and AgNP were directly mixed with PS-*b*-PVP BCP in organic solvent and deposited onto the substrate. It was observed that, indeed, after solvent vapour annealing MNPs appeared localized inside PVP domains, while silver NPs were found in PS phase of PS-*b*-PVP BCP.

As a second strategy for fabrication of ternary NP1/NP2/BCP composite, so-called step-wise approach was used. In this method, incorporation of each kind of NPs was performed in a separate step. Initially, AgNPs (NP1) covered with polystyrene brush layer, were mixed with PS-*b*-PVP in solution and deposited onto the substrate. After subsequent solvent annealing, such substrates with perpendicularly oriented BCP microdomains and having AgNPs selectively localized within polystyrene phase, were immersed into aqueous solution of second type of nanoparticles (Au, Pt, Pd or Fe<sub>3</sub>O<sub>4</sub>) stabilized with citrate ions. Such exposure led to selective NP2 deposition into PVP.

## 5.2 Outlook

Future developments in preparation and investigation of both binary NP/BCP and ternary NP1/NP2/BCP could be performed in several directions. In particular, for MNP/BCP systems it would be interesting to study the possibility of incorporation into hexagonally organized PVP microdomains of magnetic NPs, such as FePt or CoPt<sub>3</sub>, which could be transformed from superparamagnetic *fcc* phase to ferromagnetic L1<sub>0</sub> crystals upon thermal annealing step. If such thermal annealing will be performed after removal or carbonization of BCP matrix, it would lead to preserved lateral order of nanostructures on the surface. Alternatively, fabrication of perpendicularly oriented arrays of magnetic nanorods, which possess magnetic shape anisotropy with easy magnetization long axis, is of interest. Both above mentioned structures would be attractive for application in magnetic data storage devices.

Another aspect of investigation possibilities of MNP/BCP systems is related to microdomain reorientation in the presence of magnetic field during solvent annealing. For this purpose, further studies of thicker films and bulk samples are required.

Concerning AgNP/BCP system, further studies of nanoparticles macrophase segregation behaviour, in particular, formation of ring-shaped 2D structures of nanoparticles assemblies along the defect edges, is of particular interest. Since this

effect is dependent among others on annealing time, the kinetic aspect of such phenomena might give a chance to control the number and size of such self-assembled structures. The effect of substrate nature, NP/BCP composite film thickness and chain length of polymer, which stabilizes nanoparticles, are also interesting for evaluation for better understanding of main factors, responsible for particles macrophase segregation atop of thin films or their ability to remain stable within BCP matrix.

We believe, that presented and discussed above experimental results on both MNP/BCP and AgNP/BCP composites, as well as on ternary NP1/NP2/BCP hybrids, provide useful information for better understanding block copolymer based nanocomposites in terms of their preparation and prognostication of their behavior under various conditions.



## Chapter 6 List of references

- [Abe00] Abetz, V.; Goldacker, T. Formation of superlattices via blending of block copolymers *Macromol. Rapid Comm.* **2000**, *21*, 16-34.
- [Abe03a] Abes, J. I.; Cohen, R. E.; Ross, C. A. Selective growth of cobalt nanoclusters in domains of block copolymer films *Chem. Mater.* **2003**, *15*, 1125-1131.
- [Abe03b] Abes, J. I.; Cohen, R. E.; Ross, C. A. Block-copolymer-templated synthesis of iron, iron-cobalt, and cobalt-nickel alloy nanoparticles *Mat. Sci. Eng. C-Bio S.* **2003**, *23*, 641-650.
- [Ach09] Acharya, H.; Sung, J.; Sohn, B. H.; Kim, D. H.; Tamada, K.; Park, C. Tunable surface plasmon band of position selective Ag and Au nanoparticles in thin block copolymer micelle films *Chem. Mater.* **2009**, *21*, 4248-4255.
- [Aiz05] Aizpurua, J.; Bryant, G. W.; Richter, L. J.; de Abajo, F. J. G.; Kelley, B. K.; Mallouk, T. Optical properties of coupled metallic nanorods for field-enhanced spectroscopy *Phys. Rev. B* **2005**, *71*, 235420.
- [Alb10] Albert, J. N. L.; Epps, T. H. Self-assembly of block copolymer thin films *Mater.Today* **2010**, *13*, 24-33.
- [Amu91] Amundson, K.; Helfand, E.; Davis, D. D.; Quan, X.; Patel, S. S.; Smith, S. D. Effect of an electric-field on block copolymer microstructure *Macromolecules* **1991**, *24*, 6546-6548.
- [Amu93] Amundson, K.; Helfand, E.; Quan, X.; Smith, S. D. Alignment of lamellar block copolymer microstructure in an electric field. 1. Alignment kinetics *Macromolecules* **1993**, *26*, 2698-2703.
- [Amu94] Amundson, K.; Helfand, E.; Quan, X. N.; Hudson, S. D.; Smith, S. D. Alignment of lamellar block copolymer microstructure in an electric field. 2. Mechanism of alignment *Macromolecules* **1994**, *27*, 6559-6570.
- [Auz99] Auzans, E.; Zins, D.; Blums, E.; Massart, R. Synthesis and properties of Mn-Zn ferrite ferrofluids *J. Mater. Sci.* **1999**, *34*, 1253-1260.
- [Bal03] Balazs, A. C. Predicting the morphology of nanostructured composites *Curr. Opin. Solid St. M.* **2003**, *7*, 27-33.
- [Bal06] Balazs, A. C.; Emrick, T.; Russell, T. P. Nanoparticle polymer composites: Where two small worlds meet *Science* **2006**, *314*, 1107-1110.
- [Ban09] Bang, J.; Jeong, U.; Ryu, D. Y.; Russell, T. P.; Hawker, C. J. Block copolymer nanolithography: Translation of molecular level control to nanoscale patterns *Adv. Mater.* **2009**, *21*, 4769-4792.
- [Bat90] Bates, F. S.; Fredrickson, G. H. Block copolymer thermodynamics - theory and experiment *Annu. Rev. Phys. Chem.* **1990**, *41*, 525-557.
- [Bat94] Bates, F. S.; Schulz, M. F.; Khandpur, A. K.; Forster, S.; Rosedale, J. H.; Almdal, K.; Mortensen, K. Fluctuation, conformational asymmetry and block copolymer phase behavior *Faraday Discuss.* **1994**, *98*, 7-18.
- [Bea55] Bean, C. P. Hysteresis loops of mixtures of ferromagnetic micropowders *J. Appl. Phys.* **1955**, *26*, 1381-1383.
- [Bee95] Bee, A.; Massart, R.; Neveu, S. Synthesis of very fine maghemite particles *J. Magn. Mater.* **1995**, *149*, 6-9.
- [Bin86] Binnig, G.; Quate, C. F.; Gerber, C. Atomic force microscope *Phys. Rev. Lett.* **1986**, *56*, 930-933.
- [Bin08] Binder, W. H.; Weinstabl, H.; Sachsenhofer, R. Superparamagnetic iron oxide nanoparticles via ligand exchange reactions: Organic 1,2-diols as versatile building blocks for surface engineering *J. Nanomater.* **2008**, 383020.

- [Boc03] Bockstaller, M. R.; Lapetnikov, Y.; Margel, S.; Thomas, E. L. Size-selective organization of enthalpic compatibilized nanocrystals in ternary block copolymer/particle mixtures *J. Am. Chem. Soc.* **2003**, *125*, 5276-5277.
- [Boc05] Bockstaller, M. R.; Mickiewicz, R. A.; Thomas, E. L. Block copolymer nanocomposites: Perspectives for tailored functional materials *Adv. Mater.* **2005**, *17*, 1331-1349.
- [Boh10] Bohme, M.; Kuila, B.; Schlorb, H.; Nandan, B.; Stamm, M. Thin films of block copolymer supramolecular assemblies: Microphase separation and nanofabrication *Phys. Status Solidi B-Basic Solid State Phys.* **2010**, *247*, 2458-2469.
- [Bok02a] Boker, A.; Knoll, A.; Elbs, H.; Abetz, V.; Muller, A. H. E.; Krausch, G. Large scale domain alignment of a block copolymer from solution using electric fields *Macromolecules* **2002**, *35*, 1319-1325.
- [Bok02b] Boker, A.; Elbs, H.; Hansel, H.; Knoll, A.; Ludwigs, S.; Zettl, H.; Urban, V.; Abetz, V.; Muller, A. H. E.; Krausch, G. Microscopic mechanisms of electric-field-induced alignment of block copolymer microdomains *Phys. Rev. Lett.* **2002**, *89*, 135502.
- [Bre04] Breeze, A. J.; Schlesinger, Z.; Carter, S. A.; Tillmann, H.; Horhold, H. H. Improving power efficiencies in polymer - polymer blend photovoltaics *Sol. Energ. Mater.* **2004**, *83*, 263-271.
- [Bro00] Brown, K. R.; Walter, D. G.; Natan, M. J. Seeding of colloidal Au nanoparticle solutions. 2. Improved control of particle size and shape *Chem. Mater.* **2000**, *12*, 306-313.
- [Bru94] Brust, M.; Walker, M.; Bethell, D.; Schiffrin, D. J.; Whyman, R. Synthesis of thiol-derivatized gold nanoparticles in a 2-phase liquid-liquid system *J. Chem. Soc. Chem. Comm.* **1994**, 801-802.
- [Cam98] Campion, A.; Kambhampati, P. Surface-enhanced Raman scattering *Chem. Soc. Rev.* **1998**, *27*, 241-250.
- [Cap04] Capek, I. Preparation of metal nanoparticles in water-in-oil (w/o) microemulsions *Adv. Colloid Interfac.* **2004**, *110*, 49-74.
- [Car07] Caruntu, D.; Caruntu, G.; O'Connor, C. J. Magnetic properties of variable-sized Fe<sub>3</sub>O<sub>4</sub> nanoparticles synthesized from non-aqueous homogeneous solutions of polyols *J. Phys. D: Appl. Phys.* **2007**, *40*, 5801-5809.
- [Car08] Caragheorghopol, A.; Chechik, V. Mechanistic aspects of ligand exchange in Au nanoparticles *Phys. Chem. Chem. Phys.* **2008**, *10*, 5029-5041.
- [Cha92a] Chan, Y. N. C.; Craig, G. S. W.; Schrock, R. R.; Cohen, R. E. Synthesis of palladium and platinum nanoclusters within microphase-separated diblock copolymers *Chem. Mater.* **1992**, *4*, 885-894.
- [Cha92b] Chan, Y. N. C.; Schrock, R. R.; Cohen, R. E. Synthesis of silver and gold nanoclusters within microphase-separated diblock copolymers *Chem. Mater.* **1992**, *4*, 24-27.
- [Cha07] Chai, J.; Wang, D.; Fan, X. N.; Buriak, J. M. Assembly of aligned linear metallic patterns on silicon *Nat. Nanotechnol.* **2007**, *2*, 500-506.
- [Cha08] Chai, J.; Buriak, J. M. Using cylindrical domains of block copolymers to self-assemble and align metallic nanowires *ACS Nano* **2008**, *2*, 489-501.
- [Che01] Chen, D. H.; He, X. R. Synthesis of nickel ferrite nanoparticles by sol-gel method *Mater. Res. Bull.* **2001**, *36*, 1369-1377.
- [Che02] Chen, M.; Nikles, D. E. Synthesis of spherical FePd and CoPt nanoparticles *J. Appl. Phys.* **2002**, *91*, 8477-8479.



- [Che06] Cheng, J. Y.; Ross, C. A.; Smith, H. I.; Thomas, E. L. Templated self-assembly of block copolymers: Top-down helps bottom-up *Adv. Mater.* **2006**, *18*, 2505-2521.
- [Chi03] Chinnasamy, C. N.; Senoue, M.; Jeyadevan, B.; Perales-Perez, O.; Shinoda, K.; Tohji, K. Synthesis of size-controlled cobalt ferrite particles with high coercivity and squareness ratio *J. Colloid Interf. Sci.* **2003**, *263*, 80-83.
- [Chi05] Chiu, J. J.; Kim, B. J.; Kramer, E. J.; Pine, D. J. Control of nanoparticle location in block copolymers *J. Am. Chem. Soc.* **2005**, *127*, 5036-5037.
- [Con99] O'Connor, C. J.; Seip, C. T.; Carpenter, E. E.; Li, S. C.; John, V. T. Synthesis and reactivity of nanophase ferrites in reverse micellar solutions *Nanostruct. Mater.* **1999**, *12*, 65-70.
- [Cor04] Corbierre, M. K.; Cameron, N. S.; Lennox, R. B. Polymer-stabilized gold nanoparticles with high grafting densities *Langmuir* **2004**, *20*, 2867-2873.
- [Cro09] Crossland, E. J. W.; Kamperman, M.; Nedelcu, M.; Ducati, C.; Wiesner, U.; Smilgies, D. M.; Toombes, G. E. S.; Hillmyer, M. A.; Ludwigs, S.; Steiner, U.; Snaith, H. J. A bicontinuous double gyroid hybrid solar cell *Nano Lett.* **2009**, *9*, 2807-2812.
- [Cul09] Cullity, B. D.; Graham, C. D. Introduction to magnetic materials. *2nd ed.*; Wiley: **2009**, 544 p.
- [Dar07] Darling, S. B. Directing the self-assembly of block copolymers *Prog. Polym. Sci.* **2007**, *32*, 1152-1204.
- [Den02] Dennis, C. L.; Borges, R. P.; Buda, L. D.; Ebels, U.; Gregg, J. F.; Hehn, M.; Jouguelet, E.; Ounadjela, K.; Petej, I.; Prejbeanu, I. L.; Thornton, M. J. The defining length scales of mesomagnetism: A review *J. Phys.-Condens. Mat.* **2002**, *14*, R1175-R1262.
- [Den05] Deng, H.; Li, X. L.; Peng, Q.; Wang, X.; Chen, J. P.; Li, Y. D. Monodisperse magnetic single-crystal ferrite microspheres *Angew. Chem. Int. Ed.* **2005**, *44*, 2782-2785.
- [Des07] Deshmukh, R. D.; Buxton, G. A.; Clarke, N.; Composto, R. J. Nanoscale block copolymer templates decorated by nanoparticle arrays *Macromolecules* **2007**, *40*, 6316-6324.
- [Don09] Dong, X. Y.; Ji, X. H.; Wu, H. L.; Zhao, L. L.; Li, J.; Yang, W. S. Shape control of silver nanoparticles by stepwise citrate reduction *J. Phys. Chem. C* **2009**, *113*, 6573-6576.
- [Ebb04] Ebbesen, T. W.; Lezec, H. J.; Ghaemi, H. F.; Thio, T.; Wolff, P. A. Extraordinary optical transmission through sub-wavelength hole arrays *Nature* **1998**, *391*, 667-669.
- [Edw04] Edwards, E. W.; Montague, M. F.; Solak, H. H.; Hawker, C. J.; Nealey, P. F. Precise control over molecular dimensions of block-copolymer domains using the interfacial energy of chemically nanopatterned substrates *Adv. Mater.* **2004**, *16*, 1315-1319.
- [Edw06] Edwards, E. W.; Stoykovich, M. P.; Solak, H. H.; Nealey, P. F. Long-range order and orientation of cylinder-forming block copolymers on chemically nanopatterned striped surfaces *Macromolecules* **2006**, *39*, 3598-3607.
- [Eus06] Eustis, S.; El-Sayed, M. A. Why gold nanoparticles are more precious than pretty gold: Noble metal surface plasmon resonance and its enhancement of the radiative and nonradiative properties of nanocrystals of different shapes *Chem. Soc. Rev.* **2006**, *35*, 209-217.

- [Eva04] Evanoff, D. D.; Chumanov, G. Size-controlled synthesis of nanoparticles. 2. Measurement of extinction, scattering, and absorption cross sections *J. Phys. Chem. B* **2004**, *108*, 13957-13962.
- [Eva05] Evanoff, D. D.; Chumanov, G. Synthesis and optical properties of silver nanoparticles and arrays *Chemphyschem* **2005**, *6*, 1221-1231.
- [Fan05] Fang, N.; Lee, H.; Sun, C.; Zhang, X. Sub-diffraction-limited optical imaging with a silver superlens *Science* **2005**, *308*, 534-537.
- [Far57] Faraday, M. Experimental relations of gold (and other metals) to light *Philos. T. R. Soc.* **1857**, *147*, 145-181.
- [Fas00] Faselka, M. J.; Banerjee, P.; Mayes, A. M.; Pickett, G.; Balazs, A. C. Morphology of ultrathin supported diblock copolymer films: Theory and experiment *Macromolecules* **2000**, *33*, 5702-5712.
- [Fas01] Faselka, M. J.; Mayes, A. M. Block copolymer thin films: Physics and applications *Annu. Rev. Mat. Res.* **2001**, *31*, 323-355.
- [Flo41] Flory, P. J. Thermodynamics of high polymer solutions *J. Chem. Phys.* **1941**, *9*, 660-661.
- [Flo42] Flory, P. I. Thermodynamics of high polymer solutions *J. Chem. Phys.* **1942**, *10*, 51-61.
- [Flo01] Floudas, G.; Vazaiou, B.; Schipper, F.; Ulrich, R.; Wiesner, U.; Iatrou, H.; Hadjichristidis, N. Poly(ethylene oxide-*b*-isoprene) diblock copolymer phase diagram *Macromolecules* **2001**, *34*, 2947-2957.
- [For98] Forster, S.; Antonietti, M. Amphiphilic block copolymers in structure-controlled nanomaterial hybrids *Adv. Mater.* **1998**, *10*, 195-217.
- [Fre30] Frenkel, J.; Dorfman, J. Spontaneous and induced magnetisation in ferromagnetic bodies *Nature* **1930**, *126*, 274-275
- [Fre96] Fredrickson, G. H.; Bates, F. S. Dynamics of block copolymers: Theory and experiment *Annu. Rev. Mat. Sci.* **1996**, *26*, 501-550.
- [Fre09] Frey, N. A.; Peng, S.; Cheng, K.; Sun, S. H. Magnetic nanoparticles: synthesis, functionalization, and applications in bioimaging and magnetic energy storage *Chem. Soc. Rev.* **2009**, *38*, 2532-2542.
- [Fuc75] Fuchs, R. Theory of optical properties of ionic crystal cubes *Phys. Rev. B* **1975**, *11*, 1732-1739.
- [Fuk00] Fukunaga, K.; Elbs, H.; Magerle, R.; Krausch, G. Large-scale alignment of ABC block copolymer microdomains via solvent vapor treatment *Macromolecules* **2000**, *33*, 947-953.
- [Fuk10] Fukushima, Y.; Yamaguchi, Y.; Kimura, T.; Iguchi, T.; Harada, T.; Watanabe, T.; Kinoshita, H. EUV interference lithography for 22 nm node and below *J. Photopolym. Sci. Tec.* **2010**, *23*, 673-680.
- [Gan10] Ganguli, A. K.; Ganguly, A.; Vaidya, S. Microemulsion-based synthesis of nanocrystalline materials *Chem. Soc. Rev.* **2010**, *39*, 474-485.
- [Gao06] Gao, H. W.; Henzie, J.; Odom, T. W. Direct evidence for surface plasmon-mediated enhanced light transmission through metallic nanohole arrays *Nano Lett.* **2006**, *6*, 2104-2108.
- [Gar07a] Garcia, I.; Tercjak, A.; Zafeiropoulos, N. E.; Stamm, M.; Mondragon, I. Self-assembling nanomaterials using magnetic nanoparticles modified with polystyrene brushes *Macromol. Rapid Comm.* **2007**, *28*, 2361-2365.
- [Gar07b] Garcia, I.; Tercjak, A.; Zafeiropoulos, N. E.; Stamm, M.; Mondragon, I. Generation of core/shell iron oxide magnetic nanoparticles with polystyrene brushes by atom transfer radical polymerization *J. Polym. Sci. Pol. Chem.* **2007**, *45*, 4744-4750.

- [Gar08] Garcia, I.; Tercjak, A.; Gutierrez, J.; Rueda, L.; Mondragon, I. Nanostructuring via solvent vapor exposure of poly(2-vinyl pyridine-*b*-methyl methacrylate) nanocomposites using modified magnetic nanoparticles *J. Phys. Chem. C* **2008**, *112*, 14343-14347.
- [Gei99a] Geisinger, T.; Muller, M.; Binder, K. Symmetric diblock copolymers in thin films. I. Phase stability in self-consistent field calculations and Monte Carlo simulations *J. Chem. Phys.* **1999**, *111*, 5241-5250.
- [Gei99b] Geisinger, T.; Muller, M.; Binder, K. Symmetric diblock copolymers in thin films. II. Comparison of profiles between self-consistent field calculations and Monte Carlo simulations *J. Chem. Phys.* **1999**, *111*, 5251-5258.
- [Get08] Getzlaff, M. Fundamentals of Magnetism. *Springer*: **2008**, 387 p.
- [Gid93] Gido, S. P.; Gunther, J.; Thomas, E. L.; Hoffman, D. Lamellar diblock copolymer grain-boundary morphology. 1. Twist boundary characterization *Macromolecules* **1993**, *26*, 4506-4520.
- [Gid94] Gido, S. P.; Thomas, E. L. Lamellar diblock copolymer grain-boundary morphology. 4. Tilt boundaries *Macromolecules* **1994**, *27*, 6137-6144.
- [Gid97] Gido, S. P.; Thomas, E. L. Lamellar diblock copolymer grain-boundary morphology. 4. Tilt boundaries *Macromolecules* **1994**, *27*, 6137-6144.
- [Gom09] Gomez, M.; Nogales, A.; Garcia-Gutierrez, M. C.; Ezquerra, T. A.; Müller-Buschbaum, P. A Basic Introduction to Grazing Incidence Small-Angle X-Ray Scattering. In Applications of Synchrotron Light to Scattering and Diffraction in Materials and Life Sciences, *Springer Berlin / Heidelberg*: **2009**, Vol. 776, pp 61-89.
- [Gow10] Gowd, E. B.; Nandan, B.; Bigall, N. C.; Eychmuller, A.; Formanek, P.; Stamm, M. Hexagonally ordered arrays of metallic nanodots from thin films of functional block copolymers *Polymer* **2010**, *51*, 2661-2667.
- [Gra06] Grason, G. M. The packing of soft materials: Molecular asymmetry, geometric frustration and optimal lattices in block copolymer melts *Phys. Rep.* **2006**, *433*, 1-64.
- [Gri05] Grigorova, T.; Pispas, S.; Hadjichristidis, N.; Thurn-Albrecht, T. Magnetic field induced orientation in diblock copolymers with one crystallizable block *Macromolecules* **2005**, *38*, 7430-7433.
- [Gri07] Griffiths, P. R.; De Haseth, J.A. Fourier Transform Infrared Spectrometry. *Wiley-Interscience*: **2007**, 529 p.
- [Gri09] Grigorescu, A. E.; Hagen, C. W. Resists for sub-20-nm electron beam lithography with a focus on HSQ: State of the art *Nanotechnology* **2009**, *20*, 292001.
- [Gro98] Groot, R. D.; Madden, T. J. Dynamic simulation of diblock copolymer microphase separation *J. Chem. Phys.* **1998**, *108*, 8713-8724.
- [Gru07] Grubbs, R. B. Roles of polymer ligands in nanoparticle stabilization *Polym. Rev.* **2007**, *47*, 197-215.
- [Gup96] Gupta, V. K.; Krishnamoorti, R.; Kornfield, J. A.; Smith, S. D. Role of strain in controlling lamellar orientation during flow alignment of diblock copolymers *Macromolecules* **1996**, *29*, 1359-1362.
- [Gup05] Gupta, A. K.; Gupta, M. Synthesis and surface engineering of iron oxide nanoparticles for biomedical applications *Biomaterials* **2005**, *26*, 3995-4021.
- [Had03] Hadjichristidis, N.; Pispas, S.; Floudas, G. Block copolymers: Synthetic strategies, physical properties, and applications. *John Wiley and Sons*: **2003**, 419 p.
- [Hah00] Hahn, J.; Sibener, S. J. Cylinder alignment in annular structures of microphase-separated polystyrene-*b*-poly(methyl methacrylate) *Langmuir* **2000**, *16*, 4766-4769.

- [Haj94] Hajduk, D. A.; Harper, P. E.; Gruner, S. M.; Honeker, C. C.; Kim, G.; Thomas, E. L.; Fetters, L. J. The gyroid - a new equilibrium morphology in weakly segregated diblock copolymers *Macromolecules* **1994**, *27*, 4063-4075.
- [Haj97] Hajduk, D. A.; Takenouchi, H.; Hillmyer, M. A.; Bates, F. S.; Vigild, M. E.; Almdal, K. Stability of the perforated layer (PL) phase in diblock copolymer melts *Macromolecules* **1997**, *30*, 3788-3795.
- [Ham93] Hamley, I. W.; Koppi, K. A.; Rosedale, J. H.; Bates, F. S.; Almdal, K.; Mortensen, K. Hexagonal mesophases between lamellae and cylinders in a diblock copolymer melt *Macromolecules* **1993**, *26*, 5959-5970.
- [Ham94] Hamley, I. W.; Gehlsen, M. D.; Khandpur, A. K.; Koppi, K. A.; Rosedale, J. H.; Schulz, M. F.; Bates, F. S.; Almdal, K.; Mortensen, K. Complex layered phases in asymmetric diblock copolymers *J. Phys. II* **1994**, *4*, 2161-2186.
- [Ham98] Hamley, I. W. The physics of block copolymers. *Oxford University Press*: **1998**, 424 p.
- [Ham03] Hamley, I. W. Nanotechnology with soft materials *Angew. Chem. Int. Ed.* **2003**, *42*, 1692-1712.
- [Ham04] Hamley, I. W.; Castelletto, V. Small-angle scattering of block copolymers: in the melt, solution and crystal states *Prog. Polym. Sci.* **2004**, *29*, 909-948.
- [Ham09] Hamley, I. W. Ordering in thin films of block copolymers: Fundamentals to potential applications *Prog. Polym. Sci.* **2009**, *34*, 1161-1210.
- [Ham10] Hammond, M. R.; Dietsch, H.; Pravaz, O.; Schurtenberger, P. Mutual alignment of block copolymer-magnetic nanoparticle composites in a magnetic field *Macromolecules* **2010**, *43*, 8340-8343.
- [Har05] Harant, A. W.; Bowman, C. N. Solvent vapor annealed block copolymer films on organosilane self-assembled monolayers *J. Vac. Sci. Technol. B* **2005**, *23*, 1615-1621.
- [Har06] Haryono, A.; Binder, W. H. Controlled arrangement of nanoparticle arrays in block-copolymer domains *Small* **2006**, *2*, 600-611.
- [Haz00] Hazra, S.; Gibaud, A.; Désert, A.; Sella, C.; Naudon, A. Morphology of nanocermet thin films: X-ray scattering study *Physica B* **2000**, *283*, 97-102.
- [Hes66] Hess, P. H.; Parker, P. H. Polymers for stabilization of colloidal cobalt particles *J. Appl. Polym. Sci.* **1966**, *10*, 1915-1927.
- [HeS01He, S. T.; Yao, J. N.; Jiang, P.; Shi, D. X.; Zhang, H. X.; Xie, S. S.; Pang, S. J.; Gao, H. J. Formation of silver nanoparticles and self-assembled two-dimensional ordered superlattice *Langmuir* **2001**, *17*, 1571-1575.
- [Hie97] Heier, J.; Kramer, E. J.; Walheim, S.; Krausch, G. Thin diblock copolymer films on chemically heterogeneous surfaces *Macromolecules* **1997**, *30*, 6610-6614.
- [Hir04] Hiramatsu, H.; Osterloh, F. E. A simple large-scale synthesis of nearly monodisperse gold and silver nanoparticles with adjustable sizes and with exchangeable surfactants *Chem. Mater.* **2004**, *16*, 2509-2511.
- [Hon10] Hong, A. J.; Liu, C. C.; Wang, Y.; Kim, J.; Xiu, F. X.; Ji, S. X.; Zou, J.; Nealey, P. F.; Wang, K. L. Metal nanodot memory by self-assembled block copolymer lift-off *Nano Lett.* **2010**, *10*, 224-229.
- [HoR05] Ho, R. M.; Tseng, W. H.; Fan, H. W.; Chiang, Y. W.; Lin, C. C.; Ko, B. T.; Huang, B. H. Solvent-induced microdomain orientation in polystyrene-b-poly (L-lactide) diblock copolymer thin films for nanopatterning *Polymer* **2005**, *46*, 9362-9377.
- [Hou05] Hou, Y.; Kondoh, H.; Ohta, T.; Gao, S. Size-controlled synthesis of nickel nanoparticles *Appl. Surf. Sci.* **2005**, *241*, 218-222.

- [Hua98] Huang, E.; Rockford, L.; Russell, T. P.; Hawker, C. J. Nanodomain control in copolymer thin films *Nature* **1998**, *395*, 757-758.
- [Hug42] Huggins, M. L. Theory of solutions of high polymers *J. Am. Chem. Soc.* **1942**, *64*, 1712-1719.
- [Hui00] Huinink, H. P.; Brokken-Zijp, J. C. M.; van Dijk, M. A.; Sevink, G. J. A. Asymmetric block copolymers confined in a thin film *J. Chem. Phys.* **2000**, *112*, 2452-2462.
- [Hye01] Hyeon, T.; Lee, S. S.; Park, J.; Chung, Y.; Bin Na, H. Synthesis of highly crystalline and monodisperse maghemite nanocrystallites without a size-selection process *J. Am. Chem. Soc.* **2001**, *123*, 12798-12801.
- [Hye03] Hyeon, T. Chemical synthesis of magnetic nanoparticles *Chem. Commun.* **2003**, 927-934.
- [Ikk04] Ikkala, O.; ten Brinke, G. Hierarchical self-assembly in polymeric complexes: Towards functional materials *Chem. Commun.* **2004**, 2131-2137.
- [Jai07] Jain, P. K.; Huang, W. Y.; El-Sayed, M. A. On the universal scaling behavior of the distance decay of plasmon coupling in metal nanoparticle pairs: A plasmon ruler equation *Nano Lett.* **2007**, *7*, 2080-2088.
- [Jan04] Jana, N. R.; Chen, Y. F.; Peng, X. G. Size- and shape-controlled magnetic (Cr, Mn, Fe, Co, Ni) oxide nanocrystals via a simple and general approach *Chem. Mater.* **2004**, *16*, 3931-3935.
- [Kan10] Kannaiyan, D.; Kim, E.; Won, N.; Kim, K. W.; Jang, Y. H.; Cha, M. A.; Ryu, D. Y.; Kim, S.; Kim, D. H. On the synergistic coupling properties of composite CdS/TiO<sub>2</sub> nanoparticle arrays confined in nanopatterned hybrid thin films *J. Mater. Chem.* **2010**, *20*, 677-682.
- [Kas09] Kashem, M. M. A.; Perlich, J.; Diethert, A.; Wang, W. N.; Memesa, M.; Gutmann, J. S.; Majkova, E.; Capek, I.; Roth, S. V.; Petry, W.; Muller-Buschbaum, P. Array of magnetic nanoparticles via particle co-operated self-assembly in block copolymer thin film *Macromolecules* **2009**, *42*, 6202-6208.
- [Kha95] Khandpur, A. K.; Forster, S.; Bates, F. S.; Hamley, I. W.; Ryan, A. J.; Bras, W.; Almdal, K.; Mortensen, K. Polyisoprene-polystyrene diblock copolymer phase diagram near the order-disorder transition *Macromolecules* **1995**, *28*, 8796-8806.
- [Kim98] Kim, G.; Libera, M. Morphological development in solvent-cast polystyrene-polybutadiene-polystyrene (SBS) triblock copolymer thin films *Macromolecules* **1998**, *31*, 2569-2577.
- [Kim03] Kim, S. O.; Solak, H. H.; Stoykovich, M. P.; Ferrier, N. J.; de Pablo, J. J.; Nealey, P. F. Epitaxial self-assembly of block copolymers on lithographically defined nanopatterned substrates *Nature* **2003**, *424*, 411-414.
- [Kim04] Kim, S. H.; Misner, M. J.; Xu, T.; Kimura, M.; Russell, T. P. Highly oriented and ordered arrays from block copolymers via solvent evaporation *Adv. Mater.* **2004**, *16*, 226-231.
- [Kim05] Kim, B. J.; Chiu, J. J.; Yi, G. R.; Pine, D. J.; Kramer, E. J. Nanoparticle-induced phase transitions in diblock-copolymer films *Adv. Mater.* **2005**, *17*, 2618-2622.
- [Kim06a] Kimling, J.; Maier, M.; Okenve, B.; Kotaidis, V.; Ballot, H.; Plech, A. Turkevich method for gold nanoparticle synthesis revisited *J. Phys. Chem. B* **2006**, *110*, 15700-15707.
- [Kim06b] Kim, B. J.; Bang, J.; Hawker, C. J.; Kramer, E. J. Effect of areal chain density on the location of polymer-modified gold nanoparticles in a block copolymer template *Macromolecules* **2006**, *39*, 4108-4114.

- [Kim10a] Kim, H. C.; Park, S. M.; Hinsberg, W. D. Block Copolymer Based Nanostructures: Materials, Processes, and Applications to Electronics *Chem. Rev.* **2010**, *110*, 146-177.
- [Kim10b] Kim, J.; Green, P. F. Directed Assembly of Nanoparticles in Block Copolymer Thin Films: Role of Defects *Macromolecules* **2010**, *43*, 10452-10456.
- [Kit46] Kittel, C. Theory of the structure of ferromagnetic domains in films and small particles *Phys. Rev.* **1946**, *70*, 965-971.
- [Kla01] Klabunde, K. J. Nanoscale materials in chemistry. *Wiley-Interscience*: **2001**, 292 p.
- [Klo07] Klokkenburg, M.; Hilhorst, J.; Erne, B. H. Surface analysis of magnetite nanoparticles in cyclohexane solutions of oleic acid and oleylamine *Vib. Spectrosc.* **2007**, *43*, 243-248.
- [Kne97] Kneipp, K.; Wang, Y.; Kneipp, H.; Perelman, L. T.; Itzkan, I.; Dasari, R.; Feld, M. S. Single molecule detection using surface-enhanced Raman scattering (SERS) *Phys. Rev. Lett.* **1997**, *78*, 1667-1670.
- [Koe04] Koerkamp, K. J. K.; Enoch, S.; Segerink, F. B.; van Hulst, N. F.; Kuipers, L. Strong influence of hole shape on extraordinary transmission through periodic arrays of subwavelength holes *Phys. Rev. Lett.* **2004**, *92*, 183901.
- [Koh10] Koh, H. D.; Park, S.; Russell, T. P. Fabrication of Pt/Au concentric spheres from triblock copolymer *ACS Nano* **2010**, *4*, 1124-1130.
- [Kop92] Koppi, K. A.; Tirrell, M.; Bates, F. S.; Almdal, K.; Colby, R. H. Lamellae orientation in dynamically sheared diblock copolymer melts *J. Phys. II* **1992**, *2*, 1941-1959.
- [Kui10] Kuila, B. K.; Gowd, E. B.; Stamm, M. Supramolecular assembly of poly(styrene)-b-poly(4-vinylpyridine) and 1-pyrenebutyric acid in thin film and their use for nanofabrication *Macromolecules* **2010**, *43*, 7713-7721.
- [Lac05] Lacheisserie, A. D. T.; Gignoux, D.; Schlenker, M. Magnetism: Materials and applications. *Springer*: **2005**, 517 p.
- [Lan07] Lan, Q.; Liu, C.; Yang, F.; Liu, S. Y.; Xu, J.; Sun, D. J. Synthesis of bilayer oleic acid-coated Fe<sub>3</sub>O<sub>4</sub> nanoparticles and their application in pH-responsive Pickering emulsions *J. Colloid Interf. Sci.* **2007**, *310*, 260-269.
- [Lat08] Latham, A. H.; Williams, M. E. Controlling transport and chemical functionality of magnetic nanoparticles *Accounts Chem. Res.* **2008**, *41*, 411-420.
- [Lee96] Lee, J. W.; Isobe, T.; Senna, M. Magnetic properties of ultrafine magnetite particles and their slurries prepared via in-situ precipitation *Colloid Surface A* **1996**, *109*, 121-127.
- [Lee08] Lee, J. I.; Cho, S. H.; Park, S. M.; Kim, J. K.; Yu, J. W.; Kim, Y. C.; Russell, T. P. Highly aligned ultrahigh density arrays of conducting polymer nanorods using block copolymer templates *Nano Lett.* **2008**, *8*, 2315-2320.
- [Lee10] Lee, Y. H.; Chang, C. J.; Kao, C. J.; Dai, C. A. In-situ template synthesis of a polymer/semiconductor nanohybrid using amphiphilic conducting block copolymers *Langmuir* **2010**, *26*, 4196-4206.
- [Lei80] Leibler, L. Theory of microphase separation in block co-polymers *Macromolecules* **1980**, *13*, 1602-1617.
- [Lev89] Levine, J. R.; Cohen, L. B.; Chung, Y. W.; Georgopoulos, P. Grazing-incidence small-angle X-Ray scattering - new tool for studying thin-film growth *J. Appl. Crystallogr.* **1989**, *22*, 528-532.
- [Lin99] Link, S.; El-Sayed, M. A. Spectral properties and relaxation dynamics of surface plasmon electronic oscillations in gold and silver nanodots and nanorods *J. Phys. Chem. B* **1999**, *103*, 8410-8426.

- [Lin02] Lin, Z. Q.; Kim, D. H.; Wu, X. D.; Boosahda, L.; Stone, D.; LaRose, L.; Russell, T. P. A rapid route to arrays of nanostructures in thin films *Adv. Mater.* **2002**, *14*, 1373-1376.
- [Lin05] Lin, Y.; Boker, A.; He, J. B.; Sill, K.; Xiang, H. Q.; Abetz, C.; Li, X. F.; Wang, J.; Emrick, T.; Long, S.; Wang, Q.; Balazs, A.; Russell, T. P. Self-directed self-assembly of nanoparticle/copolymer mixtures *Nature* **2005**, *434*, 55-59.
- [Lis06] Listak, J.; Bockstaller, M. R. Stabilization of grain boundary morphologies in lamellar block copolymer/nanoparticle blends *Macromolecules* **2006**, *39*, 5820-5825.
- [Liu94] Liu, Y.; Zhao, W.; Zheng, X.; King, A.; Singh, A.; Rafailovich, M. H.; Sokolov, J.; Dai, K. H.; Kramer, E. J.; Schwarz, S. A.; Gebizlioglu, O.; Sinha, S. K. Surface-induced ordering in asymmetric block-copolymers *Macromolecules* **1994**, *27*, 4000-4010.
- [Liu00a] Liu, C.; Rondinone, A. J.; Zhang, Z. J. Synthesis of magnetic spinel ferrite CoFe<sub>2</sub>O<sub>4</sub> nanoparticles from ferric salt and characterization of the size-dependent superparamagnetic properties *Pure Appl. Chem.* **2000**, *72*, 37-45.
- [Liu00b] Liu, C.; Zou, B. S.; Rondinone, A. J.; Zhang, Z. J. Reverse micelle synthesis and characterization of superparamagnetic MnFe<sub>2</sub>O<sub>4</sub> spinel ferrite nanocrystallites *J. Phys. Chem. B* **2000**, *104*, 1141-1145.
- [Liu06] Liu, D. H.; Zhong, C. L. Cooperative self-assembly of nanoparticle mixtures in lamellar diblock copolymers: A dissipative particle dynamics study *Macromol. Rapid Comm.* **2006**, *27*, 458-462.
- [LiX07] Li, X.; Peng, J.; Wen, Y.; Kim, D. H.; Knoll, W. Morphology change of asymmetric diblock copolymer micellar films during solvent annealing *Polymer* **2007**, *48*, 2434-2443.
- [LiZ05] Li, Z.; Wei, L.; Gao, M. Y.; Lei, H. One-pot reaction to synthesize biocompatible magnetite nanoparticles *Adv. Mater.* **2005**, *17*, 1001-1005.
- [LoC07] Lo, C. T.; Lee, B.; Pol, V. G.; Rago, N. L. D.; Seifert, S.; Winans, R. E.; Thiyagarajan, P. Effect of molecular properties of block copolymers and nanoparticles on the morphology of self-assembled bulk nanocomposites *Macromolecules* **2007**, *40*, 8302-8310.
- [Lop03] Lopez-Quintela, M. A. Synthesis of nanomaterials in microemulsions: formation mechanisms and growth control *Curr. Opin. Colloid In.* **2003**, *8*, 137-144.
- [Lud03] Ludwigs, S.; Boker, A.; Abetz, V.; Muller, A. H. E.; Krausch, G. Phase behavior of linear poly styrene-block-poly (2-vinylpyridine)-block-poly(tert-butyl methacrylate) triblock terpolymers *Polymer* **2003**, *44*, 6815-6823.
- [LuX09] Lu, X. M.; Rycenga, M.; Skrabalak, S. E.; Wiley, B.; Xia, Y. N. Chemical synthesis of novel plasmonic nanoparticles *Annu. Rev. Phys. Chem.* **2009**, *60*, 167-192.
- [LyD07] Ly, D. Q.; Honda, T.; Kawakatsu, T.; Zvelindovsky, A. V. Kinetic pathway of gyroid-to-cylinder transition in diblock copolymer melt under an electric field *Macromolecules* **2007**, *40*, 2928-2935.
- [Maa92] Maaloum, M.; Ausserre, D.; Chatenay, D.; Coulon, G.; Gallot, Y. Edge profile of relief 2D domains at the free-surface of smectic copolymer thin films *Phys. Rev. Lett.* **1992**, *68*, 1575-1578.
- [Maj06] Majetich, S. A.; Sachan, M. Magnetostatic interactions in magnetic nanoparticle assemblies: energy, time and length scales *J. Phys. D: Appl. Phys.* **2006**, *39*, R407-R422.

- [Mal02] Malynych, S.; Luzinov, I.; Chumanov, G. Poly(vinyl pyridine) as a universal surface modifier for immobilization of nanoparticles *J. Phys. Chem. B* **2002**, *106*, 1280-1285.
- [Mar03] Martin, T. A.; Young, D. M. Correlation of the glass transition temperature of plasticized PVC using a lattice fluid model *Polymer* **2003**, *44*, 4747-4754.
- [Mas81] Massart, R. Preparation of aqueous magnetic liquids in alkaline and acidic media *IEEE T. Magn.* **1981**, *17*, 1247-1248.
- [Mas95] Massart, R.; Dubois, E.; Cabuil, V.; Hasmonay, E. Preparation and properties of monodisperse magnetic fluids *J. Magn. Magn. Mater.* **1995**, *149*, 1-5.
- [Mat94] Matsen, M. W.; Schick, M. Stable and unstable phases of a diblock copolymer melt *Phys. Rev. Lett.* **1994**, *72*, 2660-2663.
- [Mat96] Matsen, M. W.; Bates, F. S. Unifying weak- and strong-segregation block copolymer theories *Macromolecules* **1996**, *29*, 1091-1098.
- [Mat97] Matsen, M. W. Thin films of block copolymer *J. Chem. Phys.* **1997**, *106*, 7781-7791.
- [Mat02] Matsen, M. W. The standard Gaussian model for block copolymer melts *J. Phys.-Condens. Mat.* **2002**, *14*, R21-R47.
- [Mei56] Meiklejohn, W. H.; Bean, C. P. New magnetic anisotropy *Phys. Rev.* **1956**, *102*, 1413-1414.
- [Men08] Mendoza, C.; Pietsch, T.; Gindy, N.; Fahmi, A. Fabrication of 3D-periodic ordered metallic nanoparticles in a block copolymer bulk matrix via oscillating shear flow *Adv. Mater.* **2008**, *20*, 1179-1184.
- [Men09] Mendoza, C.; Pietsch, T.; Gutmann, J. S.; Jehnichen, D.; Gindy, N.; Fahmi, A. Block copolymers with gold nanoparticles: Correlation between structural characteristics and mechanical properties *Macromolecules* **2009**, *42*, 1203-1211.
- [Mie08] Mie, G. Beitrage zur Optik truber Medien, speziell kolloidaler Metallosungen *Ann. Phys.* **1908**, *25*, 377-445.
- [Mol04] van der Molen, K. L.; Segerink, F. B.; van Hulst, N. F.; Kuipers, L. Influence of hole size on the extraordinary transmission through subwavelength hole arrays *Appl. Phys. Lett.* **2004**, *85*, 4316-4318.
- [Moo65] Moore, G. E. Cramming more components onto integrated circuits *Electronics* **1965**, *38*.
- [Moo06] Moores, A.; Goettmann, F. The plasmon band in noble metal nanoparticles: an introduction to theory and applications *New J. Chem.* **2006**, *30*, 1121-1132.
- [Mor96] Morkved, T. L.; Lu, M.; Urbas, A. M.; Ehrichs, E. E.; Jaeger, H. M.; Mansky, P.; Russell, T. P. Local control of microdomain orientation in diblock copolymer thin films with electric fields *Science* **1996**, *273*, 931-933.
- [Mor97] Morkved, T. L.; Jaeger, H. M. Thickness-induced morphology changes in lamellar diblock copolymer ultrathin films *Europhys. Lett.* **1997**, *40*, 643-648.
- [Mor08] Morel, A. L.; Nikitenko, S. I.; Gionnet, K.; Wattiaux, A.; Lai-Kee-Him, J.; Labrugere, C.; Chevalier, B.; Deleris, G.; Petibois, C.; Brisson, A.; Simonoff, M. Sonochemical approach to the synthesis of Fe<sub>3</sub>O<sub>4</sub>@SiO<sub>2</sub> core-shell nanoparticles with tunable properties *ACS Nano* **2008**, *2*, 847-856.
- [Mou95] Moulder, J. F.; Stickle, W. F.; Sobol, P. E.; Bomben, K. D. Handbook of X-ray photoelectron spectroscopy: A reference book of standard spectra for identification and interpretation of XPS data. 1st ed.; Physical Electronics, Inc.: **1995**, 261 p.



- [Mue03] Muller-Buschbaum, P. Grazing incidence small-angle X-ray scattering: an advanced scattering technique for the investigation of nanostructured polymer films *Anal. Bioanal. Chem* **2003**, *376*, 3-10.
- [Nan09] Nandan, B.; Gowd, E. B.; Bigall, N. C.; Eychmuller, A.; Formanek, P.; Simon, P.; Stamm, M. Arrays of inorganic nanodots and nanowires using nanotemplates based on switchable block copolymer supramolecular assemblies *Adv. Func. Mater.* **2009**, *19*, 2805-2811.
- [Nee49] Neel, L. Influence des fluctuations thermiques sur la aimantation de grains ferromagnétiques très fins *CR Hebd. Acad. Sci.* **1949**, *228*, 664-666.
- [Nie97] Nie, S. M.; Emery, S. R. Probing single molecules and single nanoparticles by surface-enhanced Raman scattering *Science* **1997**, *275*, 1102-1106.
- [Ode04] Odenbach, S. Recent progress in magnetic fluid research *J. Phys.-Condens. Mat.* **2004**, *16*, R1135-R1150.
- [Oka94] Okamoto, S.; Saijo, K.; Hashimoto, T. Real-time SAXS observation of lamella-forming block-copolymers under large oscillatory shear deformation *Macromolecules* **1994**, *27*, 5547-5555.
- [Par00] Park, S. J.; Kim, S.; Lee, S.; Khim, Z. G.; Char, K.; Hyeon, T. Synthesis and magnetic studies of uniform iron nanorods and nanospheres *J. Am. Chem. Soc.* **2000**, *122*, 8581-8582.
- [Par01] Park, J. I.; Cheon, J. Synthesis of "solid solution" and "core-shell" type cobalt-platinum magnetic nanoparticles via transmetalation reactions *J. Am. Chem. Soc.* **2001**, *123*, 5743-5746.
- [Par02] Park, S.-M.; Yun, S.-H.; Sohn, B.-H. Variations of the lamellar period in thin films of diblock copolymers by selective staining agents *Macromol. Chem. Physic* **2002**, *203*, 2069-2074.
- [Par04] Park, J.; An, K. J.; Hwang, Y. S.; Park, J. G.; Noh, H. J.; Kim, J. Y.; Park, J. H.; Hwang, N. M.; Hyeon, T. Ultra-large-scale syntheses of monodisperse nanocrystals *Nat. Mater.* **2004**, *3*, 891-895.
- [Par07a] Park, J.; Joo, J.; Kwon, S. G.; Jang, Y.; Hyeon, T. Synthesis of monodisperse spherical nanocrystals *Angew. Chem. Int. Ed.* **2007**, *46*, 4630-4660.
- [Par07b] Park, S. M.; Stoykovich, M. P.; Ruiz, R.; Zhang, Y.; Black, C. T.; Nealey, P. E. Directed assembly of lamellae-forming block copolymers by using chemically and topographically patterned substrates *Adv. Mater.* **2007**, *19*, 607-611.
- [Par07c] Park, S.; Wang, J. Y.; Kim, B.; Chen, W.; Russell, T. P. Solvent-induced transition from micelles in solution to cylindrical microdomains in diblock copolymer thin films *Macromolecules* **2007**, *40*, 9059-9063.
- [Par09a] Park, S. M.; Rettner, C. T.; Pitera, J. W.; Kim, H. C. Directed self-assembly of lamellar microdomains of block copolymers using topographic guiding patterns *Macromolecules* **2009**, *42*, 5895-5899.
- [Par09b] Park, S.; Lee, D. H.; Xu, J.; Kim, B.; Hong, S. W.; Jeong, U.; Xu, T.; Russell, T. P. Macroscopic 10-terabit-per-square-inch arrays from block copolymers with lateral order *Science* **2009**, *323*, 1030-1033.
- [Pat08] Patungwasa, W.; Hodak, J. H. pH tunable morphology of the gold nanoparticles produced by citrate reduction *Mater. Chem. Phys.* **2008**, *108*, 45-54.
- [Pic97] Pickett, G. T.; Balazs, A. C. Equilibrium orientation of confined diblock copolymer films *Macromolecules* **1997**, *30*, 3097-3103.
- [Pil00] Pileni, M. P. Fabrication and physical properties of self-organized silver nanocrystals *Pure Appl. Chem.* **2000**, *72*, 53-65

- [Pin08] Pinna, M.; Zvelindovsky, A. V. Kinetic pathways of gyroid-to-cylinder transitions in diblock copolymers under external fields: Cell dynamics simulation *Soft Matter*. **2008**, *4*, 316-327.
- [Plo10] Ploshnik, E.; Salant, A.; Banin, U.; Shenhar, R. Hierarchical Surface Patterns of Nanorods Obtained by Co-Assembly with Block Copolymers in Ultrathin Films *Adv. Mater.* **2010**, *22*, 2774-2780.
- [Pol99] Polis, D. L.; Smith, S. D.; Terrill, N. J.; Ryan, A. J.; Morse, D. C.; Winey, K. I. Shear-induced lamellar rotation observed in a diblock copolymer by in situ small-angle X-ray scattering *Macromolecules* **1999**, *32*, 4668-4676.
- [Pop99] Pople, J. A.; Hamley, I. W.; Fairclough, J. P. A.; Ryan, A. J.; Hill, G.; Price, C. A shear induced transition of lamellar alignment in a concentrated diblock copolymer solution *Polymer* **1999**, *40*, 5709-5714.
- [Pou09] Poudyal, N.; Chaubey, G. S.; Rong, C. B.; Liu, J. P. Shape control of FePt nanocrystals *J. Appl. Phys.* **2009**, *105*, 07A749
- [Pro03] Prodan, E.; Radloff, C.; Halas, N. J.; Nordlander, P. A hybridization model for the plasmon response of complex nanostructures *Science* **2003**, *302*, 419-422.
- [Pun01] Puntès, V. F.; Krishnan, K. M.; Alivisatos, A. P. Colloidal nanocrystal shape and size control: The case of cobalt *Science* **2001**, *291*, 2115-2117.
- [Rac05] Racuciu, M.; Creanga, D. E.; Calugaru, G. Synthesis and rheological properties of an aqueous ferrofluid *J. Optoelectron. Adv. M.* **2005**, *7*, 2859-2864.
- [Rag06] Raghuraman, G. K.; Dhamodharan, R. Surface-initiated atom transfer radical polymerization of methyl methacrylate from magnetite nanoparticles at ambient temperature *J. Nanosci. Nanotechnol.* **2006**, *6*, 2018-2024.
- [Rei95] Reimer, L. *Energy-filtering transmission electron microscopy*. Springer: **1995**, 424 p.
- [Rei08] Reimer, L.; Kohl, H. Transmission electron microscopy: physics of image formation. Springer: **2008**, 587 p.
- [Roc99] Rockford, L.; Liu, Y.; Mansky, P.; Russell, T. P.; Yoon, M.; Mochrie, S. G. J. Polymers on nanopatterned, heterogeneous surfaces *Phys. Rev. Lett.* **1999**, *82*, 2602-2605.
- [Roc01] Rockford, L.; Mochrie, S. G. J.; Russell, T. P. Propagation of nanopatterned substrate templated ordering of block copolymers in thick films *Macromolecules* **2001**, *34*, 1487-1492.
- [Ron01] Rondinone, A. J.; Liu, C.; Zhang, Z. J. Determination of magnetic anisotropy distribution and anisotropy constant of manganese spinel ferrite nanoparticles *J. Phys. Chem. B* **2001**, *105*, 7967-7971.
- [Rot58] Roth, W. L. Magnetic structures of MnO, FeO, CoO and NiO *Phys. Rev.* **1958**, *110*, 1333-1341.
- [Rus89] Russell, T. P.; Coulon, G.; Deline, V. R.; Miller, D. C. Characteristics of the surface-induced orientation for symmetric diblock PS/PMMA copolymers *Macromolecules* **1989**, *22*, 4600-4606.
- [Sch96] Schulz, M. F.; Khandpur, A. K.; Bates, F. S.; Almdal, K.; Mortensen, K.; Hajduk, D. A.; Gruner, S. M. Phase behavior of polystyrene-poly(2-vinylpyridine) diblock copolymers *Macromolecules* **1996**, *29*, 2857-2867.
- [Sch10] Schmidt, K.; Pester, C. W.; Schoberth, H. G.; Zettl, H.; Schindler, K. A.; Boker, A. Electric field induced gyroid-to-cylinder transitions in concentrated diblock copolymer solutions *Macromolecules* **2010**, *43*, 4268-4274.
- [Seg01] Segalman, R. A.; Yokoyama, H.; Kramer, E. J. Graphoepitaxy of spherical domain block copolymer films *Adv. Mater.* **2001**, *13*, 1152-1155.

- [She99] Shen, L. F.; Laibinis, P. E.; Hatton, T. A. Bilayer surfactant stabilized magnetic fluids: Synthesis and interactions at interfaces *Langmuir* **1999**, *15*, 447-453.
- [Sid03] Sidorenko, A.; Tokarev, I.; Minko, S.; Stamm, M. Ordered reactive nanomembranes/nanotemplates from thin films of block copolymer supramolecular assembly *J. Am. Chem. Soc.* **2003**, *125*, 12211-12216.
- [Sie08] Siepmann, F.; Siepmann, J.; Walther, M.; MacRae, R. J.; Bodmeier, R. Polymer blends for controlled release coatings *J. Control. Release* **2008**, *125*, 1-15.
- [Sil88] Silverstein, R.; Bassler G. C.; Morrill T. C. Spectrometric Identification of Organic Compounds. 5 ed.; Wiley: **1989**, 482 p.
- [SiS05] Si, S. F.; Li, C. H.; Wang, X.; Yu, D. P.; Peng, Q.; Li, Y. D. Magnetic monodisperse Fe<sub>3</sub>O<sub>4</sub> nanoparticles *Cryst. Growth Des.* **2005**, *5*, 391-393.
- [Sku03] Skumryev, V.; Stoyanov, S.; Zhang, Y.; Hadjipanayis, G.; Givord, D.; Nogues, J. Beating the superparamagnetic limit with exchange bias *Nature* **2003**, *423*, 850-853.
- [Soh03] Sohn, B. H.; Choi, J. M.; Yoo, S. I.; Yun, S. H.; Zin, W. C.; Jung, J. C.; Kanehara, M.; Hirata, T.; Teranishi, T. Directed self-assembly of two kinds of nanoparticles utilizing monolayer films of diblock copolymer micelles *J. Am. Chem. Soc.* **2003**, *125*, 6368-6369.
- [Son09] Son, J. G.; Bae, W. K.; Kang, H. M.; Nealey, P. F.; Char, K. Placement control of nanomaterial arrays on the surface-reconstructed block copolymer thin films *ACS Nano* **2009**, *3*, 3927-3934.
- [Sta08] Staszak, K.; Prochaska, K. Investigation of the interaction in binary mixed extraction systems by Fourier Transform Infrared Spectroscopy (FT-IR) *Hydrometallurgy* **2008**, *90*, 75-84.
- [Sto48] Stoner, E. C.; Wohlfarth, E. P. A mechanism of magnetic hysteresis in heterogeneous alloys *Philos. T. R. Soc. S-A* **1948**, *240*, 599-642.
- [Sun00] Sun, S. H.; Murray, C. B.; Weller, D.; Folks, L.; Moser, A. Monodisperse FePt nanoparticles and ferromagnetic FePt nanocrystal superlattices *Science* **2000**, *287*, 1989-1992.
- [Sun02] Sun, S. H.; Zeng, H. Size-controlled synthesis of magnetite nanoparticles *J. Am. Chem. Soc.* **2002**, *124*, 8204-8205.
- [Sun04] Sun, S. H.; Zeng, H.; Robinson, D. B.; Raoux, S.; Rice, P. M.; Wang, S. X.; Li, G. X. Monodisperse MFe<sub>2</sub>O<sub>4</sub> (M = Fe, Co, Mn) nanoparticles *J. Am. Chem. Soc.* **2004**, *126*, 273-279.
- [Sund02] Sundrani, D.; Sibener, S. J. Spontaneous spatial alignment of polymer cylindrical nanodomains on silicon nitride gratings *Macromolecules* **2002**, *35*, 8531-8539.
- [Sund04] Sundrani, D.; Darling, S. B.; Sibener, S. J. Hierarchical assembly and compliance of aligned nanoscale polymer cylinders in confinement *Langmuir* **2004**, *20*, 5091-5099.
- [Sus96] Suslick, K. S.; Fang, M. M.; Hyeon, T. Sonochemical synthesis of iron colloids *J. Am. Chem. Soc.* **1996**, *118*, 11960-11961.
- [Szw56] Szwarc, M.; Levy, M.; Milkovich, R. Polymerisation initiated by electron transfer to monomer - a new method of formation of block polymers *J. Am. Chem. Soc.* **1956**, *78*, 2656-2657.
- [Tak04] Takafuji, M.; Ide, S.; Ihara, H.; Xu, Z. H. Preparation of poly(1-vinylimidazole)-grafted magnetic nanoparticles and their application for removal of metal ions *Chem. Mater.* **2004**, *16*, 1977-1983.
- [Tan07] Tanabe, K. Optical radiation efficiencies of metal nanoparticles for optoelectronic applications *Mater. Lett.* **2007**, *61*, 4573-4575.

- [Tao07] Tao, Y. F.; Zohar, H.; Olsen, B. D.; Segalman, R. A. Hierarchical nanostructure control in rod-coil block copolymers with magnetic fields *Nano Lett.* **2007**, *7*, 2742-2746.
- [Tar03] Tartaj, P.; Gonzalez-Carreno, T.; Serna, C. J. Magnetic behavior of gamma-Fe<sub>2</sub>O<sub>3</sub> nanocrystals dispersed in colloidal silica particles *J. Phys. Chem. B* **2003**, *107*, 20-24.
- [Tho66] Thomas, J. R. Preparation and magnetic properties of colloidal cobalt particles *J. Appl. Phys.* **1966**, *37*, 2914-2915.
- [Tho01] Thompson, R. B.; Ginzburg, V. V.; Matsen, M. W.; Balazs, A. C. Predicting the mesophases of copolymer-nanoparticle composites *Science* **2001**, *292*, 2469-2472.
- [Tho10] Thompson, R. B. Tilt grain boundaries in a diblock copolymer ordered nanocomposite lamellar phase *J. Chem. Phys.* **2010**, *133*, 144902.
- [Thu00a] Thurn-Albrecht, T.; DeRouchey, J.; Russell, T. P.; Jaeger, H. M. Overcoming interfacial interactions with electric fields *Macromolecules* **2000**, *33*, 3250-3253.
- [Thu00b] Thurn-Albrecht, T.; Schotter, J.; Kastle, C. A.; Emley, N.; Shibauchi, T.; Krusin-Elbaum, L.; Guarini, K.; Black, C. T.; Tuominen, M. T.; Russell, T. P. Ultrahigh-density nanowire arrays grown in self-assembled diblock copolymer templates *Science* **2000**, *290*, 2126-2129.
- [Tok05] Tokarev, I.; Krenek, R.; Burkov, Y.; Schmeisser, D.; Sidorenko, A.; Minko, S.; Stamm, M. Microphase separation in thin films of poly(styrene-block-4-vinylpyridine) copolymer – 2-(4'-hydroxybenzeneazo) benzoic acid assembly *Macromolecules* **2005**, *38*, 507-516.
- [Tol99] Tolan, M. X-ray scattering from soft-matter thin films. *Spronger*: **1999**, 197 p.
- [Tou90] Tourinho, F. A.; Franck, R.; Massart, R. Aqueous ferrofluids based on manganese and cobalt ferrites *J. Mater. Sci.* **1990**, *25*, 3249-3254.
- [Tsa04] Tsang, S. C.; Caps, V.; Paraskevas, I.; Chadwick, D.; Thompsett, D. Magnetically separable, carbon-supported nanocatalysts for the manufacture of fine chemicals *Angew. Chem. Int. Ed.* **2004**, *43*, 5645-5649.
- [Tso03] Tsori, Y.; Tournilhac, F.; Andelman, D.; Leibler, L. Structural changes in block copolymers: Coupling of electric field and mobile ions *Phys. Rev. Lett.* **2003**, *90*, 145504.
- [Tso06] Tsori, Y.; Andelman, D.; Lin, C. Y.; Schick, M. Block copolymers in electric fields: A comparison of single-mode and self-consistent-field approximations *Macromolecules* **2006**, *39*, 289-293.
- [Tur85] Turkevich, J. Colloidal gold. Part I *Gold Bull.* **1985**, *18*, 86-91.
- [Val06] Valkama, S.; Ruotsalainen, T.; Nykanen, A.; Laiho, A.; Kosonen, H.; ten Brinke, G.; Ikkala, O.; Ruokolainen, J. Self-assembled structures in diblock copolymers with hydrogen-bonded amphiphilic plasticizing compounds *Macromolecules* **2006**, *39*, 9327-9336.
- [Vig98] Vigild, M. E.; Almdal, K.; Mortensen, K.; Hamley, I. W.; Fairclough, J. P. A.; Ryan, A. J. Transformations to and from the gyroid phase in a diblock copolymer *Macromolecules* **1998**, *31*, 5702-5716.
- [Wan00] Wang, Q.; Yan, Q. L.; Nealey, P. F.; de Pablo, J. J. Monte Carlo simulations of diblock copolymer thin films confined between chemically heterogeneous hard surfaces *Macromolecules* **2000**, *33*, 4512-4525.

- [Wan05a] Wang, L. Y.; Luo, J.; Fan, Q.; Suzuki, M.; Suzuki, I. S.; Engelhard, M. H.; Lin, Y. H.; Kim, N.; Wang, J. Q.; Zhong, C. J. Monodispersed core-shell Fe<sub>3</sub>O<sub>4</sub>@Au nanoparticles *J. Phys. Chem. B* **2005**, *109*, 21593-21601.
- [Wan05b] Wang, X.; Zhuang, J.; Peng, Q.; Li, Y. D. A general strategy for nanocrystal synthesis *Nature* **2005**, *437*, 121-124.
- [Wan06] Wang, Y.; Zheng, J. X.; Brittain, W. J.; Cheng, S. Z. D. Switchable thin-film surface prepared via a simple grafting-to method using a polystyrene-*b*-poly(2-vinylpyridine) copolymer *J. Polym. Sci. Pol. Chem.* **2006**, *44*, 5608-5617.
- [Wan07] Wang, C.; Hou, Y. L.; Kim, J. M.; Sun, S. H. A general strategy for synthesizing FePt nanowires and nanorods *Angew. Chem. Int. Ed.* **2007**, *46*, 6333-6335.
- [Wil04] Willard, M. A.; Kurihara, L. K.; Carpenter, E. E.; Calvin, S.; Harris, V. G. Chemically prepared magnetic nanoparticles *Int. Mater. Rev.* **2004**, *49*, 125-170.
- [Wil06] Wiley, B. J.; Im, S. H.; Li, Z. Y.; McLellan, J.; Siekkinen, A.; Xia, Y. A. Maneuvering the surface plasmon resonance of silver nanostructures through shape-controlled synthesis *J. Phys. Chem. B* **2006**, *110*, 15666-15675.
- [Wil07] Willets, K. A.; Van Duyne, R. P. Localized surface plasmon resonance spectroscopy and sensing *Annu. Rev. Phys. Chem.* **2007**, *58*, 267-297.
- [Wil09] Wilson, N. R.; Macpherson, J. V. Carbon nanotube tips for atomic force microscopy *Nat. Nanotechnol.* **2009**, *4*, 483-491.
- [Woo03] Woo, K.; Lee, H. J.; Ahn, J. P.; Park, Y. S. Sol-gel mediated synthesis of Fe<sub>2</sub>O<sub>3</sub> nanorods *Adv. Mater.* **2003**, *15*, 1761-1763.
- [Xia05] Xia, Y. N.; Halas, N. J. Shape-controlled synthesis and surface plasmonic properties of metallic nanostructures *Mrs Bulletin* **2005**, *30*, 338-344.
- [Xua04] Xuan, Y.; Peng, J.; Cui, L.; Wang, H. F.; Li, B. Y.; Han, Y. C. Morphology development of ultrathin symmetric diblock copolymer film via solvent vapor treatment *Macromolecules* **2004**, *37*, 7301-7307.
- [XuT04] Xu, T.; Zvelindovsky, A. V.; Sevink, G. J. A.; Gang, O.; Ocko, B.; Zhu, Y. Q.; Gido, S. P.; Russell, T. P. Electric field induced sphere-to-cylinder transition in diblock copolymer thin films *Macromolecules* **2004**, *37*, 6980-6984.
- [XuT05] Xu, T.; Zvelindovsky, A. V.; Sevink, G. J. A.; Lyakhova, K. S.; Jinnai, H.; Russell, T. P. Electric field alignment of asymmetric diblock copolymer thin films *Macromolecules* **2005**, *38*, 10788-10798.
- [Yan00] Yang, X. M.; Peters, R. D.; Nealey, P. F.; Solak, H. H.; Cerrina, F. Guided self-assembly of symmetric diblock copolymer films on chemically nanopatterned substrates *Macromolecules* **2000**, *33*, 9575-9582.
- [Yon63] Yoneda, Y. Anomalous surface reflection of X-rays *Phys. Rev.* **1963**, *131*, 2010-2013.
- [YuL06] Yu, L.; Dean, K.; Li, L. Polymer blends and composites from renewable resources *Prog. Polym. Sci.* **2006**, *31*, 576-602.
- [Yun05] Yun, S. H.; Sohn, B. H.; Jung, J. C.; Zin, W. C.; Lee, J. K.; Song, O. Tunable magnetic arrangement of iron oxide nanoparticles in situ synthesized on the solid substrate from diblock copolymer micelles *Langmuir* **2005**, *21*, 6548-6552.
- [Zen08] Zeng, H.; Sun, S. H. Syntheses, properties and potential applications of multicomponent magnetic nanoparticles *Adv. Func. Mater.* **2008**, *18*, 391-400.
- [Zha96] Zhang, Y. M.; Wiesner, U.; Yang, Y. L.; Pakula, T.; Spiess, H. W. Annealing effects on orientation in dynamically sheared diblock copolymers *Macromolecules* **1996**, *29*, 5427-5431.
- [Zha01] Zhao, H. Y.; Douglas, E. P.; Harrison, B. S.; Schanze, K. S. Preparation of CdS nanoparticles in salt-induced block copolymer micelles *Langmuir* **2001**, *17*, 8428-8433.

- [Zha07] Zha, W. B.; Han, C. D.; Lee, D. H.; Han, S. H.; Kim, J. K.; Kang, J. H.; Park, C. Origin of the difference in order-disorder transition temperature between polystyrene-block-poly(2-vinylpyridine) and polystyrene-block-poly(4-vinylpyridine) copolymers *Macromolecules* **2007**, *40*, 2109-2119.
- [Zhan06] Zhang, L.; He, R.; Gu, H. C. Oleic acid coating on the monodisperse magnetite nanoparticles *Appl. Surf. Sci.* **2006**, *253*, 2611-2617.
- [Zhao06] Zhao, S. Y.; Lee, D. K.; Kim, C. W.; Cha, R. G.; Kim, Y. H.; Kang, Y. S. Synthesis of magnetic nanoparticles of Fe<sub>3</sub>O<sub>4</sub> and CoFe<sub>2</sub>O<sub>4</sub> and their surface modification by surfactant adsorption *B. Kor. Chem. Soc.* **2006**, *27*, 237-242.
- [Zha09] Zhao, Y.; Thorkelsson, K.; Mastroianni, A. J.; Schilling, T.; Luther, J. M.; Rancatore, B. J.; Matsunaga, K.; Jinnai, H.; Wu, Y.; Poulsen, D.; Frechet, J. M. J.; Alivisatos, A. P.; Xu, T. Small-molecule-directed nanoparticle assembly towards stimuli-responsive nanocomposites *Nat. Mater.* **2009**, *8*, 979-985.
- [Zhe02] Zheng, J.; Stevenson, M. S.; Hikida, R. S.; Van Patten, P. G. Influence of pH on dendrimer-protected nanoparticles *J. Phys. Chem. B* **2002**, *106*, 1252-1255.
- [Zin99] Zins, D.; Cabuil, V.; Massart, R. New aqueous magnetic fluids *J. Mol. Liq.* **1999**, *83*, 217-232.
- [Zoe08] van Zoelen, W.; Asumaa, T.; Ruokolainen, J.; Ikkala, O.; ten Brinke, G. Phase behavior of solvent vapor annealed thin films of PS-b-P4VP(PDP) supramolecules *Macromolecules* **2008**, *41*, 3199-3208.

## ***List of publications***

1) **Horechyy A.**, Nandan B., Zafeiropoulos N.E, Stamm M. Micro and macrophase separation of polymer-coated nanoparticles in block copolymer thin films: an affect of stabilizing shell nature. *Manuscript under preparation*

2) **Horechyy A.**, Nandan B., Zafeiropoulos N.E, Oertel U., Bigall N.C., Eychmüller A., Formanek P., Stamm M. A novel approach towards bi-nanoparticles patterning *via* block copolymer self-assembly. *Manuscript under preparation*

3) Tzavalas S., **Horechyy A.**, Detrembleur C., Petzold G., Schwarz S., Zafeiropoulos N.E., Stamm M., Rojas R. Role of the critical micelle concentration on the stability of carbon nanotube dispersions in water. *Submitted manuscript*

4) **Horechyy A.**, Zafeiropoulos N.E., Nandan B., Formanek P., Simon F., Kiriya A., Stamm M. Highly ordered arrays of magnetic nanoparticles prepared *via* block copolymer assembly. *Journal of Materials Chemistry*, **2010**, 20, 7734-7741.

## ***Contributions to the conferences***

1) Nandan B., **Horechyy A.**, Zafeiropoulos N., Bigall N., A. Eychmüller A., Stamm M. Block Copolymer Self-Assembly for Bi-Nanoparticles Patterning. Presented at: *International Conference on Frontiers of Polymers & Advanced Materials Macro2010*, Delhi, India, December 15-17, **2010**.

2) Nandan B., **Horechyy A.**, Zafeiropoulos N., Bigall N., A. Eychmüller A., Stamm M. Block copolymer self-assembly for bi-nanoparticles patterning. Presented at: *Polymer Science and Engineering: Emerging Dimensions PSE2010*, Chandigarh, India, November 26-27, **2010**.

3) **Horechyy A.**, Zafeiropoulos N.E., Stamm M. Nanohybrid materials with block copolymers and nanoparticles. Presented at: *10<sup>th</sup> European Symposium on Polymer Blends*, Dresden, Germany, March 7-10, **2010**.

4) **Horechyy A.**, Zafeiropoulos N.E., Nandan B., Formanek P., Simon F., Kiriya A., Stamm M. Highly ordered arrays of Fe<sub>3</sub>O<sub>4</sub> magnetic nanoparticles *via* block copolymer assembly. Presented at: *10<sup>th</sup> European Symposium on Polymer Blends*, Dresden, Germany, March 7-10, **2010**.

5) **Horechyy A.**, Zafeiropoulos N.E., Formanek P., Tsitsilianis C., Stamm M. Synthesis and selective segregation of Fe<sub>3</sub>O<sub>4</sub> nanoparticles inside of the polyvinylpyridine domain of poly(styrene-*b*-vinylpyridine). Presented at: *8<sup>th</sup> International Conference on Advanced Polymers via Macromolecular Engineering APME2009*, Dresden, Germany, October 4-7, **2009**.

6) **Horechyy A.**, Zafeiropoulos N.E., Tsitsilianis C., Stamm M. Synthesis and selective segregation of Fe<sub>3</sub>O<sub>4</sub> nanoparticles inside of the poly-2vinylpyridine domain of poly(styrene-*b*-2vinylpyridine). Presented at: *7<sup>th</sup> Hellenic Polymer Conference*, Ioannina, Greece, September 28-30, **2008**.

## VERSICHERUNG

Hiermit versichere ich, dass ich die vorliegende Arbeit ohne unzulässige Hilfe Dritter und ohne Benutzung anderer als der angegebenen Hilfsmittel angefertigt habe; die aus fremden Quellen direkt oder indirekt übernommenen Gedanken sind als solche kenntlich gemacht. Die Arbeit wurde bisher weder im Inland noch im Ausland in gleicher oder ähnlicher Form einer anderen Prüfungsbehörde vorgelegt.

Die vorliegende Arbeit wurde unter der wissenschaftlichen Betreuung von Prof. Dr. Manfred Stamm an dem Leibniz-Institut für Polymerforschung Dresden e.V. angefertigt. Keine frühere erfolglose Promotionsverfahren statt gefunden haben. Die Promotionsordnung der Technischen Universität Dresden der Fakultät Mathematik und Naturwissenschaft erkenne ich an.

Dresden,.....

Andriy Horechyy



